

**REMOTE SENSING AS A WINDOW INTO PLANETARY VOLCANIC  
ERUPTION STYLES**

by

**Marie Julia Barich Henderson**

**A Dissertation**

*Submitted to the Faculty of Purdue University*

*In Partial Fulfillment of the Requirements for the degree of*

**Doctor of Philosophy**



Department of Earth, Atmospheric, and Planetary Sciences

West Lafayette, Indiana

August 2021

**THE PURDUE UNIVERSITY GRADUATE SCHOOL  
STATEMENT OF COMMITTEE APPROVAL**

**Dr. Michelle Thompson, Chair**

Department of Earth, Atmospheric, and Planetary Sciences

**Dr. Briony Horgan**

Department of Earth, Atmospheric, and Planetary Sciences

**Dr. Lisa Gaddis**

Lunar and Planetary Institute

**Dr. Michael Sori**

Department of Earth, Atmospheric, and Planetary Sciences

**Dr. H. Jay Melosh\***

Department of Earth, Atmospheric, and Planetary Sciences

**Approved by:**

Dr. Daniel J. Czigzo

*This Dissertation is Dedicated to:*

*My grandfather, Stephen J. Barich, (Pop).*

*This dissertation would not exist without your love or support.*

*My life was improved because of you and is not the same without you.*

## ACKNOWLEDGMENTS

Fifty-two years ago today, on July 20, 1969, two humans climbed down the Lunar Module (LM) ladder and stepped on the surface of the Moon, and the world was forever changed. The first man to walk on the Moon, Neil Armstrong, and the 12<sup>th</sup> and most recent moonwalker, Gene Cernan, both attended Purdue University along with 23 other astronauts. I loved being a student at the ‘Cradle of Astronauts’ with a rich history in space exploration, where my passion was celebrated. These acknowledgments are lengthy, but I want to capture all the amazing humans who made this dissertation possible.

Indiana was not at the top of the list of places to live for five years of my life. However, my advisor Professor Dr. Briony Horgan Ph.D. ☺, made it completely worthwhile. My graduate career and this dissertation were a success because of Briony. She is inspiring, motivating, and an academic powerhouse while also being supportive and patient. When the breakdowns happened, Briony was there to help me find my footing again and never made me feel guilty for taking time for mental and physical health. I feel so much pride when I tell others about my advisor and feel very fortunate that our relationship as colleagues and friends will continue for years to come. Thank you, Briony, for everything you have done for me. I am forever grateful to have been your student.

My successful experience at Purdue extended beyond my advisor and the other members of my committee. It has been greatly enhanced by the people within Briony’s lab group, my officemates, and the graduate students and postdocs in EAPS. I loved being surrounded by people who understood this crazy life we all chose. To the future, Dr. Noel Scudder, there is no other person I would have wanted as my academic twin. Thanks for being a wonderful friend, field partner, my mineralogy go-to, an integral part of my support system, and an usher at my wedding. I’m so proud of you, and I’m so thankful we experienced this together. I would also like to acknowledge Dr. Jay Melosh; I was so fortunate to have learned from you both in the classroom and the field. You helped shape this dissertation, and I’m sad you are not here to be a part of my defense. I’m also thankful that two of my committee members, Dr. Mike Sori and Dr. Michelle Thompson, joined the faculty at Purdue and enhanced this dissertation. This department is very

different from when I started, and it has been an honor to watch the Planetary Science group grow and become a powerhouse graduate school.

Before I came to Purdue, I was fortunate to have other mentors significantly shape my life: Dr. Dave Williams, Nicole Spanovich, Dr. Joy Crisp, Dr. Herb Frey, and Dr. Ken Edgett. All of my experiences through my internships at NASA Goddard and JPL were magnificent. I was able to let my passion soar and watch my efforts become a part of space exploration. These experiences complemented my undergraduate degree from the Florida Institute of Technology and prepared me to succeed in the field of planetary science. My dreams came alive when Dave found a way to make me a multi-year Goddard ‘student contractor’ allowing me to keep working on Apollo ALSEP research and when Nicole and Joy found a way to extend my internship to a Co-Op where I experienced Curiosity’s entire first 90 sols on Mars time. Thank you all for taking the time to get to know me, provide guidance, and supporting my passion for space exploration.

My first internship was part of the NASA Lunar and Planetary Science Academy at Goddard Space Flight Center, where I worked with Dr. David R. Williams. It was the first time I saw a scientist whose love for space history and sarcasm matched my own, leading to an instant bond. I had never known that going to get a Ph.D. in planetary science was an option or how life could be as a scientist at NASA. Dave answered every question I had, found ways to take me to conferences, and introduced me to every person he could. Dave truly set me up for success and gave me the foundation to build a career. Dave, thank you for treating me like a member of your family and for calming me through the frustrating preparation of my first talk alongside Jack Schmitt.

I was first introduced to Dr. Ken Edgett as an intern at JPL before Curiosity landed. When given a chance to stand in the Mars testbed to watch a drilling test, I found my way to stand near the instrument PIs, including Ken, hoping maybe they would talk to me. Ken asked me how long I would be an intern, and I responded that my internship would end two weeks after the rover landed. With a look of disbelief, Ken replied: “What? You are going to miss the best part! There is going to be a rover on Mars. You should see if you can stay.” That response changed everything, and when the rover landed, I found a way to stay. When at a second crossroads in my life with time to spare between undergrad and grad school, I reached out to Ken again for advice. He invited me to come work for him at Malin Space Science Systems in San Diego. Working for Ken was an

unforgettable time, full of learning and amazing memories. Thank you, Ken, for sharing your passion with me, providing opportunities where I did not know they existed, and quite literally changing my life. You are an incredible scientist, mentor, and friend.

Part of this dissertation, Chapter 4, was completed at the U.S. Geological Survey Astrogeology Science Center. I'm very thankful to have gotten to the experience of working in Flagstaff and alongside my committee member Dr. Lisa Gaddis. Thank you, Lisa, for taking the time to mentor and advise me. This dissertation benefited greatly from your experience, guidance, as well as funding through your successful proposal. My time in Flagstaff was possible through the generosity and friendships of Dr. Kristen Bennett, Dr. Lauren Edgar, and Dr. Justin Hagerty. Thanks for opening your homes and offices to me and providing me with a support system, constant dog pictures, and tv fantasy leagues to help me through rough days.

Many friendships have enhanced my life. These humans have propelled me to finish this Ph.D. I could not have made it without their support and the comic relief they have provided. Thank you to my best friends, some of whom have supported me since elementary school (Lauren, Hal, Olivia, and Britt), and those I met in college (Kristen E, Ali, James, John, Shiva, and Justin R.). Thanks to my friends in San Diego who helped push me back to grad school and always welcome me back with open arms (Jason, Katie, Kevin, AJ, and the TCSD). I was also fortunate to have so many friends experience grad school with me or recently graduated giving constant support (Amanda, Adeene, Allie R., Becky, Dara, Sarah, Heather, Vanessa, and Andrea). Trying to finish a Ph.D. in a pandemic wouldn't have been possible without so many virtual chat groups that kept me connected to my friends and constantly made me laugh (7<sup>th</sup> wheel, No Rupologies, Pavel's Posse, and Quarantine Friends). When Tim and I moved to DC during a pandemic, I was fortunate to have found a new support system in our neighbors (Christopher, Justin, John Ben, Brandi, Daley, Michael, Lou, and Cherie). Thank you all for helping me through this pandemic and the final stretch of this Ph.D. A special shout-out to John Ben and Brandi for providing me a beautiful dissertation cave to use for the past two months.

A fantastic, one-of-a-kind friend of mine, Jason Van Beek, once said: "your family must really love you for supporting your effort to get a degree in something obscure like planetary science." Truer words really couldn't have been spoken. From the moment I said the words out loud that I wanted to be an astronaut, I received love, encouragement, support, and only a little bit

of fear from Mommy and Pop. They took me to museums and sent me to Space Camp's Advanced Space Academy. I've been very fortunate Mommy, Pop, and now my stepdad, Ken, have always showed up for so many moments in my life. They were always so proud and supportive, and it never mattered how far they had to travel to be there. I always feel so lucky that during every sporting event or nerdy moment in my life, I could look up and see my family. To my family, Mommy, Pop, Ken, Kristen, and Brett, you have all given me the strength, determination, and love that allowed me to get where I am today.

I also want to acknowledge my sister, Kristen, thanks for helping me survive this last year. You have always pushed me in more ways than you know. Thanks for only making a little bit fun of me when I would find myself working on vacation or only slightly rolling your eyes when I got into another conversation about space, lol. Thanks for always telling me to keep pushing through and being ready to give me a place to stay when giving talks in New York or when I got stranded with all my camping equipment on the way home from Russia.

Mommy, I really couldn't have made it through life without you. Thanks for being two parents to me. From the endless hours you spent practicing Math 24, checking every homework assignment through high school, and attending every competition, your dedication to your children is inspiring. Though I'm thrilled you didn't have to proofread this dissertation, I'm so happy you are here to share in the joy of the accomplishment. Thanks for constantly pushing me, helping me find solutions to any predicament, and continuously bringing out my competitive side; I love you.

Since I came to Purdue, I added a new member to my family, my husband, Tim. I did not expect to meet the person I would marry on the first day of grad school orientation. You have been with me through every step of earning this degree, and I'm so proud to have shared this adventure with you. Every high and every low of this Ph.D. I have found myself beside you. When I was stressed, you lifted me up, wiped my tears, and handed me a glass of wine at the end of the day. Thank you for loving me through the stress and the success and building a life with me, including adopting my favorite co-worker, Indy. I cannot wait to finally experience life with you where I am not pursuing this degree.

Lastly, I want to acknowledge the person this dissertation is dedicated to, my grandfather, Pop. There are so many things I wish I could say to you and thank you for at this moment; it is overwhelming. I know this day was the next milestone you wanted to live to see, and it destroys

me that you are not here to celebrate. Thank you for helping to raise me, constantly supporting me, and pushing me to be the best. I appreciate all the calls where you would tell me to get my work done while reminding me not to forget to rest. Thank you for always cutting out every newspaper or magazine article you saw about space, and mailing it to me, and continuing to challenge me. Also, Pop, thanks for using the savings from your hard work to take me to travel the world. Those trips were the initial sparks that led me to geology and volcanology. I am so fortunate that I first witnessed the volcanology of Hawaii, Italy, Greece, New Zealand, Iceland, and the Galapagos with you and that those memories are intricately tied to my research. I love and miss you, Pop.

# TABLE OF CONTENTS

LIST OF TABLES .....	13
LIST OF FIGURES .....	14
ABSTRACT.....	18
CHAPTER 1. INTRODUCTION.....	19
1.1 Summary and Motivation.....	19
1.2 Background and Relevant Studies.....	20
1.2.1 Explosivity of Volcanic Eruptions and Explosive Eruption Styles.....	20
1.2.2 Formation of Glass in Volcanic Eruptions .....	23
1.2.3 Explosive Volcanic Deposits on Mars .....	24
1.2.4 VNIR and TIR spectral properties of volcanic glass and tephra.....	25
1.2.5 Lunar Pyroclastic Deposits.....	27
1.2.6 Moon Mineralogy Mapper Instrument Data .....	29
1.2.7 Relevance to Future Exploration.....	30
1.3 Objectives, Tasks, and Outcomes.....	32
1.4 References .....	33
CHAPTER 2. DETERMINING THE VOLCANIC ERUPTION STYLE OF TEPHRA DEPOSITS FROM INFRARED SPECTROSCOPY .....	41
2.1 Introduction .....	41
2.2 Background.....	42
2.3 Materials and Methods .....	44
2.3.1 Sample Suite.....	44
2.3.2 X-Ray Diffraction.....	46
2.3.3 Visible/Near-Infrared Spectra .....	47
2.3.4 Thermal-Infrared Spectra .....	48
2.3.5 Mixture Study.....	51
2.4 Results .....	52
2.4.1 VNIR Spectra and Mineral Interpretations .....	52
2.4.2 TIR Spectra and Deconvolution Models .....	55
2.4.3 Mixture Study.....	59

2.5	Discussion.....	62
2.5.1	Detecting Eruption Styles in VNIR, TIR, and XRD Data .....	62
2.5.2	Strategies for Determining Eruption Styles on Mars .....	63
2.5.3	Differentiating Impact and Volcanic Glasses.....	65
2.6	Conclusions .....	65
2.7	Data Availability Statement .....	66
2.8	Acknowledgements .....	66
2.9	References .....	67
<b>CHAPTER 3. MINERALOGY OF EXPLOSIVE AND EFFUSIVE VOLCANIC EDIFICES</b>		
<b>IN THE MARIUS HILLS VOLCANIC COMPLEX.....</b>		
3.1	Introduction .....	76
3.2	Background.....	78
3.2.1	Marius Hills Volcanic Complex.....	78
3.2.2	History of MHVC Spectral Studies.....	79
3.2.3	Domes in the MHVC.....	81
3.2.4	Cones in the MHVC .....	82
3.3	Methods .....	85
3.3.1	Moon Mineralogy Mapper .....	85
3.3.2	M <sup>3</sup> Mapping.....	86
3.3.3	Spectral Parameters and Mineral Identification .....	87
3.3.4	Cone Classification and Analysis.....	90
3.4	Results .....	91
3.4.1	Spectral Mapping .....	91
3.4.2	Domes.....	95
3.4.3	Cones.....	98
3.4.4	Plateau Mare.....	102
3.5	Discussion.....	103
3.5.1	Significance of glass detection in the MHVC cones.....	103
3.5.2	Diverse Cone Morphologies in MHVC.....	105
3.5.3	Possible Primitive Volcanics Preserved in MHVC domes .....	105
3.5.4	Volcanic Evolution of the MHVC.....	106

3.5.5	Implications for Future Exploration .....	108
3.6	Conclusions .....	109
3.7	Acknowledgments .....	110
3.8	References .....	110
CHAPTER 4. SPECTRAL DIVERSITY OF EXPLOSIVE VOLCANIC DEPOSITS IN		
SCHRODINGER BASIN ON THE MOON .....		
		117
4.1	Introduction .....	117
4.2	Background.....	119
4.2.1	Schrödinger Basin .....	119
4.2.2	Lunar Pyroclastic Deposits.....	121
4.2.3	History of Schrödinger Spectral Studies .....	123
4.3	Methods .....	126
4.3.1	Moon Mineralogy Mapper .....	126
4.3.2	Spectral Parameters and Mineral Identification .....	129
4.3.3	Clementine.....	131
4.4	Results and Spectral Interpretations .....	132
4.4.1	Inner-peak ring and basin floor .....	133
4.4.2	Schrödinger Cone .....	135
4.4.3	Lobate Mafic Unit .....	135
4.4.4	Linear Ridge Unit.....	136
4.5	Discussion.....	137
4.5.1	Origin of the Schrödinger Cone and implications for SPA volcanism .....	137
4.5.2	Inner-Peak Ring Lobate Mafic Unit.....	138
4.5.3	Linear Ridge Unit.....	139
4.5.4	Relationship between volcanic units in Schrödinger .....	140
4.5.5	Constraints on eruption properties from comparison to other pyroclastic deposits	
	141	
4.5.6	Proposed Exploration .....	142
4.6	Conclusion .....	143
4.7	Acknowledgments .....	144
4.8	References .....	145

CHAPTER 5. CONCLUSION.....	151
5.1 Conclusions .....	151
5.2 Future Investigations .....	155
5.3 References .....	155
VITA.....	164

## LIST OF TABLES

Table 1-1. Various intrinsic (magma properties, green) or extrinsic (blue) parameters have been suggested to affect eruption explosivity and can be implications for planetary exploration. Modified from (Cassidy et al., 2018).....	22
Table 2-1. Summary of samples in this study.....	45
Table 2-2. Endmember Spectra Used for Quantitative TIR Linear Deconvolution Models categorized as they appear in the Figure 2-5 pie charts.....	51
Table 2-3. Summary of the VNIR Spectral Interpretation Expected TIR Assemblages by Tephra Type .....	54
Table 3-1. Definitions of spectral parameters used for spectral interpretation and making composite and band parameter maps.....	88
Table 3-2. The listed amount of each type of cinder cone morphology as outlines in the Lawrence et al. (2013) paper, compared to this study when spectroscopy was added as a distinguishing component.....	101
Table 5-1. Explosive Volcanic Endmembers that have been analyzed with M3 spectral data. .	154

## LIST OF FIGURES

Figure 1-1: Volatiles as dissolved gasses in the magma solution of the terrestrial bodies that increase fragmentation and eruption explosivity. (Airey et al., 2015; Fegley and Swindle, 1993; Kerber et al., 2009; Wallace et al., 2015; Wilson and Head, 2007) .....	21
Figure 2-1. Tephra samples used in this study (not including Tseax cinders) before being crushed, sieved, and pressed into pellets for spectral analysis. ....	46
Figure 2-2. Laboratory reference spectra of minerals common in volcanic environments in the (a) visible/near-infrared (VNIR) (Horgan et al., 2017; Kokaly et al., 2017) and (b) thermal infrared (TIR) (see citations in Table 2). ....	48
Figure 2-3. (a) Visible/near-infrared (VNIR) reflectance spectra and (b) thermal infrared (TIR) emission spectra of volcanic tephra samples, ordered by X-ray diffraction (XRD) crystallinity, decreasing from top to bottom, and colored by eruption type (purple = magmatic cinders, blue = phreatomagmatic, yellow/orange/red = magmatic). Dashed lines indicate wavelength positions of major absorption bands. ....	53
Figure 2-4. Comparison of bulk (open symbol) and groundmass (closed symbol) X-ray diffraction (XRD) crystallinities of the tephra to the position of their 1 $\mu\text{m}$ band center in VNIR spectra. The phreatomagmatic and cinder cone tephra display clear 1 $\mu\text{m}$ bands with two distinct groups of band centers: near 1.08 $\mu\text{m}$ , interpreted as due to glass, and 0.95 $\mu\text{m}$ , interpreted as due to either devitrified glass or spectrally dominant iron oxides in palagonite. Most magmatic tephra samples (e.g., scoria) do not exhibit clear 1 $\mu\text{m}$ bands and are omitted. ....	55
Figure 2-5. Tephra mineralogies modeled from linear deconvolution of thermal infrared (TIR) spectra, separated by eruption style and tephra type. Red/pink indicates X-ray amorphous phases, blues indicate alteration minerals, and green/yellow indicate crystalline igneous minerals. ....	57
Figure 2-6. Comparison of thermal infrared (TIR) modeled crystallinity to bulk (open symbol) and groundmass (closed symbol) X-ray diffraction (XRD) crystallinities. Horizontal lines indicate the range of measured XRD crystallinities for each sample. Dotted trendlines represent standard errors in TIR measurements. ....	58
Figure 2-7. Spectra of physical mixtures of glasses and San Carlos olivine and pyroxene phenocrysts, with glass content increasing in 10 wt.% intervals. (a) Visible/near-infrared (VNIR) reflectance spectra and (b) thermal infrared (TIR) emission spectra. ....	59
Figure 2-8. Analysis of physical mixture spectra. (a) The position of the 1 $\mu\text{m}$ band center with respect to the expected crystallinity in the mixing study. As the amount of glass in the mixture decreased, the band center also decreased and can be used to determine relative glass abundance and potentially eruption style. (b) Comparison of the thermal infrared (TIR) crystallinities of the mixtures to their expected X-ray diffraction (XRD) crystallinities. The glass slide endmember did not have a representative glass type in the spectral library, which could account for the diversion from the trendline at low crystallinities. This mixing study does not display the over-modeling of glass seen in the tephra samples. ....	61

Figure 3-1. a. Marius Hills Volcanic Complex is outlined on the near side of the Moon within the Oceanus Procellarum b. Perspective Image of Marius Hills taken by NASA’s Lunar Orbiter 2 in 1966 (NASA/Lunar and Planetary Institute). ..... 76

Figure 3-2. (a) Examples from Earth of volcanic morphologies previously identified in the MHVC. (a) Image of San Cristobal Island, Galapagos taken from the water by M. Henderson. The island is a shield volcano with the typical low slope flanks designated by the white dashed line. Parasitic cinder cones erupted from the shield creating the edifices designated by the arrows. The bottom of the figure shows an Earth-analog and lunar example of each cone shape classification from (Lawrence et al., 2013). (b) N-class cones that do not display a breach (lunar diameter: ~1.5km) (c) C-class cone with breach of cone wall (lunar diameter: ~1.5km) (d) E-class elongated cone representing eruption along a fissure (lunar diameter: ~1.25km). Lunar cones imaged by LROC NAC. All Earth analog images are open source photographs. .... 83

Figure 3-3. Selected continuum-removed laboratory VNIR spectra of orthopyroxene (OPX), clinopyroxene (CPX), glass, and olivine, showing the deep and broad bands due to iron centered near 1 and sometimes 2  $\mu\text{m}$  exhibited by these minerals. Variability in band center, shape, and depth within mineral groups can occur due to variations in composition and grain size. .... 89

Figure 3-4. Maps of regional-scale morphology and spectral properties of the Marius Hills Volcanic Complex (MHVC). (a) Wide-angle camera (WAC) mosaic from the Lunar Reconnaissance Orbiter Camera (LROC) (b) Topography from Lunar Orbiter Laser Altimeter (LOLA) overlaid on the LROC WAC mosaic. (c-d) Mosaicked composite RGB spectral maps from  $M^3$  data where R= glass band depth parameter, G=1 $\mu\text{m}$  band center parameter, B= 2 $\mu\text{m}$  band center parameter. (c)  $M^3$  mosaic of high-resolution cubes (140 m/pixel) collected during OP2A and OP2B. (d)  $M^3$  mosaic of low-resolution cubes (280 m/pixel) collected during OP2C. The horizontal variability and striping across the  $M^3$  frames is due to changes in resolution and sensitivity. .... 92

Figure 3-5. Glass band depth parameter maps overlaid on LROC WAC Mosaic of the Marius Hills Volcanic Complex. Warmer colors in parameter maps represent locations where the spectra are most likely to be representative of glass, but may also indicate olivine. (a) Low-resolution glass map, 280m/pixel. (b) High-resolution glass map, 140m/pixel. (c) Zoomed in section of high-resolution glass map overlaid on LROC NAC mosaic showing process of reviewing cone-like morphologies from (Lawrence et al., 2013) with  $M^3$  spectral parameters. .... 93

Figure 3-6. Selected  $M^3$  continuum-removed and smoothed spectra showing differences between the cones (blue), domes (green), and mare (red) within the MHVC. Dotted lines indicate 1 $\mu\text{m}$  and 2 $\mu\text{m}$  wavelength positions for comparison between the spectra. Gray background spectra are continuum removed and unsmoothed. .... 94

Figure 3-7. Reconstructed map in the style of Figure 1 in Lawrence et al. (2013) with updated cone types and locations overlaid on an LROC WAC mosaic. Colored shapes indicate the cinder cone morphology and the locations based on a combination of topography, visual images, and spectral data. Outlined white terrain are interpreted as dome morphologies, and the orange lines represent rille locations. .... 96

Figure 3-8. Marius Hills Cone located approximately 305.5°E and 13.8°N (solid outline) on a volcanic dome (dashed outline). (a) LROC NAC image mosaic (b)  $M^3$  RGB composite image

where R= glass band depth parameter, G=1 $\mu$ m band center parameter, B= 2 $\mu$ m band center parameter (c) Glass parameter map image where warmer colors indicate spectral shapes consistent with glass or olivine. All images show that the cone can be distinguished from the dome by morphological and spectral properties. .... 97

Figure 3-9. Spectral band parameter graphs of the MHVC cones, domes, and mare. Labels indicate the approximate parameters and trends expected based on laboratory spectra of endmembers and mixtures analyzed by (Horgan et al., 2014) and (Klima et al., 2007). .... 98

Figure 3-10. LROC NAC images depicting known volcanic cones based on morphology from Lawrence et al. (2013). Bottom: Above locations in the glass parameter maps where areas of a deeper green color represent locations where the spectra are most likely to be representative of glass. The shape and orientation of the cones are similar in both images. .... 99

Figure 3-11. A rose diagram that showing the orientation of E-class cones along fissures. The majority of cones are oriented in the NNW-NNE and SSW-SSE directions. .... 102

Figure 4-1. Schrödinger basin context. (a) LROC WAC mosaic of the South Pole showing the location of Schrödinger basin outlined in yellow. (b) LROC WAC mosaic of Schrödinger Basin, basin diameter is 320 km. (c) LOLA elevation data overlain on LROC WAC mosaic. .... 117

Figure 4-2. (a) Perspective view of Schrödinger basin. Illustration credit: NASA Scientific Visualization Studio (NASA SVS). (b) Inner-peak ring image with pyroclastic deposits analyzed in this study outlined and labeled. (c) LROC low-sun NAC mosaic. Within the box are locations of potential cones that may have been the source of the lobate mafic unit. (d) Perspective view of the vent on the Schrödinger Cones. .... 120

Figure 4-3. M<sup>3</sup> maps covering the entirety of Schrödinger Basin and enlarged to focus on the volcanic units within the inner- peak ring, compared to Clementine-derived geochemistry. (a) M<sup>3</sup> albedo map derived from reflectance at 2976 nm. (b) LOLA elevation data overlain on LROC WAC mosaic. LOLA elevation data overlain on LROC WAC mosaic (c-d) Glass band depth parameter map overlaid on LROC WAC Mosaic of Schrödinger Basin. Warmer colors in parameter maps represent locations where the spectra are most likely to represent glass. (e-f) Mosaicked composite RGB spectral maps from M<sup>3</sup> data where R= glass band depth parameter, G=1 $\mu$ m band center parameter, B= 2 $\mu$ m band center parameter. Green colors indicated OPX on the basin floor, blue indicates CPX, and yellow/pink indicates possible glass, mixtures with glass, or olivine. (g-h) Clementine UVVIS/FeO abundance data where warmer colors represent locations with higher FeO wt%. White outlines show mapped extent of possible volcanic units as labeled in Figure 2. .... 128

Figure 4-4. Subset of Schrödinger volcanic units within the inner-peak ring (a-c) focus on the pyroclastic cone (d-f) are focused on the lobate mafic and ridge units. (a,d) LOLA elevation data overlain on LROC WAC mosaic. (b,e) Mosaicked composite RGB spectral maps from M<sup>3</sup> data where R= glass band depth parameter, G=1 $\mu$ m band center parameter, B= 2 $\mu$ m band center parameter. (c,f) Glass band depth parameter map overlaid on LROC WAC Mosaic. Warmer colors in parameter maps represent locations where the spectra are most likely to be representative of glass. .... 133

Figure 4-5. (a) Selected M<sup>3</sup> continuum-removed and smoothed spectra from Schrödinger volcanic units that have been averaged to reduce noise. Spectra show differences between the

pyroclastic cone (blue), ridge unit (red), potential cones in the lobate mafic unit (orange), lobate mafic unit (purple), and the inner-peak ring floor (green). Dotted lines indicate 1 $\mu$ m and 2 $\mu$ m wavelength positions for comparison between the spectra. Gray background spectra are continuum removed and unsmoothed. (b) Spectral band parameter graphs of the Schrödinger volcanic units. Labels indicate the approximate parameters and trends expected based on laboratory spectra of endmembers and mixtures analyzed by (Horgan et al., 2014) and (Klima et al., 2007). ..... 134

## ABSTRACT

Evidence of past volcanic activity has been found on many planets and moons in our Solar System, and volcanism represents a common process that ties together the geologic history of planetary bodies. Volcanic eruptions are a unique geologic process that link the planet's interior to the surface and the atmosphere/exosphere. A key planetary science objective described in the 2013-2022 Decadal Survey is to characterize planetary surfaces and understand their modification by geologic processes, including volcanism. The Earth, Moon, and Mars have evidence of past effusive and explosive volcanic eruptions, creating a range of volcanic edifices, landforms, flows, and pyroclastic deposits. This dissertation strives to understand the composition and eruption style of explosive volcanic deposits on the terrestrial bodies of the Earth, the Moon, and Mars. These deposits provide critical insights into the volcanic and volatile histories of the bodies and may provide in situ resources for future planetary explorers. I utilize data from orbital and laboratory spectrometers to analyze volcanic tephras across the solar system. My dissertation uses new techniques from lab studies to inform orbital spectroscopy and geomorphology comparisons of explosive volcanic deposits. By identifying glass and other igneous minerals in the visible/near-infrared and thermal infrared orbital spectra of volcanic deposits we can infer volcanic eruption style and constrain the history of explosive volcanism of planetary bodies. With remote sensing, I investigated a large and ancient volcanic complex, the Marius Hills, with significant implications for the early volcanic history of the Moon and the pyroclastic deposits of a single impact basin, Schrödinger, that has been selected as a landing site for robotic missions in 2024. This dissertation expands on the previous limited understanding of explosive vs effusive volcanism on the Moon, with the ability to further constrain eruption styles with remote sensing. The results presented in this dissertation are directly relevant to the future goals of NASA and the effort to return humans to the lunar surface and have increased the science return of lunar missions like the ISRO/NASA Moon Mineralogy Mapper.

# CHAPTER 1. INTRODUCTION

## 1.1 Summary and Motivation

Evidence of past volcanic activity has been found on many planets and moons in our solar system and volcanism represents a common process that ties together the thermal evolution and geologic history of planetary bodies. Volcanic eruptions are a unique geologic process that link the planet's interior to the surface and the atmosphere/exosphere. A key planetary science objective is to characterize planetary surfaces and understand the modification by geologic processes, including volcanism (National Research Council, 2011). The Earth, Moon, and Mars have evidence of past effusive and explosive volcanic eruptions, creating a range of landforms, including positive and negative-relief features, lava flows, ponds and expansive maria, explosively erupted volcanic pyroclasts.

In this dissertation, I strive to understand the composition and eruption style of explosive volcanic deposits on the terrestrial bodies of the Earth, Moon, and Mars. These deposits have not been well understood even though they provide insight to the volcanic and volatile histories of the bodies and may have in situ resources implications for future planetary explorers. Orbital and laboratory spectrometers are used to analyze volcanic tephra as they have collected compositional data across the solar system. I identify glass and other iron-bearing minerals in the visible/near-infrared and thermal infrared spectra of volcanic deposits to infer volcanic eruption style and constrain the history of explosive volcanism of planetary bodies. This dissertation is divided into three chapters:

1. *Determining the Volcanic Eruption Style of Tephra Deposits from Infrared Spectroscopy* - Demonstrates that thermal infrared (TIR) and visible/near-infrared (VNIR) data are both sufficient to detect increased glass abundances in explosive volcanic deposits on Earth, potentially indicating volatile interactions during an eruption, and that glass-poor tephra have distinct TIR properties that can be used to infer tephra type (e.g., ignimbrite vs. scoria; Henderson et al., 2020).
2. *Mineralogy of Explosive and Effusive Volcanic Edifices in the Marius Hills Volcanic Complex* - Presents the first detections of volcanic glass in the Marius Hills Volcanic Complex, which constitutes the first detections outside of arially extensive pyroclastic

mantling deposits mapped on the Moon. This work provides new insight into the long history of volcanism in an area that is a key target for future exploration.

3. ***Spectral Investigation of Explosive Volcanic Deposits in Schrödinger Basin on the Moon*** – The first hyperspectral mapping of Schrödinger basin, an upcoming landing site, which identified multiple pyroclastic deposits to be of similar source but of variable eruption style. This chapter presents new data on the role of crustal thickness on the explosivity of lunar volcanic eruptions.

This work has direct implications for future planetary exploration. Through the techniques of spectral parameter analysis and large-scale spectral mapping, this work builds and compares datasets to answer critical questions about the causes of explosivity on the Moon. The spectral analysis of multiple pyroclastic deposits included in this dissertation in conjunction with similar analyses of other lunar pyroclastic deposits (Bennett et al., 2016; Gaddis et al., 2016; Horgan et al., 2014; McBride et al., 2016) has revealed the complexity of the composition, morphology, and occurrence of lunar explosive volcanism. However, the spectral interpretations are only part of the story. Therefore, future research will expand on this work to answer the questions: 1. What is the diversity (compositions, size, etc.) of pyroclasts from explosive eruptions on the Moon, and what are the driving mechanisms of the eruptions? 2. Can integrating additional lunar orbital datasets (e.g., topography, surface roughness, and radiometers) with the spectral interpretations give further insight into the drivers and pyroclast properties of explosive volcanic deposits?

## **1.2 Background and Relevant Studies**

### **1.2.1 Explosivity of Volcanic Eruptions and Explosive Eruption Styles**

Volcanoes can erupt with a range of explosiveness, from the effusive low-viscosity smooth lava flows seen in Hawaii to the iconic eruption of Mt. St. Helens in Washington in 1980 where the abrupt collapse of a flank released pressure allowing hot water in the system to flash to steam, initiating a hydrothermal blast through the landslide scar, and extending to the Earth's largest known explosive eruption of Toba volcano in Indonesia that expelled an estimated 2,800 cubic km of ash about 74,000 years ago (Newhall and Self, 1982). In a 'typical' explosive eruption the solid

or liquid magma is transformed into a mixture of gas and particles through fragmentation. Fragmentation occurs as magma rises, when the dissolved gases (Figure 1-1) in the magma begin to come out of solution due to depressurization. The gasses for bubbles then expand and fragment the magma. Bubbles bursting can create a more explosive eruption, especially in viscous magma. When the magma fragments are small, they can quickly quench before crystallizing. This creates glass, which is an indicator of explosive eruptions when present in large quantities (Wall et al., 2014).

				
<b>Mercury</b> Sulfur Dioxide Carbon Dioxide Carbon Monoxide or Water  [Kerber et al, 2009]	<b>Venus</b> Carbon Dioxide Water  [Airey et al, 2015]	<b>Earth</b> Water Carbon Dioxide Sulfur Chlorine Fluorine  [Wallace et al, 2015]	<b>Moon</b> Carbon Monoxide Water  [Fegley and Swindle, 1993]	<b>Mars</b> Water Carbon Dioxide Sulfur  [Wilson and Head, 2007]

Figure 1-1: Volatiles as dissolved gases in the magma solution of the terrestrial bodies that increase fragmentation and eruption explosivity. (Airey et al., 2015; Fegley and Swindle, 1993; Kerber et al., 2009; Wallace et al., 2015; Wilson and Head, 2007)

Many properties and parameters may influence volcano explosivity, both intrinsically and extrinsically (Cassidy et al., 2018). Extrinsic factors are typically related to the geologic environment where the volcano is located, while the intrinsic parameters would be limited to magma properties. These parameters may interact to create a more or less explosive eruption; there is no single way to produce an explosive eruption (Cassidy et al., 2018). Table 1-1 is a modified chart from Cassidy et al., 2018, that describes a subset of intrinsic (green) and extrinsic (blue) parameters and how these factors can have implications for planetary exploration. Investigating explosive volcanic deposits can illuminate the properties and history of a planetary body's surface and atmosphere through studying the pyroclasts' composition, morphology, and dispersal making them an ideal exploration candidate

Table 1-1. Various intrinsic (magma properties, green) or extrinsic (blue) parameters have been suggested to affect eruption explosivity and can be implications for lunar exploration. On Earth and Mars, interaction with extrinsic water can increase explosivity. Modified from (Cassidy et al., 2018).

Subset of Factors	Description	Implication for Lunar Exploration
<b>Magma Volatile Content</b>	Dissolved volatiles (e.g., water and carbon monoxide) in the magma.	Indicators of past volatiles (including water)
<b>Magma depth/pressure</b>	Density and buoyancy contrast between crust and magma, crustal structure/discontinuities.	The source and depth of lunar magmas are still unknown
<b>Magma ascent rate</b>	The speed of magma ascent to surface from magma reservoir affected by magma buoyancy, volatiles, conduit geometry, chamber overpressure, and viscosity.	Differing lunar 'atmospheric' and subsurface pressures can influence the ascent rate and decompression of the magma.
<b>Rate of decompression</b>	The speed of the release of magma pressure.	
<b>Crustal properties and conduit/vent geometries</b>	Properties of crust, regional geology, and geometry of the conduit (e.g., diameter).	Changes in lunar crustal composition and permeability can affect the degassing of magma

Magma ascent and decompression (Table 1-1) usually happen contemporaneously, and the rates of these processes are potentially the most critical parameters controlling volcanic style (Cassidy et al., 2018). These factors affect eruptive style by bringing the magma to surface before it has the chance to degas or release pressure leading to increased fragmentation. Intrinsically, increased dissolved volatiles in the magma directly influence increased fragmentation and therefore explosiveness (Cashman and Scheu, 2015). Understanding the composition, distribution, and origin of planetary volatiles in the interior is a key outstanding knowledge gap in planetary exploration (National Research Council, 2011). Because volcanic glass is often a key sign of explosive eruptions and can trap magmatic volatiles, explosive volcanic deposits are of high interest for future in situ exploration by landers, rovers, or humans, as well as for sample return to Earth.

There are five classical styles of explosive volcanic eruptions on Earth: 1. Strombolian/Hawaiian fire fountaining eruptions; 2. Vulcanian eruptions; 3. Plinian/Subplinian eruptions; 4. Hydrovolcanic eruptions (phreatomagmatic, phreatic, and hydrothermal); and 5. Submarine explosive eruptions (Houghton, 2015). The eruption styles most relevant to this dissertation and current terrestrial planet exploration are hydrovolcanic, vulcanian, and strombolian/fire

fountaining. In phreatomagmatic or hydrovolcanic explosive eruptions, meteoric water heated by contact or proximity to magma expands as it evaporates to steam, causing rapid fragmenting of the magma into smaller pyroclasts which quench quickly as glass. Vulcanian eruptions require the presence of a plug which is formed when viscous magma cools within the conduit. When pressure builds up behind the plug, the plug can be dislodged, leading to an explosive eruption. The resulting deposit will be composed of blocky plug material, surface or host-rock material (country rock), and minor glass. A strombolian or fire fountaining eruption occurs when gas bubbles within low to intermediate viscosity magma coalesce to form slugs, or giant gas pockets. The gas exsolution rate exceeds the rise rate of the magma, and the slugs ascend, creating periodic eruptions with glass-rich deposits. These eruption styles do exist on other planets, however, as outlined below the factors contributing to explosivity would change (e.g., subsurface and atmospheric pressure, magma composition and volatiles, magma source depths, and crustal properties).

### **1.2.2 Formation of Glass in Volcanic Eruptions**

Glass is an amorphous solid with an atomic structure that lacks the periodicity of crystalline material. Silicate glasses form by the quenching of melted rocks, where rapid cooling promotes vitrification and prevents the crystallization of minerals. Glass forms by numerous natural processes, including impacts, tectonics, and volcanic eruptions (Glass, 2016). Explosive volcanic eruptions form glass during fragmentation and the resulting rapid cooling of the magma, and volatiles can enhance this process both by driving the explosive fragmentation and by helping to quench the fragments. Glass can form in the entire range of volcanic compositions, from mafic to felsic magmas. Thus, magma-volatile interactions, in addition to magma viscosity and composition, affect the glass content of pyroclastic deposits.

The pyroclasts formed by Strombolian/Fire-Fountaining, Vulcanian, and Plinian eruptions cool relatively slowly, either due to prolonged residence time within a warm plume or the presence of larger clast sizes, resulting in more crystalline tephras. Hydrovolcanic eruptions, during which magma encounters external water or ice, are more explosive than magmatic eruptions of similar magma volumes. Vaporization of meteoric water causes rapid fragmentation of magma into smaller pyroclasts that are quickly quenched to create glass-rich deposits. Hydrovolcanic eruptions favor glass production because the interaction with surface or subsurface water causes a cooling

rate of  $>10^6$  K/s, while the airfall deposits from magmatic eruptions cool at rates  $\leq 10$  K/s (Szramek et al., 2010; Wallace et al., 2003; Zimanowski et al., 1997).

Eruption properties other than water interaction can lead to explosive eruptions and glass-rich tephra (Zimanowski et al., 2015). For example, one exception to the general observation that explosive magmatic eruptions produce glass-poor tephra is the high glass content of cinder cone tephra (a form of low-density scoria) formed during Strombolian cinder cone eruptions. Cinder cones form when magma works its way slowly through a crack in the surface and erupts subaerially. Dissolved magmatic gasses exsolve into bubbles within the magma before breaking through the surface, resulting in a very localized explosive eruption. As degassing progresses, cinder cone eruptions can transition to effusive lava flows. The explosiveness of this type of eruption is initially determined by volatile content and then increases by external factors such as interaction with water, conduit specifications, and clogging of the vent (Walker, 1973).

### **1.2.3 Explosive Volcanic Deposits on Mars**

Explosive volcanic eruptions are likely to have been common on Mars, as the long history of water and ice at the surface (e.g., Carr and Head, 2010) could have caused phreatomagmatic eruptions, and the lower atmospheric pressure over the past several billion years would have allowed explosive eruptions even for basaltic magmas with lower volatile contents (Wilson and Head, 2007). Low atmospheric pressure allows tephra and ash dispersion onto the surface at distances much greater than on Earth (Wilson and Head, 1994); thus, explosive eruptions may have emplaced many of the regional-scale layered sedimentary deposits on Mars (Kerber et al., 2012).

Compositional and physical evidence for explosive volcanism is identifiable on Mars. At visible to near-infrared wavelengths (VNIR; 0.3-2.5  $\mu\text{m}$ ), the OMEGA and CRISM orbital imaging spectrometers have been used to identify glass-rich deposits and altered sediments that are potentially tephra of explosive volcanic origin (Cannon et al., 2017; Edwards and Ehlmann, 2015; Horgan and Bell, 2012). At thermal infrared wavelengths (TIR; 8-30  $\mu\text{m}$ ), orbital spectra from TES and *in situ* spectra from Mini-TES on the Spirit rover have identified basaltic glass spectra and attribute deposits to an explosive volcanic source (Bandfield et al., 2012; Ruff et al., 2006). Explosive volcanic deposits may mantle the existing terrain as a fine-grained and low

thermal inertia layer identified on the martian surface within scarps, crater walls, and valley walls (e.g., Carr et al., 1973; Edgett, 1997; Hynes et al., 2003; McCoy et al., 2008; Robbins et al., 2011; Wilson and Head, 1994). However, the causes of explosive eruptions on Mars are poorly constrained due to uncertainty in the abundance, composition, and evolution of surface and interior volatile reservoirs (Wilson and Head, 2007). Identifying explosive eruption styles from orbital data of volcanic deposits would provide significant insight into Mars' volcanic and volatile history.

*Chapter 2 of this dissertation aims to develop new techniques using spectroscopy to differentiate styles of explosive volcanism and constrain tephra crystallinity.* Understanding the history of water and habitable environments on Mars is one of the primary goals of the Mars Exploration Program, and the ability to detect signs of possible water-magma interactions in the geologic record would be a novel way to place constraints on the history of water at the surface (MEPAG, 2020).

#### **1.2.4 VNIR and TIR spectral properties of volcanic glass and tephra**

In this dissertation I use visible/near-infrared (VNIR; 0.3-2.6  $\mu\text{m}$ ) and thermal infrared (TIR; 8-25  $\mu\text{m}$ ) spectroscopy to study deposits from explosive volcanic eruptions on Earth and on the Moon. These techniques are the main method we have of interrogating planetary surface composition from orbit because of the highly localized nature of landed missions. Remote sensing via VNIR or TIR spectroscopy can be deployed from orbit and allows rapid analysis of all visible outcrops from a landed mission, so the lack of accuracy of these techniques is often balanced by their ability to acquire significantly more data. On Earth, these techniques are applied in the laboratory to individual samples, and the results can be used to better interpret planetary orbital spectra.

VNIR reflectance spectroscopy is sensitive to electronic absorptions, vibrational overtones, and variations in elemental abundance and combinations (e.g., Hunt, 1977). In the VNIR spectral range, glasses exhibit a characteristic broad absorption due to crystal field effects in iron centered between 1.08 and 1.15  $\mu\text{m}$  and often exhibit a second broad band near 2  $\mu\text{m}$ . The contributors to a presence or lack of a 2 $\mu\text{m}$  band has not yet been studied in detail (Cannon et al., 2017; Dyar and Burns, 1981; Horgan et al., 2014). These absorption bands have been used to infer the presence of glass on Mars (Horgan and Bell, 2012; Horgan et al., 2014); however, they are easily obscured by

other Fe-bearing minerals like olivine and pyroxene that exhibit similar bands centered between 0.9 and 1.08  $\mu\text{m}$ . *However, previous work has focused on individual minerals and glasses, and the VNIR spectral properties of actual tephra samples from Mars are not known.*

VNIR spectra can also infer aqueous alteration, which we expect in tephtras when explosive volcanic eruptions or deposits interact with water. Narrow hydration bands at  $\sim 1.9 \mu\text{m}$  in tephtra may imply formation or alteration in a wet environment (Farrand et al., 2016). Glass that has been devitrified, or partially reordered as a result of thermal alteration (Marshall, 1961), loses the 1.1  $\mu\text{m}$  glass band and gains an iron oxide band closer to 1  $\mu\text{m}$  (Ackiss et al., 2018; Farrand et al., 2016). Palagonite can be identified by narrow VNIR absorption bands at 1.78  $\mu\text{m}$  (hydration in zeolites), 1.9  $\mu\text{m}$  (hydration in zeolites and smectites), and 2.2–2.3  $\mu\text{m}$  (smectites), and post-eruptive weathering can also cause the development of smectites on tephtra (Ackiss et al., 2018; Allen et al., 1981; Drief and Schiffman, 2004; Pauly et al., 2011). Thus, the presence of these absorptions in VNIR spectra may indicate that amorphous and/or crystalline endmembers replace some glass in the deposit through the processes of devitrification, palagonization, and/or surface weathering. These types of alteration are spectrally distinct from magmatic volatiles in the glass, which in glasses, e.g., obsidian, can result in only a 2.2  $\mu\text{m}$  absorption band without an accompanying 1.9  $\mu\text{m}$  hydration band (Horgan et al., 2014). Absorption bands due to these alteration minerals have also been detected on Mars using VNIR spectral parameter maps (Viviano-Beck et al., 2014), but glass detections have required more detailed analysis (e.g., Horgan et al., 2014). *Currently it is unknown how these alteration signatures vary across different types of explosive eruptions and how the presence of alteration minerals and processes affects the detectability of glass in tephtras.*

TIR emission spectroscopy is sensitive to molecular bending and stretching vibrational modes present in nearly all geologic materials (Thomson and Salisbury, 1993) and is sensitive to the fundamental  $\sim 10 \mu\text{m}$  Si-O absorption. Crystalline silicates exhibit a composite 10  $\mu\text{m}$  absorption band with many sharp features due to modification of the Si-O bond by variations in mineral structure. In contrast, glass exhibits a rounded  $\sim 10 \mu\text{m}$  absorption band indicative of a substantial degree of disorder of the silicate units (Crisp et al., 1990; Dufresne et al., 2009; Minitti et al., 2002; Minitti and Hamilton, 2010). TIR spectra show that devitrified glass is spectrally and thus structurally distinct from crystalline minerals. During devitrification, the rounded band changes to a doublet, with a narrow band minimum at 9.5–9.6  $\mu\text{m}$  and a broad shoulder at 10.9–

11.3  $\mu\text{m}$ , caused by the development of sheet and chain structures, respectively (Crisp et al., 1990; Farrand et al., 2016). These bands are distinct from the more complex bands expected for common crystalline igneous minerals like olivine and pyroxene, suggesting that early devitrification does not necessarily lead to crystallization. The  $\sim 10 \mu\text{m}$  silicate band's position and shape can be used to infer relative crystallinity and silica content (Michalski et al., 2005). Crystallinity can be determined from TIR linear deconvolution models by subtracting from 100 the fraction of unambiguously amorphous phases (glass, devitrified glass, partially to fully amorphous silica phases) as well as clay, oxide, and zeolite phases that are difficult to quantify using XRD and/or may be poorly crystalline when present in palagonites (Ackiss et al., 2018; Farrand et al., 2016). Previous studies of crystalline igneous rocks suggested that TIR-derived abundances are accurate within 15 vol.% (Feely and Christensen, 1999).

Previous work on TIR properties of igneous materials has focused primarily on intrusive rocks and lavas (Bandfield et al., 2000; Glotch et al., 2010; Scudder et al., 2021), and the TIR properties of explosive volcanic deposits are not known. In addition, previous workers have hypothesized that amorphous materials like glass may be overmodeled in TIR spectral models (Thorpe et al., 2015), therefore more work is needed to evaluate the accuracy of TIR unmixing methods for glass-bearing tephra.

Previous studies showed that glass is distinguishable from crystalline minerals in both VNIR and TIR spectra (Adams, 1974; Cloutis et al., 1990; Crisp et al., 1990; Dyar and Burns, 1981; Horgan et al., 2014; Minitti and Hamilton, 2010), but a survey of the spectral properties of natural tephra samples from different eruption styles had not yet been conducted. *Chapter 2 uses a suite of basaltic tephra samples to test the ability of VNIR and TIR spectra, typical data acquired from planetary orbital and landed missions, to infer eruption styles from explosive volcanic deposits.*

### **1.2.5 Lunar Pyroclastic Deposits**

Lunar pyroclastic deposits (LPD), also known as “dark mantling” deposits, are low-albedo units believed to have formed during ancient explosive volcanic eruptions (Head, 1974). These deposits are composed of juvenile magmatic minerals thought to be derived from deep within the Moon (e.g., clinopyroxene (CPX) and olivine), glass (quenched and partially crystalline glass

beads), as well as local country rock (orthopyroxene (OPX) and plagioclase in the lunar highlands; clinopyroxene in the mare) (Hawke et al., 1989). The deposits exhibit a large range of sizes (Gaddis et al., 1985) and have been previously divided into two categories: regional ( $>1000 \text{ km}^2$  in area) and local deposits ( $<1000 \text{ km}^2$  in area) (Gaddis et al., 2003). Pyroclastic deposits on the Moon represent a primitive material from ancient volcanic eruptions that could help to characterize the lunar interior and to expand our understanding of lunar basaltic magmatism (Gaddis et al., 2003).

The collection of pyroclastic samples in the form of dark glass beads from the Apollo 17 lunar landing site, Taurus Littrow, sparked an interest in the glass-rich deposits formed from volcanic eruptions (Pieters et al., 1974). Based on early spectral studies using Earth-based telescopes, localized pyroclastic deposits were theorized to result from violently explosive Vulcanian-style eruptions, which occur due to the build-up of gases behind a plug due to low eruption rates. This eruption style is capable of ejecting juvenile material along with large amounts of country rock (Head and Wilson, 1979). In contrast, regional pyroclastic deposits are believed to form from Strombolian-style eruptions (coalesced bubble explosions) or from Hawaiian-style fire-fountain eruptions (Head and Wilson, 1979), both of which occur due to high eruption rates. This eruption style produces mainly juvenile material, and deposits are thus composed of glass and partially crystalline glass beads (Gaddis et al., 1985). The Clementine spacecraft collected higher resolution ( $\sim 100\text{m}/\text{pixel}$ ) ultraviolet-visible multispectral data from lunar orbit (Nozette et al., 1994). This allowed for the first global compositional analysis of lunar pyroclastic deposits (Gaddis et al., 2003). While Clementine was able to detect some variability within regional pyroclastic deposits related to crystallinity, the data was unable to provide clear constraints on the mineralogy of the deposits (Gaddis et al., 2003; Hawke et al., 1989; Weitz and Head, 1999).

Recent orbital VNIR spectral studies of the detailed mineralogy of local pyroclastic deposits have suggested that the simple Vulcanian model may need revisiting. Gaddis et al., (2016), Jawin et al., (2015), and Bennett et al., (2016) examined mineralogical variations within and between local deposits in Alphonsus and Oppenheimer craters. Alphonsus crater contains 12 deposits smaller than  $98 \text{ km}^2$ , composed of a variable mix of juvenile CPX and glass near the vents that transition to a more distant ring of OPX-rich country rock. The clear combination of country rock and juvenile materials suggests that the Alphonsus deposits were formed through high-energy Vulcanian style eruptions followed by lower-energy fire fountaining (Gaddis et al., 2016), supporting the original models of (Head and Wilson, 1979). In contrast, Oppenheimer contains at

least 15 deposits ranging in size from 2-1500 km<sup>2</sup>, including some deposits that are “regional” in size. All of the deposits, regardless of size, are rich in glass and juvenile magmatic materials but exhibit no evidence for incorporating local country rock. This suggests that the deposits were formed by fire-fountaining and possibly effusive eruptions (Bennett et al., 2016), and the boundary between local and regional deposits might be significantly lower than the previous arbitrary boundary of 1000 km<sup>2</sup>. However, the fact that the small Oppenheimer deposits are so compositionally distinct compared to the small Alphonsus deposits also suggests that local pyroclastic deposit formation mechanisms are more complicated than indicated by (Head and Wilson, 1979). *These studies demonstrate that more work is needed to understand the eruption style of lunar pyroclastic deposits, and that orbital mineral mapping using VNIR hyperspectral imaging is effective at characterizing lunar pyroclastic deposits in detail.*

Chapters 3 and 4 attempt to expand the understanding of lunar pyroclastic deposits by studying both an ancient volcanic complex and the pyroclastic deposits of a single young impact basin with hyperspectral imaging. The aim of these chapters is to begin to unravel the complexity of explosive volcanism of the Moon through mineralogical characterization of multiple lunar eruption styles.

### **1.2.6 Moon Mineralogy Mapper Instrument Data**

Chapters 3 and 4 use data from the Moon Mineralogy Mapper (M<sup>3</sup>), which was an imaging spectrometer supported by NASA as a guest instrument on the Chandrayaan-1 lunar orbiter (Green et al., 2011; Pieters et al., 2009). Launched in 2008, M<sup>3</sup> operated in the visible to near-infrared (VNIR; 0.42μm-3.0μm), which is sensitive to absorption bands exhibited by iron-bearing minerals, including pyroxene, olivine, glass, as well as anorthosite (Adams et al., 1974; Besse et al., 2013; Cloutis and Gaffey, 1991). M<sup>3</sup> has a spatial resolution of 140 m/pixel in 86 spectral channels. M<sup>3</sup> collected data during two operational periods defined by changes in temperature and orbital distance (Green et al., 2011). Both because of the relatively high spatial resolution of M<sup>3</sup> and the fact that glass exhibits unique iron absorption bands compared to other phases in the spectral range covered by M<sup>3</sup>, recent studies using this dataset have confirmed for the first time that glass is present in local pyroclastic deposits and that there is spatial variability in the spectral signatures within the deposits (Bennett et al., 2016; Besse et al., 2013; Horgan et al., 2014; Jawin et al., 2015). The fact that glass is detectable in these deposits with M<sup>3</sup> is notable, as the

transparency of glass makes it a weak absorber. According to laboratory mixture studies, glass only dominates a VNIR spectrum when the mixtures contain more than 80-95 wt% glass. Therefore, any clear glass detection implies very high glass abundances (Horgan et al., 2014).

M<sup>3</sup> data calibrated to reflectance is available from the Planetary Data System and has nearly full coverage of the lunar surface. However, the quality and resolution (75-280 m/pixel) of the data varies across the mission. At each site of interest, I created a mosaic of M<sup>3</sup> images that prioritizes data from more optimal optical periods (1B, 2A, 2C; Green et al., 2011). Using the methods described in (Horgan et al., 2014) and (Bennett et al., 2016), the continuum of each spectrum in the mosaic will be removed using a linear convex hull with two segments between 0.6-2.6  $\mu\text{m}$ . There is residual thermal contribution above 2  $\mu\text{m}$  that could affect parameter maps utilizing this part of the spectrum; however, the 1 $\mu\text{m}$  band is not disturbed by this effect. To prevent possible error due to thermal contributions, the continuum is limited to <2.5 $\mu\text{m}$ , and I exercised caution when analyzing data at these wavelengths. Spectral noise was reduced using a median filter and a boxcar smoothing algorithm, both with widths of 5 channels.

Minerals can be identified from M<sup>3</sup> using simple arithmetical spectral parameters as well as more detailed parameterizations of the shape and position of the 1 and 2  $\mu\text{m}$  iron absorption bands. All spectral parameters are calculated using the mapped and continuum removed data. The simple spectral parameters can infer the presence and distribution of a spectral shape but do not uniquely identify minerals (Horgan et al., 2014). More objective maps can be created using the band analysis methods of (Horgan et al., 2014), which parameterize the centers of the 1 and 2  $\mu\text{m}$  iron absorption bands. Maps of these parameters are used to distinguish between OPX (band centers between 0.9-0.94 and 1.8-1.95  $\mu\text{m}$ ), CPX (0.98-1.06 and 2.05-2.4  $\mu\text{m}$ ), and iron-bearing glass (1.06-1.2 and 1.9-2.05  $\mu\text{m}$ ). Olivine exhibits a band (1.05-1.08  $\mu\text{m}$ ) that overlaps with CPX and glass but can be distinguished based on the lack of a 2  $\mu\text{m}$  band (Horgan and Bell, 2012; Horgan et al., 2014). Spectral parameter maps will be used to look for compositional variations within specific pyroclastic deposits and then verified using detailed spectral analysis.

### **1.2.7 Relevance to Future Exploration**

As described in the 2013-2022 Decadal Survey, an investigation of explosive volcanic deposits on multiple planetary bodies can: 1. Constrain the bulk composition of terrestrial planets

by studying the composition of volcanic products. 2. Characterize planetary interiors to determine how they differentiate and evolve by assessing volcanic products created through partial melts of the lunar interior. 3. Characterize planetary surfaces to understand how they are modified by geologic processes (i.e., volcanism, National Research Council, 2011).

Lunar pyroclastic deposits are targets of high interest in future exploration of the Moon for both their scientific value and resource potential. In laboratory experiments, lunar pyroclastic glasses rich in  $\text{FeO}_2$  were exposed to an  $\text{H}_2$  environment, creating  $\text{Fe}^{2+}$  and  $\text{H}_2\text{O}$ , which could be electrolyzed to yield oxygen. The pyroclastic glasses yielded the most oxygen out of any Apollo sample (Allen et al., 1996). It is costly to transport materials from the Earth to the Moon; therefore, it is crucial to use locally derived materials. Future astronauts on the Moon for an extended stay could use pyroclastic deposits as a resource for oxygen or to extract rare volatile elements needed for industrial processes, which is imperative for life support and spacecraft propulsion (Allen et al., 1996; Duke et al., 2006). By identifying the characteristics that lead to enhanced glass abundances in lunar pyroclastic deposits, this proposed work will help to recognize the glass-rich deposits that could be targeted for resource extraction, directly addressing the NASA Science Mission Directorate goal “to identify and characterize objects in the solar system that pose threats to Earth or offer resources for human exploration.” The results of this dissertation will enhance the NASA supported  $\text{M}^3$  instrument’s scientific return and addresses goals from the broader Lunar Science community.

The study and characterization of the lunar interior and lunar pyroclastic deposits are both identified explicitly as critical science goals in the National Research Council’s Scientific Context for Exploration of the Moon (2007) and the Planetary Decadal Survey (2011) reports (National Research Council, 2011). The analysis of the history and extent of explosive volcanic deposits address key lunar science questions outlined in the 2007 National Research Council (NRC) Scientific Context for the Exploration of the Moon (SCEM, National Research Council 2007), the 2017 LEAG Specific Action Team Report Advancing Science of the Moon (ASM-SAT, LEAG, 2017), and Vision and Voyages for Planetary Science in the Decade 2013–2022 (National Research Council, 2011).

The scientific outcomes of each dissertation chapter also support the NASA Human Exploration and Operations Mission Directorate (HEOMD), through the preparation of crewed

exploration of the Moon. NASA's Artemis missions will lead humans back to the Moon within the decade (NASA, 2020) and aim to understand planetary processes, the character and origin of lunar polar volatiles, and conduct experimental science in the lunar environment (Artemis SDT, 2020). The recommended investigations by the future Artemis astronauts outlined in the Artemis Science Definition Team Report (SDT) should ensure that sample collection and in situ measurements are carefully choreographed to maximize science return (Artemis SDT, 2020). This dissertation makes a significant contribution to the Artemis objectives by characterizing explosive volcanic environments using orbital investigations (SDT Finding 6.3.7-1), as these deposits are high priorities for scientific sampling and possible resource utilization (Artemis SDT, 2020). Results from this dissertation would support the Artemis science definition team Finding 6.1.4-1 which states that the optimal sample return program is built upon geologic-context observations (Artemis SDT, 2020). The Artemis III mission will focus on exploration of the South Pole, and therefore the inclusion of a spectral map of Schrödinger within this dissertation is highly relevant for mission planning.

### **1.3 Objectives, Tasks, and Outcomes**

The primary goal of this work is to use spectroscopic analysis to determine the presence of glass in volcanic deposits and infer volcanic eruption styles and volcanic history on planetary bodies, based around three specific objectives that resulted in three thesis chapters:

- 1) Develop remote sensing techniques to determine the eruption style of terrestrial volcanic samples (Chapter 2), Volcanic samples from a range of volcanic deposits and sources previously examined by an X-ray diffractometer to calculate crystallinity and infer eruption style will be analyzed with laboratory VNIR and TIR spectroscopy, which are more analogous to orbital instrumentation at Mars.
- 2) Determine the eruption history of an ancient shield/cone complex in Oceanus Procellarum using orbital VNIR spectra of the Marius Hill Volcanic Complex (Chapter 3). Identify and compare the presence of glass in effusive and explosive lunar deposits associated with domes, cinder cones, and lava flows.
- 3) Determine the volcanic history of proposed pyroclastic deposits in the South Pole Aitken Basin using orbital VNIR spectra of Schrödinger crater (Chapter 4). The analysis will

determine the eruption types of multiple pyroclastic deposits at the proposed landing site and evaluate the impact of crustal thickness on eruption explosivity.

This dissertation uses new techniques from lab studies to inform orbital spectroscopy and geomorphology comparisons (Chapter 2), investigates a large and ancient volcanic complex with significant implications for the early volcanic history of the Moon (Chapter 3), and investigates the pyroclastic deposits of a single impact basin (Chapter 4) that has been selected as a landing site for robotic missions in 2024.

Overall, this research will provide fundamental insight into the eruption history of the Moon and Mars. Inferring eruption styles from mineralogy can inform the volatile history of both planetary bodies. Understanding of planetary volcanic processes and their resource potential could influence the future exploration of the Solar System.

All three chapters are to be submitted as articles to relevant Earth and planetary science journals. Chapter 2 has been published in *Earth and Space Science*. Chapter 3 is planned for submission to *Icarus*. Lastly, Chapter 4 is planned for *Journal of Geophysical Research - Planets*. Part of this thesis was funded by the National Science Foundation Graduate Research Fellowship awarded in May 2017 and renewed through August 2020. Chapters 2 and 3 were also funded with the support of the Indiana Space Grant and the Amelia Earhart Scholarship. Chapter 4 is part of a funded NASA Lunar Data Analysis Program led by Dr. Lisa Gaddis and was completed as a part of an NSF Graduate Internship Program at the United States Geological Survey in Flagstaff, Arizona, alongside Dr. Gaddis.

## 1.4 References

Ackiss, Horgan, Scudder, Gudnason, Haberle, Thorsteinsson, 2018. The mineralogic variability of Icelandic palagonites: An analog study for Mars, in: *Lunar and Planetary Science Conference*. p. 1773.

Adams, J.B., 1974. Visible and near-infrared diffuse reflectance spectra of pyroxenes as applied to remote sensing of solid objects in the solar system. *Journal of Geophysical Research* 79, 4829–4836. <https://doi.org/10.1029/jb079i032p04829>

Adams, J.B., Pieters, C., McCord, T.B., 1974. Orange glass-Evidence for regional deposits of pyroclastic origin on the moon. *Lunar and Planetary Science Conference* 1, 171–186.

- Airey, M.W., Mather, T.A., Pyle, D.M., Glaze, L.S., Ghail, R.C., Wilson, C.F., 2015. Explosive volcanic activity on Venus: The roles of volatile contribution, degassing, and external environment. *Planet Space Sci* 113, 33–48. <https://doi.org/10.1016/j.pss.2015.01.009>
- Allen, C., Gooding, J.L., Jercinovic, M., Keil, K., 1981. Altered basaltic glass: A terrestrial analog to the soil of Mars. *Icarus* 45, 347–369. [https://doi.org/10.1016/0019-1035\(81\)90040-3](https://doi.org/10.1016/0019-1035(81)90040-3)
- Allen, C.C., Morris, R.V., McKay, D.S., 1996. Oxygen extraction from lunar soils and pyroclastic glass. *Journal of Geophysical Research: Planets* 101, 26085–26095. <https://doi.org/10.1029/96je02726>
- Artemis Science Definition Team, 2020. Artemis III Science Definition Team Report (No. NASA/SP-20205009602).
- Bandfield, J.L., Edwards, C.S., Montgomery, D.R., Brand, B.D., 2012. The dual nature of the martian crust: Young lavas and old clastic materials. *Icarus* 222, 188–199. <https://doi.org/10.1016/j.Icarus.2012.10.023>
- Bandfield, J.L., Hamilton, V.E., Christensen, P.R., 2000. A Global View of Martian Surface Compositions from MGS-TES. *Science* 287, 1626–1630. <https://doi.org/10.1126/science.287.5458.1626>
- Bennett, K.A., Horgan, B.H.N., Gaddis, L.R., Greenhagen, B.T., Allen, C.C., Hayne, P.O., III, J.F.B., Paige, D.A., 2016. Complex explosive volcanic activity on the Moon within Oppenheimer crater. *Icarus*, 273, 296–314. <https://doi.org/10.1016/j.Icarus.2016.02.007>
- Besse, S., Yokota, Y., Boardman, J., Green, R., Haruyama, J., Isaacson, P., Mall, U., Matsunaga, T., Ohtake, M., Pieters, C., Staid, M., Sunshine, J., Yamamoto, S., 2013. One Moon, many measurements 2: Photometric corrections. *Icarus* 226, 127–139. <https://doi.org/10.1016/j.Icarus.2013.05.009>
- Cannon, K.M., Mustard, J.F., Parman, S.W., Sklute, E.C., Dyar, M.D., Cooper, R.F., 2017. Spectral properties of Martian and other planetary glasses and their detection in remotely sensed data. *Journal of Geophysical Research: Planets* 122, 249–268. <https://doi.org/10.1002/2016je005219>
- Carr, M.H., Head, J.W., 2010. Geologic history of Mars. *Earth and Planetary Science Letters* 294, 185–203. <https://doi.org/10.1016/j.epsl.2009.06.042>
- Carr, M.H., Masursky, H., Saunders, R.S., 1973. A generalized geologic map of Mars. *Journal of Geophysical Research* 78, 4031–4036. <https://doi.org/10.1029/jb078i020p04031>
- Cashman, K.V., Scheu, B., 2015. *The Encyclopedia of Volcanoes* 459–471. <https://doi.org/10.1016/b978-0-12-385938-9.00025-0>
- Cassidy, M., Manga, M., Cashman, K., Bachmann, O., 2018. Controls on explosive-effusive volcanic eruption styles. *Nature Communications* 9, 2839. <https://doi.org/10.1038/s41467-018-05293-3>

- Cloutis, E.A., Gaffey, M.J., 1991. Spectral-compositional variations in the constituent minerals of mafic and ultramafic assemblages and remote sensing implications. *Earth, Moon, and Planets* 53, 11–53. <https://doi.org/10.1007/bf00116217>
- Cloutis, E.A., Gaffey, M.J., Smith, D.G.W., Lambert, R.S.J., 1990. Reflectance spectra of glass-bearing mafic silicate mixtures and spectral deconvolution procedures. *Icarus* 86, 383–401.
- Crisp, J., Kahle, A.B., Abbott, E.A., 1990. Thermal infrared spectral character of Hawaiian basaltic glasses. *Journal of Geophysical Research: Oceans* 95, 21657–21669. <https://doi.org/10.1029/jb095ib13p21657>
- Drief, A., Schiffman, P., 2004. Very Low-Temperature Alteration of Sideromelane in Hyaloclastites and Hyalotuffs from Kilauea and Mauna Kea Volcanos: Implications for the Mechanism of Palagonite Formation. *Clays and Clay Minerals* 52, 622–634. <https://doi.org/10.1346/ccmn.2004.0520508>
- Dufresne, C.D.M., King, P.L., Dyar, M.D., Dalby, K.N., 2009. Effect of SiO<sub>2</sub>, total FeO, Fe<sup>3+</sup>/Fe<sup>2+</sup>, and alkali elements in basaltic glasses on mid-infrared spectra. *Am Mineral* 94, 1580–1590. <https://doi.org/10.2138/am.2009.3113>
- Duke, M.B., Gaddis, L.R., Taylor, G.J., Schmitt, H.H., 2006. Development of the Moon. *Rev Mineralogy Geochem* 60, 597–655. <https://doi.org/10.2138/rmg.2006.60.6>
- Dyar, M.D., Burns, R., 1981. Coordination chemistry of iron in glasses contributing to remote-sensed spectra of the Moon. Lunar and Planetary Science Conference.
- Edgett, K.S., 1997. Aeolian Dunes as Evidence for Explosive Volcanism in the Tharsis Region of Mars. *Icarus* 130, 96–114. <https://doi.org/10.1006/icar.1997.5806>
- Edwards, C.S., Ehlmann, B.L., 2015. Carbon sequestration on Mars. *Geology* 43, 863–866. <https://doi.org/10.1130/g36983.1>
- Farrand, W.H., Wright, S.P., Rogers, A.D., Glotch, T.D., 2016. Basaltic glass formed from hydrovolcanism and impact processes: Characterization and clues for detection of mode of origin from VNIR through MWIR reflectance and emission spectroscopy. *Icarus* 275, 16–28. <https://doi.org/10.1016/j.Icarus.2016.03.027>
- Feely, K.C., Christensen, P.R., 1999. Quantitative compositional analysis using thermal emission spectroscopy: Application to igneous and metamorphic rocks. *Journal of Geophysical Research: Oceans* 104, 24195–24210. <https://doi.org/10.1029/1999je001034>
- Fegley, B., Swindle, T.D., 1993. Lunar volatiles: implications for lunar resource utilization. Resources of near-Earth space.
- Gaddis, L.R., Horgan, B., McBride, M., Bennett, K., Stopar, J., Gustafson, J.O., 2016. Alphonsus Crater: Compositional Clues to Eruption Styles of Lunar Small Volcanoes. Lunar and Planetary Science Conference 47, 2065.

- Gaddis, L.R., Pieters, C.M., Hawke, B.R., 1985. Remote sensing of lunar pyroclastic mantling deposits. *Icarus* 61, 461–489. [https://doi.org/10.1016/0019-1035\(85\)90136-8](https://doi.org/10.1016/0019-1035(85)90136-8)
- Gaddis, Staid, M.I., Tyburczy, J.A., Hawke, B.R., Petro, N.E., 2003. Compositional analyses of lunar pyroclastic deposits. *Icarus* 161, 262–280. [https://doi.org/10.1016/s0019-1035\(02\)00036-2](https://doi.org/10.1016/s0019-1035(02)00036-2)
- Glass, B.P., 2016. Glass: The Geologic Connection. *International Journal of Applied Glass Science*. <https://doi.org/10.1111/ijag.12240>
- Glotch, T.D., Lucey, P.G., Bandfield, J.L., Greenhagen, B.T., Thomas, I.R., Elphic, R.C., Bowles, N., Wyatt, M.B., Allen, C.C., Hanna, K.D., Paige, D.A., 2010. Highly Silicic Compositions on the Moon. *Science* 329, 1510–1513. <https://doi.org/10.1126/science.1192148>
- Green, R.O., Pieters, C., Mouroulis, P., Eastwood, M., Boardman, J., Glavich, T., Isaacson, P., Annadurai, M., Besse, S., Barr, D., Buratti, B., Cate, D., Chatterjee, A., Clark, R., Cheek, L., Combe, J., Dhingra, D., Essandoh, V., Geier, S., Goswami, J.N., Green, R., Haemmerle, V., Head, J., Hovland, L., Hyman, S., Klima, R., Koch, T., Kramer, G., Kumar, A.S.K., Lee, K., Lundeen, S., Malaret, E., McCord, T., McLaughlin, S., Mustard, J., Nettles, J., Petro, N., Plourde, K., Racho, C., Rodriguez, J., Runyon, C., Sellar, G., Smith, C., Sobel, H., Staid, M., Sunshine, J., Taylor, L., Thaisen, K., Tompkins, S., Tseng, H., Vane, G., Varanasi, P., White, M., Wilson, D., 2011. The Moon Mineralogy Mapper (M3) imaging spectrometer for lunar science: Instrument description, calibration, on-orbit measurements, science data calibration and on-orbit validation. *Journal of Geophysical Research: Planets* 116, E00G19. <https://doi.org/10.1029/2011je003797>
- Hawke, B.R., Coombs, C.R., Gaddis, L.R., 1989. Remote sensing and geologic studies of localized dark mantle deposits on the Moon. *Lunar Planet. Sci* 255–268.
- Head, J.W., 1974. Lunar dark-mantle deposits-Possible clues to the distribution of early mare deposits. *Lunar and Planetary Science Conference*.
- Head, J.W., Wilson, L., 1979. Alphonsus-type dark-halo craters: Morphology, Morphometry and eruption conditions. *Lunar and Planetary Science Conference* 10, 2861–2897.
- Henderson, M.J.B., Horgan, B.H.N., Rowe, M.C., Wall, K.T., Scudder, N.A., 2020. Determining the Volcanic Eruption Style of Tephra Deposits From Infrared Spectroscopy. *Earth Space Sci* 7. <https://doi.org/10.1029/2019ea001013>
- Horgan, B., III, J.F.B., 2012. Widespread weathered glass on the surface of Mars. *Geology* 40, 391–394. <https://doi.org/10.1130/g32755.1>
- Horgan, B.H.N., Cloutis, E.A., Mann, P., III, J.F.B., 2014. Near-infrared spectra of ferrous mineral mixtures and methods for their identification in planetary surface spectra. *Icarus* 234, 132–154. <https://doi.org/10.1016/j.Icarus.2014.02.031>

- Houghton, B., 2015. The Encyclopedia of Volcanoes (Second Edition). Part Iv Explosive Volcanism 457–458. <https://doi.org/10.1016/b978-0-12-385938-9.02006-x>
- Hunt, G.R., 1977. Spectral signatures of particulate minerals in the visible and near infrared. *Geophysics* 42, 501–513. <https://doi.org/10.1190/1.1440721>
- Hynek, B.M., Phillips, R.J., Arvidson, R.E., 2003. Explosive volcanism in the Tharsis region: Global evidence in the Martian geologic record. *Journal of Geophysical Research: Oceans* 108, 18,991. <https://doi.org/10.1029/2003je002062>
- Jawin, E.R., Besse, S., Gaddis, L.R., Sunshine, J.M., Head, J.W., Mazrouei, S., 2015. Examining spectral variations in localized lunar dark mantle deposits. *Journal of Geophysical Research: Planets* 120, 1310–1331. <https://doi.org/10.1002/2014je004759>
- Kerber, L., Head, J.W., Madeleine, J.-B., Forget, F., Wilson, L., 2012. The dispersal of pyroclasts from ancient explosive volcanoes on Mars: Implications for the friable layered deposits. *Icarus* 219, 358–381. <https://doi.org/10.1016/j.Icarus.2012.03.016>
- Kerber, L., Head, J.W., Solomon, S.C., Murchie, S.L., Blewett, D.T., Wilson, L., 2009. Explosive volcanic eruptions on Mercury: Eruption conditions, magma volatile content, and implications for interior volatile abundances. *Earth and Planetary Science Letters* 285, 263–271. <https://doi.org/10.1016/j.epsl.2009.04.037>
- LEAG, 2017. Advancing science of the Moon: Report of the Specific Action Team, held 7–8 August 2017. Houston, Texas, United States of America.
- Marshall, R.R., 1961. Devitrification of natural glass. *Geological Society of America Bulletin* 72, 1493–1520. [https://doi.org/10.1130/0016-7606\(1961\)72\[1493:dong\]2.0.co;2](https://doi.org/10.1130/0016-7606(1961)72[1493:dong]2.0.co;2)
- McBride, M.J., Horgan, B.H.N., Gaddis, L.R., 2016. Revisiting the Mineralogy of the Aristarchus Regional Pyroclastic Deposit with New M3 Analysis Techniques. *Lunar and Planetary Science Conference* 47, 3052.
- McCoy, T.J., Sims, M., Schmidt, M.E., Edwards, L., Tornabene, L.L., Crumpler, L.S., Cohen, B.A., Soderblom, L.A., Blaney, D.L., Squyres, S.W., Arvidson, R.E., Rice, J.W., Tréguier, E., d’Uston, C., Grant, J.A., McSween, H.Y., Golombek, M.P., Haldemann, A.F.C., Souza, P.A. de, 2008. Structure, stratigraphy, and origin of Husband Hill, Columbia Hills, Gusev Crater, Mars. *Journal of Geophysical Research: Oceans* 113, E02S01. <https://doi.org/10.1029/2007je003041>
- MEPAG, 2020. Mars Science Goals, Objectives, Investigations, and Priorities: 2020. LPI 2474.
- Michalski, J.R., Kraft, M.D., Sharp, T.G., Williams, L.B., Christensen, P.R., 2005. Mineralogical constraints on the high-silica martian surface component observed by TES. *Icarus* 174, 161–177. <https://doi.org/10.1016/j.Icarus.2004.10.022>

- Minitti, M.E., Hamilton, V.E., 2010. A search for basaltic-to-intermediate glasses on Mars: Assessing martian crustal mineralogy. *Icarus* 210, 135–149. <https://doi.org/10.1016/j.Icarus.2010.06.028>
- Minitti, M.E., Mustard, J.F., Rutherford, M.J., 2002. Effects of glass content and oxidation on the spectra of SNC-like basalts: Applications to Mars remote sensing. *Journal of Geophysical Research: Oceans* 107, 6-1-6–14. <https://doi.org/10.1029/2001je001518>
- Moon, C. on the S.C. for E. of the, Board, S.S., Sciences, D. on E. and P., Council, N.R., 2007. The Scientific Context for Exploration of the Moon. <https://doi.org/10.17226/11954>
- NASA, 2020. Artemis Plan: NASA’s Lunar Exploration Program Overview. [https://www.nasa.gov/sites/default/files/atoms/files/artemis\\_plan-20200921.pdf](https://www.nasa.gov/sites/default/files/atoms/files/artemis_plan-20200921.pdf)
- National Research Council (2007). The scientific context for exploration of the Moon, doi:<https://doi.org/10.17226/11954>
- National Research Council, 2011. Vision and Voyages for Planetary Science in the Decade 2013-2022. Washington, DC: National Academy Press.
- Newhall, C.G., Self, S., 1982. The volcanic explosivity index (VEI) an estimate of explosive magnitude for historical volcanism. *Journal of Geophysical Research: Oceans* 87, 1231–1238. <https://doi.org/10.1029/jc087ic02p01231>
- Nozette, S., Rustan, P., Pleasance, L.P., Horan, D.M., Regeon, P., Shoemaker, E.M., Spudis, P.D., Acton, C.H., Baker, D.N., Blamont, J.E., Buratti, B., Corson, M.P., Davies, M.E., Duxbury, T.C., Eliason, E.M., Jakosky, B.M., Kordas, J.F., Lewis, I.T., Lichtenberg, C.L., Lucey, P.G., Malaret, E., Massie, M.A., Resnick, J.H., Rollins, C.J., Park, H.S., McEwen, A.S., Robinson, M.S., Simpson, R.A., Smith, D.E., Sorenson, T.C., Breugge, R.W.V., Zuber, M.T., 1994. The Clementine mission to the moon: Scientific overview. *Science* 266, 1835–1839.
- Pauly, B.D., Schiffman, P., Zierenberg, R.A., Clague, D.A., 2011. Environmental and chemical controls on palagonitization. *Geochemistry, Geophysics, Geosystems* 12, n/a-n/a. <https://doi.org/10.1029/2011gc003639>
- Pieters, C., McCord, T.B., Charette, M.P., Adams, J.B., 1974. Lunar Surface: Identification of the Dark Mantling Material in the Apollo 17 Soil Samples. *Science* 183, 1191–1194. <https://doi.org/10.1126/science.183.4130.1191>
- Pieters, C.M., Goswami, J.N., Clark, R.N., Annadurai, M., Boardman, J., Buratti, B., Combe, J.P., Dyar, M.D., Green, R., Head, J.W., Hibbitts, C., Hicks, M., Isaacson, P., Klima, R., Kramer, G., Kumar, S., Livo, E., Lundeen, S., Malaret, E., McCord, T., Mustard, J., Nettles, J., Petro, N., Runyon, C., Staid, M., Sunshine, J., Taylor, L.A., Tompkins, S., Varanasi, P.,

2009. Character and spatial distribution of OH/H<sub>2</sub>O on the surface of the Moon seen by M3 on Chandrayaan-1. *Science* 326, 568–572. <https://doi.org/10.1126/science.1178658>
- Robbins, S.J., Achille, G.D., Hynes, B.M., 2011. The volcanic history of Mars: High-resolution crater-based studies of the calderas of 20 volcanoes. *Icarus* 211, 1179–1203. <https://doi.org/10.1016/j.Icarus.2010.11.012>
- Ruff, S.W., Christensen, P.R., Blaney, D.L., Farrand, W.H., Johnson, J.R., Michalski, J.R., Moersch, J.E., Wright, S.P., Squyres, S.W., 2006. The rocks of Gusev Crater as viewed by the Mini-TES instrument. *Journal of Geophysical Research: Oceans* 111, n/a-n/a. <https://doi.org/10.1029/2006je002747>
- Scudder, N.A., Horgan, B.H.N., Rampe, E.B., Smith, R.J., Rutledge, A.M., 2021. The effects of magmatic evolution, crystallinity, and microtexture on the visible/near-infrared and thermal-infrared spectra of volcanic rocks. *Icarus* 114344. <https://doi.org/10.1016/j.Icarus.2021.114344>
- Szramek, L., Gardner, J.E., Hort, M., 2010. Cooling-induced crystallization of microlite crystals in two basaltic pumice clasts. *American Mineralogist* 95, 503–509. <https://doi.org/10.2138/am.2010.3270>
- Thomson, J.L., Salisbury, J.W., 1993. The mid-infrared reflectance of mineral mixtures (7–14  $\mu$ m). *Remote Sensing of Environment* 45, 1–13. [https://doi.org/10.1016/0034-4257\(93\)90077-b](https://doi.org/10.1016/0034-4257(93)90077-b)
- Thorpe, M.T., Rogers, A.D., Bristow, T.F., Pan, C., 2015. Quantitative compositional analysis of sedimentary materials using thermal emission spectroscopy: 1. Application to sedimentary rocks. *Journal of Geophysical Research: Planets* 1–28. [https://doi.org/10.1002/\(issn\)2169-9100](https://doi.org/10.1002/(issn)2169-9100)
- Viviano-Beck, C.E., Seelos, F.P., Murchie, S.L., Kahn, E.G., Seelos, K.D., Taylor, H.W., Taylor, K., Ehlmann, B.L., Wiseman, S.M., Mustard, J.F., Morgan, M.F., 2014. Revised CRISM spectral parameters and summary products based on the currently detected mineral diversity on Mars. *Journal of Geophysical Research: Planets* 1403–1431. <https://doi.org/10.1002/2014je004627>
- Walker, G.P.L., 1973. Explosive volcanic eruptions — a new classification scheme. *Geologische Rundschau* 62, 431–446. <https://doi.org/10.1007/bf01840108>
- Wall, K.T., Rowe, M.C., Ellis, B.S., Schmidt, M.E., Eccles, J.D., 2014. Determining volcanic eruption styles on Earth and Mars from crystallinity measurements. *Nature Communications* 5, 5090. <https://doi.org/10.1038/ncomms6090>
- Wallace, P.J., Dufek, J., Anderson, A.T., Zhang, Y., 2003. Cooling rates of Plinian-fall and pyroclastic-flow deposits in the Bishop Tuff: inferences from water speciation in quartz-hosted glass inclusions. *Bulletin of Volcanology* 65, 105–123. <https://doi.org/10.1007/s00445-002-0247-9>

- Wallace, P.J., Plank, T., Edmonds, M., Hauri, E.H., 2015. The Encyclopedia of Volcanoes (Second Edition). Part Orig Transp Magma 163–183. <https://doi.org/10.1016/b978-0-12-385938-9.00007-9>
- Weitz, C.M., Head, J.W., 1999. Spectral properties of the Marius Hills volcanic complex and implications for the formation of lunar domes and cones. *Journal of Geophysical Research: Oceans* 104, 18933–18956. <https://doi.org/10.1029/1998je000630>
- Wilson, L., Head, J.W., 2007. Explosive volcanic eruptions on Mars: Tephra and accretionary lapilli formation, dispersal and recognition in the geologic record. *Journal of Volcanology and Geothermal Research* 163, 83–97. <https://doi.org/10.1016/j.jvolgeores.2007.03.007>
- Wilson, L., Head, J.W., 1994. Mars: Review and analysis of volcanic eruption theory and relationships to observed landforms. *Reviews of Geophysics* 32, 221–263. <https://doi.org/10.1029/94rg01113>
- Zimanowski, B., Büttner, R., Dellino, P., White, J.D.L., Wohletz, K.H., 2015. The Encyclopedia of Volcanoes (Second Edition). Part Iv Explos Volcanism 473–484. <https://doi.org/10.1016/b978-0-12-385938-9.00026-2>
- Zimanowski, B., Büttner, R., Lorenz, V., Häfele, H.-G., 1997. Fragmentation of basaltic melt in the course of explosive volcanism. *Journal of Geophysical Research: Oceans* 102, 803–814. <https://doi.org/10.1029/96jb02935>

## CHAPTER 2. DETERMINING THE VOLCANIC ERUPTION STYLE OF TEPHRA DEPOSITS FROM INFRARED SPECTROSCOPY

This chapter is published in peer-reviewed *Earth and Space Science* and can be found here: Henderson, M. J. B., Horgan, B. H. N., Rowe, M. C., Wall, K. T., & Scudder, N. A. (2020). Determining the volcanic eruption style of tephra deposits from infrared spectroscopy. *Earth and Space Science*, 7, e2019EA001013. <https://doi.org/10.1029/2019EA001013> (<https://agupubs.onlinelibrary.wiley.com/doi/full/10.1029/2019EA001013>)

### 2.1 Introduction

Explosive volcanism is driven by volatiles, either sourced from the magma or encountered during ascent and eruption. On Earth, different volatile sources and contents are a significant cause of variations in eruption styles that produce distinct surface deposits (Byrne, 2020). Volcanism is also a common process across the solar system, including on Mars, and these extraterrestrial volcanic deposits can provide a record of the history of interior and surface volatiles on other planets. Mars has likely experienced explosive volcanism throughout the planet's history, as indicated by mineralogy and geomorphology (e.g., Bandfield et al., 2012; Head & Wilson, 1979; B. Horgan and Bell, 2012; Robbins et al., 2011; Squyres et al., 2007). However, the causes of explosive eruptions on Mars are poorly constrained due to uncertainty in the abundance, composition, and evolution of surface and interior volatile reservoirs (Wilson & Head, 2007). On Mars, explosive volcanic deposits produced by interactions with both magmatic and surface volatile reservoirs are critical targets of investigation for both landed and orbital missions. Magmatic volatiles place constraints on the composition and evolution of planetary interiors, while detecting magma-water or magma-ice interactions can help constrain past surface environments and climates (National Research Council, 2011).

Thus, a method is needed for differentiating volcanic deposits produced by these two types of explosive eruptions. Previous studies have shown that the crystallinity of volcanic tephra, as determined by X-ray diffraction (XRD), can be used to infer eruption style (Wall et al., 2014); however, this technique is only applicable to landed investigations (Blake et al., 2012). Here, we propose a method for distinguishing eruption styles in volcanic deposits using laboratory visible/near-infrared (VNIR; 0.3–2.5  $\mu\text{m}$ ) reflectance spectra and thermal infrared (TIR; 8–25  $\mu\text{m}$ ) emission spectra that is analogous to orbital datasets from Mars. Identifying explosive eruption

styles from orbital data of volcanic deposits would provide significant insight into Mars' volcanic and volatile history.

## 2.2 Background

Glass forms by numerous natural processes, including impacts, tectonics, and volcanic eruptions (Glass, 2016). Glasses form via quenching of molten material, where rapid cooling prevents the crystallization of minerals. Rapid cooling can occur due to interaction with water (e.g., mid-ocean ridge eruptions), air (e.g., Plinian eruptions), or the vacuum of space (e.g., lunar pyroclastic eruptions). In explosive eruptions, volatiles like water can enhance this process by driving explosive fragmentation (smaller particles cool more efficiently) and direct cooling (during magma-water interactions). Glass can form in magmas of any composition, from mafic to felsic. More interactions with volatiles during eruption generally leads to glassier pyroclastic deposits.

Explosive eruptions can be divided into two categories: magmatic (volatile-limited) and phreatomagmatic (volatile-rich; e.g., Cashman & Sparks, 2013; Wall et al., 2014). In “magmatic” eruptions (e.g., Plinian and Strombolian eruption styles), volatiles dissolved in the magma are decompressed during ascent, increasing the volume fraction of gas and causing fragmentation. The pyroclasts formed by magmatic eruptions cool relatively slowly, either due to prolonged residence time within a warm plume or larger clast sizes, resulting in more crystalline tephra. Phreatomagmatic eruptions, during which magma encounters external water or ice, are more explosive than magmatic eruptions of similar magma volumes. Vapourization of meteoric water causes rapid fragmentation of magma into smaller pyroclasts that are quickly quenched to create glass-rich deposits. Phreatomagmatic eruptions favor glass production because the interaction with surface or subsurface water causes a cooling rate of  $>10^6$  K/s, while the airfall deposits from magmatic eruptions cool at rates  $\leq 10$  K/s (Szczepanek et al., 2010; Wallace et al., 2003; Zimanowski et al., 1997).

Eruption properties other than water interaction can lead to explosive eruptions and glass-rich tephra. For example, one exception to the general observation that explosive magmatic eruptions produce glass-poor tephra is the high glass content of cinder cone tephra (a form of low-density scoria) formed during Strombolian cinder cone eruptions. Cinder cones form when magma works its way slowly through a crack in the surface and erupts subaerially. Dissolved magmatic

gasses exsolve into bubbles within the magma before breaking through the surface, resulting in a very explosive localized eruption. As degassing progresses, cinder cone eruptions can transition to effusive lava flows. The explosiveness of this type of eruption is initially determined by volatile content and then increases by external factors such as interaction with water, conduit specifications, and clogging of the vent (Walker, 1973).

Explosive volcanic eruptions are thought to have been common on Mars. Water and/or ice have been present at the surface and in the subsurface from the Noachian to the present day (e.g., Carr & Head, 2010) and have been hypothesized to cause phreatomagmatic eruptions (e.g., Ghatan & Head, 2002). Lower atmospheric pressure in the Hesperian and Amazonian would have enhanced eruptions' explosivity even in basaltic magmas with lower volatile contents (Wilson & Head, 2007). Under low atmospheric pressures, tephra and ash would have dispersed onto the surface at distances much greater than on Earth (Wilson & Head, 1994); thus, explosive eruptions may have emplaced many of the regional-scale sedimentary deposits on Mars (Kerber et al., 2012).

Deposits potentially consistent with volcanic tephra as well as explosive volcanic edifices have been identified on Mars based on morphological and thermophysical properties (Carr et al., 1973; Edgett, 1997; Hynes et al., 2003; McCoy et al., 2008; Robbins et al., 2011; Wilson & Head, 1994). Previous investigations used orbital VNIR spectra as well as orbital and in situ TIR spectra to identify possible tephra deposits on Mars, based on the presence of glass-rich sand and altered sediments that could both be attributed to explosive volcanism (Cannon et al., 2017; Horgan & Bell, 2012; Edwards & Ehlmann, 2015). However, it is unclear from these studies whether these possible explosive volcanic deposits formed from phreatomagmatic or magmatic eruptions. This study aims to develop new techniques using spectroscopy applied to differentiate these two eruption styles. Understanding the history of water and habitable environments on Mars is one of the primary goals of the Mars Exploration Program, and the ability to detect signs of possible water-magma interactions in the geologic record would be a novel way to place constraints on the history of water at the surface (MEPAG, 2020).

Previous work suggests the crystallinity of volcanic tephra may be related to eruption styles. A study by Wall et al. (2014) investigated a suite of 16 volcanic tephtras and 14 lavas from globally distributed basaltic sources on Earth and developed a method using X-ray diffraction (XRD) to estimate their crystallinity. Their results showed that crystallinity could be used to distinguish tephtra from phreatomagmatic and magmatic eruptions, as phreatomagmatic tephtras exhibit a lower

groundmass crystallinity (<35%) than slower cooling magmatic eruptions (>44%). Applying their results to analyses by the CheMin XRD instrument on the Mars Curiosity rover showed that the moderate crystallinity (>50%; Bish et al., 2013) of the Rocknest aeolian sediment sample is consistent with magmatic tephra of Strombolian or Plinian origin.

Here, we seek to develop similar analysis techniques to constrain tephra crystallinity using spectroscopy. Orbital spectroscopy is used extensively to study the Martian surface's mineralogy (e.g., Bandfield, 2002; Murchie et al., 2009). Previous studies showed that glass is distinguishable from crystalline minerals in both VNIR and TIR spectra (Adams et al., 1974; Cloutis et al., 1990; Crisp et al., 1990; Dyar & Burns, 1981; B. H. N. Horgan et al., 2014; Minitti & Hamilton, 2010), but a survey of the spectral properties of natural tephra samples from different eruption styles has not yet been conducted.

## **2.3 Materials and Methods**

In this study, we use a suite of basaltic tephra samples to test the ability of VNIR and TIR spectra, typical data acquired from planetary orbital and landed missions, to infer eruption styles from explosive volcanic deposits. To “ground truth” these datasets, we compare the VNIR and TIR results to XRD crystallinity measurements as well as to VNIR, TIR, and XRD data from physical mixtures of glass and crystalline igneous minerals.

### **2.3.1 Sample Suite**

Basaltic tephra samples (Table 1, Figure 2-1) were collected by Wall et al. (2014; and references therein) from a range of tephra types (hydrovolcanic sand, lapilli, tuff, scoria, and ignimbrites) attributed to a range of eruption styles (phreatomagmatic, Plinian, and Strombolian). All phreatomagmatic samples in this study result from magmatic interaction with groundwater (with the exception of Surtsey, which was a submarine eruption). These samples may also be referred to as hydrovolcanic, but we maintain the usage of the term “phreatomagmatic” for consistency with previous literature and with the Wall et al. (2014) study. Two cinder samples from Craters of the Moon (CotM) National Monument (Kuntz et al., 1992) and Tseax Cone (Wuorinen, 1978) were added to the collection for this study. The cinders have a lower density and smaller clast size than other scorias in our study. Possible cinder cones have been identified

on the martian surface (Brož et al., 2015; Hauber et al., 2015; McCauley, 1967; Wood, 1979) and represent a distinct tephra type that was not considered by Wall et al. (2014). We created a physical mixture set with glasses and crystalline minerals to compare the tephra samples to well-characterized samples of known crystallinity (Section 3.4). To minimize the effects of grain size and surface area on the spectra, all samples and mixtures were crushed to <150 μm, the same size fraction examined by CheMin on the Curiosity rover (Blake et al., 2012). For spectral analysis, all samples were pressed into ~1g pellets to reduce pore space and increase spectral contrast. This preparation step compares tephra of different densities and grains sizes more consistently, which is appropriate for our study. These properties can vary widely for a given eruption and do not indicate eruption style as bulk composition. However, it should be noted that these properties may significantly affect the spectral properties of tephra deposits, particularly in the TIR.

Table 2-1. Summary of samples in this study.

Sample name	Deposit location	Eruption style	Deposit type	Wall et al. (2014) bulk crystallinity	Wall et al. (2014) groundmass crystallinity	Thermal infrared modeled crystallinity ±15%
<b>Phreatomagmatic</b>						
SA-1	Surtsey, Iceland	Phreatomagmatic	Hydrovolcanic Sand	35	34	29.2
98WN6/NL E	Newberry Volcano, OR	Phreatomagmatic	Accretionary Lapilli	N/A	31–33	28.4
FR-12-91A	Fort Rock, OR	Phreatomagmatic	Tuff	22	9–22	18.2
FR-12-97B	Fort Rock, OR	Phreatomagmatic	Tuff	47	11	34.1
LSC/Tuff 1-1m	Columbia River Basalt	Phreatomagmatic	Hyaloclastite Tuff	27–30	8	65.4
<b>Volatile-rich magmatic</b>						
CotM	Craters of the Moon, ID	Cinder Cone	Cinder	17.8	N/A	12.4
Tsx-s3	Teseax Cone, BC, Canada	Cinder Cone	Cinder	N/A	N/A	12.1
<b>Magmatic</b>						
T13-5	Mt. Tarawera, NZ	Plinian	Scoria	60–79	47–78	31.4
122 BC 1	Mt. Etna, Italy	Plinian	Scoria	47–61	N/A	56.5
122 BC 2	Mt. Etna, Italy	Plinian	Scoria	51–68	N/A	43.8
TB 1	Trailbridge, OR	Plinian	Ignimbrite Densely Welded	98	95	83.7
TB 2	Trailbridge, OR	Plinian	Ignimbrite Mod Welded	91	86	89.4
TB 3	Trailbridge, OR	Plinian	Ignimbrite Lightly Welded	95	74	93.3
LP13-1	Lake Pupuke, NZ	Strombolian	Scoria	75–79	72–79	29.1



Figure 2-1. Tephra samples used in this study (not including Tseax cinders) before being crushed, sieved, and pressed into pellets for spectral analysis.

### 2.3.2 X-Ray Diffraction

Crystallinities for the tephra samples were derived from XRD patterns by comparing the area of the broad hump due to X-ray amorphous phases, including glass, to the area of peaks due to crystalline minerals (Wall et al., 2014). This “relative crystallinity” was then calibrated to a quantitative measure using a series of known standards. Thus, these crystallinities are not just a measure of the glass content but also the presence of other X-ray amorphous phases, including assemblages like palagonite (Ackiss et al., 2018a). Palagonite is an assemblage of largely amorphous phases that forms due to hydrothermal alteration of glass during or shortly after an eruption (Ackiss et al., 2018a; Allen et al., 1981; Drief & Schiffman, 2004; Farrand et al., 2018; Pauly et al., 2011; Stroncik & Schmincke, 2001, 2002). Bulk crystallinity (groundmass/phenocrysts), as well as groundmass crystallinity (phenocrysts removed by hand) for our samples, were inferred from XRD models by Wall et al. (2014). While bulk crystallinity is more likely to be measured during orbital spectroscopy, groundmass crystallinity is more closely related to late-stage magma cooling history. In our study, the spectroscopic analyses were compared to both the bulk and groundmass crystallinities where available. We applied this same technique to determine bulk XRD crystallinities for the CotM, Tseax, and physical mixture samples, using XRD patterns we acquired following sample preparation and analytical procedures as described by Zorn et al. (2018) at the University of Auckland X-ray Centre on a PANalytical Empyrean XRD. Crystallinity was calculated using the AMORPH program (Rowe & Brewer, 2018), calibrated against physical glass-mineral mixtures (Wall et al., 2014). All XRD crystallinities are reported here as vol. %.

### 2.3.3 Visible/Near-Infrared Spectra

VNIR reflectance spectroscopy is sensitive to electronic absorptions, vibrational overtones, and element combinations (e.g., Hunt, 1977), as demonstrated by the laboratory reference spectra shown in Figure 2-2. An ASD FieldSpecPro3 spectroradiometer with a contact probe attachment collected the VNIR spectra of pelletized samples from 0.35 to 2.5  $\mu\text{m}$  at standard incidence/emission angles of  $0^\circ/30^\circ$  and as an average of 100 individual spectra with respect to a white reference. In the VNIR spectral range, glasses exhibit a characteristic broad absorption due to crystal field effects in iron centered between 1.08 and 1.15  $\mu\text{m}$  and often exhibit a second broad band near 2  $\mu\text{m}$  (Cannon et al., 2017; Dyar & Burns, 1981; Horgan et al., 2014). These absorption bands have been used to infer the presence of glass on Mars (Horgan & Bell, 2012; Horgan et al., 2014); however, they are easily obscured by other Fe-bearing minerals like olivine and pyroxene that exhibit similar bands centered between 0.9 and 1.08  $\mu\text{m}$ . As such, glass absorptions only dominate VNIR spectra for abundances  $>70\text{--}80$  wt.% (Horgan et al., 2014).

VNIR spectra can also infer aqueous alteration. Narrow hydration bands at  $\sim 1.9$   $\mu\text{m}$  in tephra may imply formation or alteration in a wet environment (Farrand et al., 2016). Absorption bands near 2.2–2.3  $\mu\text{m}$  are often attributed to Si-OH bonds in hydrated silicates like glass or Fe/Mg/Al-OH bonds in phyllosilicates (Bishop et al., 2008; Rice et al., 2013). Glass that has been devitrified, or partially reordered as a result of thermal alteration (Marshall, 1961), loses the 1.1  $\mu\text{m}$  glass band and gains an iron oxide band closer to 1  $\mu\text{m}$  (Ackiss et al., 2018a; Farrand et al., 2016). Palagonite can be identified by narrow VNIR absorption bands at 1.78  $\mu\text{m}$  (hydration in zeolites), 1.9  $\mu\text{m}$  (hydration in zeolites and smectites), and 2.2–2.3  $\mu\text{m}$  (smectites), and post-eruptive weathering can also cause the development of smectites on tephra (Ackiss et al., 2018a; Allen et al., 1981; Drief & Schiffman, 2004; Pauly et al., 2011). Thus, the presence of these absorptions in VNIR spectra may indicate that amorphous and/or crystalline endmembers replace some glass in the deposit through the processes of devitrification, palagonization, and/or surface weathering. These types of alteration are spectrally distinct from magmatic volatiles in the glass, which in glasses, e.g., obsidian, can result in only a 2.2  $\mu\text{m}$  absorption band without an accompanying 1.9  $\mu\text{m}$  hydration band (Horgan et al., 2014). Absorption bands due to these alteration minerals have also been detected on Mars using VNIR spectral parameter maps (Viviano-Beck et al., 2014), but glass detections have required more detailed analysis (e.g., Horgan et al., 2014).

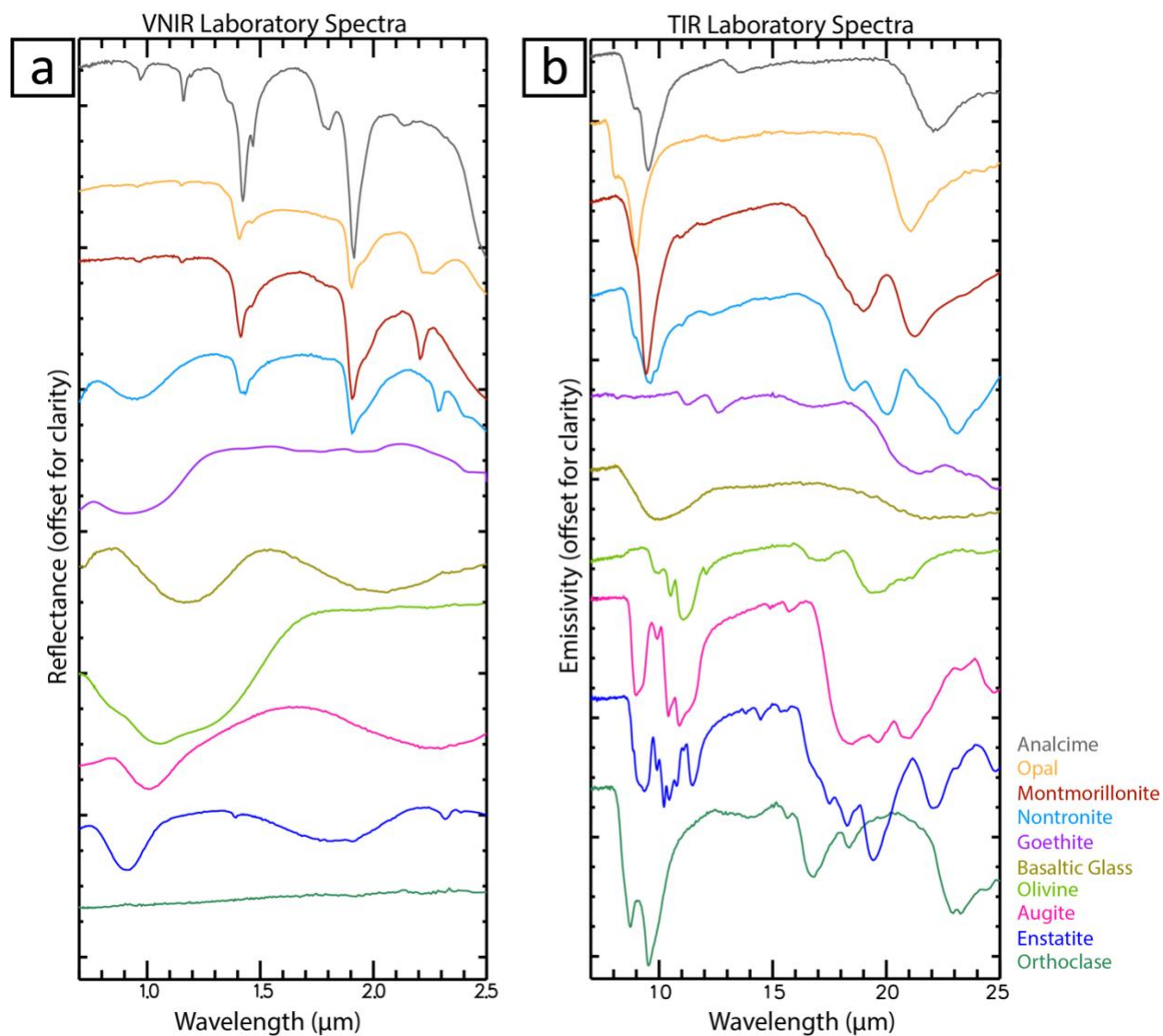


Figure 2-2. Laboratory reference spectra of minerals common in volcanic environments in the (a) visible/near-infrared (VNIR) (Horgan et al., 2017; Kokaly et al., 2017) and (b) thermal infrared (TIR) (see citations in Table 2).

### 2.3.4 Thermal-Infrared Spectra

TIR emission spectroscopy is sensitive to molecular bending and stretching vibrational modes present in nearly all geologic materials (Thomson & Salisbury, 1993), as shown in Figure 2-2. TIR spectra (8–25  $\mu\text{m}$ ) of tephra and mixture pellet samples actively heated to 80°C were acquired at Arizona State University using a Nicolet iS50R FT-IR spectrometer modified to measure emitted energy, then calibrated to emissivity (Christensen & Harrison, 1993; Ruff et al.,

1997). Spectra were measured between 200 and 2,000  $\text{cm}^{-1}$  with a resolution of 2  $\text{cm}^{-1}$  as an average of 512 scans.

TIR spectra are sensitive to the fundamental  $\sim 10 \mu\text{m}$  Si-O absorption, and crystalline silicates exhibit a composite 10  $\mu\text{m}$  absorption band with many sharp features due to modification of the Si-O bond by variations in mineral structure. In contrast, glass exhibits a rounded  $\sim 10 \mu\text{m}$  absorption band indicative of a substantial degree of disorder of the silicate units (Crisp et al., 1990; Dufresne et al., 2009; Minitti et al., 2002; Minitti & Hamilton, 2010). TIR spectra show that devitrified glass is spectrally and thus structurally distinct from crystalline minerals. During devitrification, the rounded band changes to a doublet, with a narrow band minimum at 9.5–9.6  $\mu\text{m}$  and a broad shoulder at 10.9–11.3  $\mu\text{m}$ , caused by the development of sheet and chain structures, respectively (Crisp et al., 1990; Farrand et al., 2016). These bands are distinct from the more complex bands expected for common crystalline igneous minerals like olivine and pyroxene, suggesting that early devitrification does not necessarily lead to crystallization. The  $\sim 10 \mu\text{m}$  silicate band's position and shape can be used to infer relative crystallinity and silica content (Michalski et al., 2005).

Quantitative mineralogy was determined from TIR spectra using standard nonnegative linear least-squares deconvolution with a suite of laboratory mineral endmember spectra (Ramsey & Christensen, 1998; Rogers & Christensen, 2007). Our library (Table 2) includes spectral endmembers relevant to volcanic environments, including mafic to silicic volcanic glasses (Michalski et al., 2005; Minitti et al., 2002; Minitti & Hamilton, 2010) and devitrified glass (Farrand et al., 2016), as well as pyroxenes, olivines, plagioclases, high silica alteration phases, oxides, zeolites, and clays (e.g., Christensen et al., 2000; Rogers & Christensen, 2007). Corrective spectra listed in Table 2 were used to normalize the spectra models. All TIR abundances and crystallinities are reported in vol.%. TIR linear deconvolution models of our tephra samples and physical mixtures produce RMS errors in the range 0.11–0.79 and 0.19–0.81, respectively.

Crystallinity was determined from TIR linear deconvolution models by subtracting from 100 the fraction of unambiguously amorphous phases (glass, devitrified glass, partially to fully amorphous silica phases) as well as clay, oxide, and zeolite phases that are difficult to quantify using XRD and/or may be poorly crystalline when present in palagonites (Ackiss et al., 2018a; Farrand et al., 2018). Previous studies of crystalline igneous rocks suggested that TIR-derived

abundances are accurate within 15 vol.% (Feely & Christensen, 1999). This estimate of crystallinity from TIR linear deconvolution models likely differs somewhat from XRD modeled crystallinity. While both datasets produce models of bulk mineralogy, XRD detects repeating crystal structure while TIR detects molecular bonds. Thus, materials that are X-ray amorphous and challenging to distinguish in XRD may be detected and quantified in TIR. However, this difference should be small in samples with minimal alteration products, as glass dominates their amorphous component in both XRD and TIR. Because VNIR is highly sensitive to alteration products, altered samples that may cause divergence in the models can be identified using VNIR.

Table 2-2. Endmember Spectra Used for Quantitative TIR Linear Deconvolution Models categorized as they appear in the Figure 2-5 pie charts.

Mineral library composed of mineral spectra from the Arizona State University's (ASU) spectral library <sup>a</sup>		
Glass	Pyroxene	Clay
Andesite interstitial glass (MEM-5) <sup>1</sup>	Augite (BUR-620) <sup>12,24</sup>	Antigorite (MINUN-30)
Dacite interstitial glass (MEM-4) <sup>1</sup>	Augite (NMNH-1191) <sup>24</sup>	Beidellite [pellet] (Sbid-1) <sup>16</sup>
K-rich glass <sup>2</sup>	Bronzite (BUR-1920) <sup>12,24</sup>	Biotite (BUR-840)
Martian meteorite basalt proxy glass (MEM-3) <sup>1</sup>	Diopside (HS-15.4 B) <sup>12,24</sup>	Chlorite (WAR-1924)
TES andesite proxy glass (MEM-2) <sup>1</sup>	Enstatite (HS-9.4 B) <sup>12,24</sup>	Illite <0.2 um (Imt-1) <sup>16</sup>
TES basalt proxy glass (MEM-1) <sup>1</sup>	Hedenbergite (Manganoan) (DSM-HED01) <sup>12,24</sup>	Ilmenite (WAR-4119)
	Hypersthene (NMNH-B182) <sup>12</sup>	Kaolinite (Kga-1b) <sup>17,18</sup>
<b>Devitrified Glass</b>		Montmorillonite (Sca-3) <sup>18</sup>
NMB12-14 (cut_surface_average) <sup>3</sup>	<b>Feldspar</b>	Montmorillonite (STx-1) <sup>18</sup>
NMB12-14 bulk (uncut surface average) <sup>3</sup>	Albite (WAR-0244) <sup>12</sup>	Montmorillonite (Swy-2) <sup>18</sup>
Obsidian-Devitrified <sup>4</sup>	Albite (WAR-0612) <sup>12</sup>	Muscovite (WAR-5474)
CH-02 <sup>3</sup>	Albite (WAR-0235)	Nontronite (Nau-1) <sup>18</sup>
	Andesine (BUR-240)	Saponite (Eb-1)
<b>Other Poorly Crystalline</b>	Andesine (WAR-0024) <sup>12</sup>	Serpentine (HS-8.4 B)
Allophane Si:Al 0.44 (ALLO044) <sup>5</sup>	Anorthite (BUR-340) <sup>12</sup>	
Allophane Si:Al 0.92 (ALLO092) <sup>5</sup>	Anorthoclase (WAR-0579)	<b>Oxide</b>
Aluminosilicate Gel Si:Al 5.6 (ALLO560) <sup>5</sup>	Bytownite (WAR-1384)	Goethite (GTS4) <sup>19,20</sup>
	Labradorite (WAR-4524)	Goethite-Derived Hematite (GTSH4-300) <sup>19,20</sup>
<b>Hydrated Silica</b>	Labradorite (BUR-3080A) <sup>12</sup>	Hematite (BUR-2600)
Opal-Aluminous <sup>6,7</sup>	Microcline (BUR-3460) <sup>12</sup>	Magnetite (MTS4) <sup>19,20</sup>
Opal-A <sup>8</sup>	Microcline (BUR-3460A) <sup>12</sup>	
opal-CT (02-031) <sup>8</sup>	Mircrocline (Perthite) (WAR-5802)	<b>Zeolites</b>
Cristobalite <sup>8</sup>	Oligoclase (BUR-3680)	Analcime (WAR49-0672)
	Oligoclase (BUR-060) <sup>12</sup>	Clinoptilolite (27031) <sup>18,21</sup>
<b>Olivine</b>	Oligoclase (WAR-5804) <sup>12</sup>	Heulandite (agu_heu1) <sup>22</sup>
Olivine Fo10 (KI 3008) <sup>9,10,11</sup>	Orthoclase (WAR-RGSAN01) <sup>12</sup>	
Olivine Fo25 (KI 3352) <sup>9,10,11</sup>		<b>Corrections</b>
Olivine Fo39 (KI 4143) <sup>9,10,11</sup>	<b>Other Crystalline</b>	Basalt Substrate w/473 micron <sup>23</sup>
Olivine Fo60 (KI 3362) <sup>9,10,11</sup>	Anhydrite (S9) <sup>14</sup>	Heater Spectrum 2
Olivine Fo68 (KI 3115) <sup>9,10,11</sup>	Gypsum (S8) <sup>14,15</sup>	Slope_250/247
Fayalite (WAR-FAY01) <sup>11</sup>	Hornblende (NMF-R720)	
Forsterite (AZ-01)	Kieserite (152959) <sup>15</sup>	
	Quartz (BUR-4120) <sup>2</sup>	

The 291 minerals are Categorized as they appear in the Figure 5 pie charts.

<sup>a</sup>Except where indicated, all library spectra are from the ASU spectral library: Christensen et al., 2000. <sup>1</sup>Minitti & Hamilton, 2010; <sup>2</sup>Wyatt et al., 2001; <sup>3</sup>Farrand et al., 2016; <sup>4</sup>Wards Samples; <sup>5</sup>Rampe et al., 2012; <sup>6</sup>Michalski et al., 2006; <sup>7</sup>Glotch et al., 2006; <sup>8</sup>Michalski et al., 2003; <sup>9</sup>Morse, 1996; <sup>10</sup>Hamilton, 2010; <sup>11</sup>Koeppen & Hamilton, 2008; <sup>12</sup>Hamilton & Christensen, 2000; <sup>13</sup>Lane & Christensen, 1997 <sup>14</sup>Lane & Christensen, 1998; <sup>15</sup>Lane, 2007; <sup>16</sup>Clay Mineral Society samples; <sup>17</sup>Pruett et al., 1993; <sup>18</sup>19 Morris et al., 1985; <sup>20</sup>Glotch, 2004; <sup>21</sup>Sheppard & Gude, 1982; <sup>22</sup>Ruff, 2004; <sup>23</sup>Morrison et al., 1986; <sup>24</sup>Hamilton, 2000.

### 2.3.5 Mixture Study

Previous studies have examined glass-mineral mixtures and partially crystalline basalts in the VNIR and TIR (e.g., Horgan et al., 2014; Minitti et al., 2002), but none has examined the accuracy of TIR spectral models for these mixtures. Thus, the accuracy of TIR spectral deconvolutions is unclear when amorphous phases are present. Some previous studies have

proposed that TIR linear deconvolution models may overestimate the abundance of amorphous endmembers because of their nonunique shape (e.g., Thorpe et al., 2015). To evaluate the effect on our tephra models, we include a study of the VNIR and TIR properties of physical glass-mineral mixtures.

To compare spectra of the tephra samples to spectra of samples of known crystallinity, we acquired VNIR and TIR spectra of a set of physical mixtures of glasses and crystalline minerals, analogous to the XRD calibration set created by Wall et al. (2014). Three mixture sets were created using three different glass compositions: a high-silica microscope glass slide used in Wall et al. (2014), Craters of the Moon basaltic cinders, and obsidian from a rhyolitic eruption. While the basaltic cinders are the best compositional analog for our basaltic tephra samples, the other endmembers provide insight into the effects of glass composition on their detection in VNIR and TIR spectra. Each glass was mixed in 10 wt.% increments (20 wt.% glass mixtures were skipped due to a lack of available sample during the experiment) with a crystalline mixture of San Carlos olivine and pyroxene of the same grain size (82 wt.% olivine and 18 wt.% pyroxene). Each endmember was additionally analyzed by XRD to determine the endmember crystallinity. The endmember crystallinities were used to interpolate the expected crystallinity for each mixture for comparison to VNIR and TIR derived crystallinity.

## **2.4 Results**

### **2.4.1 VNIR Spectra and Mineral Interpretations**

The VNIR reflectance spectra for the tephra samples are shown in Figure 2-3a. We have classified the tephra spectra into four spectrally distinct categories, as shown in Table 2-3: (1) Unaltered glass-dominated spectra; (2) Altered glass-dominated spectra; (3) Alteration-dominated spectra; (4) Glass-poor spectra. Unaltered glass-dominated spectra (CotM, Tseax, Surtsey) are characterized by two broad absorption bands centered between 1.05 and 1.12 and 1.9  $\mu\text{m}$  consistent with significant glass and do not display any additional absorption bands. These spectra correspond to magmatic cinder and hydrovolcanic sand samples.

However, the phreatomagmatic samples with band centers below 1  $\mu\text{m}$  have the same low crystallinity as the samples with the highest band centers. This suggests that the band shift is not due to the formation of additional crystalline phases like pyroxene and is more likely due to either

devitrified glass or the addition of a small amount of pigmentary and thus spectrally dominant crystalline iron oxides. These spectra correspond to phreatomagmatic tuffs.

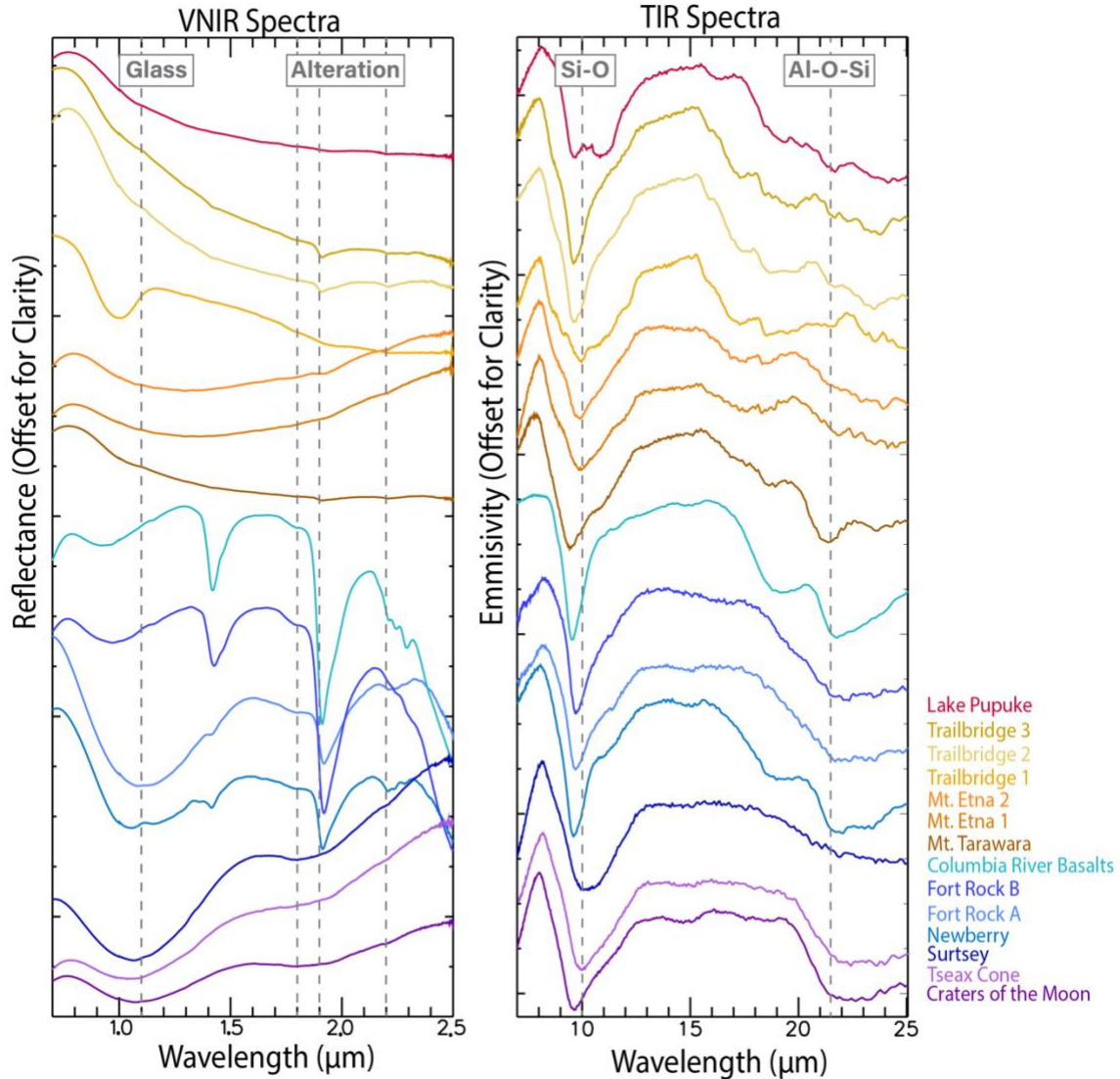


Figure 2-3. (a) Visible/near-infrared (VNIR) reflectance spectra and (b) thermal infrared (TIR) emission spectra of volcanic tephra samples, ordered by X-ray diffraction (XRD) crystallinity, decreasing from top to bottom, and colored by eruption type (purple = magmatic cinders, blue = phreatomagmatic, yellow/orange/red = magmatic). Dashed lines indicate wavelength positions of major absorption bands.

Altered glass-dominated spectra (Newberry, Fort Rock A) also exhibit a broad glass band centered between 1.05 and 1.12  $\mu\text{m}$ , but the broad 1.9  $\mu\text{m}$  glass band is obscured by additional much narrower bands attributed to alteration, including bands at 1.42, 1.78, and 1.92  $\mu\text{m}$  due to hydration in zeolites and smectites. Complex bands between 2.2 and 2.3  $\mu\text{m}$  are consistent with various phases. The asymmetric band shape and band minimum near 2.21  $\mu\text{m}$  is most consistent with hydrated glass or silica (e.g., Rice et al., 2010), but could also be due to Al-smectites. Shoulders on this band near 2.23 and 2.27–2.29  $\mu\text{m}$  are likely due to complex Al/Fe/Mg-smectites. These spectra correspond to phreatomagmatic tuff and lapilli samples.

Table 2-3. Summary of the VNIR Spectral Interpretation Expected TIR Assemblages by Tephra Type

Tephra type	VNIR spectral class	TIR assemblage
<b>Phreatomagmatic</b>		
Hydrovolcanic sand	Unaltered glass-dominated	Glass and devitrified glass-rich with minor alteration
Accretionary lapilli	Altered glass-dominated	
Tuff	Altered glass-dominated or alteration-dominated <sup>a</sup>	
<b>Volatile-rich magmatic</b>		
Low-density scoria/Cinders	Unaltered glass-dominated	Glass and devitrified glass dominated
<b>Magmatic</b>		
Scoria	Glass-poor	Glass and devitrified glass with variable feldspar
Ignimbrite	Glass-poor	Igneous crystalline dominated
<b>Post-eruption alteration</b>		
Weathered samples	Alteration-dominated	Mostly alteration minerals

<sup>a</sup>The Columbia River Basalt hyaloclastite tuff was altered by post-eruptive surface weathering. Abbreviations: TIR, thermal infrared; VNIR, visible/near-infrared.

Alteration-dominated spectra exhibit strong alteration bands at 1.42, 1.78, 1.92, and 2.2–2.3  $\mu\text{m}$  (Fort Rock B, Columbia River Basalt). Compared to the altered glass-dominated spectra, the 2.2–2.3  $\mu\text{m}$  region exhibits stronger 2.3  $\mu\text{m}$  bands, consistent with Fe/Mg-smectites. These spectra also exhibit a broad band centered between 0.92 and 0.97  $\mu\text{m}$ , which could be consistent with low-Ca pyroxenes (Adams, 1974; Cloutis & Gaffey, 1991) some iron oxides like goethite or lepidocrocite (e.g., Morris et al., 1985), partial recrystallization of nanophase ferric oxides in palagonite, or devitrified glass (Adams, 1974; Cloutis & Gaffey, 1991; Farrand et al., 2016). Crystallinity should generally increase with decreasing band center (e.g., Horgan et al., 2014), and this trend is observed in most of the samples with 1  $\mu\text{m}$  iron bands (Figure 2-4).

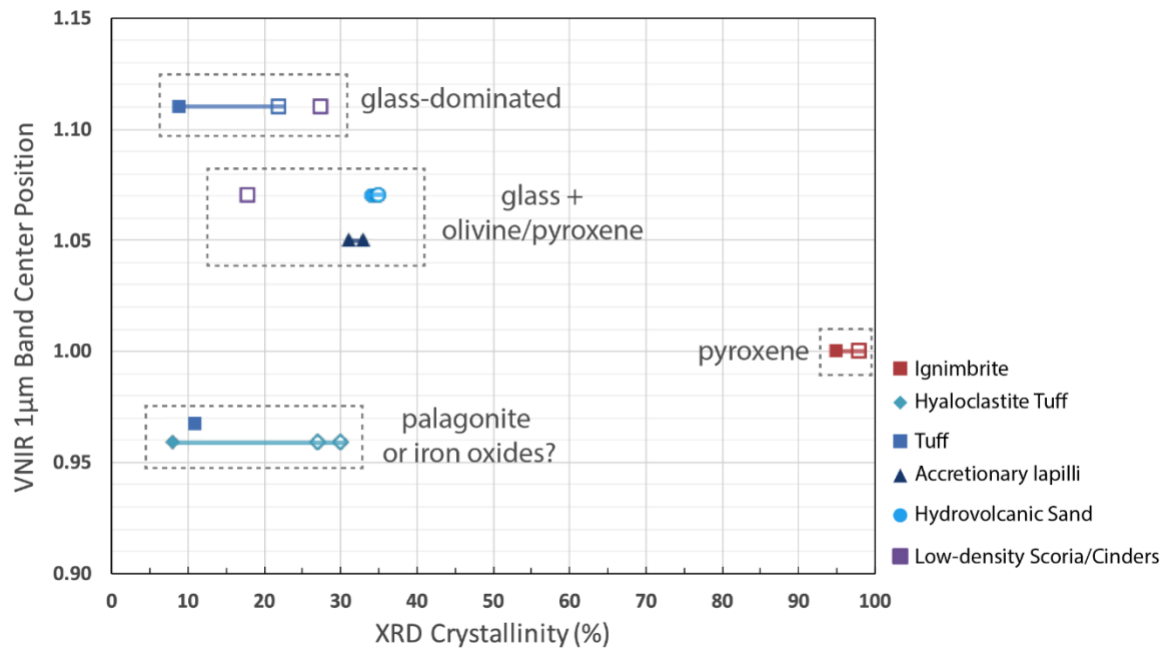


Figure 2-4. Comparison of bulk (open symbol) and groundmass (closed symbol) X-ray diffraction (XRD) crystallinities of the tephra to the position of their 1  $\mu\text{m}$  band center in VNIR spectra. The phreatomagmatic and cinder cone tephtras display clear 1  $\mu\text{m}$  bands with two distinct groups of band centers: near 1.08  $\mu\text{m}$ , interpreted as due to glass, and 0.95  $\mu\text{m}$ , interpreted as due to either devitrified glass or spectrally dominant iron oxides in palagonite. Most magmatic tephra samples (e.g., scoria) do not exhibit clear 1  $\mu\text{m}$  bands and are omitted.

Glass-poor spectra do not exhibit glass or alteration bands (Tarawara, Etna, Trailbridge, Lake Pupuke). Instead, a strong blue and concave up slope dominates these spectra. This lack of bands is most likely due to very small grain sizes for the crystalline components, potentially formed during rapid cooling, consistent with previous studies showing that aphanitic or microcrystalline basalts do not exhibit strong VNIR absorption bands (Carli et al., 2014). The narrower  $\sim 1 \mu\text{m}$  pyroxene-like absorption without a corresponding 2  $\mu\text{m}$  absorption present in the magmatic Trailbridge 1 spectrum is consistent with an aphanitic basalt (Carli et al., 2014). These spectra correspond to magmatic scoria and ignimbrites.

## 2.4.2 TIR Spectra and Deconvolution Models

The TIR emission spectra for all tephra samples are shown in Figure 2-3b. All spectra exhibit an absorption near the fundamental Si-O band at 10  $\mu\text{m}$ . A well-rounded 10  $\mu\text{m}$  band as

visible in Surtsey is consistent with glass (Crisp et al., 1990; Minitti et al., 2002; Minitti & Hamilton, 2010). The low-density scoria/cinders (CotM, Tseax) exhibit a broad V-shape, while tuff and accretionary lapilli (Fort Rock A/B, Newberry) exhibit a weak doublet in this region, composed of a narrow band near 9.6–9.8  $\mu\text{m}$  and a weak shoulder near 10.9–11.3  $\mu\text{m}$ , which is consistent with partial reordering of the glass structure due to devitrification (Farrand et al., 2016). As crystallinity increases, the 10  $\mu\text{m}$  band narrows and exhibits a more complex shape, consistent with absorption bands due to crystalline silicates like feldspar and pyroxene (Trailbridge 2/3). At longer wavelengths, four spectra (CotM, Tseax, Newberry, Fort Rock (b)) exhibit broad bands near 21  $\mu\text{m}$  (465  $\text{cm}^{-1}$ ), consistent with amorphous silicates (Ruff & Christensen, 2007). These four spectra correspond to the glass-rich phreatomagmatic and cinder samples, as well as the glass-dominated VNIR spectral class.

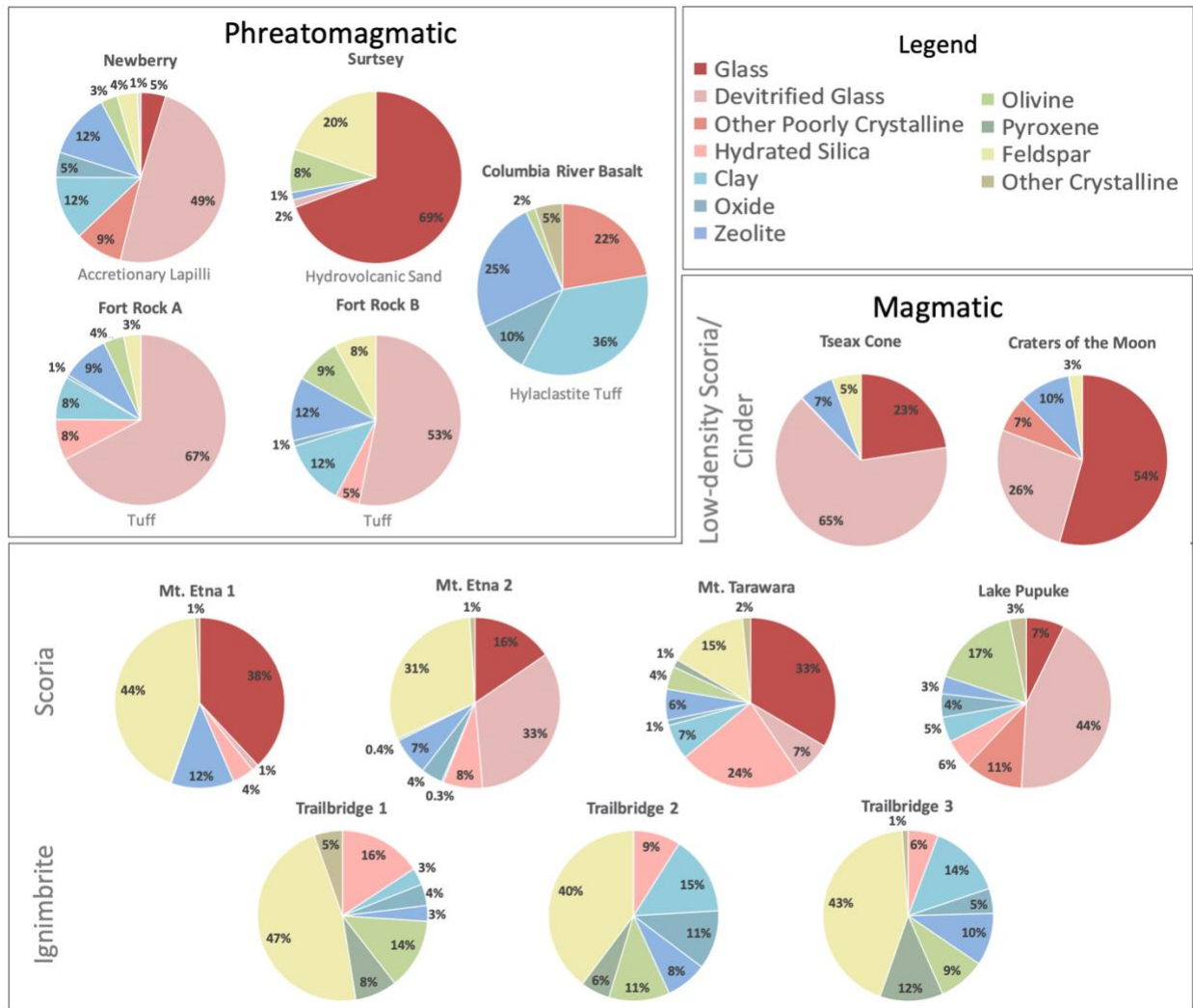


Figure 2-5. Tephra mineralogies modeled from linear deconvolution of thermal infrared (TIR) spectra, separated by eruption style and tephra type. Red/pink indicates X-ray amorphous phases, blues indicate alteration minerals, and green/yellow indicate crystalline igneous minerals.

In general, TIR linear deconvolution models (hereafter, TIR models) are able to accurately predict the lower crystallinity characteristic of phreatomagmatic tephra previously identified based on XRD crystallinity, as well as the high crystallinity of magmatic ignimbrites. Figure 2-5 shows TIR models calculated using our spectral library (Table 2), and the crystallinities derived from these TIR models are compared to their XRD counterparts in Figure 2-6. Crystallinities from TIR models (11%–46%) typically agree with XRD crystallinities (9%–35%) of samples from deposits formed in phreatomagmatic or cinder cone eruptions (Figure 2-6), and TIR models also agree with XRD measurements of ignimbrites (85%–95% for both techniques). One exception is the highly

weathered Columbia River Basalt hyaloclastite tuff, but we attribute the mismatch to the high percentage of phyllosilicate and other alteration minerals in this sample that may be difficult to characterize in XRD. However, TIR models of some scoria samples (e.g., Tarawara, Lake Pupuke) with moderate XRD crystallinity (~50%–80%) predict much lower crystallinities (up to 45% less) than determined from XRD. Previous studies of other rock types (e.g., sedimentary rocks; Thorpe et al., 2015) have also observed higher than expected TIR models of amorphous phases in some samples and postulated that this could occur if the smooth and broad TIR absorptions of amorphous phases were used to better fit other poorly modeled spectral features. However, this may not be true for igneous samples where significant glass is present, as demonstrated by our mixing study.

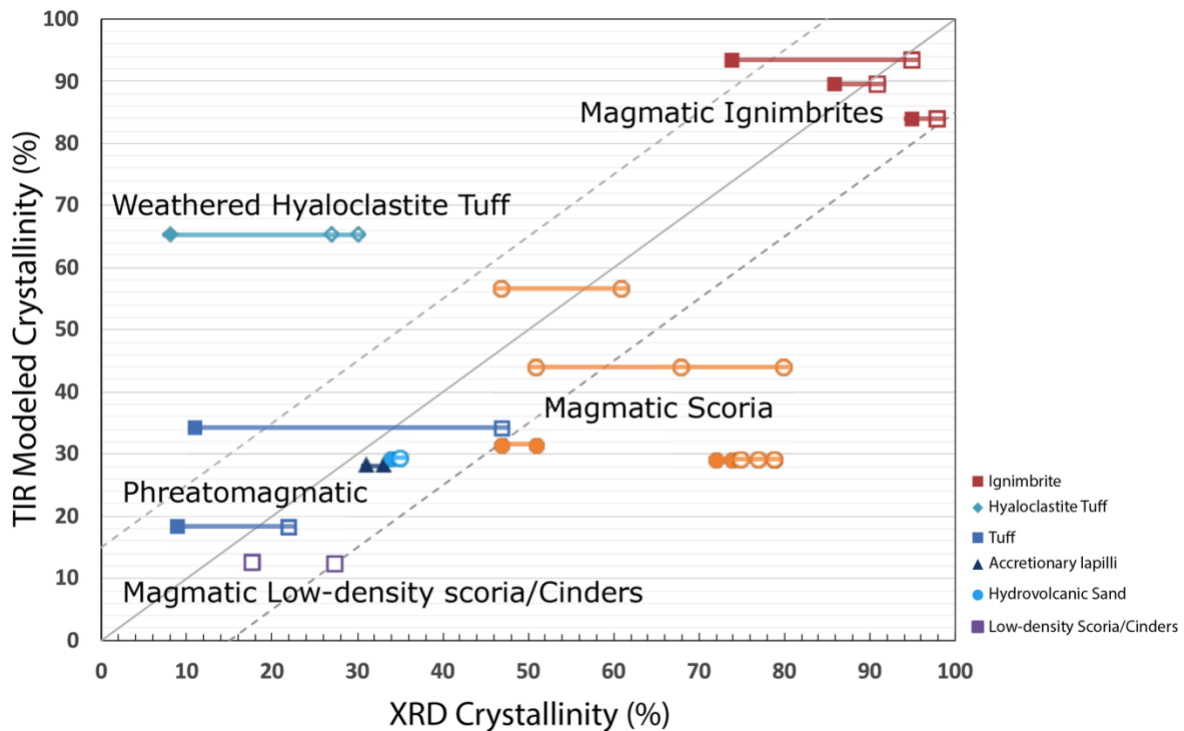


Figure 2-6. Comparison of thermal infrared (TIR) modeled crystallinity to bulk (open symbol) and groundmass (closed symbol) X-ray diffraction (XRD) crystallinities. Horizontal lines indicate the range of measured XRD crystallinities for each sample. Dotted trendlines represent standard errors in TIR measurements.

### 2.4.3 Mixture Study

VNIR spectra of our physical mixtures of crystalline minerals and glasses confirm that low abundances of glass cannot be easily identified in VNIR spectra, but high abundances of glass exhibit a unique spectral character (Figure 2-7; Cannon et al., 2017; Horgan et al., 2014). When glass of any composition is added to our crystalline endmember mixture, it dampens and broadens the 1  $\mu\text{m}$  band compared to the fully crystalline mixture's deep and narrow absorption band. However, the band center is not clearly affected until the crystallinity is reduced to 30–40 wt.% in the Fe-bearing glasses (Figure 2-8a), and Fe-poor glasses like the glass slide do not exhibit 1  $\mu\text{m}$  bands and thus do not change the band center.

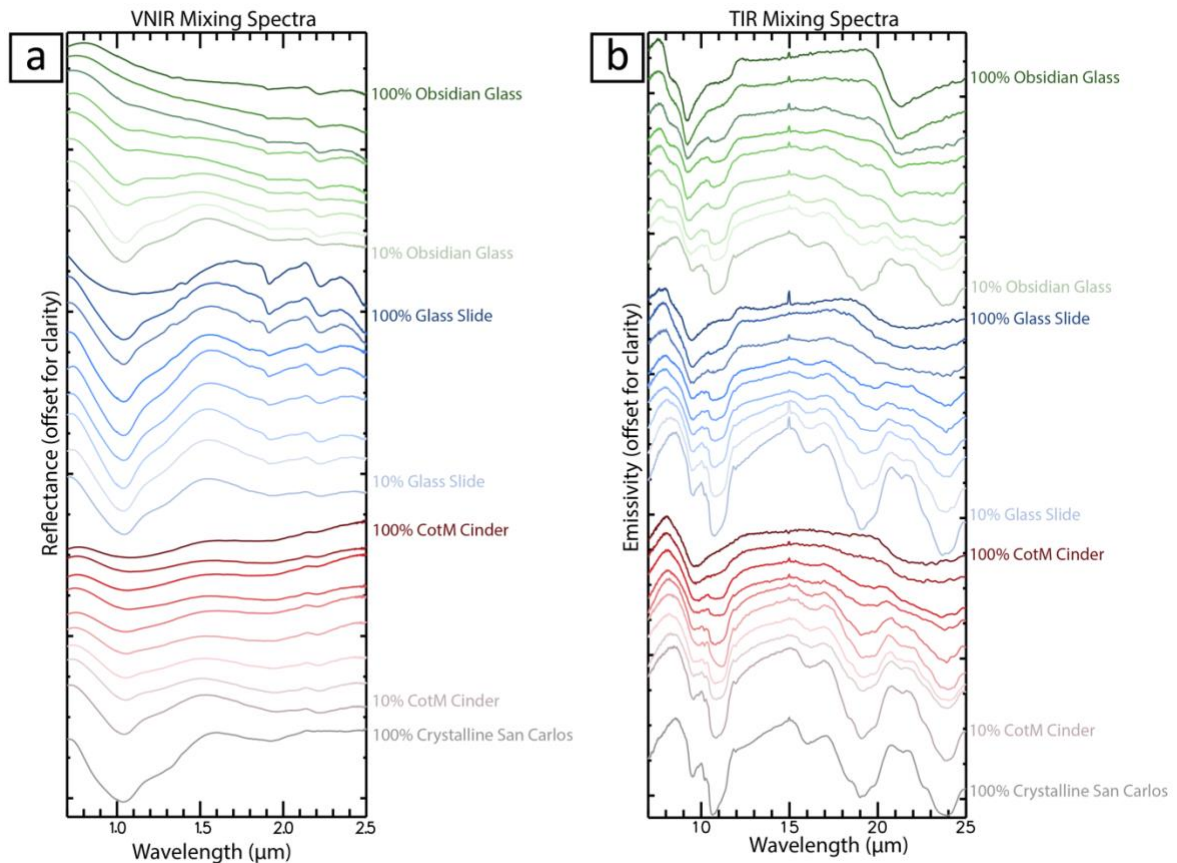


Figure 2-7. Spectra of physical mixtures of glasses and San Carlos olivine and pyroxene phenocrysts, with glass content increasing in 10 wt.% intervals. (a) Visible/near-infrared (VNIR) reflectance spectra and (b) thermal infrared (TIR) emission spectra.

In some TIR models of the magmatic tephra samples, glass is over-modeled in TIR at intermediate to high crystallinities, >45%, while some consistent over-modeling of glass in Craters of the Moon and obsidian mixtures is observed for crystallinities 50%–60%; however, it is typically within the 15% error expected for TIR models (Figure 2-8b). The opposite trend occurs for the glass slide mixture, as the TIR crystallinity is never modeled below 28%, even for the slide endmember sample, although the sample is nearly totally amorphous (1.8% XRD crystallinity). This discrepancy is likely due to a lack of a high-silica glass endmember that best matches this type of glass in our spectral library. In contrast, the other mixtures are modeled well at low crystallinities because the obsidian glass is an endmember of our library, and the Craters of the Moon sample is similar to basaltic glass samples in the library. However, the significant over-modeling of glass seen in some of our tephra samples (up to 45% above that predicted by XRD) is not observed in these physical mixtures. Thus, the mismatch between TIR and XRD crystallinity in some scoria samples may be due to other physical or compositional effects, as discussed in the next section.

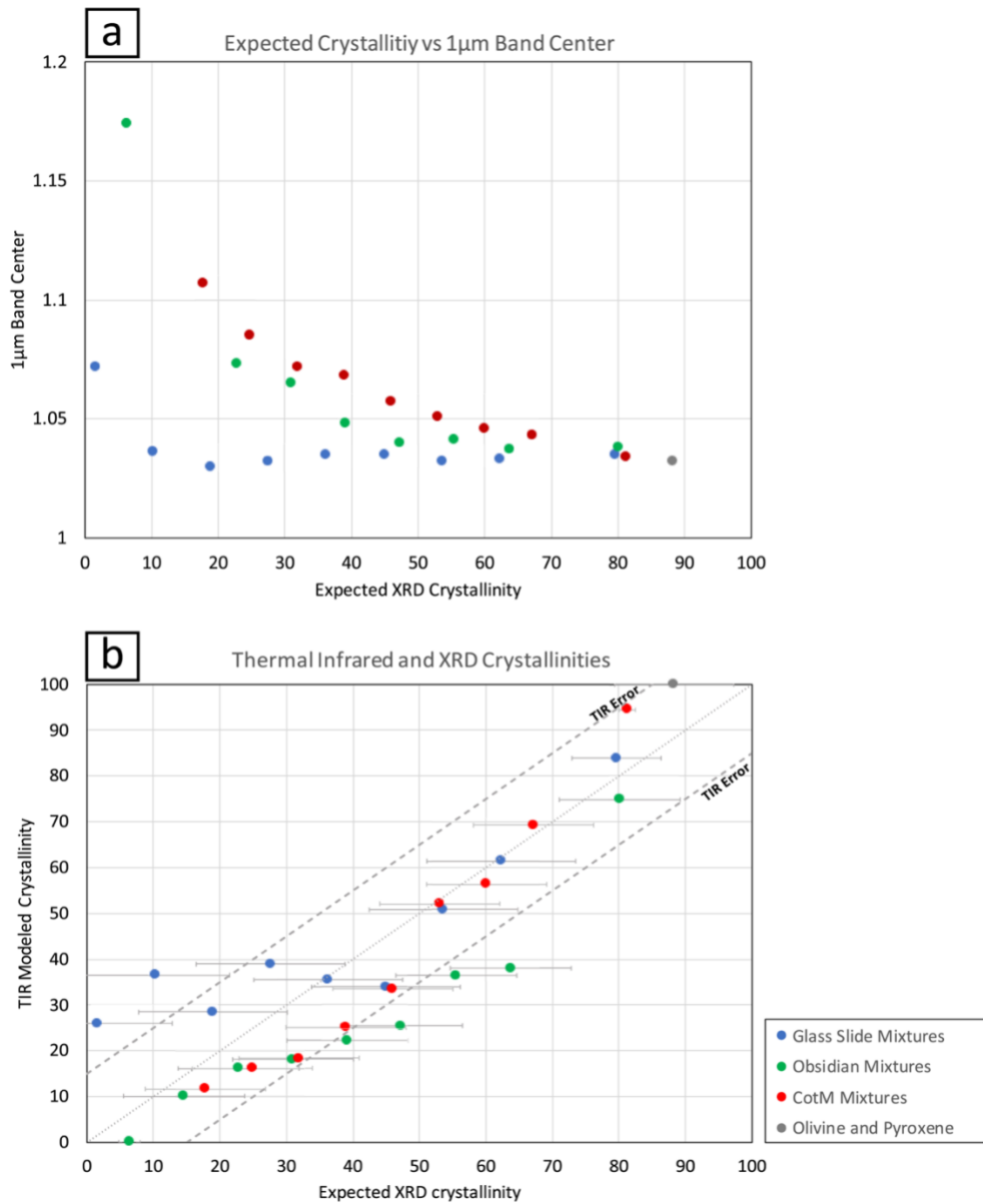


Figure 2-8. Analysis of physical mixture spectra. (a) The position of the 1  $\mu$ m band center with respect to the expected crystallinity in the mixing study. As the amount of glass in the mixture decreased, the band center also decreased and can be used to determine relative glass abundance and potentially eruption style. (b) Comparison of the thermal infrared (TIR) crystallinities of the mixtures to their expected X-ray diffraction (XRD) crystallinities. The glass slide endmember did not have a representative glass type in the spectral library, which could account for the diversion from the trendline at low crystallinities. This mixing study does not display the over-modeling of glass seen in the tephra samples.

## 2.5 Discussion

### 2.5.1 Detecting Eruption Styles in VNIR, TIR, and XRD Data

Phreatomagmatic deposits are consistently poorly crystalline (glass- and/or palagonite-rich) based on XRD and TIR models and are distinctive in VNIR spectra as glass or palagonite-rich. It is particularly notable that most phreatomagmatic deposits exhibit glass-rich signatures in VNIR spectra because previous VNIR spectral studies have shown that glass is only confidently detected when present in mixtures with crystalline minerals at abundances higher than 70–80 wt.% (Horgan et al., 2014). This is confirmed by our VNIR observations, which only exhibit clear glass bands centered between 1.08 and 1.15  $\mu\text{m}$  for XRD and TIR glass abundances  $>70\%$  (Figure 2-4). Thus, the presence of a clear glass band centered between 1.08 and 1.2  $\mu\text{m}$  in volcanic deposits implies that the deposit is either phreatomagmatic tephra or a cinder/scoria cone, which should be straightforward to differentiate based on geomorphology. However, several of our glassy samples exhibit band centers below 1.08  $\mu\text{m}$ , which could be misinterpreted due to crystalline endmembers such as olivine and pyroxene (Figure 2-2). In this case, glass can still be identified based either on the position of the 2  $\mu\text{m}$  band or based on strong palagonite signatures. Additionally, TIR models of phreatomagmatic tephtras consistently show glass abundances  $>50\%$  (Figures 2-5 and 2-6), so possible VNIR indicators of glass could be confirmed by high glass abundances from TIR models and vice versa.

Other than the cinder samples, magmatic deposits are distinct from the phreatomagmatic deposits in VNIR spectra as they do not exhibit strong 1 and 2  $\mu\text{m}$  glass bands. Instead, they exhibit a strong concave up blue spectral slope consistent with aphanitic basalt (Cheek & Pieters, 2014), but this spectral shape is challenging to differentiate from other causes of similar slopes, like leaching rinds on glass that often form in arid volcanic environments (Minitti & Hamilton, 2010).

In TIR models, the crystallinity and composition of magmatic deposits vary between specific deposit types. Samples from Etna, Tarawara, and Lake Pupuke were collected as scoria deposits. Scoria can be highly vesicular and thus cool relatively quickly, preventing extensive crystal growth. TIR and XRD crystallinities of the scoria samples are generally moderate, but some scoria TIR crystallinities are much lower than their XRD crystallinities. Some of the mismatch may be due to materials with complex crystallinities, such as hydrated silica (Figure 5), but may

also be due to variability in crystallinity within each sample. Wall et al. (2014) suggested that the large range of XRD crystallinities observed within each scoria sample is due to clast size, as larger pyroclasts would cool more slowly, allowing for more crystal growth than small pyroclasts, where the glass-rich cinders are an endmember of this trend. While TIR appears to undermodel the crystallinity of scoria, this could be due to local variability (e.g., phenocryst density within the samples due to variations in clast size or vesicularity). This may be further exacerbated by TIR sample prep techniques—phenocrysts may be challenging to mix throughout otherwise fine-grained crushed samples evenly.

In contrast, both TIR and XRD models of ignimbrites (Trailbridge 1/2/3) predict similar crystallinities, >70%. Ignimbrites are deposited as dense layers and cool more slowly, increasing crystallization. TIR models of the ignimbrites show a trend of increasing crystallinity with the degree of welding (Trailbridge 3, lightly welded, to Trailbridge 1, densely welded; Figure 5), consistent with crystallization during the sustained higher temperatures of higher degrees of welding (Keating, 2005). The glass in the samples is entirely modeled as devitrified, also consistent with welding. Therefore, the geologic context of the pyroclasts from the magmatic eruptions strongly influences the resulting crystallinity (Table 3), and both the abundance of glass and overall assemblage can be used to infer eruption style.

## **2.5.2 Strategies for Determining Eruption Styles on Mars**

A combination of VNIR and TIR spectra, along with high-resolution imagery, would be the most definitive method to determine volcanic eruption style of possible volcanic deposits on Mars from orbit. Phreatomagmatic tephra and cinders would exhibit both VNIR and TIR spectra consistent with high abundances of glass and/or palagonite (Figure 3), and geomorphology from visible imagery could help to distinguish between specific eruption styles (e.g., Ackiss et al., 2018b; Ghatan & Head, 2001). Magmatic eruptions can produce a wide range of crystallinities that are modeled to varying levels of accuracy with TIR, but the crystallinity is high enough that the spectra consistently show no clear evidence of glass in VNIR. So, for example, in cases where VNIR spectra of a deposit are indistinguishable as glass or olivine, TIR spectra could provide the resolving factor, as TIR models with high crystallinities would indicate magmatic tephra. In cases with ambiguous moderate crystallinities like our scoria samples, TIR would predict moderate to

high glass abundances, and VNIR should be able to confirm that these are magmatic deposits based on their strong blue slope and lack of glass absorption bands.

Ultimately, neither TIR nor VNIR can reproduce the quantitative XRD models' accuracy for estimating the crystallinity of volcanic tephra. This is partly because standard lab XRD utilizes an internal standard to calibrate the results, but this step requires extensive sample preparation that is not possible in XRD instruments flown on planetary missions like CheMin (Blake et al., 2012). However, previous work has shown that even without an internal standard, amorphous abundances from XRD refinements are consistently accurate (Smith et al., 2018). Thus, for landed missions, XRD still provides the gold standard for bulk assemblage analysis. However, sample acquisition for XRD analysis is labor and resource intensive, leading to a small number of total samples analyzed (e.g., 19 drilled samples by Curiosity in 6.5 years; (Rampe et al., 2020). In contrast, remote sensing via VNIR or TIR spectroscopy can be deployed from orbit and allows rapid analysis of all visible outcrops from a landed mission, so the lack of accuracy of these techniques is often balanced by their ability to acquire significantly more data.

Another advantage of VNIR and TIR spectra over XRD is that they can identify and differentiate specific amorphous phases and constrain their origin. For example, VNIR is sensitive to alteration products, even when they are poorly crystalline, which can then be used to constrain the nature of syn-eruptive alteration environments (Ackiss et al., 2018; Farrand et al., 2016). Devitrified glass can be differentiated from glass in TIR spectra and indicates distinct thermal conditions after emplacement (Farrand et al., 2016). TIR models of both welded ignimbrites and hydrovolcanic tephra are dominated by devitrified glass, indicating prolonged thermal alteration, but the hydrovolcanic tephra often also exhibits strong clay mineral absorptions, allowing us to specifically infer hydrothermal alteration (Ehlmann & Mustard, 2012; Farrand et al., 2018). Similarly, accretionary lapilli exhibit evidence for aqueous alteration in the VNIR but are dominated by glass in both VNIR and TIR, suggesting that alteration occurred under cooler and more water-limited conditions. Thus, spectroscopy of tephra deposits can be used not only to characterize eruption style but also to constrain the nature of phreatomagmatic volatiles and post-eruption alteration processes.

### **2.5.3 Differentiating Impact and Volcanic Glasses**

This study provides a framework for using spectroscopy to constrain the origin and aqueous history of possible volcanic tephra deposits on Mars. However, additional work is needed before the spectral properties of deposits can confidently infer a volcanic origin without clear supporting evidence from morphology or geologic context. In particular, while explosive volcanism is a likely hypothesis for the origin of glass-rich deposits, on other planets, impact processes could also produce these deposits, and the mineralogical and spectral properties of impact products are not yet well understood. Studies conducted to date suggest that impact and volcanic glasses are both highly variable but may exhibit some consistent compositional or spectral differences. Hydration may be one good indicator of volcanic glass. On Earth, volcanic glasses tend to have higher water contents than glasses formed by impacts due to differences in temperature of formation, and the difference in water content can constrain formation processes (Glass, 2016; Zhang, 1999). However, some impact melts formed underwater may also be hydrated (Osinski et al., 2019). Some TIR studies suggest that the narrow or broad shape of the SiO<sub>4</sub> bending feature between 21.3 and 22.2  $\mu\text{m}$  could distinguish between impact and volcanic glasses, respectively (Farrand et al., 2016; Wright et al., 2011). Many synthetic impact glasses are broadly spectrally similar to our unaltered glass-rich phreatomagmatic tephra in the VNIR (Cannon et al., 2017; Moroz et al., 2009), but it is unclear if these synthetic impact glasses are analogous to actual impact deposits. As our study has demonstrated for volcanic tephtras, understanding the spectral properties of impact glass alone is insufficient because glass abundance, macro- and micro-textures, and syn- or post-emplacement alteration can modify both the TIR and VNIR spectral properties of the actual deposits significantly. Further work is needed on the spectral properties of impact deposits, but a combination of spectral properties and geologic context would likely be the most effective method to distinguish impact deposits and pyroclastic deposits from orbit.

## **2.6 Conclusions**

Explosive volcanic deposits are records of local environmental conditions and the internal volatile content of planetary bodies. Wall et al. (2014) showed that XRD-derived crystallinity of a tephra deposit is a good indicator of the source of volatiles—magmatic volatiles produce highly crystalline tephra compared to the external volatiles that produces glass-rich (>50%) tephra during

phreatomagmatic eruptions For planetary exploration, XRD measurements would require landed missions or sample return, while VNIR and TIR spectra are far easier to collect and can be acquired from orbit over a far larger set of samples/targets or in situ. Our study suggests that high glass abundances identified using TIR and VNIR spectra of possible volcanic deposits can infer interactions with external volatiles during eruption. VNIR spectra can detect glass at high abundances and alteration minerals, both of which form during water-magma interactions. VNIR spectra are unable to detect moderate glass abundances typical of magmatic deposits and instead show featureless spectra consistent with fine-grained basalt. TIR spectral models can detect glass at all abundances; however, texture, grain size, and compositional variability of the sample influence the accuracy of TIR models. Thus, it would be ideal to use multiple remote sensing datasets as well as geomorphic context to characterize the origin of volcanic deposits. Detections of high abundance of glass (>50%) in both VNIR and TIR suggests a phreatomagmatic tephra (or a cinder cone, if present in visible imagery), while no glass detection in VNIR and moderate to low abundances of glass in TIR would suggest a magmatic tephra. These interpretations could be bolstered by the specific phases detected, where devitrified glass detected in TIR but little alteration or glass in VNIR is more likely to indicate an ignimbrite, and strong alteration and/or glass in VNIR would indicate water- or ice-magma interactions. Combining VNIR and TIR orbital data for analysis based on our new laboratory library may offer a basis for reevaluating Martian volcanic and volatile histories using existing orbital and in situ remote sensing datasets.

## **2.7 Data Availability Statement**

All spectral data and unmixing results are included in a supplementary document. The spectral library used for the deconvolutions is publicly available on the ASU TES spectral library site under the name mhenderson\_2019.

## **2.8 Acknowledgements**

This research was partially funded by the National Science Foundation Graduate Research Program DGE1333468. We appreciate the suggestions from three anonymous reviewers and W.H. Farrand, which strengthened the manuscript. Additionally, we thank Rose Gallo for contributing the Tseax Cone sample.

## 2.9 References

- Ackiss, S. E., Horgan, B. H. N., Scudder, N., Gudnason, J., Haberle, C., & Thorsteinsson, T. (2018a). The mineralogic variability of Icelandic palagonites: An analog study for Mars. *LPSC(49)*, 1773.
- Ackiss, S., Horgan, B., Seelos, F., Farrand, W., & Wray, J. (2018b). Mineralogic evidence for subglacial volcanism in the Sisyphi Montes region of Mars. *Icarus*, 311, 357–370. <https://doi.org/10.1016/j.Icarus.2018.03.026>
- Adams, J. B. (1974). Visible and near-infrared diffuse reflectance spectra of pyroxenes as applied to remote sensing of solid objects in the solar system. *Journal of Geophysical Research*, 79(32), 4829–4836. <https://doi.org/10.1029/JB079i032p04829>
- Adams, J. B., Pieters, C., & McCord, T. B. (1974). Orange glass-Evidence for regional deposits of pyroclastic origin on the moon. *LPSC*, 1, 171–186.
- Allen, C., Gooding, J. L., Jercinovic, M., & Keil, K. (1981). Altered basaltic glass: A terrestrial analog to the soil of Mars. *Icarus*, 45(2), 347–369. [https://doi.org/10.1016/0019-1035\(81\)90040-3](https://doi.org/10.1016/0019-1035(81)90040-3)
- Bandfield, J. L. (2002). Global mineral distributions on Mars. *Journal of Geophysical Research*, 107(E6), 9-1–9-20. <https://doi.org/10.1029/2001JE001510>
- Bandfield, J. L., Edwards, C. S., Montgomery, D. R., & Brand, B. D. (2012). The dual nature of the Martian crust: Young lavas and old clastic materials. *Icarus*, 222(1), 188–199. <https://doi.org/10.1016/j.Icarus.2012.10.023>
- Bish, D. L., Blake, D. F., Vaniman, D. T., Chipera, S. J., Morris, R. V., Ming, D. W., et al. (2013). X-ray diffraction results from Mars Science Laboratory: Mineralogy of rocknest at gale crater. *Science*, 341(6153), 1238932. <https://doi.org/10.1126/science.1238932>
- Bishop, J. L., Dobreá, E. Z. N., McKeown, N. K., Parente, M., Ehlmann, B. L., Michalski, J. R., et al. (2008). Phyllosilicate Diversity and Past Aqueous Activity Revealed at Mawrth Vallis, Mars. *Science*, 321(5890), 830–833. <https://doi.org/10.1126/science.1159699>
- Blake, D., Vaniman, D., Achilles, C., Anderson, R., Bish, D., Bristow, T., et al. (2012). Characterization and Calibration of the CheMin Mineralogical Instrument on Mars Science Laboratory. *Space Science Reviews*, 170, (1-4), 341–399. <https://doi.org/10.1007/s11214-012-9905-1>
- Brož, P., Čadek, O., Hauber, E., & Rossi, A. P. (2015). Scoria cones on Mars: Detailed investigation of morphometry based on high-resolution digital elevation models. *Journal of Geophysical Research: Planets*, 120(9), 1512–1527. <https://doi.org/10.1002/2015JE004873>
- Byrne, P. K. (2020). A comparison of inner Solar System volcanism. *Nature Astronomy*, 4(4), 321–327. <https://doi.org/10.1038/s41550-019-0944-3>

- Cannon, K. M., Mustard, J. F., Parman, S. W., Sklute, E. C., Dyar, M. D., & Cooper, R. F. (2017). Spectral properties of Martian and other planetary glasses and their detection in remotely sensed data. *Journal of Geophysical Research: Planets*, 122(1), 249–268. <https://doi.org/10.1002/2016JE005219>
- Carli, C., Serventi, G., & Sgavetti, M. (2014). VNIR spectral characteristics of terrestrial igneous effusive rocks: Mineralogical composition and the influence of texture. *Geological Society, London, Special Publications*, 401(1), SP401.19–158. <https://doi.org/10.1144/SP401.19>
- Carr, M. H., & Head, J. W., III. (2010). Geologic history of Mars. *Earth and Planetary Science Letters*, 294(3–4), 185–203. <https://doi.org/10.1016/j.epsl.2009.06.042>
- Carr, M. H., Masursky, H., & Saunders, R. S. (1973). A generalized geologic map of Mars. *Journal of Geophysical Research: Oceans*, 78(20), 4031–4036. <https://doi.org/10.1029/JB078i020p04031>
- Cashman, K. V., & Sparks, R. S. J. (2013). How volcanoes work: A 25 year perspective. *Geological Society of America Bulletin*, 125(5–6), 664–690. <https://doi.org/10.1130/B30720.1>
- Che, C., Glotch, T. D., Bish, D. L., Michalski, J. R., & Xu, W. (2011). Spectroscopic study of the dehydration and/or dehydroxylation of phyllosilicate and zeolite minerals. *Journal of Geophysical Research: Planets* (1991–2012), 116(E5), <https://doi.org/10.1029/2010je003740>
- Cheek, L. C., & Pieters, C. M. (2014). Reflectance spectroscopy of plagioclase-dominated mineral mixtures: Implications for characterizing lunar anorthosites remotely. *American Mineralogist*, 99(10), 1871–1892. <https://doi.org/10.2138/am-2014-4785>
- Christensen, P. R., Bandfield, J. L., Hamilton, V. E., Howard, D. A., Lane, M. D., Piatek, J. L., et al. (2000). A thermal emission spectral library of rock-forming minerals. *Journal of Geophysical Research: Oceans*, 105(E4), 9735–9739. <https://doi.org/10.1029/1998JE000624>
- Christensen, P. R., & Harrison, S. T. (1993). Thermal infrared emission spectroscopy of natural surfaces: Application to desert varnish coatings on rocks. *Journal of Geophysical Research: Oceans*, 98(B11), 19819–19834. <https://doi.org/10.1029/93JB00135>
- Cloutis, E. A., & Gaffey, M. J. (1991). Pyroxene spectroscopy revisited: Spectral-compositional correlations and relationship to geothermometry. *Journal of Geophysical Research: Oceans*, 96(E5), 22809–22826. <https://doi.org/10.1029/91JE02512>
- Cloutis, E. A., Gaffey, M. J., Smith, D. G. W., & Lambert, R. S. J. (1990). Reflectance spectra of glass-bearing mafic silicate mixtures and spectral deconvolution procedures. *Icarus*, 86(2), 383–401. Crisp, J., Kahle, A. B., & Abbott, E. A. (1990). Thermal infrared spectral character of Hawaiian basaltic glasses. *Journal of Geophysical Research: Oceans*, 95(B13), 21657–21669. <https://doi.org/10.1029/JB095iB13p21657>

- Drief, A., & Schiffman, P. (2004). Very low-temperature alteration of sideromelane in hyaloclastites and hyalotuffs from Kilauea and Mauna Kea volcanos: Implications for the mechanism of palagonite formation. *Clays and Clay Minerals*, 52(5), 622–634. <https://doi.org/10.1346/CCMN.2004.0520508>
- Dufresne, C. D. M., King, P. L., Dyar, M. D., & Dalby, K. N. (2009). Effect of SiO<sub>2</sub>, total FeO, Fe<sup>3+</sup>/Fe<sup>2+</sup>, and alkali elements in basaltic glasses on mid-infrared spectra. *American Mineralogist*, 94(11–12), 1580–1590.
- Dyar, M. D., & Burns, R. (1981). Coordination chemistry of iron in glasses contributing to remote-sensed spectra of the Moon. Lunar and Planetary Science Conference.
- Edgett, K. S. (1997). Aeolian dunes as evidence for explosive volcanism in the Tharsis region of Mars. *Icarus*, 130(1), 96–114. <https://doi.org/10.1006/icar.1997.5806>
- Edwards, C. S., & Ehlmann, B. L. (2015). Carbon sequestration on Mars. *Geology*, 43(10), 863–866. <https://doi.org/10.1130/G36983.1>
- Ehlmann, B. L., & Mustard, J. F. (2012). An in-situ record of major environmental transitions on early Mars at Northeast Syrtis Major. *Geophysical Research Letters*, 39(11), L11202. <https://doi.org/10.1029/2012gl051594>
- Farrand, W. H., Wright, S. P., Glotch, T. D., Schröder, C., Sklute, E. C., & Dyar, M. D. (2018). Spectroscopic examinations of hydro- and glaciovolcanic basaltic tuffs: Modes of alteration and relevance for Mars. *Icarus*, 309, 241–259. <https://doi.org/10.1016/j.Icarus.2018.03.005>
- Farrand, W. H., Wright, S. P., Rogers, A. D., & Glotch, T. D. (2016). Basaltic glass formed from hydrovolcanism and impact processes: Characterization and clues for detection of mode of origin from VNIR through MWIR reflectance and emission spectroscopy. *Icarus*, 275, 16–28. <https://doi.org/10.1016/j.Icarus.2016.03.027>
- Feely, K. C., & Christensen, P. R. (1999). Quantitative compositional analysis using thermal emission spectroscopy: Application to igneous and metamorphic rocks. *Journal of Geophysical Research: Oceans*, 104(E10), 24195–24210. <https://doi.org/10.1029/1999JE001034>
- Ghatan, G. J. (2002). Candidate subglacial volcanoes in the south polar region of Mars: Morphology, morphometry, and eruption conditions. *Journal of Geophysical Research*, 107(E7), <http://doi.org/10.1029/2001je001519>
- Glass, B. P. (2016). Glass: The Geologic Connection. *International Journal of Applied Glass Science*, 7(4), 435–445. <https://doi.org/10.1111/ijag.12240>
- Glotch, T. D., Morris, R. V., Christensen, P. R., & Sharp, T. G. (2004). Effect of precursor mineralogy on the thermal infrared emission spectra of hematite: Application to Martian hematite mineralization. *Journal of Geophysical Research: Planets* (1991–2012), 109(E7), <https://doi.org/10.1029/2003je002224>

- Glotch, T. D., Bandfield, J. L., Christensen, P. R., Calvin, W. M., McLennan, S. M., Clark, B. C., et al. (2006). Mineralogy of the light-toned outcrop at Meridiani Planum as seen by the Miniature Thermal Emission Spectrometer and implications for its formation. *Journal of Geophysical Research: Planets* (1991–2012), 111(E12), <https://doi.org/10.1029/2005je002672>
- Hamilton, V. E. (2000). Thermal infrared emission spectroscopy of the pyroxene mineral series. *Journal of Geophysical Research: Planets*, 105(E4), 9701–9716. <https://doi.org/10.1029/1999je001112>
- Hauber, E., Brož, P., Rossi, A. P., & Michael, G. (2015). A field of small pitted cones on the floor of Coprates Chasma: Volcanism inside Valles Marineris. *LPSC*, 46(1476).
- Head, J. W., III., & Wilson, L. (1979). Alphonsus-type dark-halo craters: Morphology, Morphometry and eruption conditions. *Lunar and Planetary Science Conference*, 10, 2861–2897. Horgan, B., & Bell, J. F., III. (2012). Widespread weathered glass on the surface of Mars. *Geology*, 40(5), 391–394. <https://doi.org/10.1130/G32755.1>
- Horgan, B. H. N., Cloutis, E. A., Mann, P., & Bell, J. F., III. (2014). Near-infrared spectra of ferrous mineral mixtures and methods for their identification in planetary surface spectra. *Icarus*, 234, 132–154. <https://doi.org/10.1016/j.Icarus.2014.02.031>
- Hunt, G. R. (1977). Spectral signatures of particulate minerals in the visible and near infrared. *Geophysics*, 42(3), 501–513. <https://doi.org/10.1190/1.1440721>
- Hynek, B. M., Phillips, R. J., & Arvidson, R. E. (2003). Explosive volcanism in the Tharsis region: Global evidence in the Martian geologic record. *Journal of Geophysical Research: Oceans*, 108(E9), 18991. <https://doi.org/10.1029/2003JE002062>
- Keating, G. N. (2005). The role of water in cooling ignimbrites. *Journal of Volcanology and Geothermal Research*, 142(1–2), 145–171. <https://doi.org/10.1016/j.jvolgeores.2004.10.019>
- Kerber, L., Head, J. W., Madeleine, J.-B., Forget, F., & Wilson, L. (2012). The dispersal of pyroclasts from ancient explosive volcanoes on Mars: Implications for the friable layered deposits. *Icarus*, 219(1), 358–381. <https://doi.org/10.1016/j.Icarus.2012.03.016>
- Koeppen, W. C., & Hamilton, V. E. (2008). Global distribution, composition, and abundance of olivine on the surface of Mars from thermal infrared data. *Journal of Geophysical Research: Planets* (1991–2012), 113(E5), <https://doi.org/10.1029/2007je002984>
- Kokaly, R. F., Clark, R. N., Swayze, G. A., Livo, K. E., Hoefen, T. M., Pearson, N. C., et al. (2017). USGS spectral library version 7: U.S. Geological Survey Data Series, 1035, 61. <https://doi.org/10.3133/ds1035>
- Kuntz, M. A., Covington, H. R., & Schorr, L. J. (1992). Chapter 12: An overview of basaltic volcanism of the eastern Snake River Plain, Idaho. *Geological Society of America Memoir*, 179, 227–268. <https://doi.org/10.1130/MEM179-p227>

- Lane, M. D., & Christensen, P. R. (1997). Thermal infrared emission spectroscopy of anhydrous carbonates. *Journal of Geophysical Research: Planets*, 102(E11), 25581–25592. <https://doi.org/10.1029/97je02046>
- Lane, M. D. (2007). Mid-infrared emission spectroscopy of sulfate and sulfate-bearing minerals. *American Mineralogist*, 92(1), 1–18. <https://doi.org/10.2138/am.2007.2170>
- Lane, M. D., & Christensen, P. R. (1998). Thermal Infrared Emission Spectroscopy of Salt Minerals Predicted for Mars. *Icarus*, 135(2), 528–536. <https://doi.org/10.1006/icar.1998.5998>
- Marshall, R. R. (1961). Devitrification of natural glass. *Geological Society of America Bulletin*, 72(10), 1493–1520. [https://doi.org/10.1130/0016-7606\(1961\)72\[1493:DONG\]2.0.CO;2](https://doi.org/10.1130/0016-7606(1961)72[1493:DONG]2.0.CO;2)
- McCauley, J. F. (1967). Geologic map of the Hevelius region of the Moon. IMAP.
- McCoy, T. J., Sims, M., Schmidt, M. E., Edwards, L., Tornabene, L. L., Crumpler, L. S., et al. (2008). Structure, stratigraphy, and origin of Husband Hill, Columbia Hills, Gusev Crater, Mars. *Journal of Geophysical Research*, 113, (E6), <https://doi.org/10.1029/2007je003041>
- MEPAG (2020). Mars science goals, objectives, investigations, and priorities: 2020. LPI(2326), 2474.
- Michalski, J. R., Kraft, M. D., Sharp, T. G., Williams, L. B., & Christensen, P. R. (2005). Mineralogical constraints on the high-silica martian surface component observed by TES. *Icarus*, 174(1), 161–177. <https://doi.org/10.1016/j.Icarus.2004.10.022>
- Michalski, J. R., Kraft, M. D., Sharp, T. G., Williams, L. B., & Christensen, P. R. (2006). Emission spectroscopy of clay minerals and evidence for poorly crystalline aluminosilicates on Mars from Thermal Emission Spectrometer data. *Journal of Geophysical Research: Planets* (1991–2012), 111(E3), <https://doi.org/10.1029/2005je002438>
- Michalski, J. R., Kraft, M. D., Diedrich, T., Sharp, T. G., & Christensen, P. R. (2003). Thermal emission spectroscopy of the silica polymorphs and considerations for remote sensing of Mars. *Geophysical Research Letters*, 30(19), <https://doi.org/10.1029/2003gl018354>
- Minitti, M. E., & Hamilton, V. E. (2010). A search for basaltic-to-intermediate glasses on Mars: Assessing Martian crustal mineralogy. *Icarus*, 210(1), 135–149. <https://doi.org/10.1016/j.Icarus.2010.06.028>
- Minitti, M. E., Mustard, J. F., & Rutherford, M. J. (2002). Effects of glass content and oxidation on the spectra of SNC-like basalts: Applications to Mars remote sensing. *Journal of Geophysical Research: Oceans*, 107(E5), 6-1–6-14. <https://doi.org/10.1029/2001JE001518>

- Moroz, L.V., Basilevsky, A.T., Hiroi, T., Rout, S.S., Baither, D., van der Bogert, C.H., et al. (2009). Spectral properties of simulated impact glasses produced from martian soil analogue JSC Mars-1. *Icarus*, 202, (1), 336–353. <http://doi.org/10.1016/j.Icarus.2009.02.007>
- Morris, R. V., Lauer, H. V., Lawson, C. A., Gibson, E. K., Nace, G. A., & Stewart, C. (1985). Spectral and other physicochemical properties of submicron powders of hematite ( $\alpha$ -Fe<sub>2</sub>O<sub>3</sub>), maghemite ( $\gamma$ -Fe<sub>2</sub>O<sub>3</sub>), magnetite (Fe<sub>3</sub>O<sub>4</sub>), goethite ( $\alpha$ -FeOOH), and lepidocrocite ( $\gamma$ -FeOOH). *Journal of Geophysical Research: Oceans*, 90(B4), 3126–3144. <https://doi.org/10.1029/JB090iB04p03126>
- Morrison, D. A., Maczuga, D. F., Phinney, W. C., & Ashwal, L. D. (1986). Stratigraphy and Petrology of the Mulcahy Lake Layered Gabbro: An Archean Intrusion in the Wabigoon Subprovince, Ontario. *Journal of Petrology*, 27(2), 303–341. [https://doi.org/10.1093/](https://doi.org/10.1093/petrology/27.2.303)
- Morse, S. A. (1996). Kiglapait Mineralogy III: Olivine Compositions and Rayleigh Fractionation Models. *Journal of Petrology*, 37(5), 1037–1061. [https://doi.org/10.1093/](https://doi.org/10.1093/petrology/37.5.1037)
- Murchie, S. L., Mustard, J. F., Ehlmann, B. L., Milliken, R. E., Bishop, J. L., McKeown, N. K., et al. (2009). A synthesis of Martian aqueous mineralogy after 1 Mars year of observations from the Mars Reconnaissance Orbiter. *Journal of Geophysical Research*, 114, <http://doi.org/10.1029/2009je003342>
- National Research Council (2011). Vision and voyages for planetary science in the decade 2013–2022. Washington, DC: The National Academies Press. <https://doi.org/10.17226/13117>
- Osinski, G. R., Grieve, R. A. F., Hill, P. J. A., Simpson, S. L., Cockell, C., Christeson, G. L. et al. (2020). Explosive interaction of impact melt and seawater following the Chicxulub impact event. *Geology*, 48(2), 108–112. <http://doi.org/10.1130/g46783.1>
- Pauly, B. D., Schiffman, P., Zierenberg, R. A., Clague, D. A. (2011). Environmental and chemical controls on palagonitization. *Geochemistry, Geophysics, Geosystems*, 12(12). <http://doi.org/10.1029/2011gc003639>
- Pruett, R. J., & Webb, H. L. (1993). Sampling and Analysis of KGa-1B Well-Crystallized Kaolin Source Clay. *Clays and Clay Minerals*, 41(4), 514–519. <https://doi.org/10.1346/ccmn.1993.0410411>
- Rampe, E.B., Blake, D.F., Bristow, T.F., Ming, D.W., Vaniman, D.T., Morris, R.V., et al. (2020). Mineralogy and geochemistry of sedimentary rocks and eolian sediments in Gale crater, Mars: A review after six Earth years of exploration with Curiosity. *Geochemistry*, 80(2), 125605. <http://doi.org/10.1016/j.chemer.2020.125605>

- Rampe, E. B., Kraft, M. D., Sharp, T. G., Golden, D. C., Ming, D. W., & Christensen, P. R. (2012). Allophane detection on Mars with Thermal Emission Spectrometer data and implications for regional-scale chemical weathering processes. *Geology*, 40(11), 995–998. <https://doi.org/10.1130/g33215.1>
- Ramsey, M. S., & Christensen, P. R. (1998). Mineral abundance determination: Quantitative deconvolution of thermal emission spectra. *Journal of Geophysical Research*, 103, 577–596.
- Rice, M. S., Bell, J. F., III., Cloutis, E. A., Wang, A., Ruff, S. W., Craig, M. A., et al. (2010). Silica-rich deposits and hydrated minerals at Gusev Crater, Mars: Vis-NIR spectral characterization and regional mapping. *Icarus*, 205(2), 375–395. <https://doi.org/10.1016/j.Icarus.2009.03.035>
- Rice, M. S., Cloutis, E. A., Bell, J. F., III., Bish, D. L., Horgan, B. H., Mertzman, S. A., et al. (2013). Reflectance spectra diversity of silica-rich materials: Sensitivity to environment and implications for detections on Mars. *Icarus*, 223(1), 499–533. <https://doi.org/10.1016/j.Icarus.2012.09.021>
- Robbins, S. J., Achille, G. D., & Hynes, B. M. (2011). The volcanic history of Mars: High-resolution crater-based studies of the calderas of 20 volcanoes. *Icarus*, 211(2), 1179–1203. <https://doi.org/10.1016/j.Icarus.2010.11.012>
- Rogers, A. D., & Christensen, P. R. (2007). Surface mineralogy of Martian low-albedo regions from MGS-TES data: Implications for upper crustal evolution and surface alteration. *Journal of Geophysical Research: Oceans*, 112(E1), 4851. <https://doi.org/10.1029/2006JE002727>
- Rowe, M. C., & Brewer, B. J. (2018). AMORPH: A statistical program for characterizing amorphous materials by X-ray diffraction. *Computers & Geosciences*, 120, 21–31. <https://doi.org/10.1016/j.cageo.2018.07.004>
- Ruff, S. W., & Christensen, P. R. (2007). Basaltic andesite, altered basalt, and a TES-based search for smectite clay minerals on Mars. *Geophysical Research Letters*, 34(10), 5042. <https://doi.org/10.1029/2007GL029602>
- Ruff, S. W., Christensen, P. R., Barbera, P. W., & Anderson, D. L. (1997). Quantitative thermal emission spectroscopy of minerals: A laboratory technique for measurement and calibration. *Journal of Geophysical Research: Planets*, 102(B7), 14899–14913. <https://doi.org/10.1029/97JB00593>
- Ruff, S. W. (2004). Spectral evidence for zeolite in the dust on Mars. *Icarus*, 168(1), 131–143. <https://doi.org/10.1016/j.Icarus.2003.11.003>
- Sheppard, R. A., & Gude, A. J. (1982). Mineralogy, chemistry, gas adsorption, and NH<sub>4</sub> exchange capacity for selected zeolitic tuffs from the Western United States (USGS Publications Warehouse). <https://doi.org/10.3133/ofr82969>

- Smith, R. J., Rampe, E. B., Horgan, B. H. N., & Dehouck, E. (2018). Deriving amorphous component abundance and composition of rocks and sediments on Earth and Mars. *Journal of Geophysical Research: Planets*, 123(10), 2485–2505. <https://doi.org/10.1029/2018JE005612>
- Squyres, S. W., Aharonson, O., Clark, B. C., Cohen, B. A., Crumpler, L., Souza, P. A. de, et al. (2007). Pyroclastic activity at home plate in gusev crater, Mars. *Science*, 316(5825), 738–742. <https://doi.org/10.1126/science.1139045>
- Stroncik, N. A., & Schmincke, H.-U. (2001). Evolution of palagonite: Crystallization, chemical changes, and element budget. *Geochemistry, Geophysics, Geosystems*, 2(7). <https://doi.org/10.1029/2000gc000102>
- Stroncik, N. A., & Schmincke, H.-U. (2002). Palagonite – a review. *International Journal of Earth Sciences*, 91(4), 680–697. Szramek, L., Gardner, J. E., & Hort, M. (2010). Cooling-induced crystallization of microlite crystals in two basaltic pumice clasts. *American Mineralogist*, 95(4), 503–509. <https://doi.org/10.2138/am.2010.3270>
- Thomson, J. L., & Salisbury, J. W. (1993). The mid-infrared reflectance of mineral mixtures (7–14  $\mu\text{m}$ ). *Remote Sensing of Environment*, 45(1), 1–13. [https://doi.org/10.1016/0034-4257\(93\)90077-B](https://doi.org/10.1016/0034-4257(93)90077-B)
- Thorpe, M. T., Rogers, A. D., Bristow, T. F., & Pan, C. (2015). Quantitative compositional analysis of sedimentary materials using thermal emission spectroscopy: 1. Application to sedimentary rocks. *Journal of Geophysical Research: Planets*, 120(11), 1956–1983. <http://doi.org/10.1002/2015je004863>
- Viviano-Beck, C. E., Seelos, F. P., Murchie, S. L., Kahn, E. G., Seelos, K. D., Taylor, H. W., et al. (2014). Revised CRISM spectral parameters and summary products based on the currently detected mineral diversity on Mars. *Journal of Geophysical Research: Planets*, 119(6), 1403–1431. <https://doi.org/10.1002/2014je004627>
- Walker, G. P. L. (1973). Explosive volcanic eruptions — a new classification scheme. *Geologische Rundschau*, 62(2), 431–446. <https://doi.org/10.1007/BF01840108>
- Wallace, P. J., Dufek, J., Anderson, A. T., & Zhang, Y. (2003). Cooling rates of plinian-fall and pyroclastic-flow deposits in the Bishop tuff: Inferences from water speciation in quartz-hosted glass inclusions. *Bulletin of Volcanology*, 65(2–3), 105–123. <https://doi.org/10.1007/s00445-002-0247-9>
- Wall, K. T., Rowe, M. C., Ellis, B. S., Schmidt, M. E., & Eccles, J. D. (2014). Determining volcanic eruption styles on Earth and Mars from crystallinity measurements. *Nature Communications*, 5, 5090. <https://doi.org/10.1038/ncomms6090>
- Wilson, L., & Head, J. W. (2007). Explosive volcanic eruptions on Mars: Tephra and accretionary lapilli formation, dispersal and recognition in the geologic record. *Journal of Volcanology and Geothermal Research*, 163(1–4), 83–97. <https://doi.org/10.1016/j.jvolgeores.2007.03.007>

- Wilson, L., & Head, J. W., III. (1994). Mars: Review and analysis of volcanic eruption theory and relationships to observed landforms. *Reviews of Geophysics*, 32(3), 221–263.  
<https://doi.org/10.1029/94RG01113>
- Wood, C. A. (1979). Cinder cones on Earth, Moon, and Mars, (1370–1372). Lunar and Planetary Science Conference.
- Wright, S. P., Christensen, P. R., & Sharp, T. G. (2011). Laboratory thermal emission spectroscopy of shocked basalt from Lunar Crater, India, and implications for Mars orbital and sample data. *Journal of Geophysical Research*, 116(E9), 5042.  
<https://doi.org/10.1029/2010JE003785>
- Wuorinen, V. (1978). Age of Aiyansh volcano, British Columbia. *Canadian Journal of Earth Sciences*, 15(6), 1037–1038.
- Wyatt, M. B., Hamilton, V. E., McSween, H. Y., Christense, P. R., & Taylor, L. A. (2001). Analysis of terrestrial and Martian volcanic compositions using thermal emission spectroscopy: 1. Determination of mineralogy, chemistry, and classification strategies. *Journal of Geophysical Research: Planets*, 106(E7), 14711–14732.  
<https://doi.org/10.1029/2000je001356>
- Zhang, Y. (1999). H<sub>2</sub>O in rhyolitic glasses and melts: Measurement, speciation, solubility, and diffusion. *Reviews of Geophysics*, 37(4), 493–516.  
<https://doi.org/10.1029/1999RG900012>
- Zimanowski, B., Büttner, R., Lorenz, V., & Häfele, H.-G. (1997). Fragmentation of basaltic melt in the course of explosive volcanism. *Journal of Geophysical Research: Oceans*, 102(B1), 803–814. <https://doi.org/10.1029/96JB02935>
- Zorn, E. U., Rowe, M. C., Cronin, S. J., Ryan, A. G., Kennedy, L. A., & Russell, J. K. (2018). Influence of porosity and groundmass crystallinity on dome rock strength: A case study from Mt. Taranaki, New Zealand. *Bulletin of Volcanology*, 80(4), 35.  
<https://doi.org/10.1007/s00445-018-1210-8>

## CHAPTER 3. MINERALOGY OF EXPLOSIVE AND EFFUSIVE VOLCANIC EDIFICES IN THE MARIUS HILLS VOLCANIC COMPLEX

### 3.1 Introduction

Within Oceanus Procellarum on the near-side of the Moon, the Marius Hills Volcanic Complex (MHVC, 13.3°N, 47.5°W; Figure 3-1) is a 35,000 km<sup>2</sup> plateau raised 100-200 m above the surrounding plains with a wide assortment and unusual concentration of volcanic features (McCauley, 1967; Whitford-Stark and Head, 1977). These volcanic features include volcanic domes/shields, lava flows, sinuous rilles, and volcanic cones. Astronauts had been planned to explore the volcanic field of the MHVC during Apollo, but unfortunately, landing site changes and Apollo mission cancellations prevented the exploration of this volcanic complex. However, the intrigue for Marius Hills and its volcanic diversity has remained, and the volcanic complex is continually suggested as a landing site for crewed or robotic missions to the Moon.

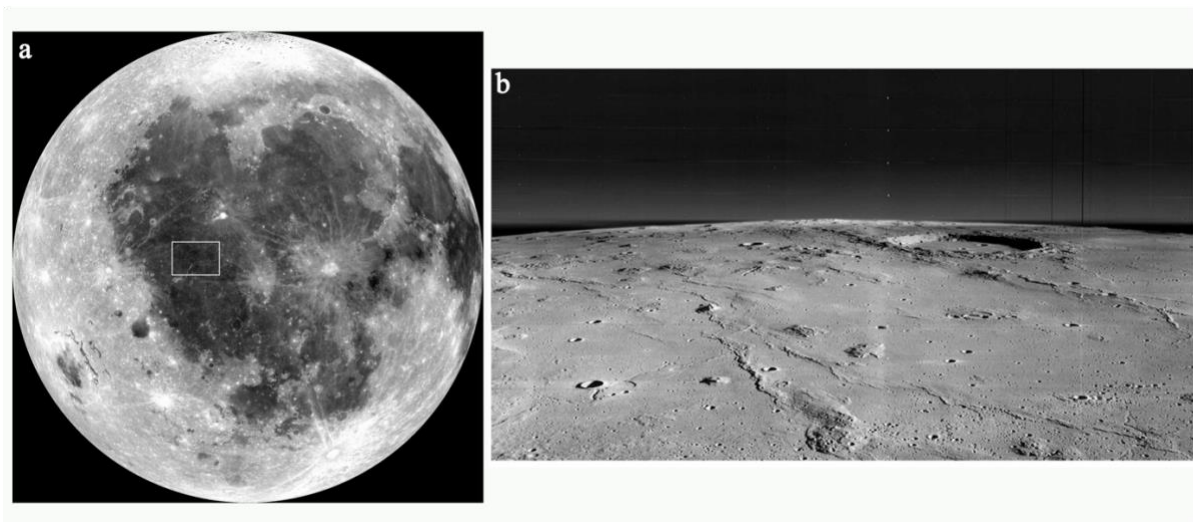


Figure 3-1. a. Marius Hills Volcanic Complex is outlined on the near side of the Moon within the Oceanus Procellarum b. Perspective Image of Marius Hills taken by NASA's Lunar Orbiter 2 in 1966 (NASA/Lunar and Planetary Institute).

The volcanic cones in the MHVC were identified initially using visible images and based on morphologies similar to cinder cones on Earth (McCauley, 1967; Wood, 1979). A definitive designation of a cinder cone would require evidence that the volcanic edifice was constructed of

ballistic pyroclasts from an explosive, volatile-rich eruption. An explosive, volatile-rich eruption produces rapidly quenched and thus glassy pyroclasts as represented by cinders on Earth. That same process is expected to occur on the lunar surface within the MHVC. The region has been previously studied using images from the Lunar Reconnaissance Orbiter Camera (LROC; Gustafson et al., 2012; Lawrence et al., 2013), 5-band multispectral Ultraviolet/Visible (UV/Vis; 415-1000 nm) data from Clementine (Heather et al., 2003; Weitz and Head, 1999), and 280 m/pixel hyperspectral visible/near-infrared (VNIR; 420-3000 nm) data from the Moon Mineralogy Mapper (Besse et al., 2011). However, studies that focused on the cones are limited. (Lawrence et al., 2013) used the Lunar Reconnaissance Orbiter Wide and Narrow Angle Cameras to complete a morphological survey of the cinder cones of the MHVC. However, spectral data were not previously utilized to differentiate morphologic features in the Marius Hills Volcanic Complex.

Marius Hills is a target for future human or robotic exploration as its diverse volcanic lithologies would help address various high-priority lunar science goals as described in the 2013-2022 Decadal Survey. An investigation of Marius Hills could: 1. Constrain the composition of terrestrial planets by studying the composition of multiple volcanic products. 2. Characterize the differentiation and evolution of planetary interiors by assessing volcanic products created through partial melting of the lunar interior. 3. Characterize how planetary surfaces are modified by geologic processes (i.e., volcanism, National Research Council, 2011; Jawin et al., 2019). Samples from multiple volcanic sources, including both explosive and effusive deposits, could be collected within the MHVC and returned to Earth or for in-situ analysis and while preserving the long-term magma evolution on the Moon. Glass samples are of particular interest for detailed analysis, as lunar volcanic glasses have been shown to preserve magmatic volatiles from within the lunar interior (Allan et al., 1996). Thus, a clear detection of glass in the MHVC cones would be critical both for confirming models of the geologic history of the area and for identifying future sampling locations.

In this study, we use 140 m/pixel spectral data collected by the Moon Mineralogy Mapper (Pieters et al., 2009) instrument on the ISRO Chandrayaan-1 spacecraft to investigate the mineralogy of the volcanic edifices previously identified in visible images as well as to evaluate the presence of volcanic edifices where analysis of visual images is ambiguous. We apply methods designed to detect glass in VNIR spectra to test the explosive origin of the MHVC cones. We also compare the mineralogy of the cones to other edifices in the area to investigate their eruptive

relationship. Correlating spectral and mineralogical information with morphological interpretations would provide insight into magmatic evolution, volatile content, and magmatic history in the region.

## **3.2 Background**

### **3.2.1 Marius Hills Volcanic Complex**

The MHVC is located in Oceanus Procellarum, is surrounded by mare basalts, and is named for Marius crater along the SE margin of the region. The MHVC exhibits the highest concentration of volcanic positive relief structures on the Moon, in the form of both domes and cones (Whitford-Stark and Head, 1977). The domes and cones have been interpreted as volcanic shields with superimposed cinder cones (Wood, 1979). The volcanic cones in the MHVC were identified initially using visible images and morphologic comparison to cinder cones on Earth (McCauley, 1967; Wood, 1979). Marius Hills' other notable volcanic features include 20 sinuous rilles located predominantly in the western region of the MHVC (Whitford-Stark and Head, 1977) and a pit crater, potentially a skylight to a lunar lava tube identified initially with the SELENE cameras and verified with the Lunar Radar Sounder (Haruyama et al., 2009; Kaku et al., 2017). Additionally, several wrinkle ridges with an SSE-NNW trend cross the MHVC and have modified volcanic constructs in the region (Lawrence et al., 2013).

It has been hypothesized that the plateau or topographic bulge that defines the MHVC is a very large volcanic shield formed before the superimposed domes and cones (Spudis et al., 2013). The rise is elongated and elliptical in shape, with a summit NW of the Marius crater. Marius Hills has been proposed as the most developed large shield of the 8 proposed on the lunar near side. Shield building is proposed to have occurred between 3.9 and 3.0 Ga, during the main phase of mare volcanism (Spudis et al., 2013).

The Lunar Prospector mission measured a positive Bouguer gravity anomaly at the Marius Hills about 200–250 km in diameter (Konopliv et al., 2001), indicating a significant volume of dense subsurface material. This dense material could be interpreted as a laccolithic intrusion or the infilling by basalt into the uppermost crust's pore spaces (Spudis et al., 2013). Gravity models from the GRAIL mission (Zuber et al., 2013) suggest that the gravity feature is produced by two dense,

subsurface bodies, one corresponding to the Marius Hills bulge (including the majority of the locations with the domes and cones) and a smaller gravity anomaly south of the central part of the Marius Hills shield. A narrow line of dense material connects the two bodies creating a “bridge”. This geophysical evidence led to the interpretation that Marius Hills was fed by a single subsurface magmatic system (Kiefer, 2013). Based on GRAIL gravity data, previous studies have hypothesized the presence of a crustal complex of vertical dikes near the center of the plateau, which would be consistent with the multiple volcanic morphologies in the MHVC (Deutsch et al., 2019).

Previous investigations of the MHVC developed a hypothesized timeline for volcanic evolution (Besse et al., 2011; Heather et al., 2003; Spudis et al., 2013; Weitz and Head, 1999; Whitford-Stark and Head, 1977). The range of volcanic features in the MHVC suggests a complex and long-lived volcanic history in the region, which may be reflected in the mafic mineralogy. Formation of the plateau as a large shield volcano is hypothesized to be the first volcanic episode in the MHVC, possibly during the main phase of mare volcanism from 3.9-3.0 Ga ago (Spudis et al., 2013). Next, the domes and superimposed cones were built with the eruption of many relatively volatile-rich, partly crystallized magmas, which resulted in the production of abundant spatter, degassing, and a’ a lava flows (Besse et al., 2011; Heather et al., 2003; Weitz and Head, 1999). Observations from NAC suggested the flows responsible for constructing the volcanic domes were sourced from the cones with breached walls, forming these features synchronously (Lawrence et al., 2013). Lastly, the youngest volcanic basalts in MHVC erupted, potentially contemporaneously with the mare basalts of Oceanus Procellarum. While the source of these flows is not well constrained, the flows appear to have embayed the raised volcanic domes and cones on the plateau in NAC images (Lawrence et al., 2013), then followed rilles and channels to the mare units of Procellarum (Besse et al., 2011). (Whitford-Stark and Head, 1977) inferred that the basalts in Oceanus Procellarum were erupted from multiple volcanic sources in the area, including but not limited to Marius Hills.

### **3.2.2 History of MHVC Spectral Studies**

The small size of the MHVC cones (~1-3 km in diameter) and the low resolution of many previous observations have made the separation of the spectral signatures from the cones and the

domes challenging (Besse et al., 2011; Heather et al., 2003; Weitz and Head, 1999). The first analyses of Marius Hills VNIR reflectance spectra targeted the proposed Apollo landing site and used Earth-based telescopes in Mt. Wilson, California, with a spectral range of 0.3-1.1 $\mu\text{m}$  (McCord et al., 1972; Pieters and McCord, 1976). The low-resolution of these observations (~2 km/pixel) prevented the ability to distinguish specific volcanic features but indicated average compositions similar to the surrounding Oceanus Procellarum mare (McCord et al., 1972). The first space-based spectral data was collected by the Galileo Solid State Imager during the Moon fly-bys while on course to Jupiter. The 6-band reflectance data between 0.4-1.0 $\mu\text{m}$  at a resolution of 1-3 km/pixel indicated differences in band ratios between the Marius Hills plateau and the surrounding mare, as well as locations with strong 1 $\mu\text{m}$  absorption bands due to mafic minerals or glass that were potentially consistent with pyroclastic deposits (Sunshine et al., 1994).

High resolution orbital compositional analyses of MHVC have been conducted using UV-VIS multispectral data from Clementine (Nozette et al., 1994), consisting of five spectral channels between 450-1000 nm with a resolution of 157 m/pixel (Heather et al., 2003; Weitz and Head, 1999), and using hyperspectral VNIR data from the Moon Mineralogy Mapper ( $M^3$ ; Pieters et al., 2009), which collected data between 0.42 $\mu\text{m}$ -3.0 $\mu\text{m}$  ranging from 80-280 m/pixel in resolution (Besse et al., 2011). Besse et al., (2011) used 6 cubes of  $M^3$  data collected at 280 m/pixel to analyze the large-scale spectral properties of the MHVC, using spectral indices to map spectral diversity across the region.

These previous high resolution orbital spectral studies have shown large-scale compositional differences due to variability in the mare on the Marius Hills plateau and identified two main mare units, interpreted as having different compositions from separate volcanic episodes (Besse et al., 2011; Heather et al., 2003; Sunshine et al., 1994; Weitz and Head, 1999). The older unit is attributed to the eruptive building of the shield volcano that created the topographic high of the MHVC (Spudis et al., 2013). Spectral interpretation of the older unit has categorized the mare as low-titanium (Weitz and Head, 1999) based on Clementine observations, and  $M^3$  spectra reveal an absorption band centered slightly below 1  $\mu\text{m}$  suggesting a high-calcium pyroxene-bearing composition (Besse et al., 2011).

The second mare unit in MHVC is interpreted as a later volcanic episode, based on the observation that it embays the volcanic domes and cones (Lawrence et al., 2013). This unit is associated with channels and rilles leading towards Oceanus Procellarum and may be a source of

Oceanus Procellarum mare basalts (Besse et al., 2011; Heather et al., 2003; Weitz and Head, 1999). Clementine spectra of the second mare unit indicated a high-titanium flow (Weitz and Head, 1999), and M<sup>3</sup> spectra exhibited a stronger 1.25  $\mu\text{m}$  shoulder on the broad 1  $\mu\text{m}$  band, interpreted as due to olivine (Besse et al., 2011). (Besse et al., 2011) theorized that the observed elemental variations could be attributed to variations in olivine content of the mare from each volcanic episode which agreed with previous regional-scale mare interpretations which identified changes in olivine content between mare units (Staid et al., 2011). These studies also examined the spectral properties of the domes and cones, which are discussed in the following sections.

### **3.2.3 Domes in the MHVC**

Shield volcanoes are a type of volcanic dome and form from effusive volcanic eruptions. Relatively low-viscosity lava flows (typically basalt) build the “shield-shaped” structure, with a base diameter that is larger than the height of the edifice, resulting in relatively low slopes (Whitford-Start, 1975). The slopes of the domes are usually steeper near the center of the dome and lower towards the base, while slopes measured with LRO data for domes in MHVC range from  $\leq 3^\circ$  to  $10^\circ$ , which is consistent with the low slopes of shield volcanoes on Earth (Lawrence et al., 2013). In some cases, shield volcanoes can exhibit a summit caldera, but it is not required for classification. In MHVC, the domes are topographic rises with irregular surfaces and diameters, irregular outlines, and range in diameter from 2 to tens of kilometers, but most are between 5 and 6 km in diameter (Lawrence et al., 2013). The surface texture of the domes, at the scale of LROC NAC, appear to have a rougher texture than the average mare surface, possibly demonstrating that ‘A’ $\bar{a}$  lava, eruptive spatter, and/or interbedded pyroclastics could contribute to the composition of the domes (Campbell et al., 2009; Lawrence et al., 2013). Some domes have superimposed cones, but not all cones are located on domes.

Previous VNIR spectral investigations with Clementine categorized the domes based on the slopes of their flanks (low vs. steep) as well as their interpreted association with high and low titanium units (Heather et al., 2003; Weitz and Head, 1999). Previous M<sup>3</sup> analysis interpreted the domes as belonging to the older high-calcium pyroxene mare unit while being embayed by later mare units but found no spectral differences between low-sloped and steep-sloped domes. These results implied that variations in eruption mechanics, rather than composition, were responsible for changes in dome morphologies (Besse et al., 2011).

More than 150 MHVC domes were more recently analyzed using data from LROC, Mini-RF, and Diviner and found to be composed of blocky lava flows that were not enhanced in silica relative to the surrounding mare basalts (Lawrence et al., 2013). Observations from the LROC NAC indicate that some of the dome-building flows originate from volcanic vents and further support the hypothesis that differences in slope angle likely occur due to changes in viscosity influenced by effusion rate, temperature, and or degree of crystallization (Lawrence et al., 2013).

### **3.2.4 Cones in the MHVC**

Silicate glasses form by the quenching of melted rocks, where rapid cooling prevents the crystallization of minerals. Glass can form by numerous natural processes, including impacts, tectonics, and volcanic eruptions (Glass, 2016). Explosive volcanic eruptions form glass during fragmentation of ascending magma. The rapid cooling of the magma enhanced by fragmentation due to the expansion of bubbles from dissolved volatiles quenches the fragments before crystals can form. Glass can form over the entire range of volcanic compositions from mafic to felsic magmas. Magma-volatile interactions, in addition to magma viscosity and composition, control the glass content of pyroclastic deposits. On Earth, the presence of significant glass can be used to distinguish if volcanic deposits were emplaced by an explosive or effusive eruption and the volatile content of that explosive eruption (Wall et al., 2014). High glass abundances in tephra from explosive eruptions are detectable in VNIR spectra (Henderson et al., 2020).

Cinder cones are one type of edifice formed during a Strombolian eruption (Walker, 1973). On Earth, cinder cones can form on the flanks of shield volcanos as “parasitic” volcanic cones (Figure 3-2a). On Earth, a parasitic cone is the cone-shaped accumulation of volcanic material not part of the central vent of a volcano forming from eruptions through fractures on the flank of the volcano. Commonly, cinder cones initially erupt explosively due to higher gas content and can be followed by a transition to an effusive eruption. On Earth, the flanks of a cinder cone are at the angle of repose,  $\sim 30^\circ$  (Wood, 1979). The slopes of the MHVC volcanic cones are drastically less, averaging around  $17^\circ$  with diameters ranging from 0.5 – 4km (Lawrence et al., 2013). The lower slope is attributed to the low gravity and lack of atmosphere in the lunar environment. Both effects would allow pyroclastic material with ballistic trajectories to travel longer distances before falling to the ground and forming a cinder cone (Whitford-Stark and Head, 1977). A definitive designation of a cinder cone would require evidence that the volcanic edifice was constructed of ballistic

pyroclasts from an explosive, volatile-rich eruption, which produces rapidly quenched, glassy pyroclasts as represented by cinders on Earth. It is expected that the same process would occur on the lunar surface within the MHVC.

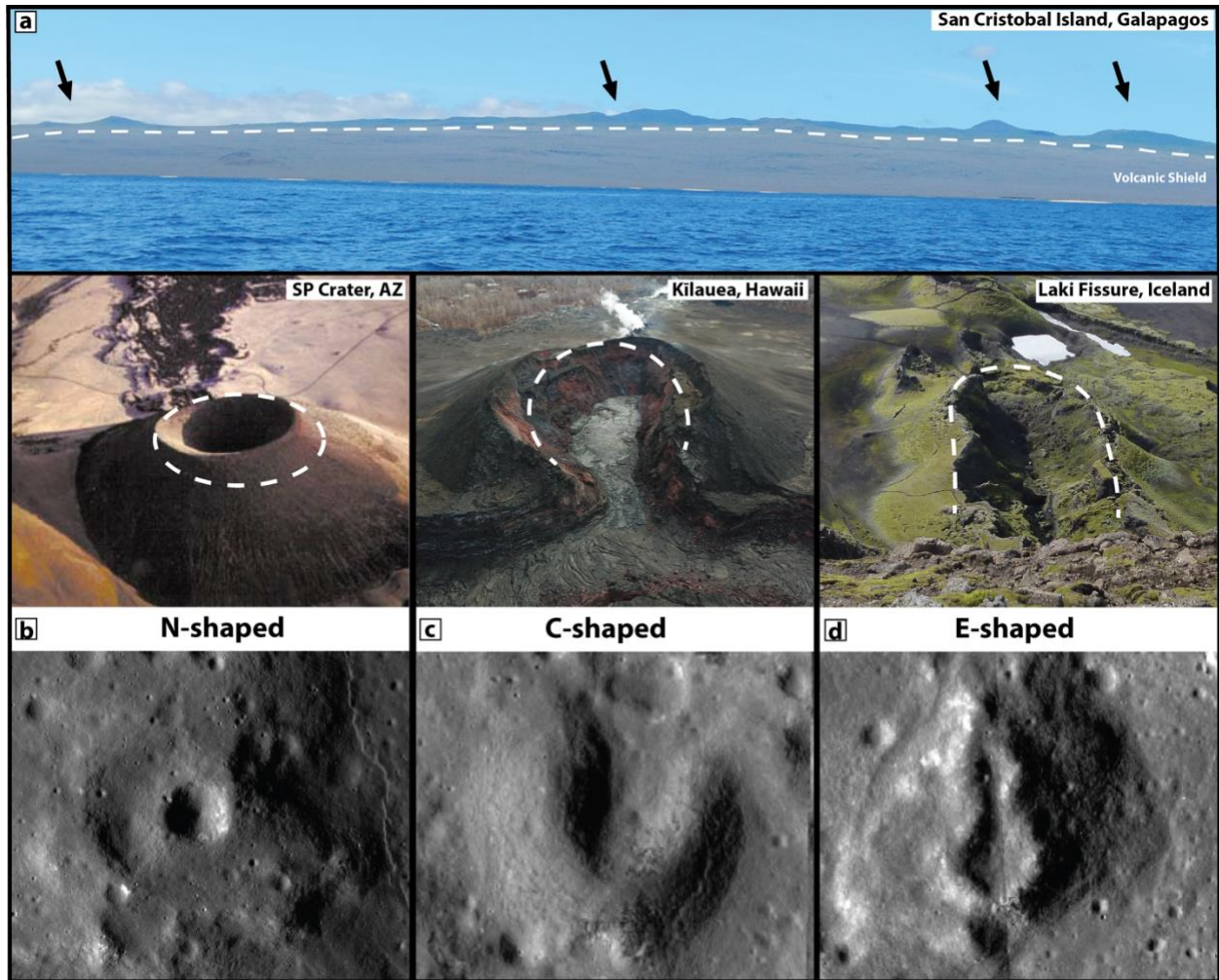


Figure 3-2. (a) Examples from Earth of volcanic morphologies previously identified in the MHVC. (a) Image of San Cristobal Island, Galapagos taken from the water by M. Henderson. The island is a shield volcano with the typical low slope flanks designated by the white dashed line. Parasitic cinder cones erupted from the shield creating the edifices designated by the arrows. The bottom of the figure shows an Earth-analog and lunar example of each cone shape classification from (Lawrence et al., 2013). (b) N-class cones that do not display a breach (lunar diameter:  $\sim 1.5$ km) (c) C-class cone with breach of cone wall (lunar diameter:  $\sim 1.5$ km) (d) E-class elongated cone representing eruption along a fissure (lunar diameter:  $\sim 1.25$ km). Lunar cones imaged by LROC NAC. All Earth analog images are open source photographs.

A correlation was identified in Clementine data between the presence of cones and spectral dark spots, or areas of lower overall albedo at visible wavelengths (Weitz and Head, 1998). Further investigation by Heather et al., (2003) revealed many cases where cones did exhibit low albedos and other instances in which the dark spots did not correspond to cones. Weitz and Head (1999) and Heather et al. (2003) proposed that glassy particles from explosive eruptions of the cones are responsible for the lower albedos; however, the lack of correlation between the volcanic constructs interpreted as cones and the dark spots showed the need for a more detailed spectral analysis to constrain the mineralogy than could be achieved with the limited spectral resolution and range of the Clementine dataset.

Using M<sup>3</sup> data from Optical Period 2C with a resolution of 240 m/pixel, the dark spots identified by Heather et al., (2003) and Weitz and Head, (1999) were confirmed on the MHVC plateau and shown to be present on both cones and some domes, but the origin of the dark spots was not resolved (Besse et al., 2011). Shadowing was ruled out based on topographic analyses, but the dark spots also showed odd correlations with phase angle as well as decreased 1  $\mu\text{m}$  band depths, leading to the interpretation that the origin of the dark spots might be more complicated, and that grain size or opaque minerals might be playing a role (Besse et al., 2011). Otherwise, the analysis did not reveal noticeable spectral differences between cones and domes, including in the properties of their 1 $\mu\text{m}$  iron band, and placed both within the HCP-bearing and olivine-poor spectral unit previously identified on MHVC.

Lawrence et al., (2013) used data from LROC NAC, Mini-RF, and Diviner to create a new map of volcanic features in Marius Hills, including specific cone morphologies. The study showed that some cones were correlated with volcanic domes while others were stand-alone volcanic features embayed by younger basalt, although the basalt may have obscured any underlying dome (Lawrence et al., 2013). Images with a resolution of approximately 0.4-1.3m per pixel enabled the ability to study layers exposed in the cone walls, which revealed intermittent lava effusions and changing eruption conditions terminating with an effusive eruption from the cone, creating thick, lobate flows observed on many of the domes (Lawrence et al., 2013).

The LROC NAC and WAC image analysis by (Lawrence et al., 2013) identified 93 volcanic cones in the MHVC, increasing from the previously reported numbers of 46 and 59 from (Weitz and Head, 1999) and (Whitford-Stark and Head, 1977), respectively. The 93 cinder cones were classified by their shape and split into three categories: N-class cones (a completely circular edifice

with no breached walls), C-class cones (a circular cone with a breached wall), and E-class cones (an elongated cone). Possible Earth analogs and lunar examples of these shape classifications are shown in Figure 3-2b-d. These cone morphologies represent different types and stages of cinder cone forming eruptions. N-class cones form from the ballistic trajectories of a volatile-rich explosive eruption. As the magma is degassed, the eruption can transition to a late-stage effusive eruption, creating a lava flow that can breach a wall of the cone, raft away from the wall material, and change the morphology from N-class to C-class. The E-class cones are consistent with fissure eruptions, where the magma erupts along a linear fissure (Lawrence et al., 2013). 64 cones were designated C-class, 12 cones were designated E-class, and 17 cones were designated N-class. In addition to the 93 cones classified by (Lawrence et al., 2013), 55 circular structures could not be definitively designated cones and were classified as U-class or uncertain constructs. The inability to definitively classify these structures as cones is due to the limitations of visible images where shadows and phase angles can cause an ambiguous interpretation, especially in cases where cones may have been degraded by later modification.

In this study, we use higher resolution (140 m/pixel)  $M^3$  data and more detailed spectral analysis techniques (Bennett et al., 2016; Horgan et al., 2014) to investigate the composition of the MHVC cones and domes. We examine whether or not glass signatures are present in the cones and map the extent of any possible glass signatures. We also use the presence of glass signatures to confirm previous cone detections from Lawrence et al. (2013) and present a new map of cones and domes in the MHVC. Finally, we investigate the spectral properties of the domes compared to the cones and surrounding mare to better constrain the magmatic history of the region.

### **3.3 Methods**

#### **3.3.1 Moon Mineralogy Mapper**

The Moon Mineralogy Mapper ( $M^3$ ) was an imaging spectrometer supported by NASA as a guest instrument on the ISRO Chandrayaan-1 lunar orbiter (Green et al., 2011; Pieters et al., 2009). Launched in 2008,  $M^3$  operated in the visible to near-infrared (VNIR; 0.42-3.0 $\mu$ m), which is sensitive to absorption bands exhibited by iron-bearing minerals, including pyroxene, olivine, glass, as well as anorthosite (Adams, 1974; Besse et al., 2013; Cloutis and Gaffey, 1991).  $M^3$  collected data during five optical periods (OP), each defined by the date of collection, orbit height,

and instrument status as described in Boardman et al., (2011), Green et al., (2011), and Isaacson et al., (2013). M<sup>3</sup> has 85 spectral channels between 0.42-3.0  $\mu\text{m}$  with a higher spectral resolution between 0.7-1.6  $\mu\text{m}$  in order to better characterize the 1  $\mu\text{m}$  iron band. M<sup>3</sup> data calibrated to reflectance (Level 2) is available from the Planetary Data System and has nearly full coverage of the lunar surface, although the quality and resolution (75-280 m/pixel) of the data varies across the mission (Green et al., 2011; Pieters et al., 2009).

### 3.3.2 M<sup>3</sup> Mapping

An M<sup>3</sup> map of the MHVC was created using 23 spectral images and constructed with bounds 300-314°E and 8-17°N using the methods described in (Horgan et al., 2014) and (Bennett et al., 2016). The map covers the Marius Hills and some surrounding mare. The 23 spectral cubes were acquired during three optical periods (OP2C, OP2A, and OP1B). Images collected in OP2C were obtained from an orbital distance of 200 km at high sun angles, with a warmer detector temperature, high signal levels, and a lower resolution of 280m/pixel. Because of their lower quality but better spatial coverage, these cubes were mosaicked separately and shown in Figure 3-4c,d. Images from OP2A and OP2B were mosaicked together into a second mosaic shown in Figure 3-4c, as they were all collected with a colder detector temperature and at higher zenith angles from an orbital distance of 100 km, resulting in higher quality spectra with a resolution of 140m/pixel (Boardman et al., 2011; Green et al., 2011; Isaacson et al., 2013).

Each M<sup>3</sup> cube is initially cropped to fit within the bounds of the desired map. Next, the backplanes and reflectance data for the cube are projected into the map using a cylindrical projection and IDL built-in mapping routines. Where multiple cubes cover a pixel, the cube with the highest overall quality is chosen based on visual inspection (e.g., least noise, least column-to-column variation). Once the complete reflectance mosaic is constructed, an approximate continuum is removed from each spectrum individually (e.g., Clark and Roush, 1984). The continuum of a spectrum is the baseline on which mineral absorptions are superimposed and is influenced by the internal mechanics of the instrument, as well as space weathering and thermal effects (Hapke, 2001; Isaacson et al., 2013). To prevent possible errors due to thermal contributions, the continuum fit is limited to <2.6  $\mu\text{m}$ , and caution was exercised when analyzing data at these longer wavelengths. The continuum of each spectrum in the mosaic is suppressed using a linear convex hull with two segments fit to endpoints near 0.70, 1.55, and 2.60  $\mu\text{m}$ . A

rough estimate of the continuum is calculated for each spectrum using these endpoints; then, these endpoints are fine-tuned for each spectrum by identifying the local maxima between 0.65–1.00, 1.35–1.60, and 2.00– 2.60  $\mu\text{m}$  in this initial continuum removed spectrum. With all of the calculated new endpoints, the final continuum of two combined linear segments is calculated from the original spectrum. All spectral plots show continuum removed spectra as well as smoothed versions of these spectra, in which spectral noise was reduced using a median filter and a boxcar smoothing algorithm, both with widths of 5 channels.

### **3.3.3 Spectral Parameters and Mineral Identification**

In this study, spectral variability was assessed using two types of spectral parameters, both applied to our continuum removed mosaic: (1) simple arithmetic spectral indices and (2) 1 and 2  $\mu\text{m}$  band position, area, and shape parameters derived from our continuum removed mosaic. The spectral indices BDOPX, BDCPX, and BDGLA, as defined in Table 3-1, are applied to smoothed continuum removed spectra, and can suggest the presence of OPX (based on enhanced absorption between 0.88-0.92  $\mu\text{m}$ ), CPX (based on enhanced absorption between 2.40-2.50  $\mu\text{m}$ ), and iron-bearing glass (based on enhanced absorption between 1.15-1.20  $\mu\text{m}$ ) as shown in Figure 3-3. Spectral indices like these do not equate to quantitative information on the abundance of a mineral but rather provide information on whether or not the spectral characteristics of a given spectrum could be consistent with the presence of that mineral. In addition, the presence of other spectrally similar minerals can also lead to high values of these parameters. For example, the prominent 1.25-1.30  $\mu\text{m}$  shoulder in olivine can also cause high values of BDGLA. These spectral indices can also vary due to spectral contrast, or the overall depth of absorption bands in a spectrum, which is often related to factors other than the abundance of these Fe-bearing silicates (e.g., grain size, space weathering, or minor changes in the abundance of opaque minerals; Pieters et al., 2000; Scudder et al., 2021).

Table 3-1. Definitions of spectral parameters used for spectral interpretation and making composite and band parameter maps.

<b>M<sup>3</sup> Spectral Parameters</b>	
<b>Glass Band Depth</b>	Average band depth below the continuum at <b>1.15μm, 1.18μm, and 1.20μm</b> Horgan <i>et al.</i> [2014]
<b>Orthopyroxene Band Depth</b>	Average band depth below the continuum at <b>0.88μm, 0.90μm, and 0.92μm</b> Bennett <i>et al.</i> [2016]
<b>Clinopyroxene Band Depth</b>	Average band depth below the continuum at <b>2.4μm, 2.45μm, and 2.5μm</b>
<b>1 μm Band Center</b>	Calculated from the wavelength position of the minimum of a fourth order polynomial fit to all channels within 75 nm of the band minimum, with a fit resolution of 5 nm Gaddis <i>et al.</i> [2013]
<b>2 μm Band Center</b>	
<b>1μm Band Asymmetry</b>	Difference between the band area to the left and right of band center, as a percent of the total area. A symmetric band has an asymmetry of 0%, and positive asymmetries correspond to bands that have more area at longer wavelengths. Horgan <i>et al.</i> [2014]
<b>Band Area Ratio</b>	Calculated ratio of the band area of absorption features centered at 1μm area and 2μm. Huang <i>et al.</i> [2020]

Once the continuum of the spectrum is removed, it is also possible to conduct more detailed parameterizations of the shape and position of the 1 and 2 μm iron absorption bands (Horgan *et al.*, 2014). The band minimum and band center parameterize the band position. The band minimum is the wavelength position of the minimum reflectance value in the band. In contrast, the band center is the wavelength position of the minimum of a fourth-order polynomial (allows for fitting of the narrower band shape characteristic of many pyroxenes) fit to all channels within 75 nm of the band minimum, with a fit resolution of 5 nm. In smooth spectra, the band minimum and band center would be very similar, but when the spectra are not ideal (e.g., noisy spectra, and when the fit has a higher resolution than the spectrum), the band center can be a better estimation of the true center of the band than the band minimum (Horgan *et al.*, 2014). Band shape is parameterized by band depth, band area, and band asymmetry. The band depth is defined as one minus the value of the polynomial fit at the band center, while the band area is the total area under each continuum segment calculated as one minus the value of each channel in this range multiplied by the spectral resolution at each channel. Band asymmetry is defined as the difference in the areas to the left and right of the band center as a percentage of the total area (Horgan *et al.*, 2014).

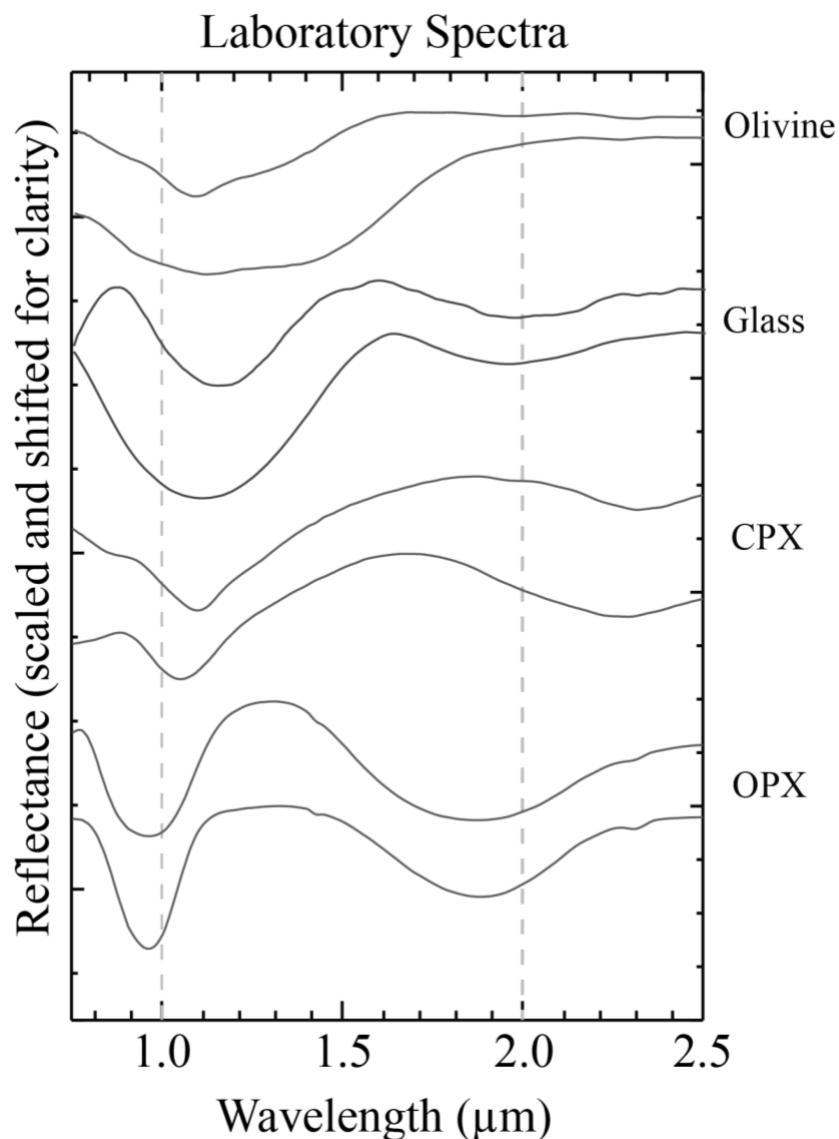


Figure 3-3. Selected continuum-removed laboratory VNIR spectra of orthopyroxene (OPX), clinopyroxene (CPX), glass, and olivine, showing the deep and broad bands due to iron centered near 1 and sometimes 2  $\mu\text{m}$  exhibited by these minerals. Variability in band center, shape, and depth within mineral groups can occur due to variations in composition and grain size.

These band parameters are useful in concert with the simple spectral indices described above because they are not strongly affected by spectral contrast, such as the low spectral contrast induced by space weathering on the Moon. Also, they can be more confidently linked to specific iron-bearing minerals and mineral mixtures (Horgan et al., 2014). OPX and CPX both exhibit two symmetric absorption bands, where OPX has bands centered near 0.90-0.94 and 1.8-2.0  $\mu\text{m}$ , and

CPX has bands centered near 0.98-1.05  $\mu\text{m}$  and 2.05-2.40  $\mu\text{m}$ . Intermediate pyroxenes (e.g., pigeonite) and pyroxene mixtures fall in between these values. Olivine exhibits a broad and asymmetric 1  $\mu\text{m}$  absorption band most often centered between 1.05-1.07  $\mu\text{m}$ , which is a combination of three bands centered near 0.85, 1.05, and 1.15  $\mu\text{m}$ , and no 2  $\mu\text{m}$  band (Sunshine et al., 1990; Sunshine and Pieters, 1998). Iron-bearing glasses exhibit a wide and symmetric absorption centered between 1.07-1.18  $\mu\text{m}$ , and in some cases, an additional absorption centered between 1.90-2.05  $\mu\text{m}$  (e.g., Cannon et al., 2017), which can therefore overlap with the 1  $\mu\text{m}$  band center of olivine and CPX. While the lack of a 2  $\mu\text{m}$  band and increased 1  $\mu\text{m}$  asymmetry can often distinguish olivine from these other ferrous minerals, mixtures of glass and pyroxene can produce olivine-like spectral shapes (Horgan and Bell, 2012; Horgan et al., 2014). Because of this ambiguity, careful spectral analysis is needed to make interpretations of iron-bearing mineralogy. Thus, following the creation of our spectral indices and parameter maps, average continuum removed spectra were extracted from representative regions of interest (ROIs) for the localities of cinder cones, volcanic domes, and the MHVC floor.

### **3.3.4 Cone Classification and Analysis**

To determine if MHVC cones exhibited spectral properties consistent with glass, as would be expected in volcanic cinder cones, our glass parameter map made using the glass band depth spectral parameter (Table 3-1) was co-registered to an LROC WAC mosaic and the Lawrence et al. (2013) map of cone morphologies. First, definitive cones characterized by (Lawrence et al., 2013) were assessed for increased glass signatures on the glass parameter map. If the glass parameter map showed a signature with a shape consistent with glass on multiple walls of the cone, it would be concluded to be spectrally and morphologically compatible with a cinder cone. An example of matching visible images and glass parameter maps is present in Figure 3-5. Following confirmation that glass parameter maps effectively identify volcanic cones, the 55 ambiguous U-class constructs identified by (Lawrence et al., 2013) were confirmed or denied cone designation. The cones were re-classified, and new cones were identified, creating a new map of the locations and morphologies of likely cinder cones in the MHVC.

A rose diagram is a standard tool in geology used to plot the frequency of directional data and recognize correlations in geologic features' direction or orientation. In this study, a rose diagram was constructed to determine if there was a common direction of cones elongated cones along

fissures. Images with multiple illumination and elevation profiles were examined to confirm the direction of E-class cones. The calculated direction of the open end of all the E-class cones was plotted on a rose diagram for comparison.

## **3.4 Results**

### **3.4.1 Spectral Mapping**

Spectral analysis of the Marius Hills volcanic complex reveals distinct spectral signatures associated with different geologic units, and  $M^3$  spectra extracted for MHVC units show clear iron-bearing absorption bands near 1 and 2  $\mu\text{m}$ . RGB composite images showcasing the spectral diversity are shown in Figures 3-4 c and d, where red is the glass band depth (BDGLA), green is the 1 $\mu\text{m}$  band center, and blue is the 2 $\mu\text{m}$  band center. In this combination, glass typically appears as yellow, CPX as blue, OPX as green, olivine as red, and CPX mixed with olivine or glass as pink. The horizontal variability across the higher resolution  $M^3$  frames in Figure 3-4c is due to changes in resolution and detector sensitivity (Besse et al., 2013; Boardman et al., 2011). The lower resolution map is comparable to maps using this same lower resolution data from Besse et al. (2011), which show the same distinct boundaries along mare regions on the western plateau with additional absorption near 1.2  $\mu\text{m}$  (here captured by the glass band depth, represented as pink colors). However, the lower resolution map shows a distinct lack of sensitivity to glass compared to the higher resolution map, which we hypothesize is due to the difficulties inherent to identifying glass in VNIR spectra. Because of the transparency of glass at these wavelengths, it needs to be present at high abundances (>80 wt.%) for it to be definitively identified (Horgan and Bell, 2012). Therefore, when the  $M^3$  data is at lower resolutions, sub-pixel mixing of glass-rich and glass-poor terrains means that more of the signal must be contributed from glass to have the same spectral response, resulting in the differences between the high and low-resolution RGB composites (Figures 3-4 c and d) and glass maps (Fig 3-5 a and b).

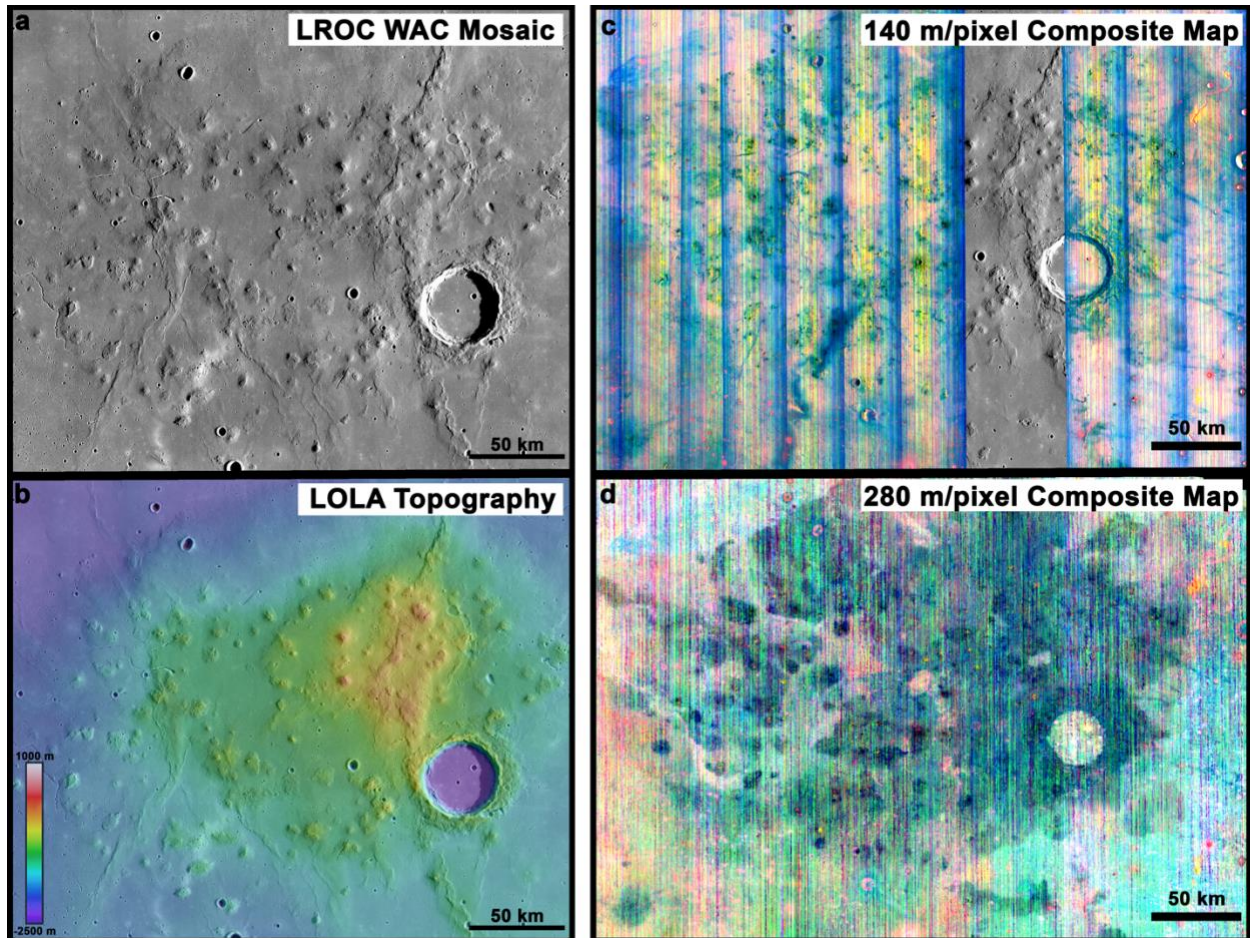


Figure 3-4. Maps of regional-scale morphology and spectral properties of the Marius Hills Volcanic Complex (MHVC). (a) Wide-angle camera (WAC) mosaic from the Lunar Reconnaissance Orbiter Camera (LROC) (b) Topography from Lunar Orbiter Laser Altimeter (LOLA) overlaid on the LROC WAC mosaic. (c-d) Mosaicked composite RGB spectral maps from  $M^3$  data where R= glass band depth parameter, G= $1\mu\text{m}$  band center parameter, B=  $2\mu\text{m}$  band center parameter. (c)  $M^3$  mosaic of high-resolution cubes (140 m/pixel) collected during OP2A and OP2B. (d)  $M^3$  mosaic of low-resolution cubes (280 m/pixel) collected during OP2C. The horizontal variability and striping across the  $M^3$  frames are due to changes in resolution and sensitivity.

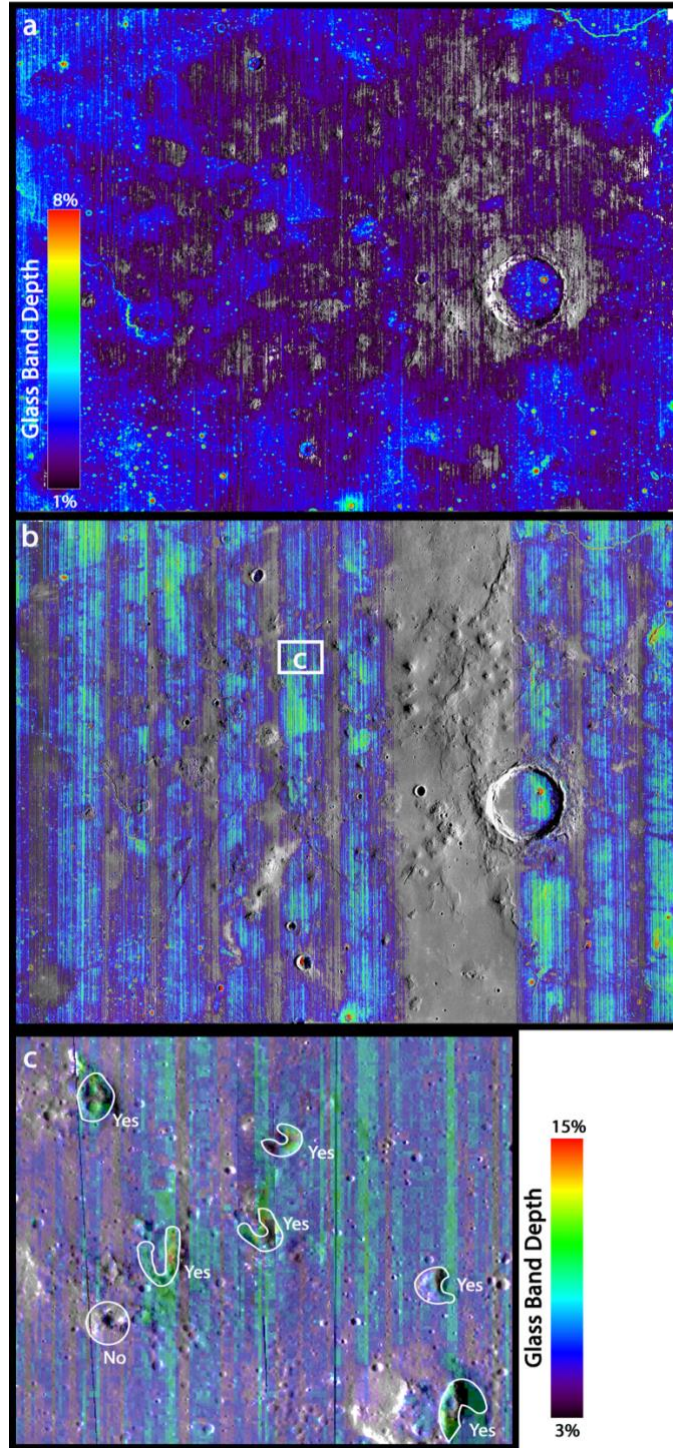


Figure 3-5. Glass band depth parameter maps overlaid on LROC WAC Mosaic of the Marius Hills Volcanic Complex. Warmer colors in parameter maps represent locations where the spectra are most likely to be representative of glass, but may also indicate olivine. (a) Low-resolution glass map, 280m/pixel. (b) High-resolution glass map, 140m/pixel. (c) Higher magnification location section of high-resolution glass map overlaid on LROC NAC mosaic showing process of reviewing cone-like morphologies from (Lawrence et al., 2013) with M<sup>3</sup> spectral parameters.

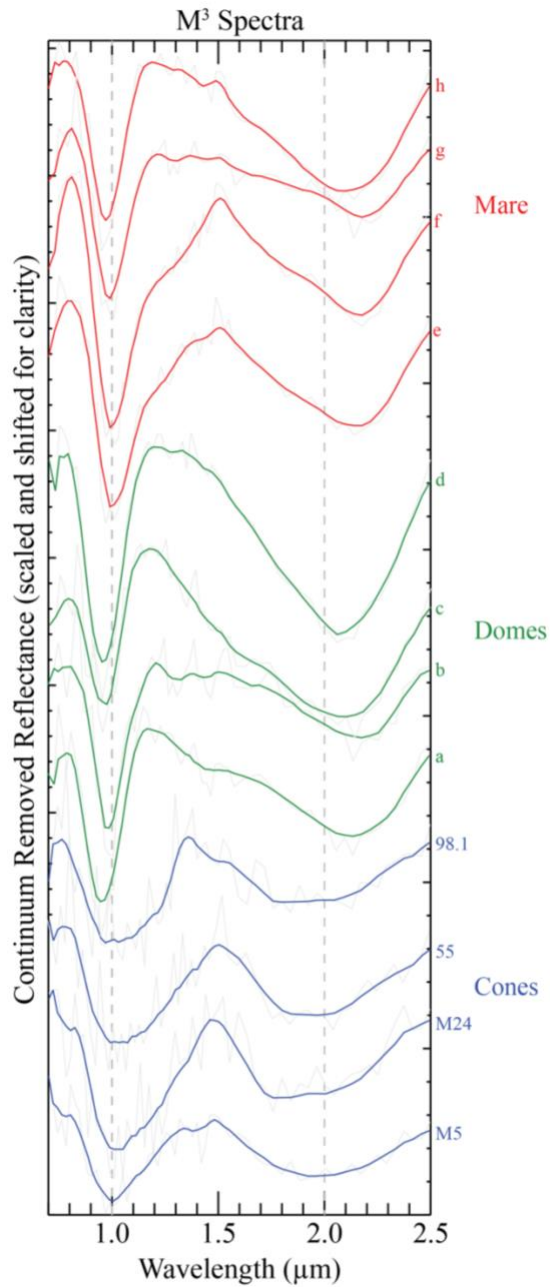


Figure 3-6. Selected M<sup>3</sup> continuum-removed and smoothed spectra showing differences between the cones (blue), domes (green), and mare (red) within the MHVC. Dotted lines indicate 1μm and 2μm wavelength positions for comparison between the spectra. Gray background spectra are continuum removed and unsmoothed.

The composite parameter maps (Figure 3-4 c and d) display the diversity of the mineralogy in the MHVC which we examine in relationship to the previously identified volcanic morphologies in the following sections. The RGB map suggests relationships between different parts of the MHVC, but the mineral interpretations detailed below are based on analysis of individual spectra averaged from specific regions of interest.

### **3.4.2 Domes**

Domes, as outlined in Figure 3-7, were identified initially by Lawrence et al., (2013). Morphologically, the domes are identified as raised topographic structures with irregular boundaries and low slopes. Figure 3-8 displays an example showing the lobate boundaries of the dome and an identified volcanic cone outlined in yellow. The majority of volcanic domes do not have associated cones, while some domes host multiple cones (Figure 3-7).

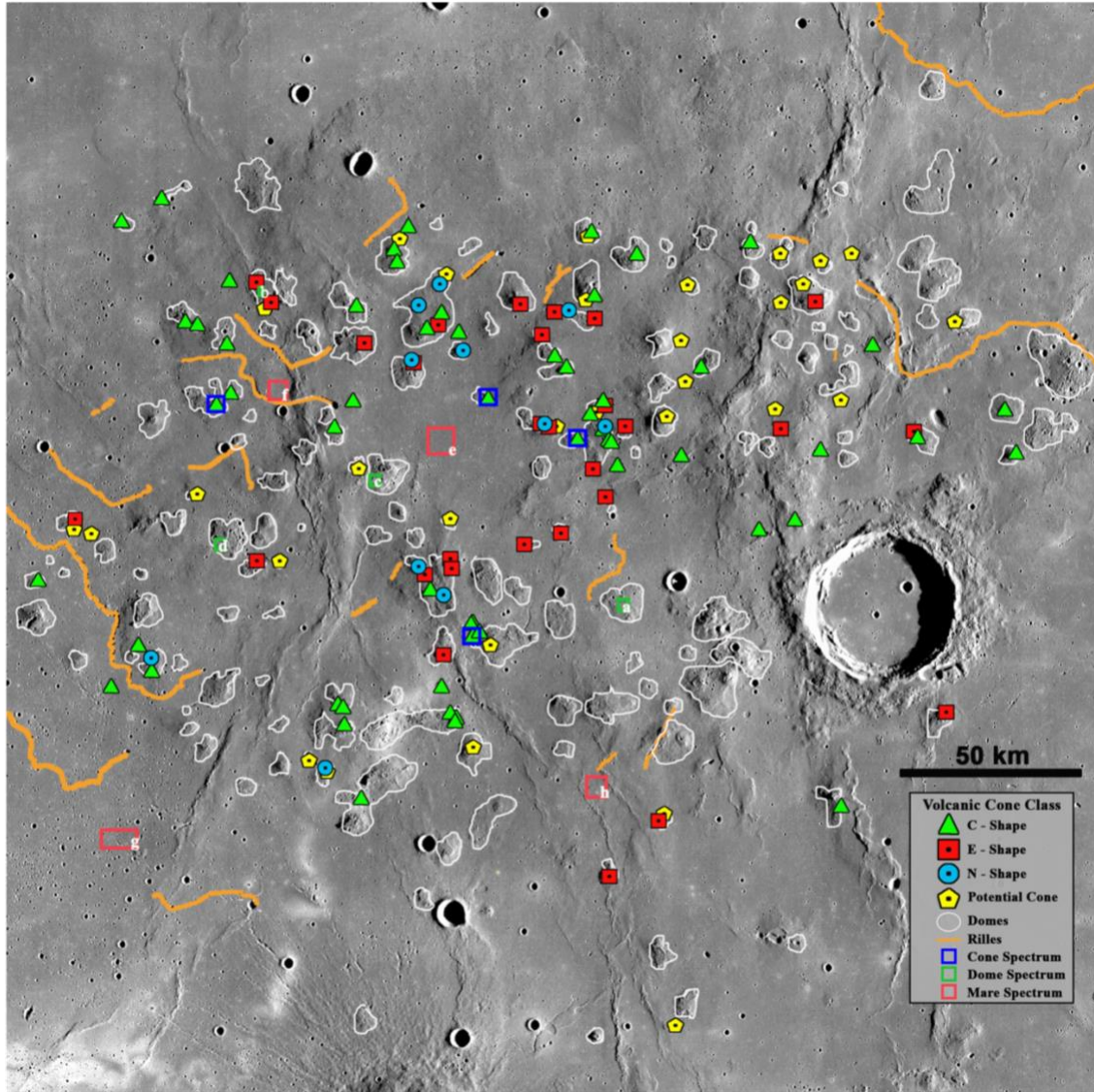


Figure 3-7. Reconstructed map in the style of Figure 1 in Lawrence et al. (2013) with updated cone types and locations overlaid on an LROC WAC mosaic. Colored shapes indicate the cinder cone morphology and the locations based on a combination of topography, visual images, and spectral data. Outlined white terrain are interpreted as dome morphologies, and the orange lines represent rille locations.

In Marius Hills, the volcanic dome structures have an  $M^3$  spectral signature with clear absorption bands centered between 0.95-0.97  $\mu\text{m}$  and 2.0-2.1  $\mu\text{m}$ , as shown in Figure 3-9. These band centers are slightly higher than expected for pure orthopyroxene. The 1  $\mu\text{m}$  band is typically symmetric, with a slightly larger band depth than the 2  $\mu\text{m}$  band, as shown in Figure 3-6. These spectral properties are consistent with an orthopyroxene-dominated spectrum mixed with some

clinopyroxene to produce intermediate band centers, perhaps also with a minor contribution from glass or olivine in some locations based on elevated band area ratios and 1  $\mu\text{m}$  band asymmetries. The presence of glass could be due to either small pyroclastic deposits or glass-rich impact melt, which emphasizes importance of understanding geologic context with respect to the spectral characterization.

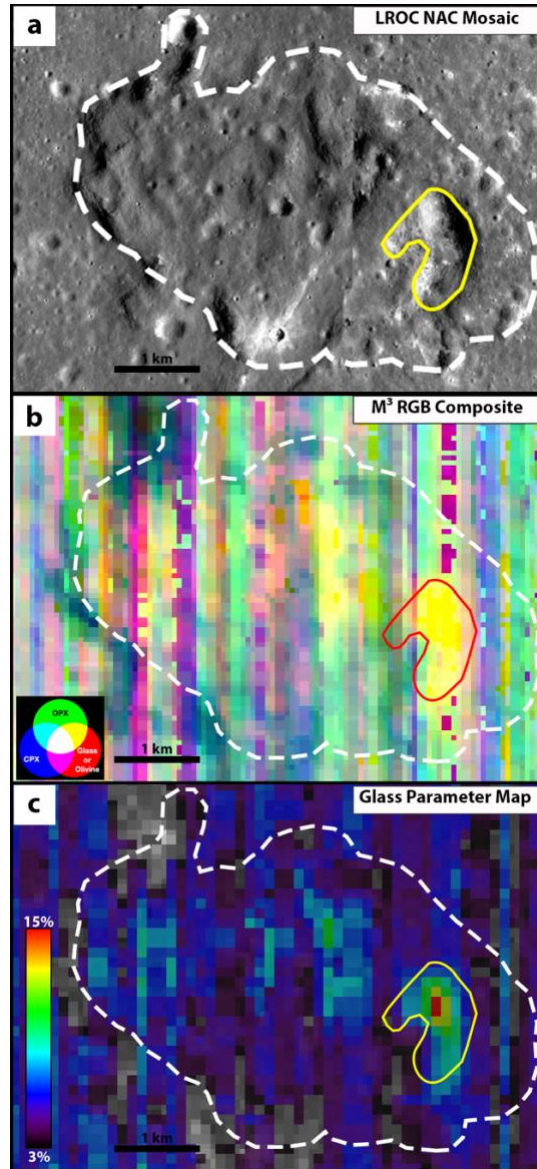


Figure 3-8. Marius Hills Cone located approximately 305.5°E and 13.8°N (solid outline) on a volcanic dome (dashed outline). (a) LROC NAC image mosaic (b) M3 RGB composite image where R= glass band depth parameter, G=1  $\mu\text{m}$  band center parameter, B= 2  $\mu\text{m}$  band center parameter (c) Glass parameter map image where warmer colors indicate spectral shapes consistent with glass or olivine. All images show that the cone can be distinguished from the dome by morphological and spectral properties.

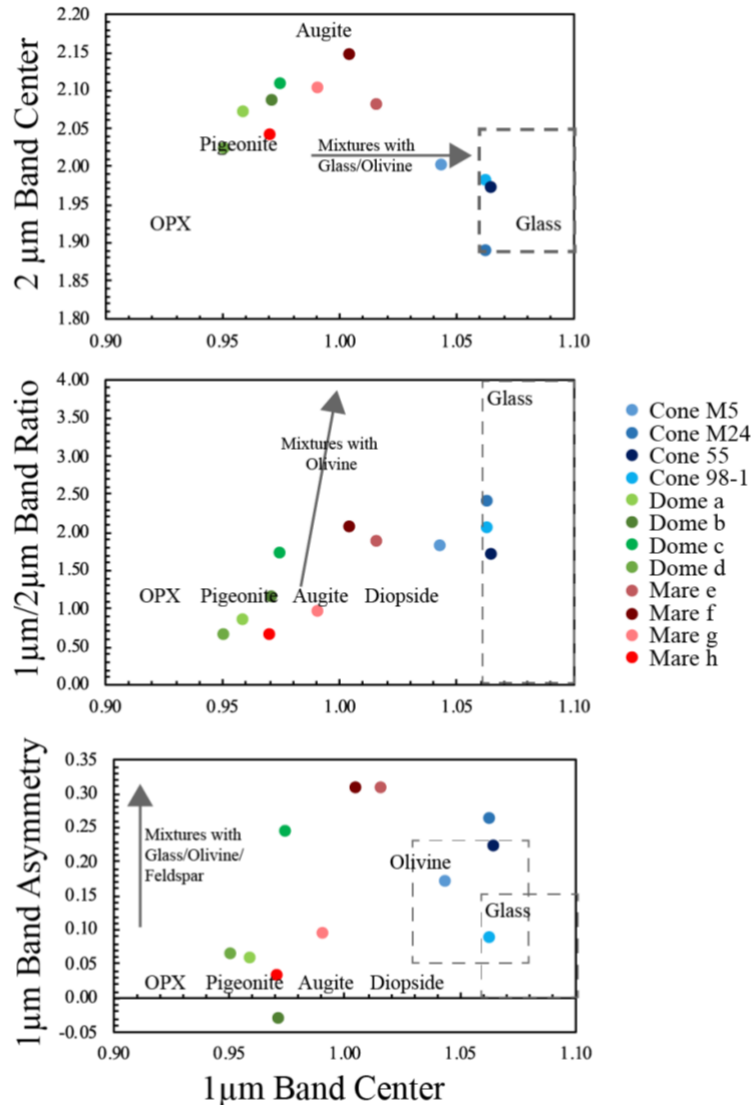


Figure 3-9. Spectral band parameter graphs of the MHVC cones, domes, and mare. Labels indicate the approximate parameters and trends expected based on laboratory spectra of endmembers and mixtures analyzed by (Horgan et al., 2014) and (Klima et al., 2007).

### 3.4.3 Cones

The majority of previously identified cones in MHVC exhibit enhanced values of our glass band depth parameter (BDGLA) relative to surrounding terrain (dome or plateau surface). Figure 3-10 displays three examples of LROC NAC images depicting known volcanic cones as well as the associated glass parameter maps. In the glass parameter maps, the shape and orientation of the volcanic cones mirror the visible images. Volcanic cones of all shape classes in the MHVC display both 1 and 2 μm bands. The 1 μm bands are centered between 1.05 and 1.1 μm, are the deeper of

the two bands, and have a slight asymmetry to longer wavelengths. The second broad and symmetric band is typically centered between 1.9-2.0  $\mu\text{m}$ , at slightly shorter wavelengths than the domes or plateau surface (Figure 3-6). We interpret this signature due to additional Fe-bearing glass compared to the domes based on the high 1 $\mu\text{m}$  band center and the low 2 $\mu\text{m}$  band center (Figure 3-9). While the slight asymmetry and location of the 1 $\mu\text{m}$  band could be consistent with olivine, which would present as a broad and asymmetric 1 $\mu\text{m}$  absorption band most often centered between 1.05-1.07  $\mu\text{m}$ , olivine exhibits no 2  $\mu\text{m}$  band (Figure 3-3) and thus is not expected to affect the 2  $\mu\text{m}$  band center (Sunshine et al., 1990; Sunshine and Pieters, 1998). The combination of these parameters is consistent with glass in the cones.

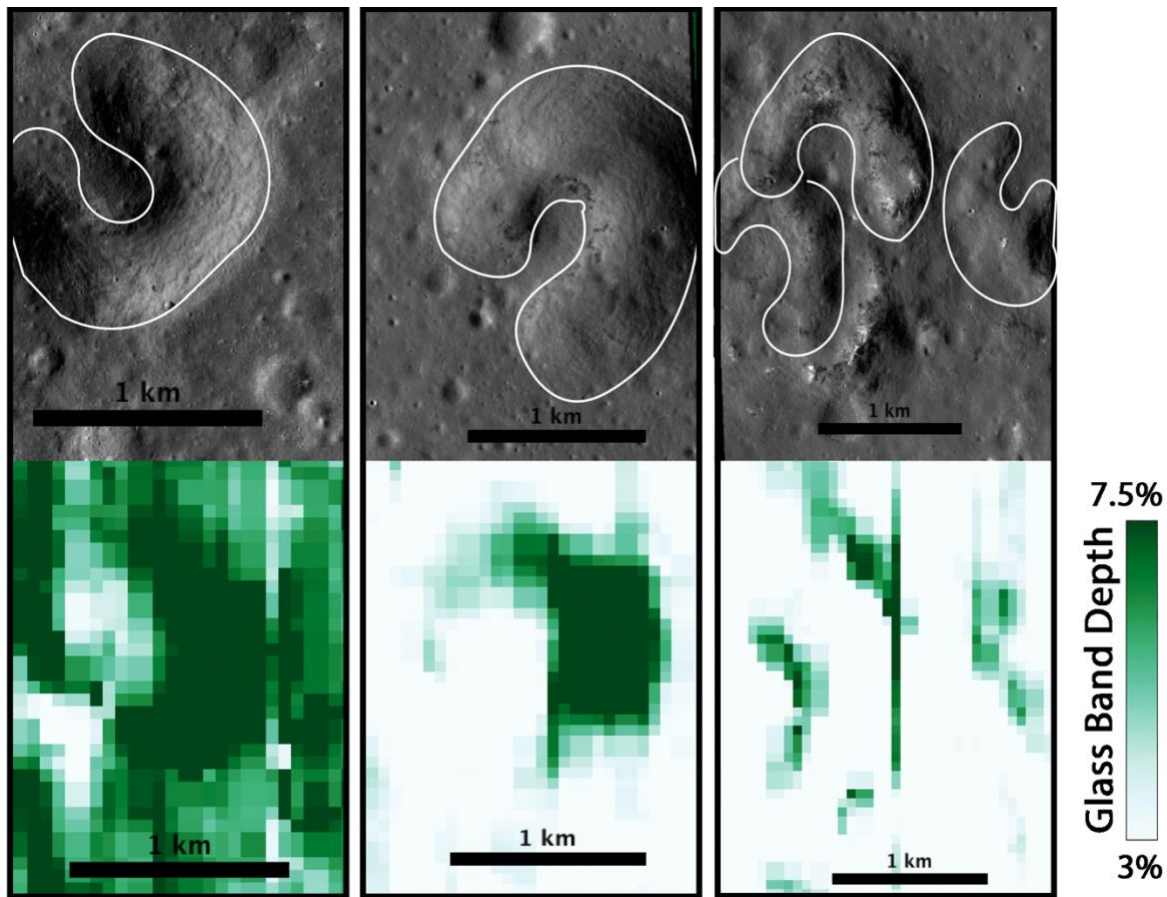


Figure 3-10. LROC NAC images depicting known volcanic cones based on morphology from Lawrence et al. (2013). Bottom: Above locations in the glass parameter maps where areas of a deeper green color represent locations where the spectra are most likely to be representative of glass. The shape and orientation of the cones are similar in both images.

These results suggest that the presence of glass spectral signatures is a good indicator for explosive tephra associated with cones in MHVC and provides a secondary test for the presence of cones in addition to previous work from Lawrence et al., (2013) using LROC images to identify volcanic cones. Using our glass band depth parameter map, we re-examined the cones and domes identified by Lawrence et al., (2013) and compared the morphological features to the  $M^3$  spectral properties. Additionally, we used the glass band depth parameter maps (Figure 3-5) to identify new potential cinder cones. Table 3-2 shows the totals and shape designations for the volcanic cones identified from this study in the MHVC.

LROC morphological studies from (Lawrence et al., 2013) identified 93 categorized cones (64 C-class, 12 E-class, and 17 N-class) and 55 potential cones. We confirmed that 99 cones identified as cones or possible cones in Lawrence et al. (2013) exhibit glass spectral signatures based on the glass band depth map and detailed spectral investigation of a subset of cones as discussed above. These confirmed cones fall into the same categories used by Lawrence et al. (2013): 58 C-class, 29 E-class, and 12 N-class. The remaining 30 cones we have categorized as potential cones, which include locations where either: 1. a clear glass signature is not present in the parameter map but with a distinct cone-like morphologic feature, or 2. a clear glass spectral signature is present but does not correspond to a clear cone morphological feature. The first category includes locations only mapped in the low-resolution mosaic (Figures 3-4c and d) where the spectral glass signature is not as strong, as is the case for nine of the U-class constructs. Finally, two C-class cones and 12 U-class constructs were removed from the original database altogether (Lawrence et al., 2013) based on a combination of a lack of clear  $M^3$  glass spectral signatures and unconvincing morphological characteristics.

Table 3-2. The listed amount of each type of cinder cone morphology as outlines in the Lawrence et al. (2013) paper, compared to this study when spectroscopy was added as a distinguishing component. The cones and their locations are listed in Appendix Table B.1.

<b>Cone Classification</b>	<b>LROC Imagery and Topography Lawrence <i>et al</i> (2013)</b>	<b>M<sup>3</sup> Spectra, Imagery, and Topography This study</b>
<b>C-class breached wall</b>	64	58
<b>E-class elongated</b>	12	29
<b>N-class circular</b>	17	12
<b>U-class uncertain construct</b>	55	30
<b>Totals</b>	93 categorized cones 55 potential cones	99 categorized cones 30 potential cones

A rose diagram was used to map the limb directions of the 29 elongated E-class cones, as shown in Figure 3-11. Elongated cones follow an NNW/SSE trend, where approximately 17 cones are oriented to the NNW while 12 are oriented to the SSE.

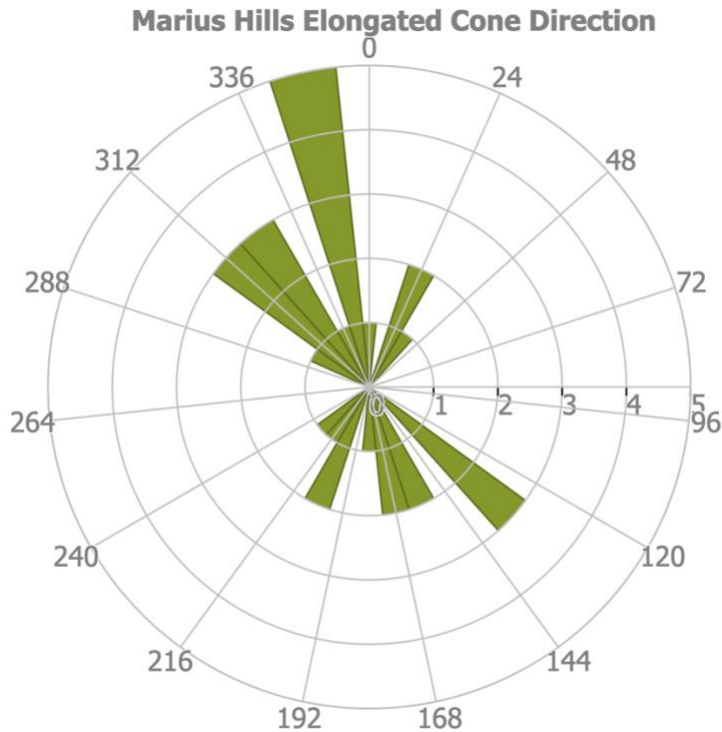


Figure 3-11. A rose diagram that showing the orientation of E-class cones along fissures. The majority of cones are oriented in the NNW-NNE and SSW-SSE directions.

### 3.4.4 Plateau Mare

The plateau of the MHVC rises above the surrounding mare plains, as visible in Figure 3-4b, but significant lava flows that embay the domes on the plateau are also interpreted as mare. Spectra were collected from a range of locations on the plateau mare to compare to previous spectral analyses (e.g., Besse et al., 2011; Heather et al., 2003; Weitz and Head, 1999). Our analysis confirmed that different spectral properties are associated with different mare surfaces in the MHVC. The varying spectral properties in the mare are easily identifiable in the lower resolution map in Figure 3-4d, which shows a clear distinction between green-blue vs. pink-blue locations on the plateau as well as the surrounding Oceanus Procellarum mare. Spectra collected from both mare types (Figure 3-6) show absorption bands near 1 and 2  $\mu\text{m}$ . In some mare areas (green in Figure 3-4d), the 1  $\mu\text{m}$  band is symmetric and centered below 1  $\mu\text{m}$  (0.96-1.0  $\mu\text{m}$ ). In contrast, other areas (pinkish-blue in Figure 3-4d) exhibit an asymmetrical band centered above 1  $\mu\text{m}$  (1.00-1.02  $\mu\text{m}$ ) with a shoulder centered between 1.20 and 1.40  $\mu\text{m}$ . Both mare units have broad 2  $\mu\text{m}$

bands centered between 2.0 and 2.15  $\mu\text{m}$ . These properties are consistent with the presence of CPX in both mare units with additional olivine in some locations, where the addition of olivine produces an asymmetric 1  $\mu\text{m}$  band centered at slightly longer wavelengths, but without significantly impacting the 2  $\mu\text{m}$  band center (Bennett et al., 2016; Horgan et al., 2014).

The spectra from both the domes and cones are thus spectrally distinguished from the surrounding mare (Figures 3-6 and 3-9). The mare spectra exhibit bands centered at longer wavelengths consistent with more CPX than in the typically more clearly OPX-dominated domes. The olivine-bearing portion of the mare show a clear shoulder on the 1  $\mu\text{m}$  band and no shift in the 2  $\mu\text{m}$  band center, whereas the cone spectra exhibit rounder 1  $\mu\text{m}$  band centered at longer wavelengths, do not show the same clear shoulder, and show a clear downward shift in the 2  $\mu\text{m}$  band center.

### **3.5 Discussion**

#### **3.5.1 Significance of glass detection in the MHVC cones**

In this study, we present the first detections of volcanic glass in the Marius Hills Volcanic Complex. The interpretive advancements made in this investigation are a result of improved spectral resolution and analysis techniques. The higher resolution spectral data from M<sup>3</sup> (140 m/pixel) was imperative to constrain the volcanic cones' mineralogy, as their diameters range from 0.5–4 km (Lawrence et al., 2013). Analysis of the spectra was completed using systematic band parameters and extracted individual spectra to characterize the Fe-bearing mineralogy of the region, as described in (Horgan et al., 2014). In the context of lunar spectroscopy, distinguishing glass from olivine has been a point of contention as the spectral shapes of glass and olivine are similar (Gaddis et al., 2003; Horgan et al., 2014). Spectra of olivine exhibit a broad and asymmetric absorption between 1.05-1.07  $\mu\text{m}$ , produced from a combination of three bands centered near 0.85, 1.05, and 1.15  $\mu\text{m}$ , and no 2  $\mu\text{m}$  band (Figure 3-3; Sunshine et al., 1990; Sunshine and Pieters, 1998). The 1 $\mu\text{m}$  band center position can also increase as the fraction of Fe-rich olivine increases (King and Ridley, 1987). The wide and symmetric absorption of iron-bearing glasses is centered between 1.07-1.18  $\mu\text{m}$ , and in some cases, glasses exhibit an additional absorption centered between 1.90-2.05  $\mu\text{m}$  (Figure 3; e.g., Cannon et al., 2017). Therefore, there can be strong similarities between glass and olivine in the 1  $\mu\text{m}$  spectral region. When there is a lack of a 2 $\mu\text{m}$

band, and a strong asymmetric 1  $\mu\text{m}$  band, a confident interpretation of olivine can usually be made; however, mixtures of glass and pyroxene can produce olivine-like asymmetric 1  $\mu\text{m}$  bands (Horgan and Bell, 2012; Horgan et al., 2014). Therefore, detailed spectral analysis was required to make our spectral interpretations for cinder cones as well as other features in the MHVC (Figure 3-6).

The cones of all shape classes in Marius Hills exhibit spectra consistent with increased glass abundances, as would be expected in a cinder cone. Spectrally, the volcanic cones all display both 1 and 2  $\mu\text{m}$  bands (Figure 3-6). The 1  $\mu\text{m}$  bands are centered between 1.05 and 1.1  $\mu\text{m}$ , are the deeper of the two bands and have a slight asymmetry to longer wavelengths. The second broad and symmetric band is centered at or below 2  $\mu\text{m}$ , shifted shortward compared to the surrounding domes and mare. This contrasts to spectra on some plateau mare units nearby, which exhibit a more asymmetric band centered near 1  $\mu\text{m}$  and no change in 2  $\mu\text{m}$  band center compared to surrounding pyroxene-dominated terrains, all of which is more consistent with olivine.

Because glass is more transparent than other Fe-bearing minerals, it is not a strong absorber and thus detecting glass in VNIR spectra suggests that it is very abundant in the surface, typically >50 wt.% (Henderson et al., 2020; Horgan et al., 2014; Scudder et al., 2021). This suggests that the MHVC cones are mostly glass-rich in composition. The combination of the glass detections and the cone-class topographic edifices (Lawrence et al., 2013) confirms the hypothesis that the cones formed from an explosive eruption resulting in the formation of cinders instead of a mantled impact crater, degraded lava flow fronts, or other lunar geologic feature.

Glass forms when melted rock is quenched, and the rapid cooling prevents the crystallization of minerals (Glass, 2016). In explosive volcanic eruptions, glass forms during fragmentation and the resulting rapid cooling of the magma. The identification of glass in VNIR spectral analysis of volcanic pyroclasts indicates an explosive volcanic origin (Henderson et al., 2020). Our detection of glass in the MHVC represents the first detection of glass in a lunar volcanic deposit outside of aerially extensive pyroclastic mantling deposits with little topographic relief mapped elsewhere across the Moon. The morphology of the cones in MHVC is consistent with cinder cones, which suggests that the glass formed as pyroclastic cinders or spatter from explosive eruptions to form an edifice with significant topographic relief. This would constitute a different style of glass on the lunar surface than the glass beads collected during the Apollo program from aerially extensive but low topographic relief pyroclastic deposits (Adams et al., 1974; Hughes et al., 1988; Zellner et al., 2002).

### **3.5.2 Diverse Cone Morphologies in MHVC**

We also used the high-resolution M<sup>3</sup> data to more precisely map the distribution of potential lunar cinder cones in MHVC. Our investigation revealed 99 confident cone detections which was more than previous investigations (Table 3-2), where 93 were reported by (Lawrence et al., 2013), 46 reported by (Weitz and Head, 1999); and 59 were reported by (Whitford-Stark and Head, 1977). The number of potential and uncategorized cones also decreased from the 55 identified by (Lawrence et al., 2013) to 30 in this study. The remaining potential cones, U-class constructs, fall within the following categories: 1. Cones that have a distinct cinder cone-like morphology but are located in areas where the spectra are not conclusive (e.g., in the portion of the M3 maps with only low-resolution data, Figures 3-4 c and d). 2. Localized concentrations of possible glass spectral features that do not have a matching cone-like morphology. In the latter case, these could be just small pyroclastic deposits without enough volume to build a cone. To further categorize these potential cones, additional LROC images could be collected to investigate their properties at different phase angles.

There are still numerous irregularly shaped features in the Marius Hills that are not mapped in our study. These features may be degraded cones, but to further classify them would require an understanding of how cones erode on the lunar surface and the extent of the later embayment of the mare around the domes and cones.

The diversity of shapes exhibited by the MHVC cones (C-, N-, and E-class cones) is significant because it also represents the same diversity of cones observed in Earth volcanic complexes, enabling the comparison of the volcanic system below the surface. The orientation of the elongated cones can provide insight into the subsurface plumbing system as they show the direction of fissures and magma movement. Elongated cones in MHVC have a consistent NNW-NNE and SSW-SSE direction (Figure 3-11), likely indicating the location and orientation of dyke swarms beneath the plateau. The presence of dyke swarms in the MHVC is supported by gravity data from the GRAIL spacecraft (Deutsch et al., 2019; Kiefer, 2013).

### **3.5.3 Possible Primitive Volcanics Preserved in MHVC domes**

The domes or low shields in Marius Hills are spectrally distinct from the cones and the embaying mare. M<sup>3</sup> spectra of the domes are orthopyroxene-dominated, likely mixed with some

clinopyroxene, based on absorption bands centered near 0.95 and 2.05  $\mu\text{m}$ . Both bands are symmetric, and the 1 $\mu\text{m}$  band has a slightly larger band depth than the 2 $\mu\text{m}$  band, as shown in Figures 3-6 and Figure 3-9. As previously hypothesized, the domes are likely small shield volcanoes formed through effusive eruptions (Head and Gifford, 1980; Heather et al., 2003; Lawrence et al., 2013; Weitz and Head, 1999).

While the domes appear to be more spectrally dominated by OPX, the surrounding and embaying mare, both on the plateau and the surrounding plains, are more spectrally dominated by CPX and olivine. Previous research hypothesized that the dome-forming eruptions potentially sourced the Oceanus Procellarum mare basalts (Besse et al., 2011; Heather et al., 2003; Weitz and Head, 1999). However, this interpretation is not well-supported by our spectral analysis, as the domes and cones are spectrally distinct from the mare deposits. Thus, if the mare erupted from within the MHVC, this suggests that the domes were not the source. To better understand the origin of mare basalts in MHVC, they should be analyzed within the broader context of Oceanus Procellarum, which is outside the scope of this investigation.

If the plateau mare were sourced from within the MHVC, this may imply significant igneous evolution in the MHVC source region, from earlier, more Fe/Mg-rich magmas producing the domes to later, more Ca-rich magmas producing the mare flows. Notably, the dome spectra have very similar spectral properties to OPX-dominated terrains in the South Pole-Aitken Basin produced from excavation of primitive materials in the upper mantle and lower crust (Melosh et al., 2017; Huang et al., 2020). In addition, when compared to VNIR lab spectra of Apollo samples, the dome spectral parameters are most similar to Apollo 16 rocks (Huang et al., 2020), which are dominated by ancient breccias excavated by large impacts. These comparisons suggest that the MHVC domes are spectrally in family with known primitive materials on the Moon and that the MHVC system could represent a unique local example of lunar magma evolution.

#### **3.5.4 Volcanic Evolution of the MHVC**

The Marius Hills plateau is raised above the Oceanus Procellarum. Raised domes and cones are embayed by younger mare flows, likely obscuring the edifices' extent in orbital datasets (Lawrence et al., 2013). Later compressional stresses, as indicated by the presence of wrinkle ridges from the mare's cooling, may have also contributed to modifying volcanic edifices and sinuous rilles (Lawrence et al., 2013). Many wrinkle ridges cross the Marius Hills and primarily

follow an SSE-NNW trend (Lawrence et al., 2013; 2010), similar to the elongated cones mapped in this study (Figure 3-11).

Combining the morphological and spectral data, we hypothesize the volcanic evolution of the region was long-lived and with distinct early edifice-forming and later mare-forming episodes. The first stage of volcanism in the region was likely a long-lived sequence of effusive eruptions to form the MHVC plateau. A large shield volcano has been hypothesized to be the cause of the MHVC plateau, which would require an edifice approximately 330 km in diameter and rising about 2.2 km above the surrounding mare plains (Spudis et al., 2013). For reference, this is on par with some of the smaller shield volcanoes on Mars (e.g., Pityusa Patera at ~230 km diameter, ~1.5 km height) and only slightly larger in diameter than Mauna Kea (~250 km diameter, ~10 km in height) on Earth. Shield volcanoes characteristically have fissure zones, serving as points of weakness where magma can reach the surface through dykes for succeeding parasitical eruptions resulting in cone and dome building (e.g., Head and Wilson, 1991; McDonald and Abbott, 1970). The consistent NNW-NNE and SSW-SSE direction of the E-class cones could indicate the direction of these fissures (Figure 3-11), and the presence of dyke swarms in the area is supported by gravity data from the GRAIL spacecraft (Deutsch et al., 2019; Kiefer, 2013).

It has been hypothesized that shield building occurred during the main phases of mare volcanism on the Moon, between 3.9 and 3.0 Ga ago (Spudis et al., 2013; Wilhelms et al., 1987; BVSP, 1981). However,  $M^3$  analysis shows that the domes are spectrally distinct from the mare and perhaps more primitive in composition. This suggests that shield building in MHVC may have occurred closer to the onset of mare volcanism or may even represent pre-mare volcanism.

In the MHVC, the domes and cones represent the last stage of shield building. The domes would have erupted effusively while the cones erupted explosively, as indicated by the presence of glass in the volcanic cones, but not the domes. Additionally, the domes and cones likely erupted concurrently in time, as indicated by NAC observations showing the dome-building flows originating from the C-class cones and through the identification of cones both on and off volcanic domes (Lawrence et al., 2013). Differences in the explosivity of the eruptions could be attributed to changes in the magma ascent rate (Lawrence et al., 2013), which can be controlled by magma buoyancy, volatiles, conduit geometry, chamber overpressure, stress fields, and viscosity (Cassidy et al., 2018). Concurrent eruption of the domes and cones would indicate that the explosiveness is not due to difference in the intrinsic properties of the magma (e.g., volatile content or viscosity),

but more likely a result of extrinsic parameters (e.g., conduit geometry, rate of decompression, or a buildup behind a clogged vent). This is distinct from the factors driving explosivity for large mantling pyroclastic deposits elsewhere on the Moon, which are thought to be due to the buildup of juvenile volatiles in deeply sourced magmas (Head and Wilson, 2017).

Lastly, the effusive eruption of mare occurred on the Marius Hills plateau. The source of these eruptions is unknown. However, the distinct mineralogy of the cones and domes from the mare and the embayment of the positive relief edifices would indicate that the mare eruptions came later. These eruptions likely contributed to the Oceanus Procellarum mare. Whitford-Stark and Head (1980) mapped the lava flows of Oceanus Procellarum and found they spatially coincided with mare mapped within the MHVC. Recent studies have continued to map the flows on the plateau and estimated ages from 2.5 to 3.3 Ga (Heather et al., 2003; Heather and Dunkin, 2002) to 0.8 to 1.3 Ga (Hiesinger et al., 2016; Huang et al., 2011).

### **3.5.5 Implications for Future Exploration**

Marius Hills has been proposed as a priority target for exploration of the Moon (Jawin et al., 2015). A history of long-lived volcanism is preserved in multiple volcanic units in MHVC, including the cones, domes, rilles, mare, and collapse pits. Marius Hills would meet multiple priorities for exploration of the Moon and would address key lunar science questions outlined in the 2007 National Research Council (NRC) Scientific Context for the Exploration of the Moon (SCEM, National Research Council 2007), the 2017 LEAG Specific Action Team Report Advancing Science of the Moon (ASM-SAT, LEAG, 2017), and Vision and Voyages for Planetary Science in the Decade 2013–2022 (National Research Council, 2011). The long-lived volcanism in the Marius Hills could provide constraints for the bombardment history of the Moon by providing age anchors through precisely dating the sampled volcanic material that could be related to relative ages across the solar system based on crater counting, and their composition could provide insight into the thermal and chemical evolution (National Research Council, 2011; Jawin et al., 2019). As described in the 2013-2022 Decadal Survey, an investigation of Marius Hills could: 1. Constrain the bulk composition of terrestrial planets by studying the composition of volcanic products. 2. Characterize planetary interiors to determine how they differentiate and evolve by assessing volcanic products created through partial melts of the lunar interior. 3.

Characterize planetary surfaces to understand how they are modified by geologic processes (i.e., volcanism, National Research Council, 2011; Jawin et al., 2019).

MHVC would be ideal for collecting samples from multiple volcanic sources, including both explosive and effusive deposits, to be returned to Earth or for in-situ analysis that may preserve long-term magma evolution on the Moon. The proximity of these deposits to one another would be amenable to in situ investigation and sampling by both robotic and human exploration. Long-range rovers with the ability to traverse the slopes of the volcanic landforms have been proposed (Robinson and Elliott, 2020; Stopar et al., 2016). The spectral mapping completed within this study would be imperative for planning a mission to the MHVC, and in-situ spectral analysis could confirm or supplement the remote sensing analysis and be extrapolated to other lunar volcanic provinces (Spudis et al., 2013).

### **3.6 Conclusions**

Volcanic glass has been detected for the first time in the cones of the Marius Hills Volcanic Complex. The Marius Hills Volcanic Complex is unique with multiple visible positive relief volcanic edifices representative of explosive volcanism compared to other lunar pyroclastic deposits (Gaddis et al., 2003; Gustafson et al., 2012). M<sup>3</sup> spectral analysis shows that the cones in MHVC exhibit spectra consistent with glass, confirming cinder cone origin and the identification of glass consistent with pyroclasts not constrained to glass beads. Domes in MHVC exhibit spectra consistent with more OPX than in surrounding CPX-dominated mare.

Spectral analysis of the MHVC reveals distinct spectral signatures associated with different geologic units, and M<sup>3</sup> spectra extracted for MHVC units show clear iron-bearing absorption bands near 1 and 2  $\mu\text{m}$ . This research provides evidence to showing spectroscopy can identify volcanic landforms when visible images and morphology fail. This is important for future exploration of volcanic terrains where visible images may not be ideal.

The domes and cones likely erupted concurrently in time, and differences in the mineralogy of the resulting edifices add supporting evidence to the hypothesis that extrinsic properties (e.g., ascent rate), not changes in magma composition (e.g., amount of volatiles), led to the different volcanic morphologies. The source for the domes and cones may be the result of eruptions from numerous dykes (Head and Wilson, 1991) supported by dyke swarms identified by the GRAIL spacecraft (Deutsch et al., 2019; Kiefer, 2013). Combining the morphology and the spectral data,

we hypothesize the magma evolution of the region was long-lived and with distinct early edifice-forming and later mare-forming episodes. This time difference may have resulted in magma evolution, as reflected in the distinct pyroxene mineralogies of the domes vs. mare. The long-lived volcanism visible through multiple volcanic units within close proximity in MHVC would be ideal for future exploration of the Moon.

### 3.7 Acknowledgments

We would like to thank Suraya Whitaker for volunteering to provide a second opinion on the classification and existence of the cones. Additionally, we would like to thank Sebastian Besse for invaluable discussions regarding the M<sup>3</sup> dataset and spectral interpretation of this region. This material is based upon work supported by the National Science Foundation Graduate Research Fellowship Program under Grant No. (DGE-1333468). Any opinions, findings, and conclusions or recommendations expressed in this material are those of the author(s) and do not necessarily reflect the views of the National Science Foundation. This work was also supported in part by the NASA Lunar Data Analysis Program, grant number NNX17AC63G.

### 3.8 References

- Adams, J.B., 1974. Visible and near-infrared diffuse reflectance spectra of pyroxenes as applied to remote sensing of solid objects in the solar system. *Journal of Geophysical Research* 79, 4829–4836. <https://doi.org/10.1029/jb079i032p04829>
- Adams, J.B., Pieters, C., McCord, T.B., 1974. Orange glass-Evidence for regional deposits of pyroclastic origin on the moon. *Lunar and Planetary Science Conference* 1, 171–186.
- Basaltic Volcanism Study Project (1981) *Basaltic Volcanism on the Terrestrial Planets*. Pergamon Press, Inc., New York. 1286 pp.
- Bennett, K.A., Horgan, B.H.N., Gaddis, L.R., Greenhagen, B.T., Allen, C.C., Hayne, P.O., III, J.F.B., Paige, D.A., 2016. Complex explosive volcanic activity on the Moon within Oppenheimer crater. *Icarus* 273, 296–314. <https://doi.org/10.1016/j.Icarus.2016.02.007>
- Besse, S., Sunshine, J.M., Staid, M.I., Petro, N.E., Boardman, J.W., Green, R.O., Head, J.W., Isaacson, P.J., Mustard, J.F., Pieters, C.M., 2011. Compositional variability of the Marius Hills volcanic complex from the Moon Mineralogy Mapper (M3). *Journal of Geophysical Research* 116, E00G13. <https://doi.org/10.1029/2010je003725>

- Besse, S., Yokota, Y., Boardman, J., Green, R., Haruyama, J., Isaacson, P., Mall, U., Matsunaga, T., Ohtake, M., Pieters, C., Staid, M., Sunshine, J., Yamamoto, S., 2013. One Moon, many measurements 2: Photometric corrections. *Icarus* 226, 127–139. <https://doi.org/10.1016/j.Icarus.2013.05.009>
- Boardman, J.W., Pieters, C.M., Green, R.O., Lundeen, S.R., Varanasi, P., Nettles, J., Petro, N., Isaacson, P., Besse, S., Taylor, L.A., 2011. Measuring moonlight: An overview of the spatial properties, lunar coverage, selenolocation, and related Level 1B products of the Moon Mineralogy Mapper. *Journal of Geophysical Research: Oceans* 116, 65. <https://doi.org/10.1029/2010je003730>
- Campbell, B.A., Hawke, B.R., Campbell, D.B., 2009. Surface morphology of domes in the Marius Hills and Mons Rümker regions of the Moon from Earth-based radar data. *J Geophys Res Planets* 1991 2012 114. <https://doi.org/10.1029/2008je003253>
- Cannon, K.M., Mustard, J.F., Parman, S.W., Sklute, E.C., Dyar, M.D., Cooper, R.F., 2017. Spectral properties of Martian and other planetary glasses and their detection in remotely sensed data. *Journal of Geophysical Research: Planets* 122, 249–268. <https://doi.org/10.1002/2016je005219>
- Cassidy, M., Manga, M., Cashman, K., Bachmann, O., 2018. Controls on explosive-effusive volcanic eruption styles. *Nature Communications* 9, 2839. <https://doi.org/10.1038/s41467-018-05293-3>
- Clark, R.N., Roush, T.L., 1984. Reflectance spectroscopy: Quantitative analysis techniques for remote sensing applications. *Journal of Geophysical Research: Oceans* 89, 6329–6340. <https://doi.org/10.1029/jb089ib07p06329>
- Cloutis, E.A., Gaffey, M.J., 1991. Spectral-compositional variations in the constituent minerals of mafic and ultramafic assemblages and remote sensing implications. *Earth, Moon, and Planets* 53, 11–53. <https://doi.org/10.1007/bf00116217>
- Deutsch, A.N., Neumann, G.A., Head, J.W., Wilson, L., 2019. GRAIL-identified gravity anomalies in Oceanus Procellarum: Insight into subsurface impact and magmatic structures on the Moon. *Icarus* 331, 192–208. <https://doi.org/10.1016/j.Icarus.2019.05.027>
- Gaddis, Staid, M.I., Tyburczy, J.A., Hawke, B.R., Petro, N.E., 2003. Compositional analyses of lunar pyroclastic deposits. *Icarus* 161, 262–280. [https://doi.org/10.1016/s0019-1035\(02\)00036-2](https://doi.org/10.1016/s0019-1035(02)00036-2)
- Glass, B.P., 2016. Glass: The Geologic Connection. *International Journal of Applied Glass Science*. <https://doi.org/10.1111/ijag.12240>

- Green, R.O., Pieters, C., Mouroulis, P., Eastwood, M., Boardman, J., Glavich, T., Isaacson, P., Annadurai, M., Besse, S., Barr, D., Buratti, B., Cate, D., Chatterjee, A., Clark, R., Cheek, L., Combe, J., Dhingra, D., Essandoh, V., Geier, S., Goswami, J.N., Green, R., Haemmerle, V., Head, J., Hovland, L., Hyman, S., Klima, R., Koch, T., Kramer, G., Kumar, A.S.K., Lee, K., Lundeen, S., Malaret, E., McCord, T., McLaughlin, S., Mustard, J., Nettles, J., Petro, N., Plourde, K., Racho, C., Rodriguez, J., Runyon, C., Sellar, G., Smith, C., Sobel, H., Staid, M., Sunshine, J., Taylor, L., Thaisen, K., Tompkins, S., Tseng, H., Vane, G., Varanasi, P., White, M., Wilson, D., 2011. The Moon Mineralogy Mapper (M3) imaging spectrometer for lunar science: Instrument description, calibration, on-orbit measurements, science data calibration and on-orbit validation. *Journal of Geophysical Research: Planets* 116, E00G19. <https://doi.org/10.1029/2011je003797>
- Gustafson, J.O., Bell, J.F., Gaddis, L., Hawke, B.R., Giguere, T.A., 2012. Characterization of previously unidentified lunar pyroclastic deposits using Lunar Reconnaissance Orbiter Camera data. *Journal of Geophysical Research* E00H25. <https://doi.org/10.1029/2011je003893>
- Hapke, B., 2001. Space weathering from Mercury to the asteroid belt. *Journal of Geophysical Research: Oceans* 106, 10039–10073. <https://doi.org/10.1029/2000je001338>
- Haruyama, J., Hioki, K., Shirao, M., Morota, T., Hiesinger, H., Bogert, C.H. van der, Miyamoto, H., Iwasaki, A., Yokota, Y., Ohtake, M., Matsunaga, T., Hara, S., Nakanotani, S., Pieters, C.M., 2009. Possible lunar lava tube skylight observed by SELENE cameras. *Geophysical Research Letters* 36, 412. <https://doi.org/10.1029/2009gl040635>
- Head, J.W., Gifford, A., 1980. Lunar mare domes: Classification and modes of origin. *The moon and the planets* 22, 235–258. <https://doi.org/10.1007/bf00898434>
- Head, J.W., Wilson, L., 2017. Generation, ascent and eruption of magma on the Moon: New insights into source depths, magma supply, intrusions and effusive/explosive eruptions (Part 2: Predicted emplacement processes and observations). *Icarus* 283, 176–223. <https://doi.org/10.1016/j.Icarus.2016.05.031>
- Head, J.W., Wilson, L., 1991. Absence of large shield volcanoes and calderas on the Moon: Consequence of magma transport phenomena? *Geophys Res Lett* 18, 2121–2124. <https://doi.org/10.1029/91gl02536>
- Heather, D.J., Dunkin, S.K., 2002. A stratigraphic study of southern Oceanus Procellarum using Clementine multispectral data. *Planet Space Sci* 50, 1299–1309. [https://doi.org/10.1016/s0032-0633\(02\)00124-1](https://doi.org/10.1016/s0032-0633(02)00124-1)
- Heather, D.J., Dunkin, S.K., Wilson, L., 2003. Volcanism on the Marius Hills plateau: Observational analyses using Clementine multispectral data. *Journal of Geophysical Research: Planets* 108, 5017. <https://doi.org/10.1029/2002je001938>
- Henderson, M.J.B., Horgan, B.H.N., Rowe, M.C., Wall, K.T., Scudder, N.A., 2020. Determining the Volcanic Eruption Style of Tephra Deposits From Infrared Spectroscopy. *Earth Space Sci* 7. <https://doi.org/10.1029/2019ea001013>

- Hiesinger, H., Gebhart, J., Bogert, C.H. van der, Pasckert, J.H., Weinauer, J., Lawrence, S.J., Stopar, J.D., Robinson, M.S., 2016. Stratigraphy of Low Shields and Mare Basalts of the Marius Hills Region, Moon. Lunar and Planetary Science Conference 1877.
- Horgan, B., III, J.F.B., 2012. Widespread weathered glass on the surface of Mars. *Geology* 40, 391–394. <https://doi.org/10.1130/g32755.1>
- Horgan, B.H.N., Cloutis, E.A., Mann, P., III, J.F.B., 2014. Near-infrared spectra of ferrous mineral mixtures and methods for their identification in planetary surface spectra. *Icarus* 234, 132–154. <https://doi.org/10.1016/j.Icarus.2014.02.031>
- Huang, J., Xiao, L., He, X., Qiao, L., Zhao, J., Li, H., 2011. Geological characteristics and model ages of Marius Hills on the Moon. *Journal of Earth Science* 22, 601–609. <https://doi.org/10.1007/s12583-011-0211-8>
- Huang, Jun (黄俊), Zhiyong Xiao (肖智勇), Long Xiao (肖龙), Briony Horgan, Xiaoyi Hu (胡晓依), Paul Lucey, Xiao Xiao (肖潇), Siyuan Zhao (赵思源), Yuqi Qian (钱煜奇), Hao Zhang (张昊), Chunlai Li (李春来), Rui Xu (徐睿), Zhiping He (何志平), Jianfeng Yang (杨建峰), Bin Xue (薛彬), Qi He (何琦), Jie Zhong (钟杰), Hongyu Lin (林宏宇), Changning Huang (黄长宁), Jianfeng Xie (谢剑锋), 2020, Diverse rock types detected in the lunar South Pole–Aitken Basin by the Chang’E-4 lunar mission: *Geology*, v. 48, p. 723–727, doi:10.1130/G47280.1
- Hughes, S.S., Delano, J.W., Schmitt, R.A., 1988. Apollo 15 yellow-brown volcanic glass: Chemistry and petrogenetic relations to green volcanic glass and olivine-normative mare basalts. *Geochimica et Cosmochimica Acta* 52, 2379–2391. [https://doi.org/10.1016/0016-7037\(88\)90295-5](https://doi.org/10.1016/0016-7037(88)90295-5)
- Isaacson, P.J., Petro, N.E., Pieters, C.M., Besse, S., Boardman, J.W., Clark, R.N., Green, R.O., Lundeen, S., Malaret, E., McLaughlin, S., Sunshine, J.M., Taylor, L.A., 2013. Development, importance, and effect of a ground truth correction for the Moon Mineralogy Mapper reflectance data set. *Journal of Geophysical Research: Planets* 118, 369–381. <https://doi.org/10.1002/jgre.20048>
- Jawin, E.R., Valencia, S.N., Watkins, R.N., Crowell, J.M., Neal, C.R., Schmidt, G., 2019. Lunar Science for Landed Missions Workshop Findings Report. *Earth and Space Science* 6, 2–40. <https://doi.org/10.1029/2018ea000490>
- Kaku, T., Haruyama, J., Miyake, W., Kumamoto, A., Ishiyama, K., Nishibori, T., Yamamoto, K., Crites, S.T., Michikami, T., Yokota, Y., Sood, R., Melosh, H.J., Chappaz, L., Howell, K.C., 2017. Detection of Intact Lava Tubes at Marius Hills on the Moon by SELENE (Kaguya) Lunar Radar Sounder. *Geophys Res Lett* 44, 10,155–10,161. <https://doi.org/10.1002/2017gl074998>

- Kiefer, W.S., 2013. Gravity constraints on the subsurface structure of the Marius Hills: The magmatic plumbing of the largest lunar volcanic dome complex. *Journal of Geophysical Research: Planets* 118, 733–745. <https://doi.org/10.1029/2012je004111>
- King, T.V.V., Ridley, W.I., 1987. Relation of the spectroscopic reflectance of olivine to mineral chemistry and some remote sensing implications. *J Geophys Res Solid Earth* 92, 11457–11469. <https://doi.org/10.1029/jb092ib11p11457>
- Klima, R.L., Pieters, C.M., Dyar, M.D., 2007. Spectroscopy of synthetic Mg-Fe pyroxenes I: Spin-allowed and spin-forbidden crystal field bands in the visible and near-infrared. *Meteorit Planet Sci* 42, 235–253. <https://doi.org/10.1111/j.1945-5100.2007.tb00230.x>
- Konopliv, A., Asmar, S.W., Carranza, E., Sjogren, W.L., Yuan, D.N., 2001. Recent Gravity Models as a Result of the Lunar Prospector Mission. *Icarus* 150, 1–18. <https://doi.org/10.1006/icar.2000.6573>
- Lawrence, S.J., Stopar, J.D., Hawke, B.R., Greenhagen, B.T., Cahill, J.T.S., Bandfield, J.L., Jolliff, B.L., Denevi, B.W., Robinson, M.S., Glotch, T.D., Bussey, D.B.J., Spudis, P.D., Giguere, T.A., Garry, W.B., 2013. LRO observations of morphology and surface roughness of volcanic cones and lobate lava flows in the Marius Hills. *Journal of Geophysical Research: Planets* 118, 615–634. <https://doi.org/10.1002/jgre.20060>
- LEAG, 2017. Advancing science of the Moon: Report of the Specific Action Team, held 7–8 August 2017. Houston, Texas, United States of America.
- MacDonald G. A. and A. T. Abbott (1970), *Volcanoes in the Sea: The Geology of Hawaii*, 441 pp., Univ. Hawaii Press, Honolulu, Haw.
- McCauley, J.F., 1967. Geologic map of the Hevelius region of the moon. IMAP.
- McCord, T.B., Charette, M.P., Johnson, T.V., Lebofsky, L.A., Pieters, C., 1972. Spectrophotometry (0.3 to 1.1 $\mu$ ) of visited and proposed apollo lunar landing sites. *Moon* 5, 52–89. <https://doi.org/10.1007/bf00562105>
- Melosh, H.J., Kendall, J., Horgan, B., Johnson, B.C., Bowling, T., Lucey, P.G., Taylor, G.J., 2017. South Pole–Aitken basin ejecta reveal the Moon’s upper mantle. *Geology* 45, 1063–1066. <https://doi.org/10.1130/g39375.1>
- Moon, C. on the S.C. for E. of the, Board, S.S., Sciences, D. on E. and P., Council, N.R., 2007. The Scientific Context for Exploration of the Moon. <https://doi.org/10.17226/11954>
- National Research Council, 2011. *Vision and Voyages for Planetary Science in the Decade 2013-2022*. Washington, DC: National Academy Press.

- Nozette, S., Rustan, P., Pleasance, L.P., Horan, D.M., Regeon, P., Shoemaker, E.M., Spudis, P.D., Acton, C.H., Baker, D.N., Blamont, J.E., Buratti, B., Corson, M.P., Davies, M.E., Duxbury, T.C., Eliason, E.M., Jakosky, B.M., Kordas, J.F., Lewis, I.T., Lichtenberg, C.L., Lucey, P.G., Malaret, E., Massie, M.A., Resnick, J.H., Rollins, C.J., Park, H.S., McEwen, A.S., Robinson, M.S., Simpson, R.A., Smith, D.E., Sorenson, T.C., Breugge, R.W.V., Zuber, M.T., 1994. The Clementine mission to the moon: Scientific overview. *Science* 266, 1835–1839.
- Pieters, C., McCord, T.B., 1976. Characterization of lunar mare basalt types. IA remote sensing study using reflection spectroscopy of surface soils. *Lunar Planet. Sci* 7th, 2677–2690.
- Pieters, C.M., Taylor, L.A., Noble, S.K., Keller, L.P., Hapke, B., Morris, R.V., Allen, C.C., McKay, D.S., Wentworth, S., 2000. Space weathering on airless bodies: Resolving a mystery with lunar samples. *Meteoritics & Planetary Science* 35, 1101–1107. <https://doi.org/10.1111/j.1945-5100.2000.tb01496.x>
- Pieters, C.M., Boardman, J., Buratti, B., Chatterjee, A., 2009. The Moon mineralogy mapper (M3) on Chandrayaan-1. *Curr Sci*.
- Robinson, M., Elliott, J., 2020. Intrepid Planetary Mission Concept Study Report.
- Scudder, N.A., Horgan, B.H.N., Rampe, E.B., Smith, R.J., Rutledge, A.M., 2021. The effects of magmatic evolution, crystallinity, and microtexture on the visible/near-infrared and thermal-infrared spectra of volcanic rocks. *Icarus* 114344. <https://doi.org/10.1016/j.Icarus.2021.114344>
- Spudis, P.D., McGovern, P.J., Kiefer, W.S., 2013. Large shield volcanoes on the Moon. *Journal of Geophysical Research: Planets* 118, 1063–1081. <https://doi.org/10.1002/jgre.20059>
- Staid, M.I., Pieters, C.M., Besse, S., Boardman, J., Dhingra, D., Green, R., Head, J.W., Isaacson, P., Klima, R., Kramer, G., Mustard, J.M., Runyon, C., Sunshine, J., Taylor, L.A., 2011. The mineralogy of late stage lunar volcanism as observed by the Moon Mineralogy Mapper on Chandrayaan-1. *Journal of Geophysical Research: Oceans* 116. [https://doi.org/10.1029/2010je003735@10.1002/\(issn\)2169-9100.moonmmi1](https://doi.org/10.1029/2010je003735@10.1002/(issn)2169-9100.moonmmi1)
- Stopar, Lawrence, Jolliff, Speyerer, Robinson, 2016. Defining Long-Duration Traverses of Lunar Volcanic Complexes with LROC NAC Images, in: Annual Meeting of the Lunar Exploration Analysis Group. p. 5074.
- Sunshine, J.M., Pieters, C.M., 1998. Determining the composition of olivine from reflectance spectroscopy. *Journal of Geophysical Research: Planets* 103. <https://doi.org/10.1002/jgre.v103.e6>
- Sunshine, J.M., Pieters, C.M., III, J.W.H., 1994. New evidence for compositional diversity on the Marius Hills plateau from Galileo Multi-Spectral Imaging. *Lunar Planet. Sci* XXV.

- Sunshine, J.M., Pieters, C.M., Pratt, S.F., 1990. Deconvolution of mineral absorption bands: An improved approach. *Journal of Geophysical Research* 95, 6955–6966. <https://doi.org/10.1029/jb095ib05p06955>
- Walker, G.P.L., 1973. Explosive volcanic eruptions — a new classification scheme. *Geologische Rundschau* 62, 431–446. <https://doi.org/10.1007/bf01840108>
- Wall, K.T., Rowe, M.C., Ellis, B.S., Schmidt, M.E., Eccles, J.D., 2014. Determining volcanic eruption styles on Earth and Mars from crystallinity measurements. *Nature Communications* 5, 5090. <https://doi.org/10.1038/ncomms6090>
- Weitz, C.M., Head, J.W., 1999. Spectral properties of the Marius Hills volcanic complex and implications for the formation of lunar domes and cones. *Journal of Geophysical Research: Oceans* 104, 18933–18956. <https://doi.org/10.1029/1998je000630>
- Weitz, C.M., Head, J.W.I., 1998. Diversity of Lunar Volcanic Eruptions at the Marius Hills Complex. *Lunar and Planetary Science Conference* 29.
- Whitford-Stark, J. L. (1975), Shield volcanoes, in *Volcanoes of Earth Moon and Mars*, edited by G. Fielder and L. Wilson, pp. 66–74, Elek Science, London, U.K.
- Whitford-Stark, J.L., Head, J.W., 1977. The Procellarum volcanic complexes: contrasting styles of volcanism. *Lunar Planet. Sci* 8, 2705–2724.
- Wilhelms, McCauley, Trask, 1987. *The Geologic History of the Moon*. Professional Paper. <https://doi.org/10.3133/pp1348>
- Wood, C.A., 1979. Cinder Cones on Earth, Moon, and Mars. *Lunar and Planetary Science Conference*.
- Zellner, N.E.B., Spudis, P.D., Delano, J.W., Whittet, D.C.B., 2002. Impact glasses from the Apollo 14 landing site and implications for regional geology. *Journal of Geophysical Research: Planets* 107, 12-1-12–13. <https://doi.org/10.1029/2001je001800>
- Zuber, M.T., Smith, D.E., Lehman, D.H., Hoffman, T.L., Asmar, S.W., Watkins, M.M., 2013. Gravity Recovery and Interior Laboratory (GRAIL): Mapping the Lunar Interior from Crust to Core. *Space Sci Rev* 178, 3–24. <https://doi.org/10.1007/s11214-012-9952-7>

## CHAPTER 4. SPECTRAL DIVERSITY OF EXPLOSIVE VOLCANIC DEPOSITS IN SCHRÖDINGER BASIN ON THE MOON

### 4.1 Introduction

Schrödinger basin has been an area of heightened interest for lunar exploration due to the proximity of well-preserved impact and volcanic materials that could be accessed in a single mission, but its location in the lunar south pole had previously inhibited human and robotic exploration. However, Schrödinger is slated to be the landing site for two payload suites delivered in tandem on a robotic lander by the Commercial Lunar Payload Services Contract (CLPS) in 2024 (NASA, 2020). Schrödinger (Figure 4-1) is a 320 km diameter Imbrium-aged (~3.8 billion years old) impact crater located within South Pole-Aitken (SPA) basin on the lunar far side, centered at 138°E, 75°S (Wilhelms et al., 1979). Schrödinger is thought to be the second youngest basin on the lunar surface (Shoemaker et al., 1994). Pre-Nectarian-aged (~4.533-3.92 billion years old) SPA basin is a 2400 km by 2050 km impact structure centered at 53°S, 191°E on the far side (Bethell & Zuber, 2005).

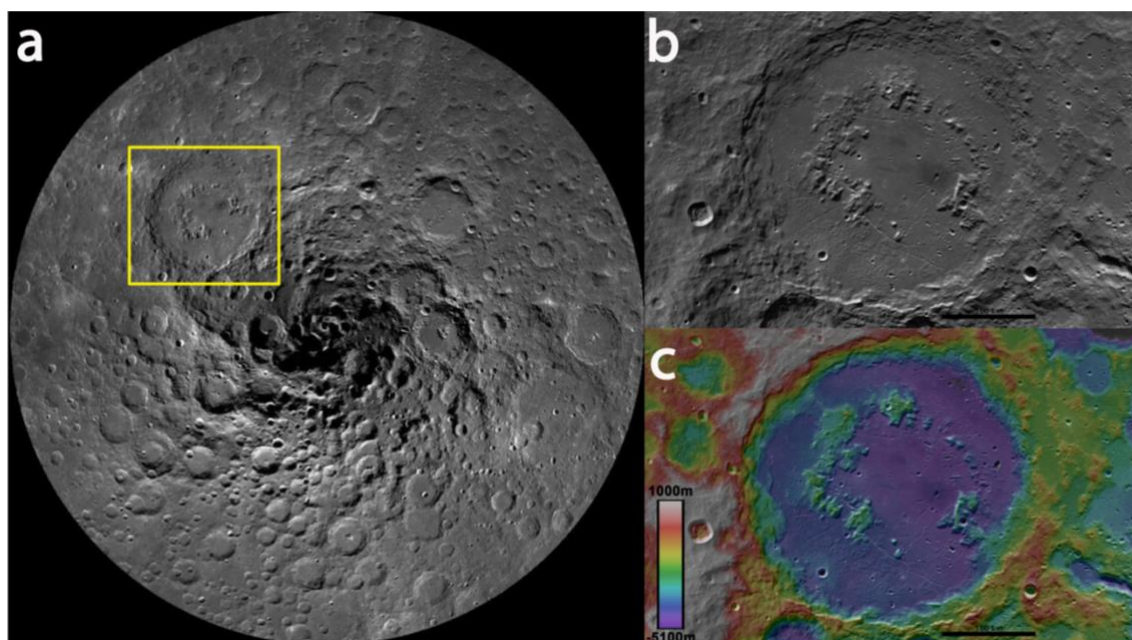


Figure 4-1. Schrödinger basin context. (a) LROC WAC mosaic of the South Pole showing the location of Schrödinger basin outlined in yellow. (b) LROC WAC mosaic of Schrödinger Basin, basin diameter is 320 km. (c) LOLA elevation data overlain on LROC WAC mosaic.

Schrödinger is a target for future human or robotic exploration as its diverse lithologies would help address various high-priority lunar science goals (Jawin et al., 2019; Kring & Robinson, 2018; O’Sullivan et al., 2011). Schrödinger contains a large conical edifice surrounded by a low-albedo region interpreted as a large cinder cone and associated pyroclastic deposit, and a low-albedo lobate deposit interpreted as a lava flow (Shoemaker et al., 1994; Pieters et al., 2009; Shanker et al., 2012). These volcanic deposits are located near the center of the basin, within the uplifted peak ring, which is composed of Pre-Schrödinger crust (Potts et al., 2014). The relative adjacency and the accessibility of these deposits can help to answer questions about the history of volcanic and impact processes on the Moon in a single mission, which would fulfill goals outlined in the Decadal Survey (National Research Council, 2011).

However, the relationship between the volcanic deposits in Schrödinger is not well understood, and a variety of origins have been hypothesized for the cone, flow, and other possibly related features in the basin. Here we use orbital reflectance spectroscopy to determine the mineralogy and crystallinity of the volcanic deposits in Schrödinger, and ultimately to assess the volcanic eruption history of the basin. In particular, this study aims to characterize the eruption style of volcanic deposits in Schrödinger, both whether eruptions in the basin were explosive vs. effusive, and the nature of any explosive eruptions (e.g., Strombolian, Hawaiian, Vulcanian). Understanding the eruption properties of the Schrödinger volcanics provides key insights into magma source regions in the lunar interior and will provide context for the Lunar Interior Temperature and Materials Suite (LITMS). LITMS will investigate the lunar interior's heat flow and electrical conductivity in the Schrödinger basin when delivered by the CLPS lander in 2024. Finally, the Schrödinger cone is the largest conical edifice identified to date on the lunar surface, and if it is explosive in origin, represents a key endmember within the population of lunar pyroclastic deposits (LPDs). By comparing the eruption history of any explosive volcanic deposits in Schrödinger to other LPDs, we aim to better understand the relationship between deposit size, deposit morphology, geologic context, and eruption style.

This investigation of Schrödinger addresses a NASA Strategic Knowledge Gap (SKG) by analyzing the composition, distribution, and presence of lunar volatiles in pyroclastic deposits and at the lunar poles (Jawin et al., 2019). SKGs represent gaps in knowledge or information required to decrease risk, increase effectiveness, and improve the design of robotic and human space exploration missions (See <https://www.nasa.gov/exploration/library/skg.html>).

## 4.2 Background

### 4.2.1 Schrödinger Basin

Schrödinger basin is the second youngest impact basin on the Moon and is located within the oldest and largest impact basin, South Pole-Aitken (SPA). Schrödinger contains well-preserved materials generated through both impact and volcanic processes (Gaddis et al., 2003; Shoemaker et al., 1994).

The SPA basin is pre-Nectarian in age, has an ellipsoidal shape with axes of 2400 km by 2050 km, has a maximum depth of 18 km, and is centered at 53°S 191°E on the lunar far side (Bethell & Zuber, 2005). SPA is characterized by high thorium and iron anomalies (Jolliff et al., 2000). The SPA basin-forming event has been hypothesized to have exposed the lunar upper mantle (Pieters et al., 2001), and spectroscopic analysis combined with impact modeling confirmed that orthopyroxene-rich materials consistent with the upper mantle were exposed during the SPA basin impact (Melosh et al., 2017; Moriarty et al., 2021). The floor of the SPA basin was recently explored by China's Chang'E-4 lunar far-side lander and its rover Yutu-2 (Li et al., 2015, 2019). Observations from the Visible and Near Infrared Spectrometer (VNIS; Huang et al., 2020) identified the presence of orthopyroxene derived from the upper mantle and corroborating the orbital spectral interpretation (Melosh et al., 2017).

Schrödinger basin is a distinctive feature near the western rim of SPA (138°E and 75°), measuring 320 km in diameter, 4.5 km deep, and exhibiting a prominent inner peak ring (Wilhelms et al., 1979). It is believed to be the second youngest lunar basin with an early Imbrium age (~3.8 billion years old) and includes secondary craters on the basin floor from the formation of Orientale (Shoemaker et al., 1994). The peak-ring rises 1–2.5 km above the basin floor with a diameter of 125 km (Wilhelms et al., 1979). Possible mare-like lava flow plains have been identified within the peak ring on the basin floor as well as a conical edifice that rises to a height of ~415 m that is located along a wide graben (Wilhelms et al., 1979). Graben within Schrödinger are circumferential to the center of the basin and roughly follow the arc of the peak ring (Shoemaker et al., 1994). Within the basin are two distinct rilles: Vallis Schrödinger is approximately 315 km long with a radial direction of 315°, and Vallis Planck is ~600 km long and has a radial direction of 350° (Wilhelms et al., 1979). These rilles have been hypothesized to be the likely source of the

inner-peak ring mare plains (Mest 2011; Shankar et al., 2012; Shoemaker et al., 1994). Multiple geologic maps (Kramer et al., 2013; Scott C Mest, 2011; Shankar et al., 2012; Shoemaker et al., 1994) of the Schrödinger basin have been completed and can be referenced for distinguishing units. In the LROC WAC mosaic (Figure 4-1b), low albedo units within the inner-peak ring stand out as distinct from the basin floor. Figure 4-2b outlines and labels these units as the cone, lobate mafic unit (previously referred to as the mare plains), and ridge unit.

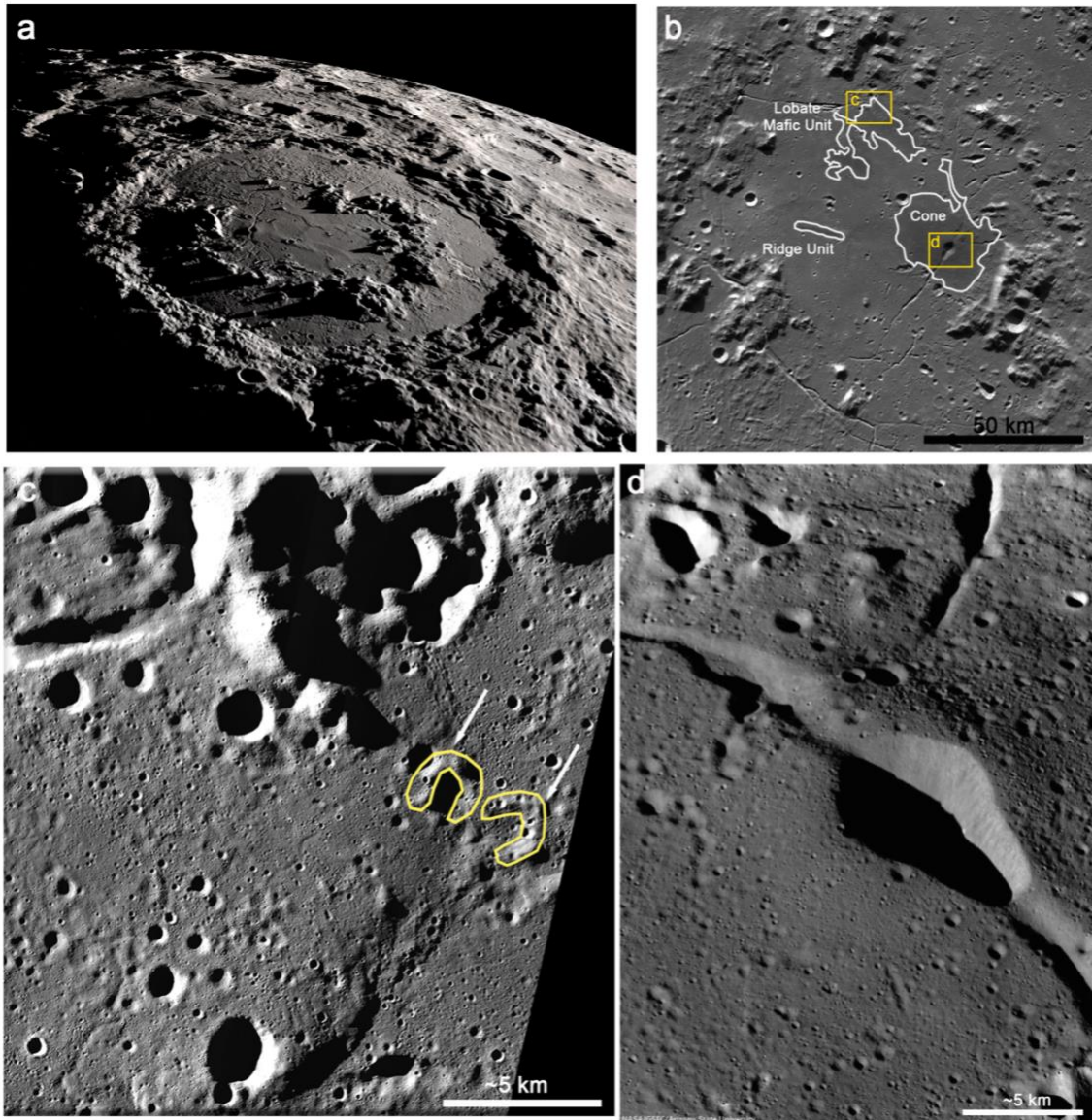


Figure 4-2. (a) Perspective view of Schrödinger basin. Illustration credit: NASA Scientific Visualization Studio (NASA SVS). (b) Inner-peak ring image with pyroclastic deposits analyzed in this study outlined and labeled. (c) LROC low-sun NAC mosaic. Outlined are locations of potential cones that may have been a source of the lobate mafic unit. (d) Perspective view of the vent on the Schrödinger Cones.

#### 4.2.2 Lunar Pyroclastic Deposits

The potential explosive volcanic deposits in Schrödinger can be compared to hypothesized explosive volcanic deposits elsewhere on the Moon. Lunar pyroclastic deposits (LPD), also known as “dark mantling” deposits, are low-albedo and low-relief units believed to have formed during ancient explosive volcanic eruptions (Head, 1974). These deposits are composed of juvenile magmatic minerals (*e.g.*, clinopyroxene (CPX) and olivine), glass (quenched and partially crystalline glass beads), as well as local country rock (orthopyroxene (OPX) and plagioclase in the lunar highlands; clinopyroxene in the mare; Hawke et al., 1989). The deposits exhibit an extensive range of sizes and have been previously divided into two categories: regional (>1000 km<sup>2</sup> in area) and local deposits (<1000 km<sup>2</sup> in area; Gaddis et al., 2003). Pyroclastic deposits erupted from deep within the lunar interior represent primitive materials that could help further characterize the lunar interior and expand our understanding of lunar basaltic magmatism (Gaddis et al., 2003).

The collection of pyroclastic samples in the form of dark glass beads from the Apollo 17 lunar landing site, Taurus Littrow, sparked an interest in the glass-rich deposits formed from volcanic eruptions (Pieters et al., 1974). Based on early spectral studies using Earth-based telescopes, localized pyroclastic deposits were theorized to result from violently explosive Vulcanian-style eruptions due to the buildup of gases behind a plug due to low eruption rates. This eruption style can eject juvenile material along with large amounts of country rock (Head & Wilson 1979). In contrast, regional pyroclastic deposits are believed to form from Strombolian-style eruptions (coalesced bubble explosions) or from Hawaiian-style fire-fountain eruptions (Head & Wilson 1979), both of which occur due to high eruption rates. This eruption style produces mainly juvenile material, and deposits are thus composed of glass and partially crystalline glass beads (Gaddis et al., 1985). The Clementine spacecraft collected higher resolution (~100m/pixel) ultraviolet-visible multispectral data from lunar orbit (Nozette et al., 1994). This allowed for the first global compositional analysis of lunar pyroclastic deposits (Gaddis et al., 2003). While Clementine was able to detect some variability within regional pyroclastic deposits related to crystallinity, the data could not provide explicit constraints on the mineralogy of the deposits (Gaddis et al., 2003; Hawke et al., 1989; Weitz et al., 1999).

More recently, higher resolution spectral data has provided new insights into the mineralogy of pyroclastic deposits on the Moon and has suggested that this simple model between

small Vulcanian eruptions and large strombolian eruptions does not represent the full diversity of volcanic eruption styles. In some cases, this diversity is apparent even at local scales. Oppenheimer crater is a floor-fractured crater located at 35°S and 166°W that is also located within the SPA. Pre-Nectarian in age, Oppenheimer has a diameter of about 200 km with a population of over 15 distinct pyroclastic deposits. The Oppenheimer pyroclastic deposits often have clear vents and are located along fractures in the crater floor (Bennett et al., 2016) The deposits range in size from a few square kilometers to 1500 km<sup>2</sup>, crossing the boundary between local and regional deposits (Gaddis et al., 2003). Spectral examination of the Oppenheimer deposits revealed mineralogical evidence for the existence of a range in eruption styles in the deposits from Vulcanian to fire-fountaining and Strombolian, with evidence of effusive activity observed as well (Bennett et al., 2016).

Bennett et al. (2016) hypothesized that the low crustal thickness in SPA may have allowed easier access for deep and volatile-rich magma to the surface, thus creating more volatile-rich and explosive eruptions even for small volumes of magma. However, this hypothesis requires more analysis of lunar pyroclastic deposits within and outside of low crustal thickness areas, interpreted by GRAIL gravity data (Wieczorek et al., 2013) to confirm. If crustal thickness does play an essential role in controlling the explosivity of lunar volcanic eruptions, then it is possible that volcanic deposits in Schrödinger also experienced a stronger pressure gradient during ascension, resulting in higher eruption rates than expected for other eruptions with the same volatile content.

There are still many unknowns regarding explosive volcanic deposits on the Moon, including the drivers of explosivity (Cassidy et al., 2018) and how eruption characteristics are recorded in the mineralogical and morphological diversity of the resulting pyroclasts. Understanding if the primary driver of explosive volcanism on the Moon is magmatic volatile content or extrinsic geologic factors (e.g., rate of decompression, crustal properties, and conduit/vent geometries; (Cassidy et al., 2018) could have implications for In-Situ Resource Utilization (ISRU). Lunar volcanic glasses rich in FeO<sub>2</sub> could be exposed to an H<sub>2</sub> environment, creating Fe<sup>2+</sup> and H<sub>2</sub>O, which could be electrolyzed to yield oxygen. The pyroclastic glasses produced the most oxygen out of any Apollo sample (Allen et al., 1996) and lending support for these materials as important feedstocks for future human exploration. Additionally, rare volatile elements needed for industrial processes could be extracted from lunar pyroclastic deposits (Duke et al., 2006). Observations of Schrödinger can inform this knowledge gap by assessing the

composition of the volcanic deposits and determining the eruption style to help understand any resulting pyroclasts proposed as potential sources of oxygen for future astronauts.

### 4.2.3 History of Schrödinger Spectral Studies

Visible wavelength images (Robinson et al., 2010) reveal that the pyroclastic deposits within the Schrödinger basin may be relatively complex, with multiple pyroclastic deposits and an unusually high albedo (Figure 4-1) compared to other lunar pyroclastic deposits (Gaddis et al., 2003). The Clementine Ultraviolet Visible (UVVIS) multispectral instrument (Nozette et al., 1994) provided the first spectral analysis of Schrödinger basin (Shoemaker et al., 1994). (Shanker *et al.* 2012) analyzed a single M<sup>3</sup> image to test their Clementine results. Kramer et al. (2013) previously examined the Schrödinger basin with Level 1 M<sup>3</sup> hyperspectral data (Pieters et al., 2009) and limited their analysis to fresh material exposed by impact craters. These studies examined the spectral properties of the peak-ring, inner peak-ring floor, as well as the pyroclastic units, including the cone, mafic, and ridge units.

The uplifted peak-ring rises to 1-2.5 km high and appears as a circular mountain range. It was formed during the impact that created the Schrödinger basin, and the mineralogy could provide insight into the peak ring formation process. M<sup>3</sup> analysis performed by Kramer et al., (2013) confirmed the Kaguya Multispectral Imager identification of olivine and anorthosite (Ohtake et al., 2009; Yamamoto et al., 2010) as well as the Clementine interpretations of pyroxene and feldspar (Shankar et al., 2012). Notably, the only M<sup>3</sup> spectral signatures of olivine in Schrödinger basin were found within the peak-ring (Kramer et al., 2013). The peak-ring is hypothesized to be composed of massive blocks with the composition of orthopyroxene-bearing (norite) and olivine-rich (troctolite or dunite) cumulates that have been hypothesized as the remnants of the lunar magma ocean and subsequent magmatic intrusions into the crust (Kramer et al., 2013).

The inner-peak ring floor had previously been separated into two units based on texture. A rough plains unit exhibits gentle hummocks, swales, and low knobs, while the smooth plains unit has no distinguishable relief (Shoemaker et al., 1994). Both inner-peak ring floor units, when analyzed by Clementine, were interpreted to be noritic in composition with an impact melt origin (Shoemaker et al., 1994). However, limited previous M<sup>3</sup> investigations largely worked with noisy spectra with shallow 1000 nm iron bands without a discernable 2000 nm band. The inner peak-

ring floor was interpreted as a thick glass-rich impact melt with low spectral contrast caused by space weathering (Kramer et al., 2013).

The most distinct volcanic deposit in Schrödinger is a conical edifice raised 415 m above the floor and an associated pyroclastic deposit with an area of 1250 km<sup>2</sup> located near the uplifted peak ring (Shoemaker et al., 1994; Wilhelms et al., 1979). Throughout the manuscript, the conical deposit will be referred to as the Schrödinger cone. While the cone was initially interpreted as a maar-type volcano (Shoemaker et al., 1994), later investigations revealed a positive relief conical deposit with a low albedo that was interpreted as a large pyroclastic deposit potentially emplaced via more continuous Hawaiian-style fire-fountain eruptions (Gaddis et al., 2003; Wilson & Head, 1981). Analysis with Clementine revealed that the sizeable conical edifice was spectrally distinct from the nearby mare with a higher reflectance ratio in the 750-nm versus the 415-nm bands, but did not find evidence of an iron absorption near 1000 nm that would indicate olivine, pyroxene, or glass (Shoemaker et al., 1994). However, a later investigation with Clementine spectral data showed that the conical vent and other potential pyroclastic deposits predominantly did exhibit spectra with distinctive absorption features near 1µm and 2µm, interpreted as olivine and pyroxene (Shankar et al., 2012). A more recent M<sup>3</sup> analysis of the Schrödinger basin (Kramer et al., 2011, 2013) interpreted the cone to be glass-rich from the low albedo and a single spectrum collected from the sun-facing slope of the interior of the volcanic vent exhibiting broad and weak mafic absorption features, with a steep, linear continuum slope. However, these previous studies were unable to provide a thorough spectral analyses including spectral mapping and the analyses of multiple individual spectra of the cone with spectral band parameters. Therefore, further M<sup>3</sup> analysis is required to determine the mineralogy and crystallinity of the Schrödinger cone and associated pyroclastic deposits.

The low albedo inner-peak ring lobate mafic unit (Figure 4-2b,c) has been called by many names through the previous publications including, ‘mare’ (Shoemaker et al., 1994), ‘dark plains material’ (Mest, 2011), ‘inner-basin mare unit’ (Kramer et al., 2013), and ‘mare patches’ (Shankar et al., 2012). Many of these names included the interpretive term mare, which implies effusive volcanic deposits. This interpretation was made based on the lobed margins of the deposit that resemble lava flow features. Within this investigation, we use the name Lobate Mafic Unit as a non-interpretive term with respect to the originating eruption style.

Some previous studies have divided the lobate mafic unit into two units, while other studies have combined them into one unit. Within this study, we refer to this as a singular unit based on the most recent geologic maps (Kramer et al., 2013; Mest, 2011), in which a break between the units was not identified through either morphology or spectroscopy. Radar observations of the lobate mafic unit with the Mini-RF radar revealed that the textures were relatively rough, atypical of lunar mare patches (Shankar et al., 2012) and exceed those of rough terrestrial lava flows at radar wavelengths (Campbell et al., 1997).

The lobate mafic unit has been identified as spectrally distinct from the inner-peak ring floor. Clementine spectral observations of the lobate mafic units identified an absorption band near 1000 nm interpreted as basaltic rocks similar to mare elsewhere on the lunar surface (Shoemaker et al., 1994). Further investigations of the Clementine data revealed a strong mafic signature (based on the 950 nm/750 nm ratio vs. 750 nm reflectance) and were interpreted as suggesting mixed anorthositic and mafic material (Mest, 2011). A previous M<sup>3</sup> investigation led to the interpretation of a pyroxene-rich unit based on an absorption centered below 1  $\mu\text{m}$  and a broad band centered near 2  $\mu\text{m}$  (Shankar et al., 2012). Kramer et al., (2013) extracted M<sup>3</sup> spectra from limited fresh craters in the lobate mafic unit and found the unit to be spectrally indistinguishable from the orthopyroxene-rich inner-peak ring basin floor, and therefore interpreted the unit as a very thin layer and that was hypothesized to be glass-rich based on the low albedo that could indicate a pyroclastic deposit. (Kramer et al., 2013).

The ridge unit is a small lenticular unit within the inner-peak ring. The unit is about 22 km long and ranges between ~1.5 km and 4.5 km wide and rises about 115-200 m above the inner-peak ring floor. The unit appears to be asymmetric in the slope profile, where one side has a sharper, more distinct margin, while the other has a more gradual descent into the inner-peak ring floor. This unit has also had many unit names: the 'ridged unit' (Shoemaker et al., 1994), the 'tectonic ridge' (Shankar et al., 2012), the 'ridge crest' (Mest, 2011) and the 'Bluff' (Kramer et al., 2013). Many previous investigations struggled to accurately identify the composition of the ridge unit (Shankar et al., 2012; Shoemaker et al., 1994) and it has been hypothesized to be of either tectonic or volcanic origin.

Shoemaker et al., (1994) hypothesized that this ridge may represent an intrusion of viscous magma raised slightly above the basin floor or due to buckling of the melt sheet (Shoemaker et al.,

1994). However, LOLA topography showing that there is a topographic rise disproved the buckling melt sheet hypothesis. (Kramer *et al.*, 2013) instead interpreted the unit as a blind thrust fault that formed in the thickest section of the initial melt sheet then experienced compressional stress. The asymmetry in the ridge suggested faulting rather than buckling indicating a wrinkle ridge, resulting from a thrust fault (Kramer *et al.*, 2013).

In this study, we create a hyperspectral map of the Schrödinger basin using a more recent calibration of the M<sup>3</sup> data (Level 2; Boardman *et al.*, 2011) than was available for previous studies, and we analyze the spectral properties of the various volcanic units using more sensitive spectral parameters (Horgan *et al.*, 2014). This analysis will enable us to compare specific units within the basin and confirm the presence of glass and iron-bearing minerals. Through these observations, we seek to better constrain the volcanic eruption styles that emplaced the Schrödinger deposits as well as to provide insight into the volcanic history within the basin.

## 4.3 Methods

### 4.3.1 Moon Mineralogy Mapper

The Moon Mineralogy Mapper (M<sup>3</sup>) was an imaging spectrometer supported by NASA as an instrument on the ISRO Chandrayaan-1 lunar orbiter (Green *et al.*, 2011; Pieters *et al.*, 2009). M<sup>3</sup> was launched in 2008 and operated in the visible to near-infrared (VNIR; 0.42-3.0 $\mu$ m). M<sup>3</sup> collected data during five optical periods (OP), each defined by the date of collection, orbit height, and instrument status as described in (Boardman *et al.*, 2011), (Green *et al.*, 2011), and (Isaacson *et al.*, 2013). VNIR is sensitive to absorption bands exhibited by iron-bearing minerals, including pyroxene, olivine, glass, and anorthosite (Adams, 1974; Besse *et al.*, 2013; Cloutis and Gaffey, 1991). M<sup>3</sup> has 85 spectral channels between 0.42-3.0  $\mu$ m with a higher spectral resolution between 0.7-1.6  $\mu$ m to better characterize the 1  $\mu$ m iron band. M<sup>3</sup> data calibrated to reflectance (Level 2) is available from the Planetary Data System and has nearly full coverage of the lunar surface, although the quality and resolution (75-280 m/pixel) of the data varies across the mission (Green *et al.*, 2011; Pieters *et al.*, 2009).

M<sup>3</sup> observations of Schrödinger have a resolution of 280 m/pixel in 86 spectral channels (Pieters *et al.*, 2009). Schrödinger M<sup>3</sup> data were obtained in optical period 2C with an orbital height

of 200 km at high sun angles, with a warmer instrument temperature, high signal levels, and a lower resolution of 280m/pixel relative to other optical periods (Isaacson et al., 2013). Because of these less ideal observation conditions, spectra extracted from M<sup>3</sup> images in Schrödinger tend to exhibit significant noise.

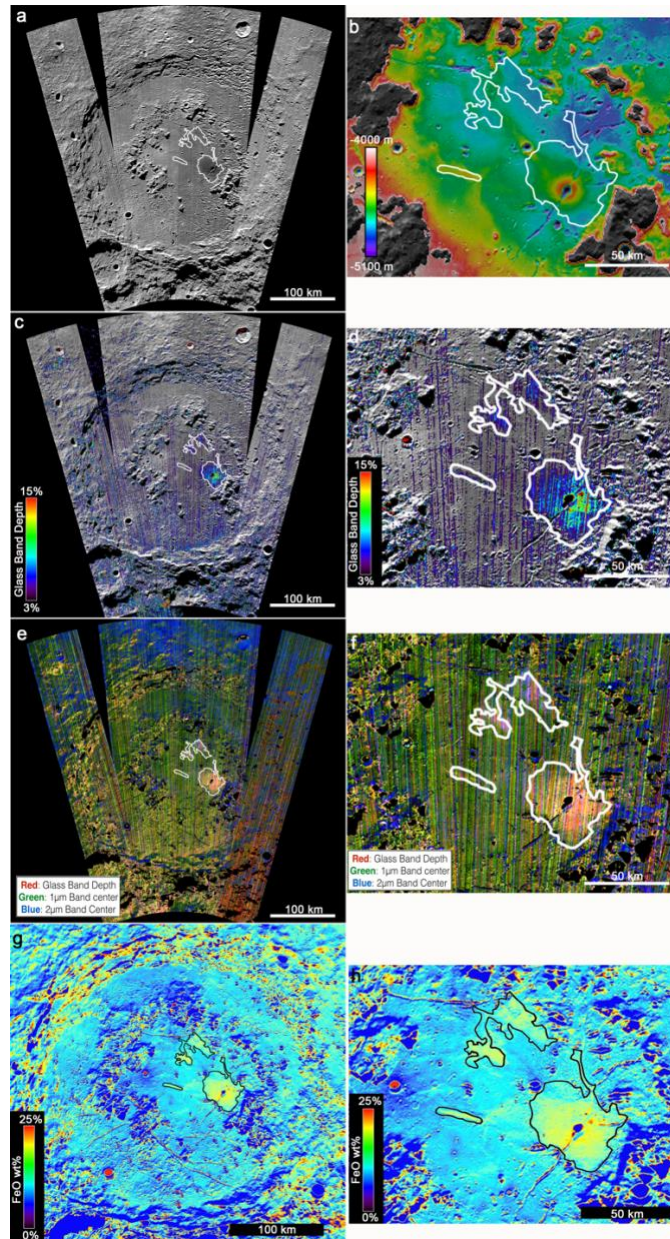


Figure 4-3.  $M^3$  maps covering the entirety of Schrödinger Basin and enlarged to focus on the volcanic units within the inner- peak ring, compared to Clementine-derived geochemistry. (a)  $M^3$  albedo map derived from reflectance at 2976 nm. (b) LOLA elevation data overlain on LROC WAC mosaic. LOLA elevation data overlain on LROC WAC mosaic (c-d) Glass band depth parameter map overlaid on LROC WAC Mosaic of Schrödinger Basin. Warmer colors in parameter maps represent locations where the spectra are most likely to represent glass. (e-f) Mosaicked composite RGB spectral maps from  $M^3$  data where R= glass band depth parameter, G=1  $\mu\text{m}$  band center parameter, B= 2  $\mu\text{m}$  band center parameter. Green colors indicated OPX on the basin floor, blue indicates CPX, and yellow/pink indicates possible glass, mixtures with glass, or olivine. (g-h) Clementine UVVIS/FeO abundance data where warmer colors represent locations with higher FeO wt%. White/black outlines show mapped extent of possible volcanic units as labeled in Figure 4-2b.

An M<sup>3</sup> mosaic of the basin was constructed with bounds 110-155°E and 82-67°N in an orthographic projection with six spectral images (Figure 4-3), using the methods described in (Horgan et al., 2014), (Bennett et al., 2016) and (Chapter 3). During mapping, each M<sup>3</sup> cube is initially cropped to fit within the bounds of the desired map. Next, the backplanes and reflectance data for the cube are projected into the map using a cylindrical projection and IDL built-in mapping routines. Where multiple cubes cover a map pixel, the cube with the highest overall quality is chosen based on visual inspection (e.g., least noise, least column-to-column variation). Once the complete reflectance mosaic is constructed, the continuum is calculated for each spectrum individually (e.g., Clark & Roush, 1984). The continuum of a spectrum is the baseline on which mineral absorptions are superimposed and is influenced by the internal mechanics of the instrument, as well as space weathering and thermal effects (Hapke, 2001; Isaacson et al., 2013).

The continuum of each spectrum in the mosaic is determined using a linear convex hull with two segments fit to endpoints near 0.70, 1.55, and 2.60  $\mu\text{m}$ . A rough estimate of the continuum is calculated for each spectrum using these endpoints; then, these endpoints are fine-tuned for each spectrum by identifying the local maxima between 0.65–1.00, 1.35–1.60, and 2.00– 2.60  $\mu\text{m}$  in this initial continuum removed spectrum. With all the calculated new endpoints, the final continuum of two combined linear segments is calculated from the original spectrum. This function is then divided out of the reflectance spectrum to produce continuum-removed spectra. To prevent possible errors due to thermal contributions, the continuum fit is limited to <2.6  $\mu\text{m}$ , and caution was exercised when analyzing data at these longer wavelengths. All spectral plots show continuum removed spectra over plotted with smoothed versions of these spectra, in which spectral noise was reduced using a median filter and a boxcar smoothing algorithm, both with widths of 5 channels.

### **4.3.2 Spectral Parameters and Mineral Identification**

Spectral diversity maps of Schrödinger basin were created by parameterizing the shape, position, and depth of the 1- and 2- $\mu\text{m}$  absorption bands in the M<sup>3</sup> mosaic. In this study, spectral variability was assessed using two types of spectral parameters: (1) spectral indices using simple arithmetic and (2) 1 and 2  $\mu\text{m}$  band position, area, and shape parameters derived from our continuum removed mosaic. The spectral indices BDOPX, BDCPX, and BDGLA are defined in

Chapter 3 (Table 3-1) and applied to smoothed reflectance spectra. Spectral indices can suggest the presence of OPX (based on enhanced absorption between 0.88-0.92  $\mu\text{m}$ ), CPX (based on enhanced absorption between 2.40-2.50  $\mu\text{m}$ ), and iron-bearing glass (based on enhanced absorption between 1.15-1.20  $\mu\text{m}$ ), respectively, as shown in laboratory spectra (Figure 3-3). These spectral indices do not equate to quantitative information on the abundance of a mineral but rather provide information on whether or not the spectral characteristics of a given spectrum could be consistent with the presence of that mineral. Additionally, the presence of other spectrally similar minerals can also lead to high values of these parameters. For example, the prominent 1.25-1.30  $\mu\text{m}$  shoulder in olivine can also cause high values of BDGLA. These spectral indices can also vary due to spectral contrast, or the overall depth of absorption bands in a spectrum, which is often related to factors other than the abundance of these Fe-bearing silicates (e.g., grain size, space weathering, or minor changes in the abundance of opaque minerals; Pieters et al., 2000; Scudder et al., 2021).

Once the continuum of the spectrum is removed, it is possible to conduct more detailed parameterizations of the shape and position of the 1 and 2  $\mu\text{m}$  iron absorption bands (Horgan et al., 2014). The calculated band minimum and band center parameterize the band position (Table Chapter 3-1). The band minimum is the wavelength position of the minimum reflectance value in the band. In contrast, the band center is the wavelength position of the minimum of a fourth-order polynomial (allows for the narrower band center characteristic of many pyroxenes) fit all channels within 75 nm of the band minimum, with a fit resolution of 5 nm. In smooth spectra, the band minimum and band center would be very similar, but when the spectra are not ideal (e.g., noisy spectra, and when the fit has a higher resolution than the spectrum), the band center can be a better estimation of the true center of the band than the band minimum (Horgan et al., 2014). Band shape is parameterized by band depth, band area, and band asymmetry. The band depth is defined as one minus the value of the polynomial fit at the band center, while the band area is the total area under each continuum segment calculated as one minus the value of each channel in this range multiplied by the spectral resolution at each channel. Band asymmetry is defined as the difference in the areas to the band center's left and right as a percentage of the total area (Horgan et al., 2014).

These band parameters are useful in concert with the simple spectral indices described above because they are not strongly affected by spectral contrast, such as the low spectral contrast induced by space weathering on the Moon. Also, they can be linked to specific iron-bearing

minerals and mineral mixtures (Horgan et al., 2014). OPX and CPX both exhibit two symmetric absorption bands, where OPX has bands centered near 0.90-0.94 and 1.8-2.0  $\mu\text{m}$ , and CPX has bands centered near 0.98-1.05  $\mu\text{m}$  and 2.05-2.4  $\mu\text{m}$ . Intermediate pyroxenes (e.g., pigeonite) and pyroxene mixtures fall in between these values. Olivine exhibits a broad and asymmetric 1  $\mu\text{m}$  absorption band most often centered between 1.05-1.07  $\mu\text{m}$ , which is a combination of three bands centered near 0.85, 1.05, and 1.15  $\mu\text{m}$ , and no 2  $\mu\text{m}$  band (Sunshine & Pieters, 1998; Sunshine et al., 1990). Iron-bearing glasses exhibit a wide and symmetric absorption centered between 1.07-1.18  $\mu\text{m}$ , and in some cases, an additional absorption centered between 1.90-2.05  $\mu\text{m}$  (e.g., Cannon et al., 2017) therefore overlapping with the 1  $\mu\text{m}$  band center of olivine and CPX. While the lack of a 2  $\mu\text{m}$  band and increased 1  $\mu\text{m}$  asymmetry can often distinguish olivine from these other ferrous minerals, mixtures of glass and pyroxene can produce olivine-like spectral properties (Horgan and Bell, 2012; Horgan et al., 2014). Because of this ambiguity, careful spectral analysis is needed to make interpretations of iron-bearing mineralogy. Thus, following the creation of our spectral indices and parameter maps, average continuum removed spectra were extracted from representative regions of interest (ROIs) for the localities of the cone as well as the mafic and ridge units in Schrödinger Basin.

### **4.3.3 Clementine**

Clementine was launched to the Moon on January 25, 1994, as a joint project between the Dept of Defense and NASA. The Clementine Ultraviolet Visible (UVVIS) multispectral instrument (S. Nozette et al., 1994) provided the first spectral analysis of Schrödinger basin (Shoemaker et al., 1994). For this study, the spectral data derived from M<sup>3</sup> was compared to the Clementine-derived iron abundance (as weight percent iron oxide, FeO). The Clementine iron abundance map provides a qualitative value that can be useful for comparisons of relative values. The data has a spatial resolution of 200 meters per pixel. This FeO map (Figure 4-3g,f) was accessed through JMars and is derived from Clementine Ultraviolet/Visible camera (UVVIS) data as described by Lawrence et al. (2002), with FeO weight percent ranges from 0 to ~25% in this map (Lawrence et al., 2002; Lucey et al., 1998, 2000).

#### 4.4 Results and Spectral Interpretations

The volcanic deposits are spectrally distinct units within Schrödinger. Morphologically, the volcanic units have been mapped through precise boundaries and surface expressions (Kramer et al., 2013; Mest & Arsdall, 2008; Shoemaker et al., 1994). A lower albedo is observed in the M<sup>3</sup> 2.8  $\mu\text{m}$  reflectance (Figures 4-3a) of the volcanic units compared to the surrounding inner peak-ring floor. RGB composite images highlighting the spectral diversity are shown in (Figures 4-3e,f), where red is the glass band depth (BDGLA), green is the 1 $\mu\text{m}$  band center, and blue is the 2 $\mu\text{m}$  band center which highlights the mineralogical diversity of the Schrödinger units. Green in this combination indicates OPX, blue indicates CPX, yellow indicates glass or olivine, and pink indicates mixtures of pyroxene with glass or olivine. The subtle horizontal striping across the higher resolution M<sup>3</sup> frames in (Figures 4-3,4-4) maps is due to slight resolution and detector sensitivity changes. Analysis of these data reveals that the volcanic terrains of the pyroclastic cone and the inner-peak ring pyroclastic deposits are spectrally distinct from impact features as well as the inner-peak ring floor.

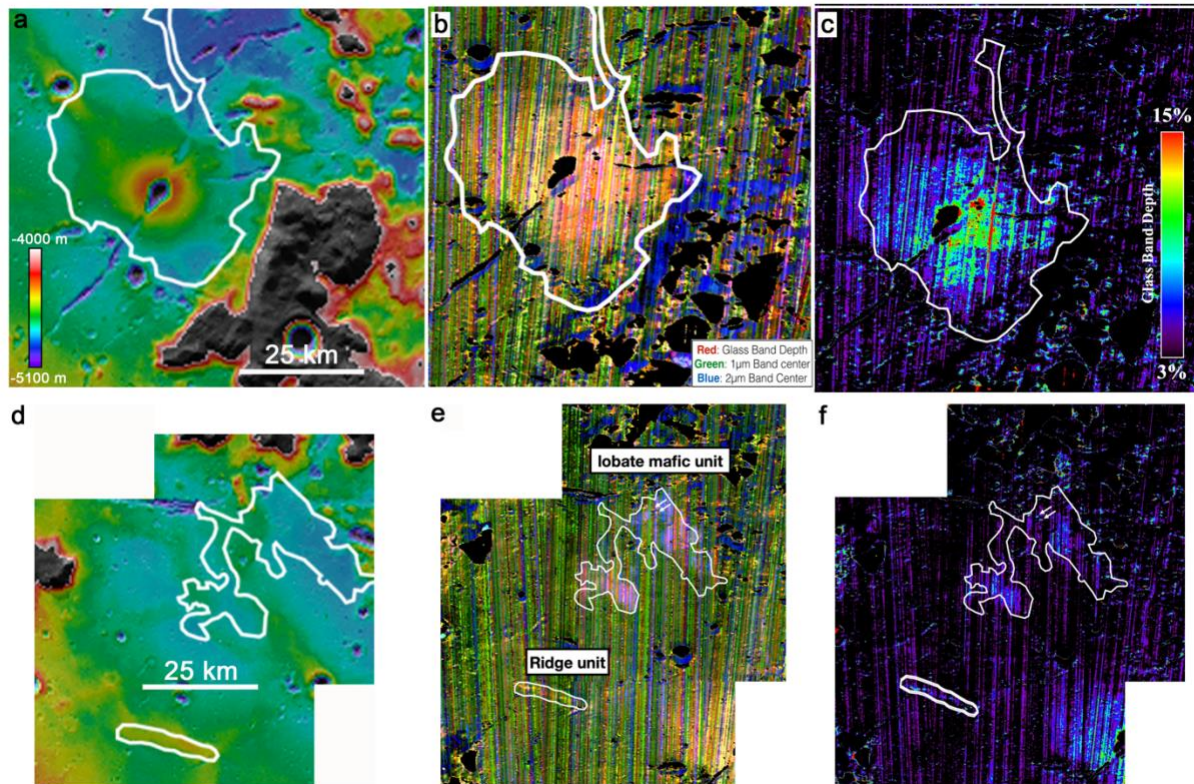


Figure 4-4. Subset of Schrödinger volcanic units within the inner-peak ring (a-c) focus on the pyroclastic cone (d-f) are focused on the lobate mafic and ridge units. (a,d) LOLA elevation data overlain on LROC WAC mosaic. (b,e) Mosaicked composite RGB spectral maps from M<sup>3</sup> data where R= glass band depth parameter, G=1 µm band center parameter, B= 2 µm band center parameter. (c,f) Glass band depth parameter map overlaid on LROC WAC Mosaic. Warmer colors in parameter maps represent locations where the spectra are most likely to be representative of glass. Arrows point to locations of potential volcanic cones.

#### 4.4.1 Inner-peak ring and basin floor

Spectral mapping of the basin floor (Figure 4-3e,f) reveals a consistent spectral signature that is not affected by the texture of the geologic units identified through Clementine observations (Shoemaker et al., 1994). Spectra collected from the inner-peak ring basin floor exhibit bands centered near 0.97-0.99 and 1.70-1.80 µm (Figure 4-5) consistent with orthopyroxene (OPX). OPX is common throughout the SPA and is interpreted to be upper mantle material excavated by the SPA impact (Melosh et al., 2017). The only locations with a strong glass band parameter identified in the inner-peak ring floor were within impact craters, interpreted as impact melt glass (Neish et

al., 2021). Possible glass signatures are also present in the peak ring, but this may instead be due to olivine, which has been identified in the area (Kramer et al., 2013).

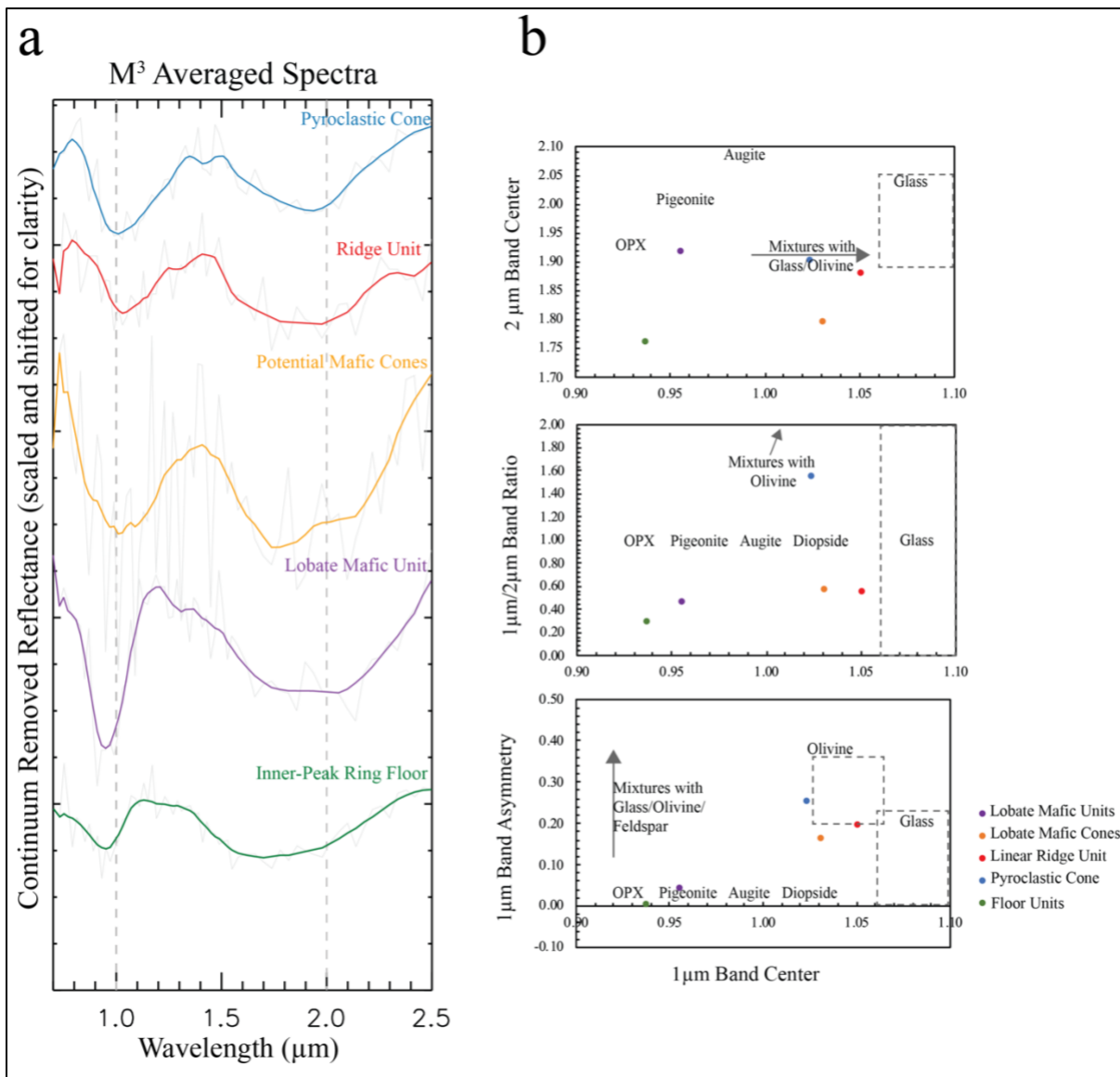


Figure 4-5. (a) Selected M<sup>3</sup> continuum-removed and smoothed spectra from Schrödinger volcanic units that have been averaged to reduce noise. Spectra show differences between the pyroclastic cone (blue), ridge unit (red), potential cones in the lobate mafic unit (orange), lobate mafic unit (purple), and the inner-peak ring floor (green). Dotted lines indicate 1 $\mu\text{m}$  and 2 $\mu\text{m}$  wavelength positions for comparison between the spectra. Gray background spectra are continuum removed and unsmoothed. (b) Spectral band parameter graphs of the Schrödinger volcanic units. Labels indicate the approximate parameters and trends expected based on laboratory spectra of endmembers and mixtures analyzed by (Horgan et al., 2014) and (Klima et al., 2007).

#### 4.4.2 Schrödinger Cone

The large Schrödinger cone has a distinct spectral signature compared to other units in the basin. From the vent and down beyond the cone's flanks and onto the apron (outlined in Figure 4-2b), the cone has a glassy spectral signature as shown by the yellow color in (Figures 4-3e,f,4-4b). The 'yellow' glassy material does become more diffuse before transitioning to spectra dominated by the OPX inner-peak ring basin floor signatures. The glass parameter map (Figure 4-3c) shows the highest density of possible glass signatures to the SE of the vent. Impact ejecta resulting from the fresh craters in the inner-peak ring floor could account for the diffusion of glass-rich spectral signature NW of the vent.  $M^3$  spectra of the Schrödinger volcanic cone are consistent with a clinopyroxene and glass mixture, supporting an explosive origin. The conical edifice in Schrödinger basin has bands centered near 0.98-1.10 and 1.85-2.00  $\mu\text{m}$ , and strong shoulders to long wavelengths on the 1  $\mu\text{m}$  band, consistent with a mixture of glass and pyroxene (Cloutis & Gaffey, 1991; Horgan et al., 2014). Olivine is unlikely to be a major contributor to these spectra based the band center positions, the presence of the 2 $\mu\text{m}$  band, and the 1 $\mu\text{m}$  band asymmetry. The detection of glass spectral signatures in the cone suggests that it is comprised of glass-rich volcanic materials, as laboratory measurements have shown that that glass is only confidently detected in VNIR spectra when present in mixtures with crystalline minerals at abundances higher than 70–80 wt.% (Horgan et al., 2014; Henderson et al., 2020).

#### 4.4.3 Lobate Mafic Unit

The inner-peak ring basin lobate mafic unit was previously hypothesized to be mare-like deposits based on the presence of flow-like morphologies and the raised FeO abundance (Shoemaker et al., 1994), or an explosive deposit too thin to extract a conclusive spectrum (Kramer et al., 2013). Our  $M^3$  analysis reveals that the unit is spectrally distinct from the inner-peak ring floor material. With spectral mapping (Figures 4-3e,f and 4-4e), the lobate mafic unit mostly presents as magenta in color, in contrast to the yellow shown in the glassy cone and green in the OPX-dominated floor. The magenta color would suggest a mixture of glass and CPX and this interpretation is confirmed by individual spectra, as seen in Figure 4-5. Most of the inner peak-ring lobate mafic unit exhibits bands near 0.95-1.05  $\mu\text{m}$  and 1.8-2.0  $\mu\text{m}$ , and the 1  $\mu\text{m}$  band is narrow without any additional absorption at long wavelengths that could be attributed to olivine

or glass. The overall upward shift in the 1 and 2  $\mu\text{m}$  band centers can be attributed to the increased influence of clinopyroxene (CPX) relative to the basin floor.

Integrating the spectral map and the visual imagery from LROC with the morphology of the lobate mafic unit leads to the first possible identification of small secondary vents or cones in Schrödinger (Figures 4-2c,4-4e,f). The two C-shaped topographic rises resembling breached cones have diameters of 1.5 and 3.0 km (Figure 4-2c), are consistent with locations of enhanced possible glass signatures in the glass parameter map (Figure 4-4f), and show up as yellow in the RGB combination map (Figure 4-4e). Spectra of the cones are difficult to extract due to their small size, but an average spectrum taken from both cones together shows band centers near 1.03-1.05  $\mu\text{m}$  and 1.80-1.90  $\mu\text{m}$ , with a broad 1  $\mu\text{m}$  band that may be consistent with glass (Figure 4-5). Based on their cone-shaped morphology, possible glass signatures, and association with the lobate margin volcanic unit, we hypothesize that these edifices are remnants of cinder cones.

#### **4.4.4 Linear Ridge Unit**

The linear ridge unit is a thin lenticular unit that is isolated within the inner-peak ring basin (Figure 4-2b). While the ridge unit is spectrally distinct from the floor in Clementine FeO abundance models (Figures 4-3g,h), it has an FeO abundance similar to the mafic and cone units, suggesting that it is related to the volcanic units in the basin. Spectral mapping of the inner-peak ring basin showed that the ridge unit exhibits a similar yellow color to the cone in our RGB composite map (Figure 4-4e), suggesting a similar composition. Within the glass band parameter map (Figure 4-4f), a line of potentially glass-dominated spectra corresponds with the location of the topographically raised ridge. The distinct linear ridge on the floor exhibit bands centered near 0.97  $\mu\text{m}$  and 1.9-2.0  $\mu\text{m}$  (Figure 4-5), attributed to the influence of clinopyroxene (CPX). The 1  $\mu\text{m}$  band is wider than expected for CPX alone and exhibits additional absorption at long wavelengths, suggesting a limited contribution from glass. Spectral from the linear ridge unit are similar in shape, but less pronounced, than spectra from the large cone.

## 4.5 Discussion

### 4.5.1 Origin of the Schrödinger Cone and implications for SPA volcanism

The Schrödinger cone has spectral signatures consistent with a mixture of pyroxene and significant glass, indicating an explosive emplacement, and consistent with previous studies (Gaddis et al., 2003; Kramer et al., 2011). The spectral differences in the west and east side of the volcanic vent (Figure 4-4b) can potentially be attributed to the covering of the volcanic deposits by ejecta from more recent impacts.

The Schrödinger cone is the largest conical edifice identified to date on the lunar surface. There are other large domes and shield volcanoes on the Moon, but the slope and spectral signatures consistent with a significant glass component support the interpretation of a volcanic cone. Shoemaker *et al.*, 1994 interpreted the cone as a large maar-type volcano (Shoemaker et al., 1994). However, a maar-type volcano would require significant groundwater interaction with the magma, which seems unlikely in the lunar environment (Mest, 2011). Strombolian eruptions have been hypothesized as the source for the largest lunar pyroclastic deposits (LPDs), including Schrödinger (Gaddis et al., 2003; Wilson & Head, 1981). However, spectral interpretations of multiple LPDs have shown that size is not a sufficient basis for determining eruption styles, as explosive eruptions on the Moon are significantly more complex than previously assumed. As described in Bennett et al. (2016) for similar spectral signatures in large Oppenheimer pyroclastic deposits, the spectral interpretation of significant glass with minor CPX on the cone could indicate that Schrödinger could have been built by a Vulcanian eruption followed by a continuous fire fountaining eruption, a sustained Strombolian/fire fountaining eruption, or some combination of the two. In all cases, the cone could have built up through multiple early, explosive volcanic episodes.

A Vulcanian eruption style would be caused by a low ascent rate, likely due to low volatile content, which results in buildup of magma under the crater floor (Jozwiak et al., 2012). An initial Vulcanian eruption would clear the plug in the conduit and would produce an initial layer that includes blocky country-rock deposits (Bennett et al., 2016). In the Schrödinger basin, the inner mare floor (OPX-dominated in VNIR spectra) is thought to be the most-likely composition of the country-rock that Vulcanian eruptions would incorporate, and CPX and glass would be considered

juvenile magmatic material. Alphonsus crater has a similar floor composition and several pyroclastic deposits, and in that case rings of OPX-bearing materials are observed on the margins of the glass-rich pyroclastic deposits, supporting a Vulcanian eruption style (Gaddis et al., 2016). Similar patterns are not observed around the Schrödinger cone. However, the presence of a volcanic plug could be entirely obscured by the continuous eruption of juvenile magmatic material, so a Vulcanian eruption style cannot be entirely ruled out.

In a Strombolian/fire-fountaining eruption, higher ascent rates and thus higher volatile content result in a more direct emergence of magma, likely through a fracture or graben in the crater floor. The presence of the cone along the large radial graben in Schrödinger does support the hypothesis that the Schrödinger cone originated from a Strombolian or fire-fountaining eruption, driven by high magma ascent rates. However, an initially slow explosive eruption that evolved into a more continuous fire-fountain with intermittent effusion of magma cannot be ruled out based on these data. In any case, the earlier simple model of emplacement (Gaddis et al., 2003) does not seem to apply at Schrodinger.

#### **4.5.2 Inner-Peak Ring Lobate Mafic Unit**

The lobate mafic unit within the peak ring is spectrally distinct from the other volcanic units in the Schrödinger basin. The lobate mafic unit has been identified as a location of interest for exploration within Schrödinger (Kring & Robinson, 2018; O’Sullivan et al., 2011). The spectral signature of the unit indicates a CPX-dominated composition for the majority of the unit. Previously, the lobate mafic unit was considered a mare unit that has erupted effusively instead of explosively (Shoemaker et al., 1994; Shanker et al., 2012; Kramer et al., 2013). However, we have also identified possible glass signatures on the flow associated with small edifices that appear to be small cinder cones. We hypothesize that the unit first erupted explosively, building an edifice similar to a terrestrial cinder cone, and then erupted the flow component to create the lobate morphology of the margins. The flow may have been emplaced through one of two possible mechanisms. 1. Similar to terrestrial cinder cones, as the magma becomes degassed transitioning the explosive eruption to an effusive eruption creating smooth lava flows. 2. There was only an explosive eruption, and the large molten pyroclasts or blebs coalesced and did continue to flow and slowly cool (Bennett et al., 2016) . This slow cooling may have been facilitated by an optically

thick eruption column (Head & Wilson, 1989) that created a temporary ‘atmosphere’, which would have given the emplaced crystalline juvenile material (e.g., CPX) the time to slowly crystallize instead of immediately quenching as glass. To differentiate between the hypotheses, we can incorporate radar of the lobate mafic unit from Mini-RF (Nozette et. al., 2010). The radar response is more consistent with a unit with a rougher texture than typical lunar mare (Campbell et al., 1997; Shankar et al., 2012). Therefore, the roughness observation corroborates the hypothesis that the large blebs/pyroclasts coalesced and continued to slowly flow before they crystallized, versus a transition to a smooth effusive flow.

The cones within the Marius Hills Volcanic Complex (MHVC; 13.3°N, 47.5°W) can be compared to the cones in the lobate mafic unit. The MHVC is a 35,000 km<sup>2</sup> plateau raised 100-200 m above Oceanus Procellarum with a wide assortment and unusual concentration of volcanic features (McCauley, 1967; Stark & Head, 1980) including volcanic domes/shields, lava flows, sinuous rilles, and volcanic cones. Small glass-rich cones of similar sizes have been identified in the Marius Hills Volcanic Complex (Lawrence et al., 2013) (Chapter 3). The yellow glass-rich spectral signature (Figure 4-4e) and glass parameter response (Figure 4-4f) along with the shape of the potential cones in the lobate mafic unit match the cone morphology and spectral response consistent with cones identified in Marius Hills (Figures 3-5, 3-8, 3-10). In the MHVC, the cones would erupt explosively, and in some cases, transition to an effusive eruption. However, the resulting flows from the small cones were not spectrally distinct as they are within the Schrödinger mafic lobate unit. The flows from the cones in Marius Hills also did not have a CPX spectral signature. Comparing the similar sized volcanic edifices and their resulting pyroclasts between MHVC and Schrödinger reinforces the hypothesis that the lobate mafic units are composed of material that erupted from a glass-rich cone and then coalesced to flow and cool slowly, allowing the CPX juvenile component to crystallize.

### **4.5.3 Linear Ridge Unit**

The ridge unit is a small lenticular unit within the inner-peak ring with a length of about 22 km long and a width ranging from ~1.5 km to 4.5 km. LOLA topography (Figure 4-3b) shows that the unit rises about 115-200m above the inner-peak ring floor. The unit appears to have an asymmetry where the one side has a sharper, more distinct margin, while the other has a more

gradual descent into the inner-peak ring floor. Raised topography of the unit has disproved the hypothesis that the unit was potentially a buckled impact melt sheet (Shoemaker et al., 1994), and subsequent hypotheses have included a magma intrusion (Shoemaker et al., 1994) or a blind thrust fault or wrinkle ridge (Kramer et al., 2013).

The ridge unit is spectrally distinct from the inner-peak ring floor material as seen in the albedo (Figure 4-3a) and the Clementine FeO abundance map (Figure 4-3h) but also shows similarities in FeO wt% to the other volcanic units in Schrödinger. These properties alone strongly support a volcanic, rather than tectonic, origin. Spectral mapping observations revealed increased detection of potential glass within the color composite and glass parameter maps (Figures 4-4e,f). Further investigation with  $M^3$  spectra revealed that the spectra collected from the linear ridge exhibit wide bands shifted to near 0.97  $\mu\text{m}$  and 1.9-2.0  $\mu\text{m}$  (Figure 4-5), attributed to the increased influence of clinopyroxene (CPX) and with a potentially with a limited contribution from glass relative to the basin floor. This detection corroborates the volcanic origin hypothesis because CPX and glass both likely represent juvenile magmatic material, similar to the lobate mafic unit. The presence of juvenile magmatic material with the location separated from the radial fractures lead us to believe that this was a magmatic intrusion erupted through a fissure that created a thin layer of erupted material that cooled quickly overlaying the inner-peak ring floor.

#### **4.5.4 Relationship between volcanic units in Schrödinger**

The spectral observations using  $M^3$  data in this study were compared to the Clementine-derived iron abundance (as weight percent iron oxide FeO). The Clementine iron abundance map (Figures 4-3g,h) has a spatial resolution of 200 meters per pixel and the FeO weight percent ranges from 0 to ~25% in this map (Lawrence et al., 2002; Lucey et al., 1998, 2000). The FeO abundance map shows significant correlations with our  $M^3$  parameter maps. The  $M^3$  maps show highlight subtle differences in mineralogy (Figure 4-3f) while the Clementine FeO abundance map (Figure 4-3h) shows similar compositions for the cone, linear ridge, and lobate mafic units. Similar iron abundances support volcanic origins for these units versus impact or tectonic origins. The similarity in the iron-abundance signature could also be indicator that a similar magma source could have possibly fed these eruptions and that other factors including conduit geometry and crustal properties could have caused the differences in crystallinity and edifice/deposit

morphology. Thus, more explosive eruptions could create the very glass-rich deposits that form the cone, whereas more crystalline juvenile minerals like CPX in the lobate margin and ridge units could have resulted from less explosive eruptions where the extruded magma was able to cool more slowly and potentially flow. Further investigation of Schrödinger with Diviner (Paige et al., 2009) could further illuminate the differences between the deposits and other features within Schrödinger with respect to iron content.

Previously, there were multiple hypotheses for how the smaller volcanic units are connected to the large conical pyroclastic deposit (Henderson et al., 2020). 1. A single volcanic vent may have produced a large explosive volcanic edifice before transitioning to effusive flows that were later segmented by impacts. 2. Alternatively, Schrödinger deposits could result from multiple volcanic vents, similar to the multiple volcanic pyroclastic deposits ranging in crystallinity observed in Oppenheimer crater, located farther north within the SPA basin (Bennett et al., 2016). Identifying cones as the source of the lobate mafic unit and the glass-rich ridge unit interpreted as a fissure eruption would eliminate the single vent hypothesis and provide evidence for the multiple vent hypothesis.

#### **4.5.5 Constraints on eruption properties from comparison to other pyroclastic deposits**

Oppenheimer crater is a floor-fractured crater also located within the South Pole–Aitken basin (35°S, 166°W) exhibiting more than a dozen localized pyroclastic deposits associated with the fractures (Bennett et al., 2016). While the largest deposit in Oppenheimer is comparable in size to the large deposit in Schrödinger, it is flat compared to the 415 m conical edifice in Schrödinger. This could be consistent with the eruption of a similar volume of magma from one vent compared to seven. The inner mafic deposits of Schrödinger have spectral properties compatible with CPX mixed with glass, similar to some Oppenheimer floor deposits (Bennett et al., 2016). These Oppenheimer LPDs have been hypothesized to have formed during a fire fountaining or Strombolian event where large blebs of molten magma accumulated near the vent and formed a lava flow and crystallized (Bennett et al., 2016). Combining the spectral analysis of Oppenheimer and Schrödinger suggests that complex volcanic eruption styles may be typical among SPA pyroclastic deposits.

We hypothesize that high magma ascent rates are plausible in Oppenheimer and Schrödinger based on their location within SPA. Within SPA, the crust is thinner, about 20 km as opposed to 30-50 km thick typical lunar crust (Wieczorek et al., 2013); therefore, the magma could more easily reach the lunar surface. This would allow magmas from deeper source depths with possibly higher volatile content to reach the surface, resulting in more explosive eruptions as well as increased resource potential. This is consistent with the apparent high ascent rate inferred for even small LPD's in Oppenheimer (Bennett et al., 2016).

Many large LPDs are flat and relatively thin draping deposits that do not exhibit the significant positive relief edifice seen in the Schrödinger cone. Even in Oppenheimer, the volcanic deposits are characterized by a large number of small to large low relief LPD's, rather than the single large cone in Schrödinger. Potential factors that could have influenced the building of a cone include extrinsic factors like crustal properties, which could influence the magma plumbing system below Schrödinger, and vent geometries, which could restrict pyroclast distribution. It is also possible the cone was constructed because there was a much larger available magma volume than other LPDs (an intrinsic magma property). This suggests that some other LPDs would have grown into cones if they had the same magma reserves. However, eruption styles and edifice morphologies are the result of both extrinsic and intrinsic factors, so the presence of the cone could be the result of complex coupling between any of these factors within Schrödinger (Cassidy et al., 2018).

#### **4.5.6 Proposed Exploration**

Schrödinger is a target for future human or robotic exploration as its diverse lithologies would help address various high-priority lunar science goals (Jawin et al., 2019; Kring & Robinson, 2018; O'Sullivan et al., 2011). This study has shown that Schrödinger contains a variety of volcanic deposits that may share a magma source, but exhibit different crystallinities and morphologies, likely due to both local geologic context and temporal or spatial variations in volatile content. Investigating and sampling these features together would provide valuable insight into the role of eruption mechanics and volatile content on the resulting properties of volcanic deposits helping constrain the properties of their source reservoir.

These diverse volcanic deposits are located near the Pre-Schrödinger crust uplifted peak ring (Potts et al., 2014). The proximity of these deposits can answer questions about the history of volcanic and impact processes in a singular mission, which would fulfill goals outlined in the Decadal Survey (National Research Council, 2011). Missions to Schrödinger would meet multiple priorities for exploration of the Moon. They would address key lunar science questions outlined in the 2007 National Research Council (NRC) Scientific Context for the Exploration of the Moon (SCEM; National Research Council, 2007) the 2017 LEAG Specific Action Team Report Advancing Science of the Moon (ASM-SAT; LEAG, 2017), and Vision and Voyages for Planetary Science in the Decade 2013–2022 (National Research Council, 2011). Schrödinger has been selected as a landing site for two payload suites delivered in tandem by the Commercial Lunar Payload Services Contract (CLPS) in 2024 (NASA, 2020).

As described in the 2013-2022 Decadal Survey, an investigation of Schrödinger could: 1. Constrain the bulk composition of terrestrial planets by analyzing the diversity of lithologies present in the basin, including the peak ring and volcanic units. 2. Characterize planetary interiors to determine how they differentiate and evolve by studying the volcanic mafic, ridge, and cone formed from partial melts of the lunar interior. 3. Characterize planetary surfaces to understand how they are modified by geologic processes (i.e., volcanism and impacts). 4. Understand the composition and distribution of volatile chemical compounds in the volcanic deposits (National Research Council, 2011; Jawin et al., 2019).

#### **4.6 Conclusion**

We completed the first hyperspectral mapping of the Schrödinger inner basin with Moon Mineralogy Mapper data. We identify three distinct volcanic units within the inner-peak ring basin -- the large cone, the lobate mafic unit, and the ridge unit -- all of which are spectrally distinct from the inner-peak ring floor and have similar FeO abundances, potentially indicating a single magmatic source. Glass signatures in  $M^3$  spectra support a pyroclastic origin of the cone. We hypothesize that the Schrödinger cone originated from a Strombolian or fire-fountaining eruption, which may be related to its location along the large radial graben within the central basin. Smaller cones with potentially glassy spectral signatures have been identified within the lobate mafic units, suggesting an initial explosive pyroclastic eruption that later transitioned to an effusive component

where coalesced pyroclasts flowed to create the lobed flow margins and a rough flow surface in radar images. The linear ridge unit exhibits spectra consistent with CPX and possible glass, which is unlike the basin floor but similar to the lobate mafic unit, thus confirming a volcanic origin over a tectonic feature.

Comparing the diversity of pyroclastic deposits in Schrödinger to LPDs in Oppenheimer, also located within SPA, suggests that high magma ascent rates resulting in complex volcanic eruption styles over a range of deposit sizes may be typical among SPA pyroclastic deposits. Therefore, the geologic context of SPA, in particular the thin crust in the SPA basin, may be a large contributor to the explosiveness of eruptions in the south pole.

Schrödinger basin and the lunar south pole are sites of interest for crewed and robotic exploration (Jawin et al., 2019; Kring & Robinson, 2018; O’Sullivan et al., 2011; Artemis III SDT, 2020) the location has been selected for a CLPS landing site in 2024. The work presented in this study will provide context for instruments observation and potentially future traverse planning. Ultimately, Schrödinger is another endmember in the diverse suite of explosive volcanic eruption styles that have been observed on the Moon and more research is required to understand the extent and range of lunar explosive volcanism.

#### **4.7 Acknowledgments**

We would like to thank David Mayer from the USGS Astrogeology Science Center for invaluable help with assisting with the integration challenges presented by an orthographic projection. This material is based upon work supported by the National Science Foundation Graduate Research Fellowship Program under Grant No. (DGE-1333468) and was completed in partnership with the U.S. Geological Survey Astrogeology Science Center through an NSF Graduate Research Internship Program (GRIP). Any opinions, findings, and conclusions or recommendations expressed in this material are those of the author(s) and do not necessarily reflect the views of the National Science Foundation. This work was also supported in part by the NASA Lunar Data Analysis Program, grant number NNX17AC63G.

## 4.8 References

- Allen, C. C., Morris, R. V., & McKay, D. S. (1996). Oxygen extraction from lunar soils and pyroclastic glass. *Journal of Geophysical Research: Planets*, *101*(E11), 26085–26095. <https://doi.org/10.1029/96je02726>
- Artemis III Science Definition Team, (2020). *Artemis III Science Definition Team Report* (No. NASA/SP-20205009602).
- Bennett, K. A., Horgan, B. H. N., Gaddis, L. R., Greenhagen, B. T., Allen, C. C., Hayne, P. O., et al. (2016). Complex explosive volcanic activity on the Moon within Oppenheimer crater. *Icarus*, *273*, 296–314. <https://doi.org/10.1016/j.Icarus.2016.02.007>
- Bethell, I. G., & Zuber, M. T. (2005). An indigenous origin for the South Pole Aitken basin thorium anomaly. *Geophysical Research Letters*, *32*(13), 2347. <https://doi.org/10.1029/2005gl023142>
- Boardman, J. W., Pieters, C. M., Green, R. O., Lundeen, S. R., Varanasi, P., Nettles, J., et al. (2011). Measuring moonlight: An overview of the spatial properties, lunar coverage, selenolocation, and related Level 1B products of the Moon Mineralogy Mapper. *Journal of Geophysical Research: Oceans*, *116*(E6), 65. <https://doi.org/10.1029/2010je003730>
- Campbell, B. A., Hawke, B. R., & Thompson, T. W. (1997). Regolith composition and structure in the lunar maria: Results of long-wavelength radar studies. *Journal of Geophysical Research: Planets*, *102*(E8), 19307–19320. <https://doi.org/10.1029/97je00858>
- Cannon, K. M., Mustard, J. F., Parman, S. W., Sklute, E. C., Dyar, M. D., & Cooper, R. F. (2017). Spectral properties of Martian and other planetary glasses and their detection in remotely sensed data. *Journal of Geophysical Research: Planets*, *122*(1), 249–268. <https://doi.org/10.1002/2016je005219>
- Cassidy, M., Manga, M., Cashman, K., & Bachmann, O. (2018). Controls on explosive-effusive volcanic eruption styles. *Nature Communications*, *9*(1), 2839. <https://doi.org/10.1038/s41467-018-05293-3>
- Clark, R. N., & Roush, T. L. (1984). Reflectance spectroscopy: Quantitative analysis techniques for remote sensing applications. *Journal of Geophysical Research: Oceans*, *89*(B7), 6329–6340. <https://doi.org/10.1029/jb089ib07p06329>
- Cloutis, E. A., & Gaffey, M. J. (1991). Spectral-compositional variations in the constituent minerals of mafic and ultramafic assemblages and remote sensing implications. *Earth, Moon, and Planets*, *53*(1), 11–53. <https://doi.org/10.1007/bf00116217>
- Duke, M.B., Gaddis, L.R., Taylor, G.J., Schmitt, H.H., 2006. Development of the Moon. *Rev Mineralogy Geochem* *60*, 597–655. <https://doi.org/10.2138/rmg.2006.60.6>

- Gaddis, Staid, M. I., Tyburczy, J. A., Hawke, B. R., & Petro, N. E. (2003). Compositional analyses of lunar pyroclastic deposits. *Icarus*, *161*(2), 262–280. [https://doi.org/10.1016/s0019-1035\(02\)00036-2](https://doi.org/10.1016/s0019-1035(02)00036-2)
- Gaddis, L R, Horgan, B., McBride, M., Bennett, K., Stopar, J., & Gustafson, J. O. (2016). Alphonsus Crater: Compositional Clues to Eruption Styles of Lunar Small Volcanoes. *Lunar and Planetary Science Conference*, *47*, 2065.
- Gaddis, Lisa R, Pieters, C. M., & Hawke, B. R. (1985). Remote sensing of lunar pyroclastic mantling deposits. *Icarus*, *61*(3), 461–489. [https://doi.org/10.1016/0019-1035\(85\)90136-8](https://doi.org/10.1016/0019-1035(85)90136-8)
- Green, R. O., Pieters, C., Mouroulis, P., Eastwood, M., Boardman, J., Glavich, T., et al. (2011). The Moon Mineralogy Mapper (M3) imaging spectrometer for lunar science: Instrument description, calibration, on-orbit measurements, science data calibration and on-orbit validation. *Journal of Geophysical Research: Planets*, *116*(E10), E00G19. <https://doi.org/10.1029/2011je003797>
- Hapke, B. (2001). Space weathering from Mercury to the asteroid belt. *Journal of Geophysical Research: Oceans*, *106*(E5), 10039–10073. <https://doi.org/10.1029/2000je001338>
- Hawke, B. R., Coombs, C. R., & Gaddis, L. R. (1989). Remote sensing and geologic studies of localized dark mantle deposits on the Moon. *Lunar Planet. Sci*, 255–268.
- Head, J. W. (1974). Lunar dark-mantle deposits-Possible clues to the distribution of early mare deposits. *Lunar and Planetary Science Conference*.
- Head, J. W., & Wilson, L. (1979). Alphonsus-type dark-halo craters: Morphology, Morphometry and eruption conditions. *Lunar and Planetary Science Conference*, *10*, 2861–2897.
- Head, J. W., & Wilson, L. (1989). Basaltic pyroclastic eruptions: Influence of gas-release patterns and volume fluxes on fountain structure, and the formation of cinder cones, spatter cones, rootless flows, lava ponds and lava flows. *Journal of Volcanology and Geothermal Research*, *37*(3–4), 261–271. [https://doi.org/10.1016/0377-0273\(89\)90083-8](https://doi.org/10.1016/0377-0273(89)90083-8)
- Henderson, M. J. B., B.Horgan, Gaddis, L., & Bennett, K. A. (2020). Spectral Diversity of Explosive Volcanic Deposits in Schrödinger Basin with Moon Mineralogy Mapper Data. In *European Lunar Symposium*.
- Horgan, B. H. N., Cloutis, E. A., Mann, P., & III, J. F. B. (2014). Near-infrared spectra of ferrous mineral mixtures and methods for their identification in planetary surface spectra. *Icarus*, *234*, 132–154. <https://doi.org/10.1016/j.Icarus.2014.02.031>
- Huang (黄俊) J., (肖智勇) Z. X., (肖龙) L. X., Horgan, B., (胡晓依) X. H., Lucey, P., et al. (2020). Diverse rock types detected in the lunar South Pole–Aitken Basin by the Chang'E-4 lunar mission. *Geology*, *48*(7), 723–727. <https://doi.org/10.1130/g47280.1>
- Isaacson, P. J., Petro, N. E., Pieters, C. M., Besse, S., Boardman, J. W., Clark, R. N., et al. (2013). Development, importance, and effect of a ground truth correction for the Moon

- Mineralogy Mapper reflectance data set. *Journal of Geophysical Research: Planets*, 118(3), 369–381. <https://doi.org/10.1002/jgre.20048>
- Jawin, E. R., Valencia, S. N., Watkins, R. N., Crowell, J. M., Neal, C. R., & Schmidt, G. (2019). Lunar Science for Landed Missions Workshop Findings Report. *Earth and Space Science*, 6(1), 2–40. <https://doi.org/10.1029/2018ea000490>
- Jolliff, B. L., Gillis, J. J., Haskin, L. A., Korotev, R. L., & Wieczorek, M. A. (2000). Major lunar crustal terranes: Surface expressions and crust-mantle origins. *Journal of Geophysical Research: Oceans*, 105(E2), 4197–4216. <https://doi.org/10.1029/1999je001103>
- Jozwiak, L. M., Head, J. W., Zuber, M. T., Smith, D. E., & Neumann, G. A. (2012). Lunar floor-fractured craters: Classification, distribution, origin and implications for magmatism and shallow crustal structure. *Journal of Geophysical Research: Planets (1991–2012)*, 117(E11), n/a-n/a. <https://doi.org/10.1029/2012je004134>
- Kramer, G. Y., Kring, D. A., Pieters, C. M., Head, J. W., Isaacson, P. J., Klima, R. L., et al. (2011). Analysis of Schrödinger Basin Using Moon Mineralogy Mapper Spectra. In *42nd Lunar and Planetary Science Conference* (p. 1545). Retrieved from <https://www.lpi.usra.edu/meetings/lpsc2011/pdf/1545.pdf>
- Kramer, G. Y., Kring, D. A., Nahm, A. L., & Pieters, C. M. (2013). Spectral and photogeologic mapping of Schrödinger Basin and implications for post-South Pole-Aitken impact deep subsurface stratigraphy. *Icarus*, 223(1), 131–148. <https://doi.org/10.1016/j.Icarus.2012.11.008>
- Kring, D. A., & Robinson, K. L. (2018). A Lunar Sample Return Strategy for the Schrödinger Basin that taps into the Volatile Cycle of the Lunar Farside. *European Lunar Symposium*. <https://doi.org/10.1098/rsta.2013.0254>
- Lawrence, D. J., Feldman, W. C., Elphic, R. C., Little, R. C., Prettyman, T. H., Maurice, S., et al. (2002). Iron abundances on the lunar surface as measured by the Lunar Prospector gamma-ray and neutron spectrometers. *Journal of Geophysical Research: Planets (1991–2012)*, 107(E12), 13-1-13–26. <https://doi.org/10.1029/2001je001530>
- Lawrence, S. J., Stopar, J. D., Hawke, B. R., Greenhagen, B. T., Cahill, J. T. S., Bandfield, J. L., et al. (2013). LRO observations of morphology and surface roughness of volcanic cones and lobate lava flows in the Marius Hills. *Journal of Geophysical Research: Planets*, 118(4), 615–634. <https://doi.org/10.1002/jgre.20060>
- LEAG, (2017). Advancing science of the Moon: Report of the Specific Action Team, held 7–8 August 2017. Houston, Texas, United States of America. Retrieved from <https://www.lpi.usra.edu/leag/reports/ASM-SAT-Report-final.pdf>
- Li, C., Liu, J., Ren, X., Zuo, W., Tan, X., Wen, W., et al. (2015). The Chang’e 3 Mission Overview. *Space Science Reviews*, 190(1–4), 85–101. <https://doi.org/10.1007/s11214-014-0134-7>

- Li, C., Liu, D., Liu, B., Ren, X., Liu, J., He, Z., et al. (2019). Chang'E-4 initial spectroscopic identification of lunar far-side mantle-derived materials. *Nature*, 1–16. <https://doi.org/10.1038/s41586-019-1189-0>
- Lucey, P. G., Blewett, D. T., & Hawke, B. R. (1998). Mapping the FeO and TiO<sub>2</sub> content of the lunar surface with multispectral imagery. *Journal of Geophysical Research: Oceans*, 103(E2), 3679–3699. <https://doi.org/10.1029/97je03019>
- Lucey, P. G., Blewett, D. T., Taylor, G. J., & Hawke, B. R. (2000). Imaging of lunar surface maturity. *Journal of Geophysical Research: Oceans*, 105(E8), 20377–20386. <https://doi.org/10.1029/1999je001110>
- McCauley, J. F. (1967). Geologic map of the Hevelius region of the moon. *IMAP*.
- Melosh, H. J., Kendall, J., Horgan, B., Johnson, B. C., Bowling, T., Lucey, P. G., & Taylor, G. J. (2017). South Pole–Aitken basin ejecta reveal the Moon's upper mantle. *Geology*, 45(12), 1063–1066. <https://doi.org/10.1130/g39375.1>
- Mest, S C, & Arsdall, L. E. van. (2008). Geologic Mapping of the Schrödinger Basin Area, Lunar South Pole. *Annual Meeting of the Lunar Exploration Analysis Group*, 1415.
- Mest, Scott C. (2011). The geology of Schrödinger basin: Insights from post–Lunar Orbiter data. In W. A. Ambrose & D. A. Williams (Eds.) (Vol. 477, pp. 95–115). Geological Society of America.
- Moriarty, D.P., Watkins, R.N., Valencia, S.N., Kendall, J.D., Evans, A.J., Dygert, N., Petro, N.E., 2021. Evidence for a Stratified Upper Mantle Preserved Within the South Pole-Aitken Basin. *J Geophys Res Planets* 126. <https://doi.org/10.1029/2020je006589>
- NASA. (2020). *Artemis Plan: NASA's Lunar Exploration Program Overview*. Retrieved from [https://www.nasa.gov/sites/default/files/atoms/files/artemis\\_plan-20200921.pdf](https://www.nasa.gov/sites/default/files/atoms/files/artemis_plan-20200921.pdf)
- National Research Council (2007). The scientific context for exploration of the Moon, [doi:https://doi.org/10.17226/11954](https://doi.org/10.17226/11954)
- National Research Council, (2011). Vision and Voyages for Planetary Science in the Decade 2013-2022. *Washington, DC: National Academy Press*. Retrieved from <http://solarsystem.nasa.gov/docs/131171.pdf>
- Neish, C. D., Cannon, K. M., Tornabene, L. L., Flemming, R. L., Zanetti, M., & Pilles, E. (2021). Spectral properties of lunar impact melt deposits from Moon Mineralogy Mapper (M3) data. *Icarus*, 114392. <https://doi.org/10.1016/j.Icarus.2021.114392>
- Nozette, S., Rustan, P., Pleasance, L. P., Horan, D. M., Regeon, P., Shoemaker, E. M., et al. (1994). The Clementine mission to the moon: Scientific overview. *Science*, 266(5192), 1835–1839.

- Nozette, Stewart, Spudis, P., Bussey, B., Jensen, R., Raney, K., Winters, H., et al. (2010). The Lunar Reconnaissance Orbiter Miniature Radio Frequency (Mini-RF) Technology Demonstration. *Space Science Reviews*, 150(1–4), 285–302. <https://doi.org/10.1007/s11214-009-9607-5>
- Ohtake, M., Matsunaga, T., Haruyama, J., Yokota, Y., Morota, T., Honda, C., et al. (2009). The global distribution of pure anorthosite on the Moon. *Nature*, 461(7261), 236. <https://doi.org/10.1038/nature08317>
- O’Sullivan, K. M., Kohout, T., Thaisen, K. G., & Kring, D. A. (2011). Calibrating several key lunar stratigraphic units representing 4 b.y. of lunar history within Schrödinger basin. In W. A. Ambrose & D. A. Williams (Eds.) (Vol. 477, pp. 117–127). Geological Society of America.
- Paige, D. A., Foote, M. C., Greenhagen, B. T., Schofield, J. T., Calcutt, S., Vasavada, A. R., et al. (2009). The Lunar Reconnaissance Orbiter Diviner Lunar Radiometer Experiment. *Space Science Reviews*, 150(1–4), 125–160. <https://doi.org/10.1007/s11214-009-9529-2>
- Pieters, McCord, T. B., Charette, M. P., & Adams, J. B. (1974). Lunar surface: Identification of the dark mantling material in the Apollo 17 soil samples. *Science*.
- Pieters, C. M., Head, J. W., Gaddis, L., Jolliff, B., & Duke, M. (2001). Rock types of South Pole-Aitken basin and extent of basaltic volcanism. *Journal of Geophysical Research: Oceans*, 106(E11), 28001–28022. [https://doi.org/10.1029/2000je001414@10.1002/\(issn\)2169-9100.newviews1](https://doi.org/10.1029/2000je001414@10.1002/(issn)2169-9100.newviews1)
- Pieters, C. M., Goswami, J. N., Clark, R. N., Annadurai, M., Boardman, J., Buratti, B., et al. (2009). Character and spatial distribution of OH/H<sub>2</sub>O on the surface of the Moon seen by M3 on Chandrayaan-1. *Science*, 326(5952), 568–572. <https://doi.org/10.1126/science.1178658>
- Pieters, C. M., Boardman, J., Buratti, B., & Chatterjee, A. (2009). The Moon mineralogy mapper (M3) on Chandrayaan-1. *Curr Sci*.
- Potts, N. J., Gullikson, A., Curran, N. M., Dhaliwal, J. K., Leader, M. K., Rege, R. N., & Kring, D. A. (2014). Mapping solar irradiance within Schrödinger Basin for future robotic sample return missions. *Lunar and Planetary ...*
- Robinson, M. S., Brylow, S. M., Tschimmel, M., Humm, D., Lawrence, S. J., Thomas, P. C., et al. (2010). Lunar Reconnaissance Orbiter Camera (LROC) Instrument Overview. *Space Science Reviews*, 150(1–4), 81–124. <https://doi.org/10.1007/s11214-010-9634-2>
- Shankar, B., Osninski, G. R., Antonenko, I., & Neish, C. D. (2012). A multispectral geological study of the Schrödinger impact basin. *Canadian Journal of Earth Sciences*. <https://doi.org/10.1139/e2012-053>
- Shoemaker, E. M., Robinson, M. S., Eliason, E. M., & 1994. (1994). The south pole region of the Moon as seen by Clementine. *Science*, 266(5192), 1851–1854.

- Stark, J. L. W., & Head, J. W. (1980). Stratigraphy of Oceanus Procellarum basalts: Sources and styles of emplacement. *Journal of Geophysical Research: Oceans*, 85(B11), 6579–6609. <https://doi.org/10.1029/jb085ib11p06579>
- Sunshine, J M, & Pieters, C. M. (1998). Determining the composition of olivine from reflectance spectroscopy. *Journal of Geophysical Research: Planets*, 103(E6). <https://doi.org/10.1002/jgre.v103.e6>
- Sunshine, Jessica M, Pieters, C. M., & Pratt, S. F. (1990). Deconvolution of mineral absorption bands: An improved approach. *Journal of Geophysical Research*, 95(B5), 6955–6966. <https://doi.org/10.1029/jb095ib05p06955>
- Weitz, C. M., Rutherford, M. J., III, J. W. H., & McKay, D. S. (1999). Ascent and eruption of a lunar high-titanium magma as inferred from the petrology of the 74001/2 drill core. *Meteoritics & Planetary Science*, 34(4), 527–540. <https://doi.org/10.1111/j.1945-5100.1999.tb01361.x>
- Wieczorek, M. A., Neumann, G. A., Nimmo, F., Kiefer, W. S., Taylor, G. J., Melosh, H. J., et al. (2013). The Crust of the Moon as Seen by GRAIL. *Science*, 339(6120), 671–675. <https://doi.org/10.1126/science.1231530>
- Wilhelms, D. E., Howard, K. A., & Wilshire, H. G. (1979). *Geologic map of the south side of the Moon*.
- Wilson, L., & III, J. H. (1981). Ascent and eruption of basaltic magma on the Earth and Moon. *Journal of Geophysical Research*, 86(B4), 2971–3001.
- Yamamoto, S., Nakamura, R., Matsunaga, T., Ogawa, Y., Ishihara, Y., Morota, T., et al. (2010). Possible mantle origin of olivine around lunar impact basins detected by SELENE. *Nature Geoscience*, 3(8), 533–536. <https://doi.org/10.1038/ngeo897>

## CHAPTER 5. CONCLUSION

### 5.1 Conclusions

In this dissertation, I aimed to further understand the composition and eruption style of explosive volcanic deposits on the terrestrial bodies of the Earth, Moon, and Mars. Explosive volcanic deposits can illuminate the composition and structure of planetary interiors, as well as volcanic and volatile histories, but are not well understood. The volatiles within erupted pyroclasts may provide in situ resources for future planetary explorers, as lunar volcanic glasses rich in FeO<sub>2</sub> could be exposed to an H<sub>2</sub> environment, creating Fe<sup>2+</sup> and H<sub>2</sub>O, which could be electrolyzed to yield oxygen. In previous in situ resource utilization (ISRU) laboratory experiments, the pyroclastic glasses produced the most oxygen out of any Apollo sample (Allen et al., 1996).

Orbital and laboratory spectroscopy was utilized in this dissertation to analyze volcanic tephtras. Spectroscopy is applicable to both terrestrial and planetary analyses, as spectrometers can be used in a laboratory or field setting and have collected data across the solar system, enabling large-scale compositional observations. In this dissertation, spectral observations have provided a window into the emplacement history of explosive and effusive volcanic deposits. By identifying glass and other iron-bearing minerals in the visible/near-infrared (VNIR) and thermal infrared (TIR) spectra of volcanic deposits, I was able to develop new techniques for using spectroscopy to infer volcanic eruption styles on Mars and constrain the history of explosive volcanism on the Moon.

In Chapter 2, Mars analog tephtra samples were used to investigate if eruption styles and the past presence of water during the eruption of possible volcanic deposits on Mars can be determined using orbital spectroscopy. VNIR reflectance and TIR emission spectra were collected of basaltic volcanic tephtras sourced from a range of eruption styles and deposit types on Earth. Our research demonstrates that TIR and VNIR data are both sufficient to detect increased glass abundances in volcanic deposits, potentially indicating volatile interactions during an eruption and that glass-poor tephtras have distinct TIR properties that can be used to infer tephtra type (e.g., ignimbrite vs. scoria). Combining VNIR and TIR orbital data for analysis based on our new laboratory spectral endmember library may allow a reevaluation of Martian volcanic and volatile histories using current and future planetary orbital and in situ spectral datasets. Using spectral observations to

constrain crystallinity directly contributes to the Mars Exploration Program's goal of understanding the history of water and habitable environments on Mars (MEPAG, 2020). The ability to detect signs of possible water-magma interactions in the geologic record would be a novel way to place constraints on the history of water at the surface (Henderson et al., 2020).

Chapters 3 and 4 focused on the composition and originating eruption style of lunar pyroclastic deposits. Lunar pyroclastic deposits and volcanic cones are expected to be the result of explosive volcanism. Our results show that explosive volcanism is primarily driven by dissolved magmatic volatiles but that the eruption style is modified by extrinsic geologic factors like crustal thickness and ascent rate. The presence of magmatic volatiles in these deposits could have implications for lunar In-Situ Resource Utilization (ISRU) (Allen et al., 1996) and could help define the scientific objectives for future surface exploration missions. Through spectral observations, multiple explosive eruption styles have been identified (Bennett et al., 2016), sometimes in close proximity (Chapters 3 and 4). This dissertation is timely as multiple sites with evidence of explosive volcanism have been proposed (Jawin et al., 2019) or chosen as landing sites for Commercial Lunar Payload Services Contract (CLPS) missions (NASA, 2020).

In Chapter 3, volcanic glass was detected for the first time in the cones of the Marius Hills Volcanic Complex. The interpretive advancements made in this investigation are a result of improved spectral resolution and analysis techniques. Moon Mineralogy Mapper (M<sup>3</sup>) spectral analysis shows that the cones in MHVC exhibit spectra consistent with glass, confirming a cinder cone origin and suggesting the presence of scoria-like glass-rich pyroclasts that should be morphologically distinct from the glass beads collected during Apollo. This research also provides evidence that spectroscopy can identify volcanic landforms when visible images and morphology fail. This is important for future exploration of volcanic terrains where visual images may not be ideal. The likely concurrent eruption of the domes and cones with the differences in the mineralogy of the resulting edifices add supporting evidence to the hypothesis that extrinsic properties (e.g., ascent rate), not changes in magma composition (e.g., amount of volatiles), led to the different volcanic morphologies. Combining the morphology and the spectral data, I hypothesize that the magma evolution of the region was long-lived and with distinct early edifice-forming and later mare-forming episodes. The long-lived volcanism recorded in multiple volcanic units within close proximity in MHVC would be ideal for future exploration and eventual sample return.

In Chapter 4, I investigated previously proposed volcanic deposits within the Schrödinger basin in an effort to understand the contribution of geologic context to lunar explosive eruptions through the creation of the first hyperspectral map of the Schrödinger basin with M<sup>3</sup>. The detection of glass-dominated M<sup>3</sup> spectra supports a pyroclastic origin of the cone originating from a Strombolian or fire-fountaining eruption. The other volcanic units present within the inner-peak ring are spectrally distinct from the inner-peak ring floor and have similar FeO abundances as the cone, potentially indicating a single magmatic source. Smaller cones with glass-dominated signatures were identified within the lobate mafic units, suggesting that these deposits may have had an explosive pyroclastic origin with a later component where coalesced pyroclasts flowed, creating the lobed flow margins. Comparing the diversity of pyroclastic deposits in Schrödinger to LPDs in Oppenheimer crater, also located within the South Pole Aitken Basin (SPA), suggest that high magma ascent rates resulting in complex volcanic eruption styles over a range of deposit sizes may be typical among SPA pyroclastic deposits. Therefore, the geologic context of SPA, in particular the thin crust in the SPA basin, may be a significant contributor to the explosiveness of eruptions in the south pole. This investigation was timely as Schrödinger basin and the lunar south pole have are sites of interest for crewed and robotic exploration (Jawin et al., 2019; Kring and Robinson, 2018; O’Sullivan et al., 2011; Artemis III SDT, 2020). The location has been selected for a CLPS landing site in 2024. The study will provide context for instruments observations and potentially future traverse planning.

Spectral analyses of multiple LPDs, including those studied in Chapters 3 and 4 (Bennett et al., 2016; Gaddis et al., 2016; Henderson et al., 2020; Henderson and Horgan, 2021; Horgan et al., 2014; McBride et al., 2016), were completed using M<sup>3</sup> VNIR spectral observations (Green et al., 2011; Pieters et al., 2009). The range of results from these investigations can act as endmembers in the pursuit to further constrain the drivers of explosivity and resulting pyroclast morphologies of lunar explosive volcanism. Table 5-1 summarizes the identified explosive volcanic endmembers with their spectral interpretation and inferred eruption styles and outlines scientific unknowns and possible sampling locations.

Table 5-1. Explosive Volcanic Endmembers that have been analyzed with M3 spectral data.

<b>Explosive Volcanic Site</b>	<b>Location</b>	<b>Morphology Description</b>	<b>Spectral Interpretation and References</b>	<b>Endmember Description &amp; Eruption Style</b>	<b>Scientific Unknowns</b>	<b>Sampling</b>
<b>Aristarchus</b>	Oceanus Procellarum	Largest LPD draping deposit on raised plateau	<b>Glass-dominated</b> [McBride et al., 2016]	Explosive due to dissolved volatiles <b>Strombolian Eruption</b>	Timing and relationship to mare Source of deposit	Multiple locations of LPD and Prinz Crater Cobrahead
<b>Marius Hills</b>	Oceanus Procellarum	Multiple cones and domes Largest concentration of lunar volcanic edifices	<b>Glass-dominated cones</b> <b>OPX-rich domes</b> [Chapter 3]	multiple types of volcanic edifices <b>Multiple eruption styles</b>	Timing and relationship to mare cause of high concentration of edifices	Cones Domes Mare
<b>Schrödinger</b>	South Pole	Isolated Conical vent on a fracture: 1250km <sup>2</sup> multiple small deposits	<b>Glass-rich cone</b> <b>CPX-dominated lobate mafic units</b> <b>Glass influenced ridge units</b> [Chapter 4]	Large cone located in the South Pole <b>Multiple eruption styles</b>	Driver of building an edifice compared to a draping deposit Influence of thinner SPA crust	Cone near vent and flank lobate mafic units ridge units
<b>Alphonsus</b>	Highlands east of Mare Nubium	Floor Fractured Crater 12 deposits smaller than 98 km <sup>2</sup>	Rich in juvenile <b>CPX and glass</b> , transitions to a ring of <b>OPX</b> country rock [Gaddis et al., 2016]	multiple small deposits <b>Vulcanian Eruption</b>	Complex nature of small lunar volcanos	systematic sampling from the vent outward
<b>Oppenheimer</b>	South Pole	Floor Fractured Crater 15 deposits ranging in size from 2-1500 km <sup>2</sup>	<b>Glass</b> and juvenile magmatic materials, no evidence of incorporated country rock [Bennett et al., 2016]	multiple small deposits <b>Strombolian Eruption</b>	Geologic context influencing eruption style cause of Fe-rich glass?	sample each of 3 categories of deposits

These orbital VNIR spectral studies of the detailed mineralogy of lunar explosive deposits suggest that the simple eruption model based on deposit size introduced in Chapter 1 may need to be revisited. Mineralogical analysis of the local deposits in Alphonsus and Oppenheimer craters (Bennett et al., 2016; Gaddis et al., 2016) revealed different spectral signatures indicating a range of crystallinities and variable incorporation of country rock (Table 5-1). The fact that the small Oppenheimer deposits are so compositionally distinct compared to the small Alphonsus deposits suggests that local pyroclastic deposit formation mechanisms are more complicated than previously indicated (Head and Wilson, 1979). Since deposit size does not seem to be correlated to eruption style, we hypothesize that geologic context (surface/subsurface geology including deposit location) and volatile magma content are the major contributors to the formation mechanisms of explosive volcanic deposits. This hypothesis is further substantiated by the spectral analyses of Aristarchus (McBride et al., 2016), Marius Hills (Chapter 3), and Schrödinger (Chapter 4). Aristarchus and Marius Hills are proximally located but exhibit very different explosive volcanic deposits: a very large draping glass-rich pyroclastic deposit vs. multiple glass-rich small edifices (cones), respectively (Henderson and Horgan, 2021; McBride et al., 2016). Schrödinger is located in the South Pole, where the crust is thinner (Wieczorek et al., 2013) and has a colossal glass-rich edifice (cone) and some smaller pyroclastic deposits (Henderson et al., 2020).

The comparisons of these sites have revealed the diversity in deposits and eruption styles that will inform future observations of LPDs. The discussion in Chapter 4 shows that comparisons to

other LPDs played a prominent role in understanding the deposits within Schrödinger basin. Therefore, continued observations of other lunar LPDs will continue to set constraints on our understanding of lunar explosive volcanism.

## **5.2 Future Investigations**

The spectral interpretations are only part of the story of explosive volcanism on the Moon. Therefore, future research aims to answer the questions: 1. What constraints does integrating additional data lunar orbital datasets with the spectral interpretations presented here place on the drivers and pyroclast properties of explosive volcanic deposits? 2. On Earth, volcanic textures can provide clues for volcanic eruption type and eruption dynamics; how would these textures translate to the lunar environment and lunar eruptions? And 3. How can combining spectral and morphological observations with the physical properties of explosive volcanic environments develop techniques and strategies for lunar exploration?

I have proposed a future study to the NASA Postdoctoral Program with the primary goal to create a framework for understanding explosive deposits on the Moon in preparation for future exploration through orbital and physical observations. The research will take a systematic approach for preparing to explore explosive volcanic sites on the Moon. First, orbital analysis from multiple instruments (M<sup>3</sup>, Diviner, LROC, LOLA, and Mini-RF) will be used to investigate the explosive volcanic endmember sites listed in Table 5-1. Second, based on the orbital mapping hypotheses, physical geology hypotheses will be made to predict the pyroclast types and textures that could be identified by crewed or robotic exploration. Third, combining orbital and surface hypotheses and strategies informing the techniques and methodology will be developed for their exploration.

## **5.3 References**

- Allen, C.C., Morris, R.V., McKay, D.S., 1996. Oxygen extraction from lunar soils and pyroclastic glass. *Journal of Geophysical Research: Planets* 101, 26085–26095.  
<https://doi.org/10.1029/96je02726>
- Artemis Science Definition Team, 2020. Artemis III Science Definition Team Report (No. NASA/SP-20205009602).

- Bennett, K.A., Horgan, B.H.N., Gaddis, L.R., Greenhagen, B.T., Allen, C.C., Hayne, P.O., III, J.F.B., Paige, D.A., 2016. Complex explosive volcanic activity on the Moon within Oppenheimer crater. *Icarus* 273, 296–314. <https://doi.org/10.1016/j.Icarus.2016.02.007>
- Gaddis, L.R., Horgan, B., McBride, M., Bennett, K., Stopar, J., Gustafson, J.O., 2016. Alphonsus Crater: Compositional Clues to Eruption Styles of Lunar Small Volcanoes. *Lunar and Planetary Science Conference* 47, 2065.
- Green, R.O., Pieters, C., Mouroulis, P., Eastwood, M., Boardman, J., Glavich, T., Isaacson, P., Annadurai, M., Besse, S., Barr, D., Buratti, B., Cate, D., Chatterjee, A., Clark, R., Cheek, L., Combe, J., Dhingra, D., Essandoh, V., Geier, S., Goswami, J.N., Green, R., Haemmerle, V., Head, J., Hovland, L., Hyman, S., Klima, R., Koch, T., Kramer, G., Kumar, A.S.K., Lee, K., Lundeen, S., Malaret, E., McCord, T., McLaughlin, S., Mustard, J., Nettles, J., Petro, N., Plourde, K., Racho, C., Rodriquez, J., Runyon, C., Sellar, G., Smith, C., Sobel, H., Staid, M., Sunshine, J., Taylor, L., Thaisen, K., Tompkins, S., Tseng, H., Vane, G., Varanasi, P., White, M., Wilson, D., 2011. The Moon Mineralogy Mapper (M3) imaging spectrometer for lunar science: Instrument description, calibration, on-orbit measurements, science data calibration and on-orbit validation. *Journal of Geophysical Research: Planets* 116, E00G19. <https://doi.org/10.1029/2011je003797>
- Head, J.W., Wilson, L., 1979. Alphonsus-type dark-halo craters: Morphology, Morphometry and eruption conditions. *Lunar and Planetary Science Conference* 10, 2861–2897.
- Henderson, M. J.B., B.Horgan, Gaddis, L., Bennett, K.A., 2020. Spectral Diversity of Explosive Volcanic Deposits in Schrödinger Basin with Moon Mineralogy Mapper Data, in: *European Lunar Symposium*.
- Henderson, M.J.B., Horgan, B.H.N., 2021. Spectral Analysis of Explosive and Effusive Volcanic Edifices in the Marius Hills Volcanic Complex with Moon Mineralogy Mapper 2465.
- Henderson, M. J. B., Horgan, B.H.N., Rowe, M.C., Wall, K.T., Scudder, N.A., 2020. Determining the Volcanic Eruption Style of Tephra Deposits From Infrared Spectroscopy. *Earth Space Sci* 7. <https://doi.org/10.1029/2019ea001013>
- Horgan, B.H.N., Cloutis, E.A., Mann, P., III, J.F.B., 2014. Near-infrared spectra of ferrous mineral mixtures and methods for their identification in planetary surface spectra. *Icarus* 234, 132–154. <https://doi.org/10.1016/j.Icarus.2014.02.031>
- Jawin, E.R., Valencia, S.N., Watkins, R.N., Crowell, J.M., Neal, C.R., Schmidt, G., 2019. Lunar Science for Landed Missions Workshop Findings Report. *Earth and Space Science* 6, 2–40. <https://doi.org/10.1029/2018ea000490>
- Kring, D.A., Robinson, K.L., 2018. A Lunar Sample Return Strategy for the Schrödinger Basin that taps into the Volatile Cycle of the Lunar Farside. *European Lunar Symposium*. <https://doi.org/10.1098/rsta.2013.0254>

- McBride, M.J., Horgan, B.H.N., Gaddis, L.R., 2016. Revisiting the Mineralogy of the Aristarchus Regional Pyroclastic Deposit with New M3 Analysis Techniques. Lunar and Planetary Science Conference 47, 3052.
- MEPAG, 2020. Mars Science Goals, Objectives, Investigations, and Priorities: 2020. LPI 2474.
- NASA, 2020. Artemis Plan: NASA's Lunar Exploration Program Overview.
- O'Sullivan, K.M., Kohout, T., Thaisen, K.G., Kring, D.A., 2011. Calibrating several key lunar stratigraphic units representing 4 b.y. of lunar history within Schrödinger basin, in: Ambrose, W.A., Williams, D.A. (Eds.), Recent Advances and Current Research Issues in Lunar Stratigraphy. Geological Society of America, pp. 117–127.
- Pieters, C.M., Boardman, J., Buratti, B., Chatterjee, A., 2009. The Moon mineralogy mapper (M3) on Chandrayaan-1. *Curr Sci*.
- Wieczorek, M.A., Neumann, G.A., Nimmo, F., Kiefer, W.S., Taylor, G.J., Melosh, H.J., Phillips, R.J., Solomon, S.C., Andrews-Hanna, J.C., Asmar, S.W., Konopliv, A.S., Lemoine, F.G., Smith, D.E., Watkins, M.M., Williams, J.G., Zuber, M.T., 2013. The Crust of the Moon as Seen by GRAIL. *Science* 339, 671–675. <https://doi.org/10.1126/science.1231530>.

## **APPENDIX A. CHAPTER 2 SUPPORTING INFORMATION**

### **INTRODUCTION**

The measured visible/near-infrared (VNIR) and thermal-infrared spectra data for the tephra samples and glass mixtures are included in an associated excel worksheet available within the Supporting Information of the published paper located at <https://agupubs.onlinelibrary.wiley.com/doi/full/10.1029/2019EA001013>. Additionally, the TIR unmixing results are included for both the tephra samples and the glass mixtures. The spectral library used for the deconvolutions listed in the main text Table 2 is publicly available on the ASU TES spectral library site (<http://speclib.asu.edu/>) under the name mhenderson\_2019.

## APPENDIX B. CHAPTER 3 SUPPORTING INFORMATION

Table B-1. List of cones within Marius Hills identified by Lawrence et al. (2013) and through the spectral observations in Chapter 3. New cones identified are located at the bottom of the table.

Identifier	Latitude	Longitude	Class	Origin	E Direction
124	12.01	301.39	C	Lawrence <i>et al.</i> (2013)	
M61	12.52	301.67	U	This Study	
123	12.57	301.70	E	Lawrence et al. (2013)	216°
194	12.49	301.85	U	Lawrence et al. (2013)	
050	15.30	302.08	C	Lawrence et al. (2013)	
126	11.09	302.10	C	Lawrence et al. (2013)	
104	11.47	302.32	C	Lawrence et al. (2013)	
M34	11.33	302.43	N	This Study	
049	15.52	302.43	C	Lawrence et al. (2013)	
085	11.18	302.46	C	Lawrence et al. (2013)	
049 -2	15.65	302.66	no	Lawrence et al. (2013)	
M57	14.40	302.71	C	This Study	
M1	12.84	302.76	No	This Study	
M2	12.85	302.81	U	This Study	
M6	14.41	302.83	C	Lawrence et al. (2013)	
119	14.67	302.87	No	Lawrence et al. (2013)	
M5	13.66	303.00	C	This Study	
034-2	14.24	303.08	C	Lawrence et al. (2013)	
034-1	14.32	303.10	no	Lawrence et al. (2013)	
100	14.78	303.11	C	Lawrence et al. (2013)	
M4	13.76	303.12	C	This Study	
121	13.55	303.28	no	Lawrence et al. (2013)	
039	14.77	303.35	E	Lawrence et al. (2013)	348°
M3	12.28	303.40	E	This Study	356°
036-C	14.57	303.45	U	This Study	
036-P	14.68	303.46	No	Lawrence et al. (2013)	
036-I	14.61	303.47	E	Lawrence et al. (2013)	325°
097	12.28	303.62	U	Lawrence et al. (2013)	
038	14.59	303.65	No	Lawrence et al. (2013)	
193	10.45	303.92	U	Lawrence et al. (2013)	
M31	10.39	304.07	N	This Study	
041	13.47	304.10	C	Lawrence et al. (2013)	
M32	10.36	304.10	U	This Study	

M54	10.99	304.20	C	This Study	
045	14.62	304.21	C	Lawrence et al. (2013)	
075	10.79	304.24	C	Lawrence et al. (2013)	
M30	13.72	304.29	C	This Study	
M60	13.11	304.33	U	This Study	
M33	10.33	304.35	C	This Study	
025	13.04	304.36	No	Lawrence et al. (2013)	
M56	14.24	304.34	E	This Study	25 <sup>o</sup>
090	10.82	304.60	No	Lawrence et al. (2013)	
M52	15.09	304.63	C	This Study	
M51	15.07	304.63	No	This Study	
046	14.97	304.66	C	Lawrence et al. (2013)	
M53	15.19	304.67	U	This Study	
063	12.72	304.74	No	Lawrence et al. (2013)	
101	15.31	304.76	C	Lawrence et al. (2013)	
M55	14.07	304.78	E	This Study	310 <sup>o</sup>
M15	14.11	304.82	N	This Study	
M14	14.60	304.88	N	This Study	
005	14.31	304.88	No	Lawrence et al. (2013)	
M13	12.24	304.91	N	This Study	
M16	14.38	304.95	C	This Study	
M12	12.17	304.96	E	This Study	139 <sup>o</sup>
M11	12.01	305.01	C	This Study	
102-2	14.41	305.05	E	Lawrence et al. (2013)	322 <sup>o</sup>
M17	14.78	305.06	N	This Study	
102	14.53	305.07	C	Lawrence et al. (2013)	
M18	14.88	305.12	U	This Study	
154	11.98	305.13	N	Lawrence et al. (2013)	
219	11.14	305.13	C	Lawrence et al. (2013)	
M10	11.44	305.15	E	Lawrence et al. (2013)	316 <sup>o</sup>
186	12.65	305.17	U	Lawrence et al. (2013)	
M8	10.91	305.18	C	Lawrence et al. (2013)	
M58	12.28	305.19	E	This Study	139 <sup>o</sup>
M59	12.18	305.20	E	This Study	349 <sup>o</sup>
M7	10.87	305.23	C	Lawrence et al. (2013)	
118	14.35	305.25	C	Lawrence et al. (2013)	
M9	10.83	305.25	C	Lawrence et al. (2013)	
M19	14.20	305.28	N	Lawrence et al. (2013)	
098-3	11.71	305.41	C	Lawrence et al. (2013)	

098-1	11.61	305.41	C	Lawrence et al. (2013)	
M35	10.60	305.43	U	This Study	
098-2	11.63	305.46	C	Lawrence et al. (2013)	
M24	13.77	305.52	C	Lawrence et al. (2013)	
003	14.37	305.53	no	Lawrence et al. (2013)	
M36	11.55	305.58	U	This Study	
M20	14.65	305.83	E	Lawrence et al. (2013)	359 <sup>o</sup>
43	12.46	305.87	E	Lawrence et al. (2013)	141 <sup>o</sup>
M37	13.53	306.01	E	This Study	348 <sup>o</sup>
M22	14.33	306.02	E	This Study	342 <sup>o</sup>
M38	13.54	306.05	N	This Study	
M39	13.51	306.07	E	This Study	156 <sup>o</sup>
M40	13.54	306.12	U	This Study	
M21	14.56	306.12	E	Lawrence et al. (2013)	24 <sup>o</sup>
163	14.16	306.13	C	Lawrence et al. (2013)	
M23	14.05	306.25	C	Lawrence et al. (2013)	
103	14.57	306.25	N	Lawrence et al. (2013)	
055	13.40	306.35	C	Lawrence et al. (2013)	
M27	15.30	306.41	no	This Study	
M26	15.21	306.41	U	Lawrence et al. (2013)	
M25	15.26	306.42	C	This Study	
059-1	13.43	306.45	no	Lawrence et al. (2013)	
M29	14.68	306.47	U	This Study	
061-1	13.64	306.48	C	Lawrence et al. (2013)	
M28	14.71	306.49	C	Lawrence et al. (2013)	
059	13.14	306.50	E	Lawrence et al. (2013)	174 <sup>o</sup>
164	14.48	306.50	E	Lawrence et al. (2013)	323 <sup>o</sup>
059-2	13.34	306.51	no	Lawrence et al. (2013)	
061-l	13.65	306.52	U	Lawrence et al. (2013)	
061	13.74	306.59	C	Lawrence et al. (2013)	
061-2	13.71	306.60	E	Lawrence et al. (2013)	158 <sup>o</sup>
M41	12.89	306.62	E	This Study	188 <sup>o</sup>
060-1	13.51	306.62	N	Lawrence et al. (2013)	
185-2	13.40	306.63	C	Lawrence et al. (2013)	
060-2	13.45	306.65	C	Lawrence et al. (2013)	
185-1	13.36	306.67	C	Lawrence et al. (2013)	
218	13.25	306.69	no	Lawrence et al. (2013)	
M44	9.48	306.70	E	Lawrence et al. (2013)	175 <sup>o</sup>
184	13.17	306.74	C	Lawrence et al. (2013)	

M43	13.54	306.82	E	This Study	206 <sup>o</sup>
M42	15.05	306.88	C	This Study	
M73	14.35	307.10	no	This Study	
129	9.96	307.17	E	Lawrence et al. (2013)	230 <sup>o</sup>
M63	13.63	307.19	U	Lawrence et al. (2013)	
092	8.10	307.21	no	Lawrence et al. (2013)	
129	10.03	307.21	U	Lawrence et al. (2013)	
018	14.29	307.31	U	Lawrence et al. (2013)	
107	13.24	307.31	C	Lawrence et al. (2013)	
M74	13.93	307.35	U	This Study	
M68	14.77	307.39	U	Lawrence et al. (2013)	
M75	14.05	307.52	C	This Study	
M62	11.09	307.61	no	This Study	
M67	15.20	307.94	C	Lawrence et al. (2013)	
M65	12.58	308.05	C	Lawrence et al. (2013)	
M66	12.61	308.15	no	Lawrence et al. (2013)	
172	13.68	308.16	U	Lawrence et al. (2013)	
179	14.34	308.17	no	Lawrence et al. (2013)	
M69	15.10	308.23	U	This Study	
225	14.66	308.23	U	Lawrence et al. (2013)	
188	13.50	308.26	E	Lawrence et al. (2013)	38 <sup>o</sup>
M64	12.69	308.36	C	This Study	
M71	14.82	308.43	U	This Study	
M76	13.66	308.52	no	This Study	
076	14.68	308.56	E	Lawrence et al. (2013)	205 <sup>o</sup>
M70	15.03	308.59	U	Lawrence et al. (2013)	
015	13.31	308.60	C	Lawrence et al. (2013)	
M61	10.23	308.73	no	This Study	
021	13.77	308.80	U	Lawrence et al. (2013)	
139	10.11	308.82	C	Lawrence et al. (2013)	
147	15.11	308.88	U	Lawrence et al. (2013)	
M72	14.26	309.09	C	This Study	
M49	13.51	309.49	E	This Study	4 <sup>o</sup>
M48	13.46	309.51	C	Lawrence et al. (2013)	
M45	10.92	309.80	E	This Study	331 <sup>o</sup>
M50	14.43	309.85	U	Lawrence et al. (2013)	
173	14.31	310.01	no	Lawrence et al. (2013)	
M47	13.66	310.33	C	Lawrence et al. (2013)	
016	13.31	310.42	C	Lawrence et al. (2013)	

M46	11.73	311.43	N	This Study	
<b>New Cones</b>					
M77	10.96	304.23	C	This Study	
M78	11.70	305.41	C	This Study	
M79	12.57	306.24	E	This Study	331 <sup>o</sup>

## VITA

### Marie Julia (McBride) Henderson

#### Education

Doctoral Candidate in **Planetary Science** at Purdue University August 2015-August 2021

Advisor: Dr. Briony Horgan Defense Date: July 20, 2021

Dissertation Title: Remote Sensing as a Window into Planetary Volcanic Eruption Styles

Bachelor of Science in **Solar, Earth, and Planetary Sciences**

Florida Institute of Technology Graduated Cum laude – December 2013

#### Professional Experience

##### Graduate Research and Teaching Assistant

- Purdue University, West Lafayette, IN, August 2015-August 2021
- Spectral analysis of glass in lunar pyroclastic deposits using Moon Mineralogy Mapper data
- Laboratory analysis of terrestrial volcanic tephra using Visible/near-infrared and thermal infrared spectrometers analogous to orbital instrumentation at Mars.
- Mars Science Laboratory Participating Scientist Collaborator – participating in Curiosity surface operations in the roles of MAHLI and MARDI Payload Uplink Lead

##### Assistant to the MSL MAHLI camera Principal Investigator, Dr. Ken Edgett

- Malin Space Science Systems, San Diego, CA, January 2014 – July 2015
- Processed and analyzed MAHLI images for the MSL science team and NASA press releases
- Presented weekly to MSL Science Team on the scope and science results of MAHLI images
- Prepared metadata for NASA Planetary Data System (NASA PDS) Archive

##### Hidden Lunar Impact Basins Researcher

- NASA Goddard Space Flight Center, Greenbelt, MD, May 2013 – August 2013
- Used GRAIL gravity and LOLA topography data to identify and catalog hidden Lunar Impact Basins with Dr. Herbert Frey

##### Mars Science Laboratory Science Operations Intern

- NASA/Caltech Jet Propulsion Laboratory, Pasadena, CA, June 2012- November 2012
- Intern for MSL landing (August 5, 2012) and Mars time surface operations
- Supported Science and Operations mission teams for MSL landing and surface operations with Nicole Spanovich and Dr. Joy Crisp

##### NASA Lunar and Planetary Science Academy

- NASA Goddard Space Flight Center, Greenbelt, MD, June 2011 – August 2011
- Restoration and Calibration of the Apollo Lunar ALSEP Data with Dr. David R. Williams

##### Fieldwork Experience

- International Volcanology Field School in Kamchatka, Kamchatka, Russia, 2017

- Martian analog for chemical weathering in glacial volcanic environments, aqueous geochemistry assistant, Three Sisters, OR, 2016 and 2017
- Andes and Galapagos Volcanology Field Camp, Ecuador and Galapagos Islands, 2016
- NASA Planetary Volcanology Workshop, Island of Hawai'i, 2016
- Geologic Field Methods Class mapping field trip to Johnson Shut-Ins State Park, MO, 2016

## Support Current and Past

- 2021 Purdue College of Science Graduate School Summer Research Grant
- 2018-2019 National Science Foundation Graduate Research Internship Program  
*Geologic Study of Lunar Volcanic Deposits in Schrödinger Crater (PI: Dr. Lisa Gaddis)*
- 2017-2021 National Science Foundation Graduate Research Fellowship Program  
*Evaluating the Resource Potential of Lunar Pyroclastic Deposits (PI: Dr. Briony Horgan)*
- 2015-2019 Student Co-I, NASA Lunar Data Analysis Program  
*Lunar Pyroclastic Deposits: Window to the Lunar Interior (PI: Dr. Lisa Gaddis)*
- 2017-2018 Amelia Earhart Fellowship – Zonta International  
*Investigation of Lunar Pyroclastic Deposits*
- 2015-2018 Indiana Space Grant Consortium Fellowship  
*Evaluating the Resource Potential of Lunar Pyroclastic Deposits*
- 2011-2013 Florida Space Grant Consortium Continuing Research Sponsorship  
*Restoration of Apollo ALSEP data (PI: Dr. David R. Williams)*
- 2011-2013 NASA Motivating Undergraduates in Science and Technology Scholarship

## Publications

1. **Henderson M. J.**, Horgan B.H.N, Rowe M.C., Wall K.T., Scudder, N.A. (2020) Determining the Volcanic Eruption Style of Tephra Deposits from Infrared Spectroscopy. *Earth and Space Science*, 7, 2019EA001013. <https://doi.org/10.1029/2019EA001013>
2. Bennett, K. A., et al. including **Henderson, M.J.**, (2021). Diagenesis revealed by fine-scale features at Vera Rubin ridge, Gale crater, Mars. *Journal of Geophysical Research: Planets*, 126, e2019JE006311. <https://doi.org/10.1029/2019JE006311>.
3. Edgett, K.S., et al. including **Henderson, M.J.**, 2020, Extraformational sediment recycling on Mars: *Geosphere*, v. 16, no. 6, pp. 1508–1537. doi:10.1130/GES02244.1
4. Stack, K. M., et al., including **M.J. McBride**. (2019), Evidence for plunging river plume deposits in the Pahrump Hills member of the Murray formation, Gale crater, Mars. *Sedimentology*. doi:10.1111/sed.12558
5. Yingst, R. A., Edgett, K. S., Kennedy, M. R., Krezoski, G. M., **McBride, M. J.**, Minitti, M. E., Ravine, M. A., and Williams, R. M. E.: (2016) MAHLI on Mars: lessons learned operating a geoscience camera on a landed payload robotic arm, *Geosci. Instrum. Method. Data Syst.*, 5, 205-217, doi:10.5194/gi-5-205-2016
6. Lanza, N. L., et al., including **M.J. McBride** (2016). Oxidation of manganese in an ancient aquifer, Kimberley formation, Gale crater, Mars. *Geophysical Research Letters*. <http://doi.org/10.1002/2016GL069109>

7. VanBommel et al. including **M.J. McBride** (2016), "Deconvolution of distinct lithology chemistry through oversampling with the Mars Science Laboratory Alpha Particle X-ray Spectrometer" *Journal of X-ray Spectrometry*.
8. Yingst, R. A., et al., including **M.J. McBride** (2016). Characteristics of pebble and cobble-sized clasts along the Curiosity rover traverse from sol 100 to 750: Terrain types, potential sources, and transport mechanisms. *Icarus*. <http://doi.org/10.1016/j.Icarus.2016.03.001>
9. Grotzinger, J. P. et al., including **M.J. McBride** (2015). Deposition, exhumation, and paleoclimate of an ancient lake deposit, Gale crater, Mars. *Science*, 350(6257).

## **Honors and Awards**

- Purdue Earth, Atmospheric, & Planetary Sciences Dept, Outstanding Graduate Student, 2021
- LEAG Bernard Ray Hawke Next Lunar Generation Career Development Award, 2018
- Purdue Graduate Student International Travel Grant, 2017
- NASA Group Achievement Award - MSL Extended Mission-1 Science & Ops Team, 2017
- National Science Foundation, Graduate Research Fellowship Program, 2017
- Amelia Earhart Fellowship, 2017
- Indiana Space Grant Fellowship, 2016, 2017
- National Science Foundation, Graduate Research Fellowship, Honorable Mention, 2016
- Lunar and Planetary Institute Career Development Award, 2016
- Project appointed Expert Consultant to the MSL Science Team, Oct 2015
- NASA Group Achievement Award - MSL Prime Mission Science & Ops Team, 2015
- NASA Group Achievement Award - MSL Science Operations Team, 2013
- John Mather (Nobel Prize in Physics, 2006) Nobel Scholar, 2013
- Northrop Grumman's' College of Science Champion - Florida Tech Senior Showcase, 2013
- Best in Show for Dept. of Space Sciences at Florida Tech's' Senior Design Showcase, 2013
- Gerald A. Soffen Memorial Fund Travel Grant -2012
- Dean's' List, Florida Institute of Technology, 2009-2013

## **Invited Talks**

- NASA Goddard Space Flight Center – Greenbelt, MD, May 2021
- Queens Public Library – Jamaica, NY, February 2021
- Cradle of Aviation Museum – Garden City, NY, March 2018
- Zonta Club of Indianapolis Meeting – Indianapolis, IN, January 2018
- Zonta International District 6 Fall Meeting – Madison, WI, October 2017
- Lane Technical College Prep High School – Chicago, IL, May 2017
- Physics Department Colloquium at Trinity University – San Antonio, TX, November 2013
- NASA-Florida Space Grant Consortium Board Meeting – Kennedy Space Center, FL, Nov 2013
- NASA-National Space Grant Directors Meeting – Charleston, NC, October 2013
- Mission Space and Range Pioneers Fall Dinner – Cocoa, FL, October 2013

## **Press Conferences and Press Coverage**

### **American Geophysical Union- Fall Meeting 2012 Press Conference**

- Selected panel member: At 40, Apollo Lunar Samples Still Yielding New Data
- Panel members: Dr. Harrison Schmitt, Apollo 17 moonwalker, and Prof. Dr. Bradley Jolliff,
- [www.youtube.com/watch?v=e2Ugfx8-Ccs](http://www.youtube.com/watch?v=e2Ugfx8-Ccs)

### **Earth Magazine – April 2013, Cover Image and Article**

- "Apollo science, 40 years later: Scientists reopen a lunar cold case"
- [www.earthmagazine.org/article/apollo-science-40-years-later-scientists-reopen-lunar-cold-case](http://www.earthmagazine.org/article/apollo-science-40-years-later-scientists-reopen-lunar-cold-case)

### **Florida Tech Today Magazine – Spring 2013, Cover Image and Article**

- "Resurrecting Apollo"
- [www.fit.edu/media/site-specific/wwwfitedu/florida-tech-magazine/documents/ftt-spring2013.pdf](http://www.fit.edu/media/site-specific/wwwfitedu/florida-tech-magazine/documents/ftt-spring2013.pdf)

### **Local News Story about astronaut application – WTHR Indianapolis – March 8, 2016**

- [www.wthr.com/article/purdue-grad-among-over-18000-applying-for-nasa-astronaut-program](http://www.wthr.com/article/purdue-grad-among-over-18000-applying-for-nasa-astronaut-program)

### **Purdue Insights Magazine – Fall 2016 Issue, Article**

- "The Right Stuff"
- [purdueinsights.freeflowdp.com/purdueinsights/2974698994555645?pg=18#pg18](http://purdueinsights.freeflowdp.com/purdueinsights/2974698994555645?pg=18#pg18)

### **Women in Planetary Science – June 2017, Article**

- "Flying High: Two planetary scientists receive Zonta Amelia Earhart Fellowship"
- [womeninplanetaryscience.wordpress.com/2017/06/29/flying-high-two-planetary-scientists-receive-zonta-amelia-earhart-fellowship/](http://womeninplanetaryscience.wordpress.com/2017/06/29/flying-high-two-planetary-scientists-receive-zonta-amelia-earhart-fellowship/)

### **Purdue Earth, Atmospheric, and Planetary Sciences – June 2017, Article**

- "EAPS Graduate Student Awarded Multiple Fellowships"
- [www.eaps.purdue.edu/news/articles/2017/mcbride-fellowships.html?platform=hootsuite](http://www.eaps.purdue.edu/news/articles/2017/mcbride-fellowships.html?platform=hootsuite)

## **Selected Conference Presentations**

1. **Henderson, M. J.**, Horgan, B.H.N., Mineralogy of Explosive and Effusive Volcanic Edifices in the Marius Hills Volcanic Complex, LPSC, 52, 2465, 2021.
2. **Henderson, M. J.**, Horgan, B.H.N., Gaddis, L.R., Bennett, K.A., Spectral Diversity of Explosive Volcanic Deposits in Schrödinger Basin with Moon Mineralogy Mapper Data, European Lunar Symposium, 2020.
3. **McBride M. J.** Horgan B.H.N. Gaddis, L.R., Moon Mineralogy Mapper Analysis of Volcanic Deposits in Schrödinger Basin, LPSC, 50, 1985, 2019.
4. **McBride M. J.** Horgan B.H.N., Lawrence S.J., Spectral Analysis of Explosive and Effusive Volcanism in the Marius Hills Volcanic Complex, Geological Society of America Fall Meeting, Indianapolis, IN, 2018.
5. **McBride M. J.**, Horgan B.H.N., Gaddis L.R., Lawrence S.J., Diversity of Volcanic Eruption Styles in the Central Procellarum Region of the Moon, European Lunar Symposium, Toulouse, France 2018.
6. **McBride, M.J.**, B.H.N. Horgan, and S. J. Lawrence., Spectral Analysis of Lunar Cinder Cones in the Marius Hills Volcanic Complex, LPSC, 49, 2798, 2018.
7. **McBride M. J.** Horgan B.H.N., Rowe M.C., Wall K.T., Oxley B.M., 2017, Using Spectroscopy to Infer the Eruption Style and Volatile History of Volcanic Tephra, Abstract V33F-0568, presented at 2017, AGU, New Orleans, LA, Dec. 11-17.
8. **McBride M. J.** Horgan B.H.N. Gaddis L.R., Mapping Glass in the Marius Hills Volcanic Complex with Moon, Lunar and Planetary Science Conference, 48, 2989, 2017.
9. **McBride M. J.** Horgan B.H.N., Rowe M.C., Wall K.T., Oxley B.M., Determining Glass Content and Eruption Style from Spectral Analysis of Volcanic Tephra, Geological Society of America Cordilleran Meeting, Honolulu, HI 2017.

10. **McBride, Marie. J.**, Horgan, Briony H.N., Oxley, Benjamin M., Rowe, Michael C., Wall, Kellie T. 2016, The Effects of Glass Crystallinity and Eruption Style on Visible/Near-Infrared and Thermal Infrared Spectra of Volcanic Tephra. *Geological Society of America Abstracts with Programs*. Vol. 48, No.7
11. **McBride, M. J.**, Horgan, B.H.N., Gaddis, L.R., Revisiting the Mineralogy of the Aristarchus Regional Pyroclastic Deposit with New M<sup>3</sup> Analysis Techniques, Lunar and Planetary Science Conference, 47, 3052, 2016.
12. **McBride M. J.** et al., Mars Hand Lens Imager (MAHLI) Observations at the Pahrump Hills Field Site, Gale Crater, Lunar and Planetary Science Conference, 46, 2855, 2015.
13. **McBride, M. J.**, Frey, H.V., Improving Techniques for Determination of Lunar Basin Crater Retention Ages, Lunar and Planetary Science Conference, 45, 2150, 2014.
14. **McBride, M. J.**, Williams, D. R., Hills, H. K., 2013, Continued Analysis and Restoration of Apollo DTREM Instrument Data, Abstract P13B-1756 presented at 2013, Fall Meeting, AGU, San Francisco, CA, 9-13 December.
15. **McBride, M. J.**, Williams, D. R., Hills, H. K., Turner, N. E., First Time Analysis of Completely Restored DTREM Instrument Data from Apollo 14 and 15, Lunar and Planetary Science Conference, 44, 2868, 2013.
16. **McBride, M.J.**, D.R. Williams, H.K. Hills (2012), Restoration and Future Analysis of the Apollo Lunar Dust Detector Data, Abstract P43B-1925 presented at 2012 Fall Meeting, AGU, San Francisco, Calif., 3-7 Dec.
17. **McBride, M.**, D.R. Williams, & H.K. Hills, Restoration and reexamination of Apollo Lunar Dust Detector from original telemetry files, Lunar and Planetary Science Conference, 43, 2075, 2012.
18. **McBride, M.J.**, D.R. Williams, H.K. Hills, and N.E. Turner, Restoration and Reexamination of Data from the Apollo 11, 12, 14, and 15 Dust, Thermal and Radiation Engineering Measurements Experiments, Lunar Science 2012 Forum, NASA Ames Research Center, July 2012.

## Service

**NASA Review Panel:** Executive Secretary, 2019a, 2019b, 2021

**NASA Planetary Data System (NASA PDS):** Dataset Reviewer

**Lunar Surface Science Workshop: LSSW 8:** Structuring Real-Time Science Support of Artemis Crewed Operations: Facilitator, prepared community reviewed formal report for NASA HQ

## Athletics and Certificates

Ironman Louisville Triathlon, Finisher, October 14, 2018

Florida Athletic Coaching Certification, Completed required coursework December 2013

Triathlon Club of San Diego, 2014-Present

Florida Tech Women Varsity Rowing, 2009-2011

## Outreach

**Purdue 50<sup>th</sup> Anniversary of Apollo 11 Organization Team and EAPS Lead**

- A member of a university-wide action team that planned an event for over 5000 people to celebrate the 50<sup>th</sup> anniversary of Apollo 11 on July 20, 2019

- Prepared displays, activities (including procuring real Apollo samples from NASA), and trained volunteers in preparation for the event

**Tiger Techs Robotics Mentor, Sharon Jr./Sr. High School, Sharon, PA, 2018-Present**

- Help three robotics teams identify problems in space exploration as well as projects to research and assist in preparing for regional and national competitions

**School Presentations, 1-3 times a year, 2009-Present**

- Presenting talks and assemblies to K-12 and college students on: preparing for college, earning internships/jobs, and informal discussions about my research or space missions involvement

**Oasis Indianapolis Class Leader – Non-profit organization for healthy aging**

- Lecture: 50 years of Lunar Science – July 10, 2019
- Lecture: Roving Mars: NASA's' search for life on the red planet – August 2, 2019

**Retirement Community Speaker, Whispering Oaks, Hermitage, PA, June 2, 2018**

**Ionta Elementary School Speaker, Hermitage, PA, Mars Rover**

- Assemblies for Kindergarten - 3<sup>rd</sup> grade students, May 2018

**Women in STEM Panelist, Cradle of Aviation Museum, Garden City, NY, March 12, 2018**

- Speaker on a panel of women in aviation and aerospace careers as a program for about 175 high-school-aged girls. The goal of the event was to encourage girls to enter STEM careers.

**Hickory High School Career Day Panelist, Hermitage, PA, February 2018**

- Answered questions from about 200 10<sup>th</sup> grade students about careers and experiences with NASA and pursuing STEM fields

**Wabash Area Lifetime Learning Association Instructor, October-November 2017**

- Taught a "Roving Mars" class for senior citizens in the Wabash River region of Indiana

**Imagination Station Children's Museum, 2016-2018**

- Organizer and presenter for multiple events focused on planetary science and STEM fields to local children and summer camp groups
- EAPS Passport Day – Planetary Lead - 2016

**Purdue University, Dept Earth, Atmospheric, & Planetary Sciences Outreach, 2016-2018**

- Volunteer for multiple events focused on geosciences for local events and school groups

**Indianapolis Symphony Orchestra, February 2016**

- During a space-themed concert, I created a booth displaying images from the Curiosity Rover mission and spoke to patrons about the mission and the science being conducted.

**Purdue Engineering EPICS Project Reviewer, Spring 2016**

- Review and mentor student engineering projects being developed for museum displays or public events that have a Mars rover focus

**Malin Space Science Systems Public Outreach Team, 2014-2015**

- Volunteering time to increase the presence and understanding of MSSS, NASA, and space exploration in the surrounding community.